

CHAPTER 6

Experimental Setup of Inter-channel Mixing

6.1 Introduction

In this chapter, we describe the basic experimental setup and the inflow conditions used for the inter-channel mixing experiment. In §6.2, we provide the details of the instruments used for the experiments, which include the flow loop setup, the geometry of the test section, flow conditioning methods, and details of all instruments used for the experiment. In §6.3, we provide the boundary layer conditions of each flow measured by the Laser Doppler Velocimetry (LDV).

6.2 Experimental Setup

6.2.1 Flow loop and test section

The flow loop consists of a test section with an adjustable gap, two centrifugal pumps which can condition the flow rate of the channel A and B separately. Each inlet and outlet of channel A and B has a turbine volume flow rate sensor, and static pressure transducers and one differential pressure transducer are installed at the inlet of channel A and B. We installed a baffle box and a contraction at the inlet of each channel to trip the boundary layer at the wall. Additionally, we added a 0.5 mm protrusion immediately after the contraction to encourage the turbulent flow near the wall. Water reservoir is used to provide conditioned water source for PIV and fluorescein concentration measurement. A positive displacement pump controls the amount of dye injected into the inlet of channel B. Fig. 6.1 shows the piping and instrument diagram of the flow loop.

The test section consists of two square channels and a rectangular gap between them. Both channel A and B have the dimension of 127 mm \times 127 mm in cross section. The gap width W_g and length L_g are fixed at 228.6 mm and 1219.2 mm, respectively. The gap

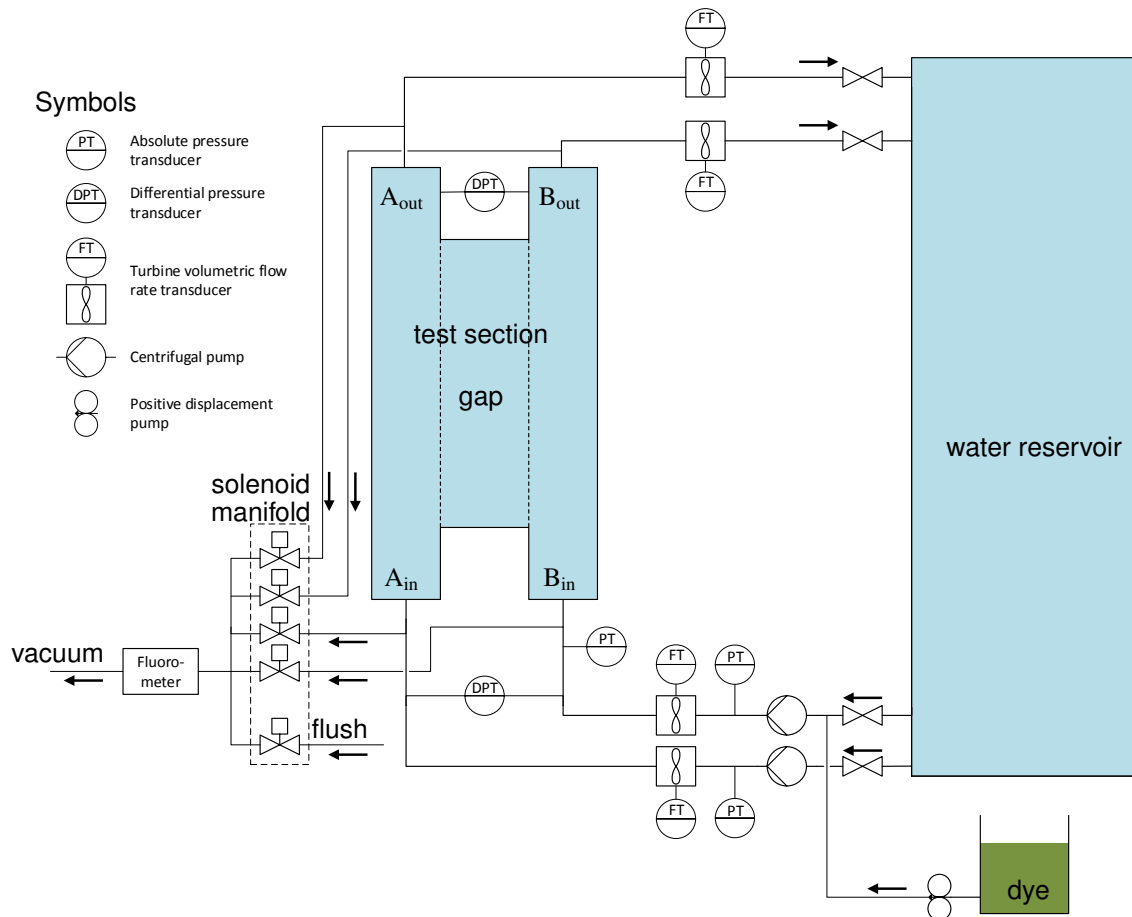


Figure 6.1: Piping and instrument diagram of the flow loop. The flow loop consists of a test section with an adjustable gap, two centrifugal pumps which can condition the flow rate of the channel A and B separately. Each inlet and outlet of channel A and B has a turbine volume flow rate sensor. Two static pressure transducers and one differential pressure transducer are installed at the inlet. A baffle box and a contraction is installed at the inlet of each channel to trip the boundary layer. Water reservoir is used to provide conditioned water source for PIV and fluorescein concentration measurement. A positive displacement pump controls the amount of dye injected into the inlet of channel B.

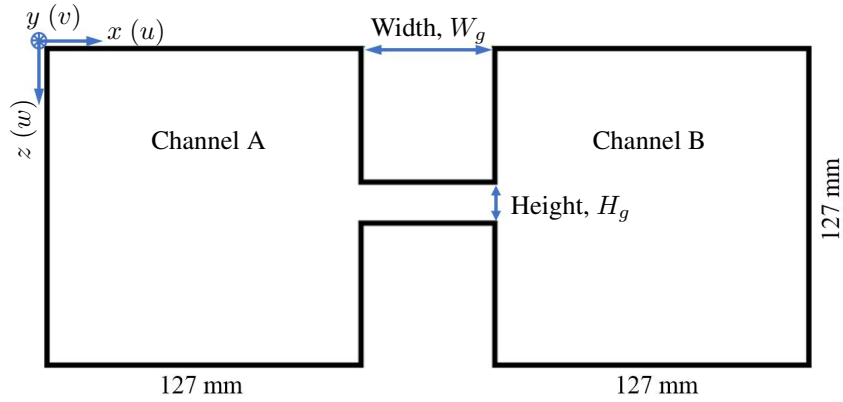


Figure 6.2: Cross sectional geometry of the test section and the coordinate system used for the boundary layer description. Axes convention follows the ‘right hand rule,’ with the origin $y = 0$ defined at the beginning of the gap.

height H_g can be varied from 0 to 50 mm. Fig. 6.2 shows the cross sectional geometry of the test section. The hydraulic diameter D_h is defined as $D_h = 4A_w/P_w$ where A_w is the cross-sectional area and P_w is the wetted perimeter of the channel. For the given test section, the hydraulic diameter of both channels is $D_h = 127\text{mm}$.

6.2.2 Flow conditioning

The 6-to-1 ratio inlet contractions were designed to produce a uniform and low turbulence inflow to the rectangular channel. The baffle box located at the bottom of the contraction contains perforated plates and screens, producing a relatively uniform inflow into the contraction. Immediately after the contraction, an attempt is made to trip the boundary layer to become turbulent. At $Re_{D_h} = 10^5$, to have a fully developed channel flow upstream of the gap would have require greater than 36 channel hydraulic diameters of run-up length (approximately 4.6 m) [17], and hence it was decided to forgo having a fully developed inflow. Fig. 6.3 shows the detailed sectional drawing of the test section, contraction, baffle box, and the trip plate.

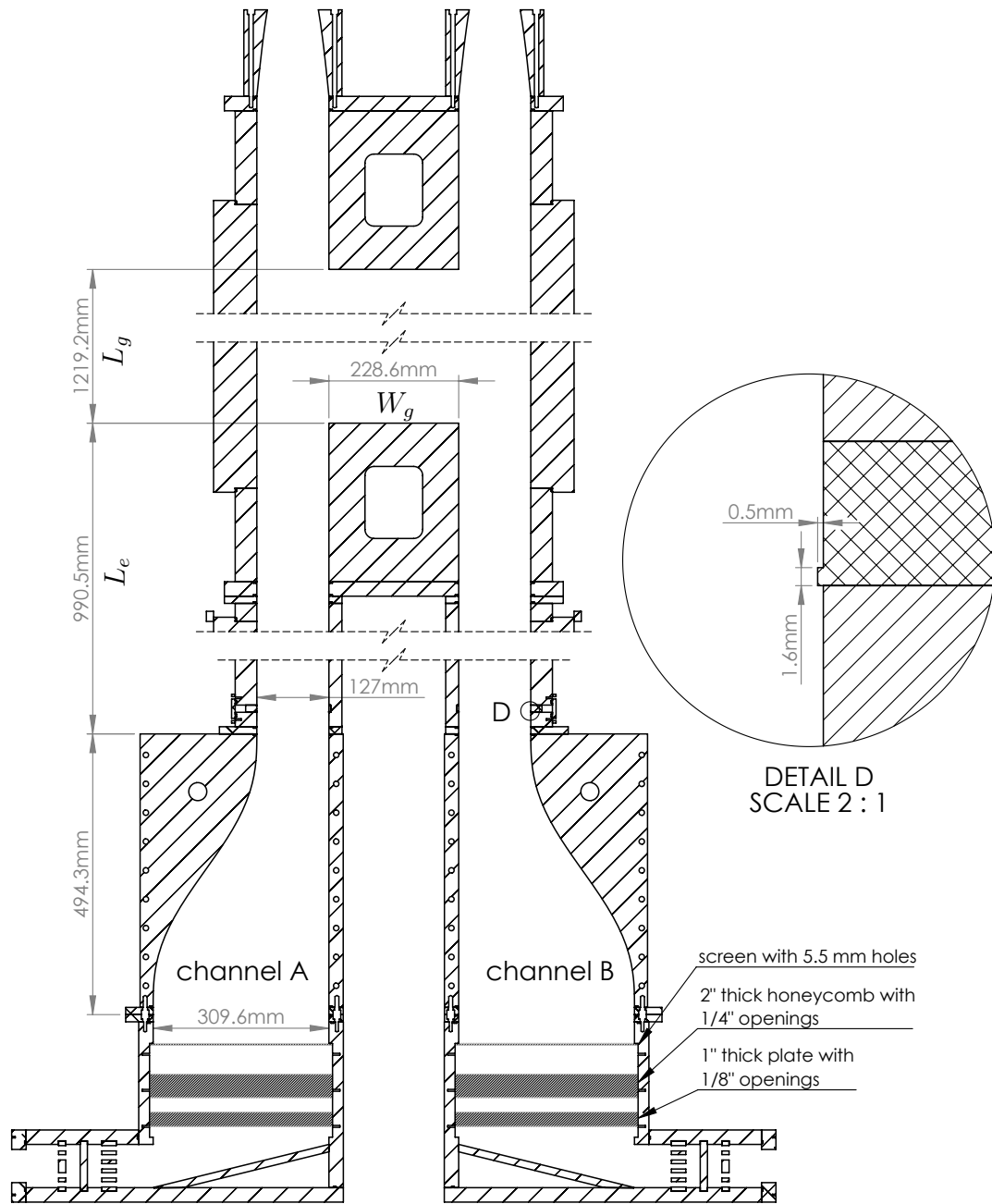


Figure 6.3: Sectional geometry of the test section, contraction, baffle box and the trip plate. Detail D shows the detailed view of the trip plate, where 0.5mm protrusion is applied to trip the boundary layer.

6.2.3 Instrumentation and Equipment

The measurements performed and instrumentation used include:

1. Volumetric flow rates at the inlets
 - Omega Engineering SYS/FTB-109/FLSC-18B turbine flow meter
 - Manufacturer specified accuracy $\pm 0.5\%$ of reading
 - Manufacturer supplied gal/pulse calibration used (15-225 gpm)
Note: Side B inlet flow meter was replaced between runs 28 and 29. (The old flow meter suffered a sudden failure. Run 29 was a repeat of run 28 conditions after replacing the flow meter, and yielded the same results, thus giving confidence that the old flow meter had not been providing erroneous data prior to failure.)
2. Volumetric flow rates at the outlets
 - Omega Engineering FTB740 turbine flow meter with FTB700-T blind 4-20 mA transmitters
 - Manufacturer specified accuracy $\pm 1\%$ FS (± 6 gpm) for turbine flow meter
 - Manufacturer specified accuracy $\pm 1\%$ for 4-20 mA transmitter with 3 sec response time (95% FS)
 - Manufacturer supplied gal/pulse calibration used (6-600 gpm)
3. Fluorescein sodium salt concentration on both sides before and after the test section
 - Turner Designs Cyclops 7 fluorometer, PN 2100-000/2108-000, serial number 2180463, F (for Fluorescein dye)
 - Custom made fluorometer. Used only to compare against C7 to detect anomalous readings as they occurred.
 - Uncertainty defined as $\pm 0.5\%$ or reading + 1 ppb.
 - Dye used : Fluorescein sodium salt (F6377, Sigma-Aldrich)
4. Water temperature at both inlets and outlets
 - Ultra precise 4-wire 100 Ohm platinum Resistance Temperature Detector (RTD) sensor P-M-A-1/4-6-0-P-3
 - Manufacturer specified accuracy $\pm (0.15 + 0.002|T|)$ °C from -100 to 450 °C

- Checked in ice bath, and read the temperature within 0.4 °C (giving a high reading), and at room temperature agreed with Mannix DLAF-8000 within 0.3 °C.
5. Static pressure immediately downstream of the boundary layer trip in channel B
 - Absolute pressure transducer PX219-030A10V with PS-4E snubber
 - Manufacturer specified accuracy ± 0.25 % FS
 6. Static pressures at outlets of both pumps (for the primary purpose of general system performance monitoring and operator safety, and hence less accurate measurement was sufficient)
 - Omega Engineering PX303-200G5V
 - Manufacturer specified accuracy ± 0.25 % BFSL (± 0.5 psi)
 7. Static pressures at inlets to both baffle boxes (for the primary purpose of general system performance monitoring and operator safety, and hence less accurate measurement was sufficient)
 - Omega Engineering PX303-200G5V
 - Manufacturer specified accuracy ± 0.25 % BFSL (± 0.5 psi)
 8. Pressure difference between sides A and B, $6.45 D_h$ (32.25 inches) upstream of the gap
 - Omega Engineering PX760-06WCDI
 - Manufacturer specified accuracy ± 0.17 % FS of nominal range
 - Also measured using a water-air manometer with estimated accuracy of ± 0.03 inches (± 0.76 mm) H₂O.
 - Lines to both transducers were flushed every day to remove bubbles.

Both pumps were controlled by identical Yaskawa E7 variable frequency drives with bypass option (model: E7LVD024CFX).

Dye injected via Pulsatron ChemTech Peristaltic Pump Model Series XPV-100 - Dual Head. Model Number XP100-LG-LX. According to manufacturer specifications, the flow rate is repeatable within ± 5 %.

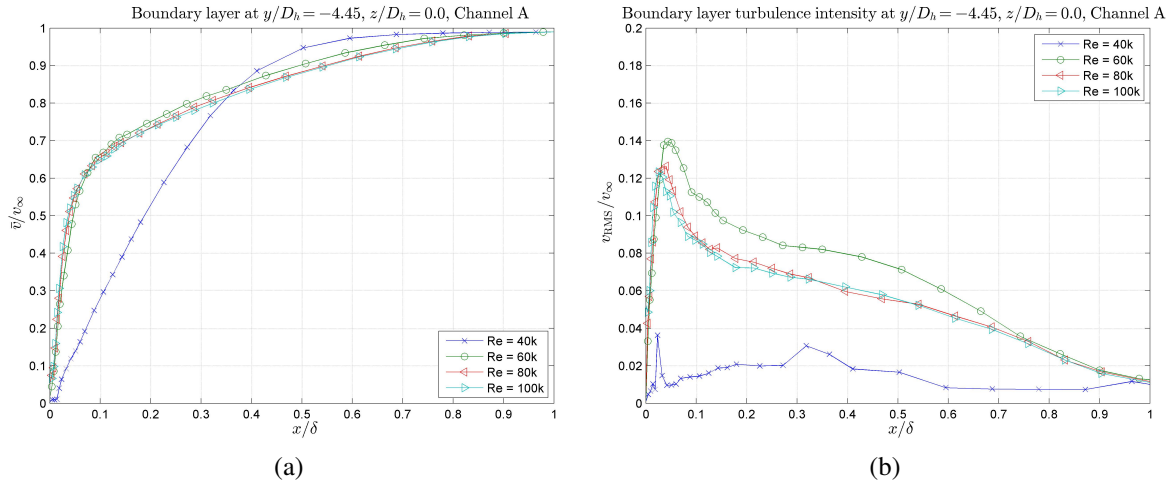


Figure 6.4: Boundary layer profiles of (a) the average and (b) RMSD streamwise velocity at various Reynolds numbers at $y/D_h = -4.45$ in test section A, where the origin $y = 0$ is defined at the beginning of the gap [19].

6.3 Inflow Conditions to Test Section

The incoming flow speed in each channel can be independently varied, enabling the study of the effect of velocity difference for inter-channel mixing. Nominally the Reynolds number based on the channels hydraulic diameter in both incoming channels was varied $Re_{D_h} = 40k, 60k, 80k, \text{ to } 10k$. For nominally 20 °C water, these correspond to average inlet flow speeds of 0.315, 0.472, 0.630 and 0.787 m/s, respectively.

The flow conditions upstream of the gap were thoroughly surveyed by performing LDV scans of the axial velocity spanning the entire cross-section of the channel, and 1D boundary layer scans. For the inflow LDV data, the gap was closed. The LDV data was post-processed in Matlab, where the velocity subranging was also employed to remove any erroneous near-zero velocity bursts from the data. Fig. 6.4 shows the boundary layer profiles and Fig. 6.5 shows a sample 2-D slice of the inflow. Note that the inlet flow was nearly symmetric with no strong secondary flows in the corners. Table 6.1 summarizes the boundary layer conditions. Typical shape factor H_s is 2.4 for the turbulent flow, and 2.6 for the laminar flow [18]. Based on the shape factor H_s in Table 6.1, one can see that at $Re_{D_h} = 100k, 80k, \text{ and } 60k$, the boundary layers are turbulent, while $Re_{D_h} = 40k$ is transient close to laminar.

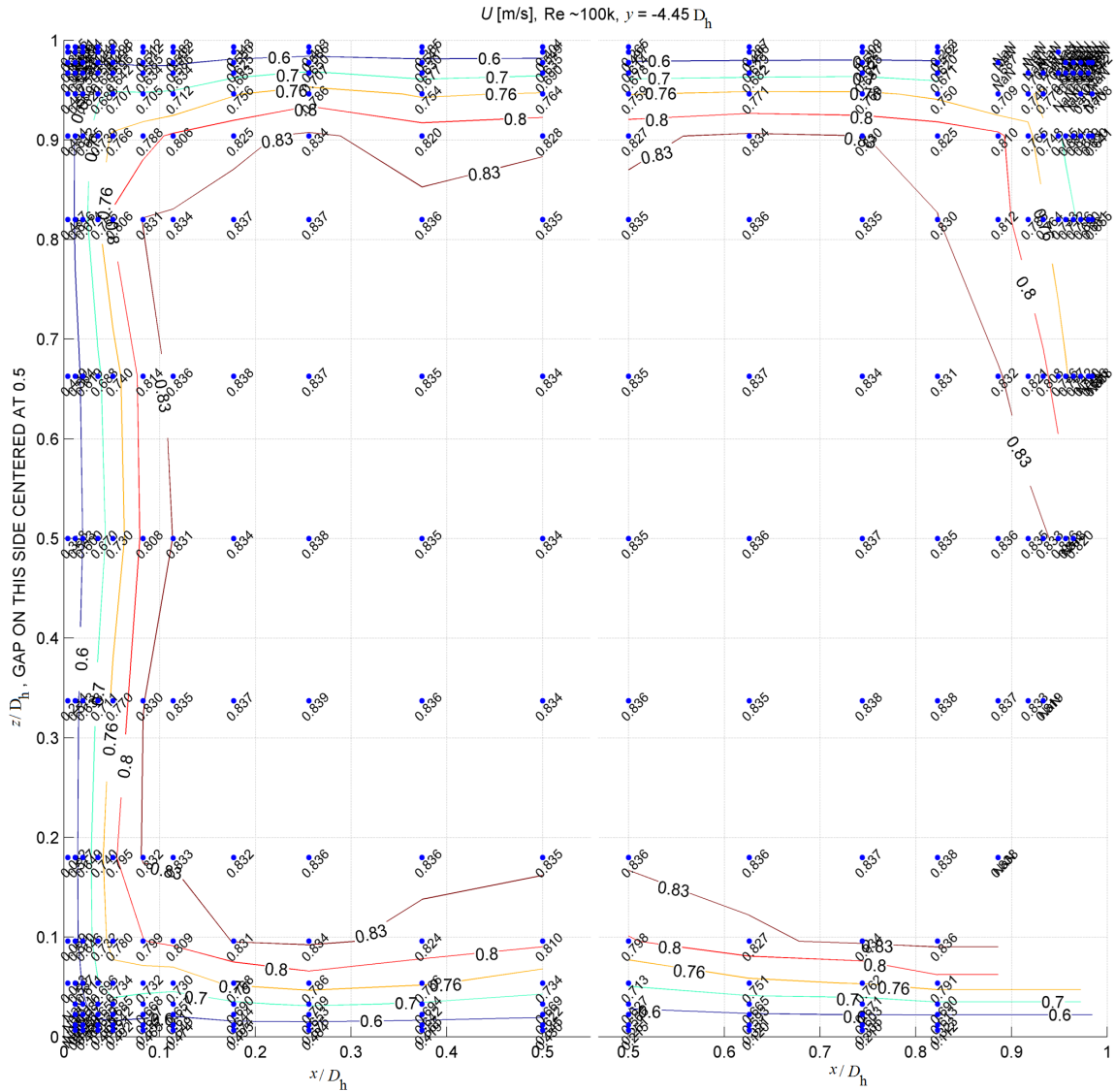


Figure 6.5: Contours of streamwise velocity at Reynolds numbers 10^5 at $y/D_h = -4.45$ in test section A. The channel was scanned in two sections overlapping at $x/D_h = 0.5$, and the lower right corner was in the shadow of the channels frame. Gap is centered at $z/D_h = 0.5$, $y/D_h = 1$ [19].

Table 6.1: Details of the boundary layer; boundary layer thickness δ , displacement thickness δ^* , momentum thickness θ , shear stress τ_w , frictional velocity $u_\tau = \sqrt{\tau_w/\rho}$, and viscous length $l^+ = \nu/\sqrt{(\tau_w/\rho)}$. The latter two were calculated assuming water temperature $T_w = 20$ °C and hence the density of water $\rho_w = 998.3$ kg/m³ and kinematic viscosity of water $\nu = 1.004 \times 10^{-6}$ m²/s [19].

Re_{Dh}	U_∞ (m/s)	δ (mm)	δ^* (mm)	θ (mm)	H_s	τ_w (N/m ²)	u_τ (m/s)	l^+ (μ m)
100,000	0.84	13.8	2.2	1.5	1.5	1.4	0.037	27
80,000	0.67	13.8	2.2	1.5	1.5	0.95	0.031	33
60,000	0.5	12.7	1.9	1.3	1.5	0.59	0.024	41
40,000	0.34	10.8	2.4	1	2.4	0.084	0.009	109

BIBLIOGRAPHY

- [1] L. Meyer and K. Rehme, “Large-Scale Turbulence Phenomena in Compound Rectangular Channels,” *Exp. Therm. Fluid Sci.*, vol. 8, no. 4, pp. 286–304, 1994.
- [2] A. Mahmood, M. Rohde, T. H. J. J. van der Hagen, R. F. Mudde, T. van der Hagen, and R. F. Mudde, “Contribution of Large-Scale Coherent Structures towards the Cross Flow in Two Interconnected Channels,” in *NURETH-13*, Kanazawa, Japan, 2009. [Online]. Available: <http://inis.iaea.org/Search/search.aspx?orig{}q=RN:43036722>
- [3] F. Baratto, S. Bailey, and S. Tavoularis, “Measurements of frequencies and spatial correlations of coherent structures in rod bundle flows,” *Nucl. Eng. Des.*, vol. 236, no. 17, pp. 1830–1837, sep 2006. [Online]. Available: <http://linkinghub.elsevier.com/retrieve/pii/S0029549306001257>
- [4] W. Eifler and R. Nijssing, “Experimental investigation of velocity distribution and flow resistance in a triangular array of parallel rods,” *Nucl. Eng. Des.*, vol. 5, pp. 22–42, 1967.
- [5] T. Krauss, “Characteristics of turbulent velocity and temperature in a wall channel of a heated rod bundle,” *Exp. Therm. Fluid Sci.*, vol. 12, no. 1, pp. 75–86, jan 1996. [Online]. Available: <http://linkinghub.elsevier.com/retrieve/pii/0894177795000763>
- [6] T. Krauss and L. Meyer, “Experimental investigation of turbulent transport of momentum and energy in a heated rod bundle,” *Nucl. Eng. Des.*, vol. 180, pp. 185 – 206, 1998.
- [7] S. V. Moller, “On Phenomena of Turbulent Flow Through Rod Bundles,” *Exp. Therm. Fluid Sci.*, pp. 25–35, 1991.
- [8] ———, “Single-Phase Turbulent Mixing in Rod Bundles,” *Exp. Therm. Fluid Sci.*, pp. 26–33, 1992.

- [9] L. Meyer, “From discovery to recognition of periodic large scale vortices in rod bundles as source of natural mixing between channels - A review,” *Nucl. Eng. Des.*, pp. 1575–1588, 2010.
- [10] D. Chang and S. Tavoularis, “Convective Heat Transfer in Turbulent Flow Near a Gap,” *J. Heat Transfer*, vol. 128, no. 7, p. 701, 2006. [Online]. Available: <http://link.aip.org/link/JHTRAO/v128/i7/p701/s1{&}Agg=doi>
- [11] —, “Numerical simulation of turbulent flow in a 37-rod bundle,” *Nucl. Eng. Des.*, vol. 237, no. 6, pp. 575–590, mar 2007. [Online]. Available: <http://linkinghub.elsevier.com/retrieve/pii/S0029549306004705>
- [12] D. Home, G. Arvanitis, M. Lightstone, and M. Hamed, “Simulation of flow pulsations in a twin rectangular sub-channel geometry using unsteady Reynolds Averaged NavierStokes modelling,” *Nucl. Eng. Des.*, vol. 239, no. 12, pp. 2964–2980, dec 2009. [Online]. Available: <http://linkinghub.elsevier.com/retrieve/pii/S0029549309004403>
- [13] J. Derksen, “Simulations of lateral mixing in cross-channel flow,” *Comput. Fluids*, vol. 39, no. 6, pp. 1058–1069, jun 2010. [Online]. Available: <http://linkinghub.elsevier.com/retrieve/pii/S0045793010000162>
- [14] D. Home and M. F. Lightstone, “Numerical investigation of quasi-periodic flow and vortex structure in a twin rectangular subchannel geometry using detached eddy simulation,” *Nucl. Eng. Des.*, vol. 270, pp. 1–20, 2014. [Online]. Available: <http://dx.doi.org/10.1016/j.nucengdes.2014.01.002>
- [15] E. Merzari, H. Ninokata, A. Mahmood, and M. Rohde, “Proper orthogonal decomposition of the flow in geometries containing a narrow gap,” *Theor. Comput. Fluid Dyn.*, vol. 23, no. 5, pp. 333–351, sep 2009. [Online]. Available: <http://www.springerlink.com/index/10.1007/s00162-009-0152-3>
- [16] J. Ko, D. Lucor, and P. Sagaut, “Sensitivity of two-dimensional spatially developing mixing layers with respect to uncertain inflow conditions,” *Phys. Fluids*, vol. 20, no. 7, p. 077102, 2008. [Online]. Available: <http://link.aip.org/link/PHFLE6/v20/i7/p077102/s1{&}Agg=doi>
- [17] F. Anselmet, F. Ternat, M. Amielh, O. Boiron, P. Boyer, and L. Pietri, “Axial development of the mean flow in the entrance region of turbulent pipe and duct flows,” *Comptes Rendus Mécanique*, vol. 337, no. 8, pp. 573–584, aug 2009. [Online]. Available: <http://linkinghub.elsevier.com/retrieve/pii/S1631072109001090>

- [18] H. Schlichting, *Boundary-layer theory*. McGraw-Hill, 1968.
- [19] S. A. Mäkiharju, S. L. Ceccio, J. R. Buchanan, A. G. Mychkovsky, K. J. Hogan, and K. T. Lowe, “Experimental Characterization of Interchannel Mixing Through a Narrow Gap,” in *Int. Top. Meet. Nucl. React. Therm. Hydraul.*, 2015, pp. 4394–4409.

CHAPTER 7

Time-averaged Inter-channel Mixing

7.1 Control Volume Analysis

In this chapter, we investigate the rate of mixing based on the dye concentration. We introduce the mixing coefficients f_A and f_B to quantify the total amount of mixing, where f_A is the time-averaged fraction of water mass transferred from A to B, and f_B is the time-averaged fraction of water mass transferred from B to A. The total amount of mixing can be calculated based on the conservation of mass of water and of the tracer (fluorescein dye) in a fixed control volume. We define two control volumes, one for each channel, as shown in Fig. 7.1. From mass conservation in control volumes A and B shown in Fig. 7.1, the following four equations can be derived:

$$\dot{m}_{AO} = \dot{m}_{AI}(1 - f_A) + \dot{m}_{BI}f_B \quad (7.1)$$

$$\dot{m}_{BO} = \dot{m}_{AI}f_A + \dot{m}_{BI}(1 - f_B) \quad (7.2)$$

$$\dot{m}_{AO}C_{AO} = \dot{m}_{AI}C_{AI}(1 - f_A) + \dot{m}_{BI}C_{BI}f_B \quad (7.3)$$

$$\dot{m}_{BO}C_{BO} = \dot{m}_{AI}C_{AI}f_A + \dot{m}_{BI}C_{BI}(1 - f_B) \quad (7.4)$$

where \dot{m} is the mass flow rate in kg/s, and C is the tracer concentration in units of kg of tracer per kg of water. Eqn. (7.1) and (7.2) are the mass conservation of water in control volumes A and B, respectively, and Eqn. (7.3) and (7.4) are the mass conservation of tracer in control volumes A and B. From the sum of Eqn. (7.1) and (7.2), and (7.3) and (7.4), the mass conservation equations of the water and tracer in the global control volume can be obtained as:

$$\dot{m}_{AO} + \dot{m}_{BO} = \dot{m}_{AI} + \dot{m}_{BI}, \quad (7.5)$$

$$\dot{m}_{AO}C_{AO} + \dot{m}_{BO}C_{BO} = \dot{m}_{AI}C_{AI} + \dot{m}_{BI}C_{BI}, \quad (7.6)$$

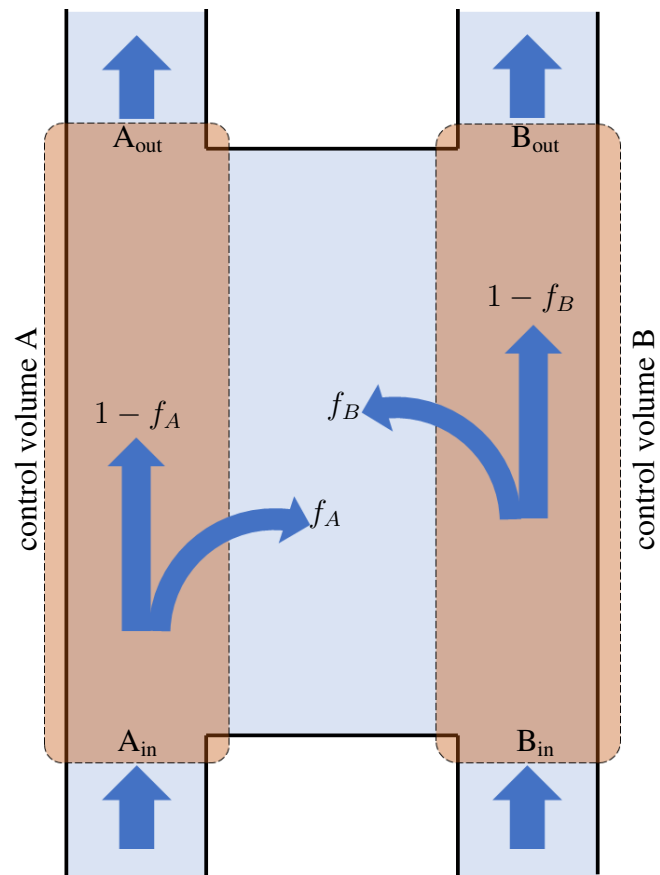


Figure 7.1: Schematic drawing of the test section, inlets, outlets and control volumes

The system is over-determined as there are four independent equations with only two unknowns, f_A and f_B . As a result, four possible sets of solutions can be derived. Because of the experimental error, the data do not satisfy the global conservation equations shown in Eqn. (7.5) and (7.6).

$$f_A^{(1)} = 1 - \frac{\dot{m}_{AO}(C_{AO} - C_{BI})}{\dot{m}_{AI}(C_{AI} - C_{BI})}, \quad (7.7)$$

$$f_B^{(1)} = \frac{\dot{m}_{AO}(C_{AI} - C_{AO})}{\dot{m}_{BI}(C_{AI} - C_{BI})}, \quad (7.8)$$

$$f_A^{(2)} = \frac{\dot{m}_{BO}(C_{BO} - C_{BI})}{\dot{m}_{AI}(C_{AI} - C_{BI})}, \quad (7.9)$$

$$f_B^{(2)} = 1 - \frac{\dot{m}_{BO}(C_{AI} - C_{BO})}{\dot{m}_{BI}(C_{AI} - C_{BI})}, \quad (7.10)$$

$$f_A^{(3)} = \frac{-\dot{m}_{AI}C_{BI} + \dot{m}_{AO}C_{BI} - \dot{m}_{BI}C_{BI} + \dot{m}_{BO}C_{BO}}{\dot{m}_{AI}(C_{AI} - C_{BI})}, \quad (7.11)$$

$$f_B^{(3)} = \frac{-\dot{m}_{AI}C_{AI} + \dot{m}_{AO}C_{AI} - \dot{m}_{BI}C_{BI} + \dot{m}_{BO}C_{BO}}{\dot{m}_{BI}(C_{AI} - C_{BI})}, \quad (7.12)$$

$$f_A^{(4)} = \frac{\dot{m}_{AI}C_{AI} - \dot{m}_{AO}C_{AO} + \dot{m}_{BI}C_{BI} - \dot{m}_{BO}C_{BI}}{\dot{m}_{AI}(C_{AI} - C_{BI})}, \quad (7.13)$$

$$f_B^{(4)} = \frac{\dot{m}_{AI}C_{AI} - \dot{m}_{AO}C_{AO} + \dot{m}_{BI}C_{AI} - \dot{m}_{BO}C_{AI}}{\dot{m}_{BI}(C_{AI} - C_{BI})}. \quad (7.14)$$

The uncertainty of the mixing coefficient f_A , $\delta f_A^{(i)}$, can be derived from the propagation of uncertainty. The uncertainties of the inlet and outlet flow meters $\delta \dot{m}$ were based on manufactures specs taken to be as 0.5% of reading and 1% of full scale, respectively, as listed in §6.2.3. The uncertainties of the tracer concentration was assumed to be accurate within +/- (0.5% of reading + 1 ppm). Assuming all measurements are independent, the uncertainty for $f_A^{(i)}$ can be computed as :

$$\delta f_A^{(i)} = \left[\left(\frac{\partial f_A^{(i)}}{\partial \dot{m}_{AI}} \right)^2 \delta \dot{m}_{AI}^2 + \left(\frac{\partial f_A^{(i)}}{\partial \dot{m}_{AO}} \right)^2 \delta \dot{m}_{AO}^2 + \left(\frac{\partial f_A^{(i)}}{\partial \dot{m}_{BI}} \right)^2 \delta \dot{m}_{BI}^2 + \left(\frac{\partial f_A^{(i)}}{\partial \dot{m}_{BO}} \right)^2 \delta \dot{m}_{BO}^2 + \left(\frac{\partial f_A^{(i)}}{\partial C_{AI}} \right)^2 \delta C_{AI}^2 + \left(\frac{\partial f_A^{(i)}}{\partial C_{AO}} \right)^2 \delta C_{AO}^2 + \left(\frac{\partial f_A^{(i)}}{\partial C_{BI}} \right)^2 \delta C_{BI}^2 + \left(\frac{\partial f_A^{(i)}}{\partial C_{BO}} \right)^2 \delta C_{BO}^2 \right]^{1/2}. \quad (7.15)$$

Note that the equations for $f_A^{(i)}$ are linear, thus the linear approximation (7.15) is the exact solution of the uncertainty of $f_A^{(i)}$. The uncertainty of $\delta f_B^{(i)}$ can be obtained by simply substituting $f_A^{(i)}$ with $f_B^{(i)}$ in Eqn. (7.15). Averaged values of the four sets of $f_A^{(i)}$ and $f_B^{(i)}$ derived in Eqn. (7.7) to (7.14) are used as a final solutions \bar{f}_A and \bar{f}_B .

$$\bar{f}_A = \sum_{i=1}^4 f_A^{(i)}, \quad (7.16)$$

$$\bar{f}_B = \sum_{i=1}^4 f_B^{(i)}. \quad (7.17)$$

The uncertainties of \bar{f}_A and \bar{f}_B can be derived from the propagation of uncertainty:

$$\begin{aligned} \delta \bar{f}_A &= \left[\left(\frac{\partial \bar{f}_A}{\partial \dot{m}_{AI}} \right)^2 \delta \dot{m}_{AI}^2 + \dots + \left(\frac{\partial \bar{f}_A}{\partial C_{BO}} \right)^2 \delta C_{BO}^2 \right]^{1/2} \\ &= \frac{1}{4} \left[\left(\sum_{i=1}^4 \frac{\partial f_A^{(i)}}{\partial \dot{m}_{AI}} \right)^2 \delta \dot{m}_{AI}^2 + \dots + \left(\sum_{i=1}^4 \frac{\partial f_A^{(i)}}{\partial C_{BO}} \right)^2 \delta C_{BO}^2 \right]^{1/2}. \end{aligned} \quad (7.18)$$

Data were taken by two separate acquisition system with different sampling rates. Flow rates were recorded with 1.525 second time step, fluorescein concentrations were recorded with 0.5470 second time step. Values of mass flow rates and dye concentrations are averaged over the last 100 time steps before the end of the dye concentration measurement.

7.2 Results

Total of 7 flow conditions with 11 different gap sizes are investigated. Flow conditions are defined by Reynolds numbers of the nominal inlet flows, defined based on the hydraulic diameter of the channels, i.e.,

$$\text{Re}_{A \text{ (or B)}} = \frac{\bar{V}_{A \text{ (or B)}} D_h}{\nu} \quad (7.19)$$

where $\bar{V}_{A \text{ (or B)}}$ is the nominal inlet velocity of channel A (or B), D_h is the hydraulic diameter of channel A and B, ν is the kinematic viscosity of water. Hereinafter, Reynolds numbers of channel A and B are written in the shorthand as $\text{Re}[a, b]k$ for the Reynolds number of the channel A, $\text{Re}_A = a \times 10^3$, and the Reynolds number of the channel B, $\text{Re}_B = b \times 10^3$. For balanced flow, the following 4 cases of flow conditions are considered: $\text{Re}[100 \ 100]k$, $\text{Re}[80 \ 80]k$, $\text{Re}[60 \ 60]k$, and $\text{Re}[40 \ 40]k$. For unbalanced flow, the following 3 cases of

flow conditions are considered: Re[80 100]k, Re[60 100]k, and Re[40 100]k. For each inlet condition, 11 gap heights are considered: 2, 4, 6, 8, 10, 12, 14, 16, 20, 30, and 50.

7.2.1 Balanced Flow

Fig. 7.2 to 7.5 show the result of \bar{f}_A and \bar{f}_B and their uncertainties for Re[100 100]k, Re[80 80]k, Re[60 60]k, and Re[40 40]k, respectively. All corresponding mixing coefficients are tabulated in Table 7.1 to 7.4. Intuitively, the averaged mixing coefficients \bar{f}_A and \bar{f}_B must have the same value at each Reynolds number as it forms an symmetric nominal flow, which is true as shown in Fig. 7.2 to Fig. 7.4. The deviation between \bar{f}_A and \bar{f}_B in Re[40 40]k (Fig. 7.5) seems mainly due to the large uncertainty when the flow is slow.

Fig. 7.6 show the average mixing coefficients $(\bar{f}_A + \bar{f}_B)/2$ plotted against the gap/channel ratio H_g/D_h . The mixing coefficients show weak dependency on Reynolds numbers when the gap ratio H_g/D_h is larger than 0.06. However, when $H_g/D_h < 0.06$, mixing coefficients deviate notably depending on Reynolds number, and there is no recognizable mixing in any flow velocity when $H_g/D_h < 0.025$.

When a flow enters into a sudden contraction, a separation occurs at the downstream of the contraction. Those separated flow forms a bottleneck, and the flow losses energy when it passes the contraction. Based on the shape factor of the boundary layer shown in Table 6.1, one can see that the flow conditions Re[100 100]k, Re[80 80]k, Re[60 60]k are turbulent, while Re[40 40]k is transient (nearly laminar). Turbulence delays the separation of the flow, thus the energy loss due to the flow separation is relatively low. As a result, the mixing due to the coherent mode decreases significantly when the gap is narrow, and the effect is greater when the Reynolds number is low. As the gap height becomes wider, the effect of this separated flow at the gap entrance becomes less significant. For $0.06 < H_g/D_h < 0.14$, the mixing coefficients converge and increase proportional to the gap height.

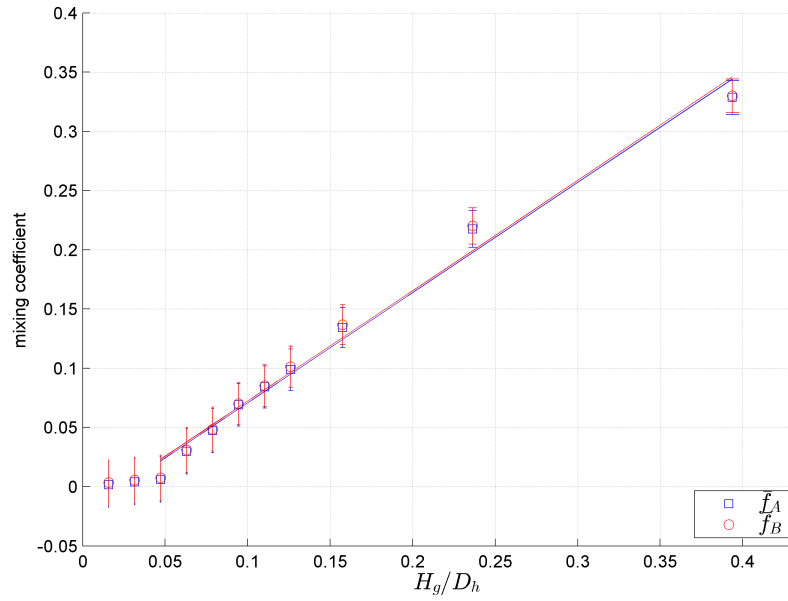


Figure 7.2: Mixing coefficients \bar{f}_A and \bar{f}_B for $Re = [100\ 100]k$. Circles and squares with bars represent the measured data of \bar{f}_A and \bar{f}_B and their uncertainties (bar) at each data point. Solid blue and red lines show the linear trend lines of f_A and y based on the results of the gap height from 6 mm to 50 mm.

Table 7.1: Mixing coefficients \bar{f}_A and \bar{f}_B for $Re = [100\ 100]k$.

h_g	\bar{f}_A	$\delta\bar{f}_A$	\bar{f}_B	$\delta\bar{f}_B$
2	0.0015	0.0192	0.0034	0.0192
4	0.0040	0.0193	0.0055	0.0192
6	0.0062	0.0192	0.0075	0.0192
8	0.0297	0.0190	0.0309	0.0189
10	0.0474	0.0186	0.0485	0.0185
12	0.0689	0.0179	0.0700	0.0178
14	0.0841	0.0178	0.0853	0.0176
16	0.0988	0.0174	0.1012	0.0173
20	0.1343	0.0169	0.1367	0.0167
30	0.2176	0.0156	0.2201	0.0154
50	0.3286	0.0142	0.3299	0.0141

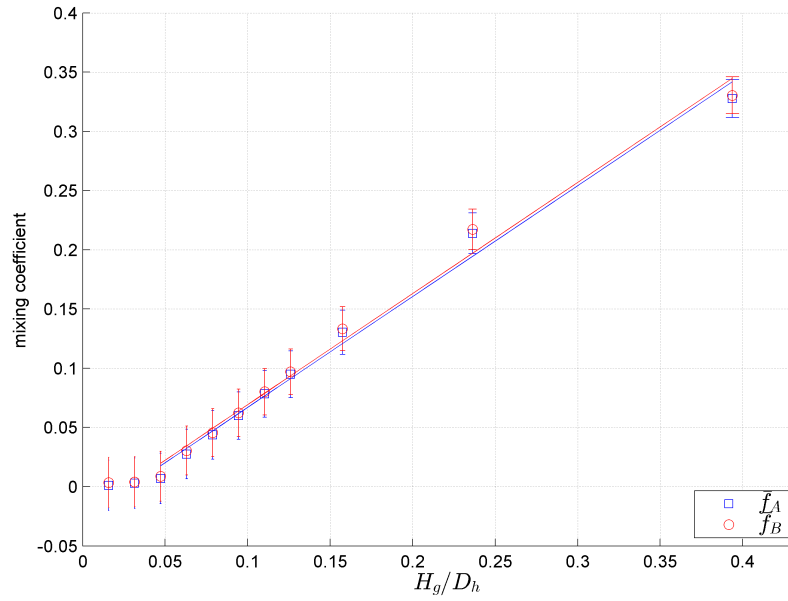


Figure 7.3: Mixing coefficients \bar{f}_A and \bar{f}_B for $Re = [80\ 80]k$. Circles and squares with bars represent the measured data of \bar{f}_A and \bar{f}_B and their uncertainties (bar) at each data point. Solid blue and red lines show the linear trend lines of f_A and y based on the results of the gap height from 6 mm to 50 mm.

Table 7.2: Mixing coefficients \bar{f}_A and \bar{f}_B for $Re = [80\ 80]k$.

h_g	\bar{f}_A	$\delta\bar{f}_A$	\bar{f}_B	$\delta\bar{f}_B$
2	0.0010	0.0214	0.0035	0.0212
4	0.0030	0.0214	0.0041	0.0212
6	0.0070	0.0213	0.0087	0.0211
8	0.0276	0.0209	0.0305	0.0207
10	0.0438	0.0204	0.0456	0.0202
12	0.0600	0.0201	0.0623	0.0200
14	0.0783	0.0198	0.0802	0.0196
16	0.0949	0.0196	0.0971	0.0192
20	0.1303	0.0187	0.1334	0.0185
30	0.2139	0.0173	0.2172	0.0171
50	0.3277	0.0160	0.3303	0.0156

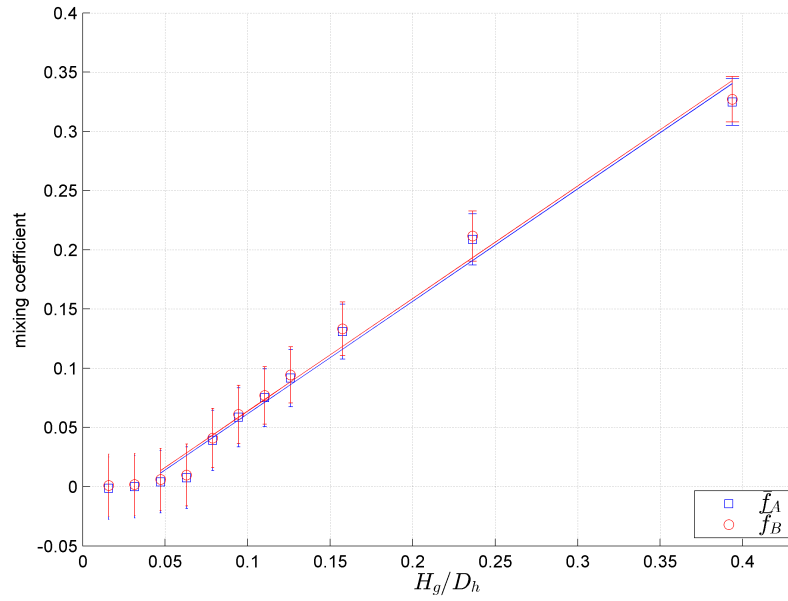


Figure 7.4: Mixing coefficients \bar{f}_A and \bar{f}_B for $Re = [60\ 60]k$. Circles and squares with bars represent the measured data of \bar{f}_A and \bar{f}_B and their uncertainties (bar) at each data point. Solid blue and red lines show the linear trend lines of f_A and y based on the results of the gap height from 6 mm to 50 mm.

Table 7.3: Mixing coefficients \bar{f}_A and \bar{f}_B for $Re = [60\ 60]k$.

h_g	\bar{f}_A	$\delta\bar{f}_A$	\bar{f}_B	$\delta\bar{f}_B$
2	-0.0014	0.0264	0.0011	0.0263
4	-0.0001	0.0264	0.0017	0.0263
6	0.0041	0.0262	0.0060	0.0261
8	0.0076	0.0261	0.0098	0.0261
10	0.0390	0.0254	0.0411	0.0251
12	0.0585	0.0249	0.0610	0.0246
14	0.0752	0.0244	0.0770	0.0242
16	0.0916	0.0242	0.0943	0.0237
20	0.1309	0.0232	0.1333	0.0228
30	0.2087	0.0215	0.2116	0.0212
50	0.3247	0.0199	0.3270	0.0192

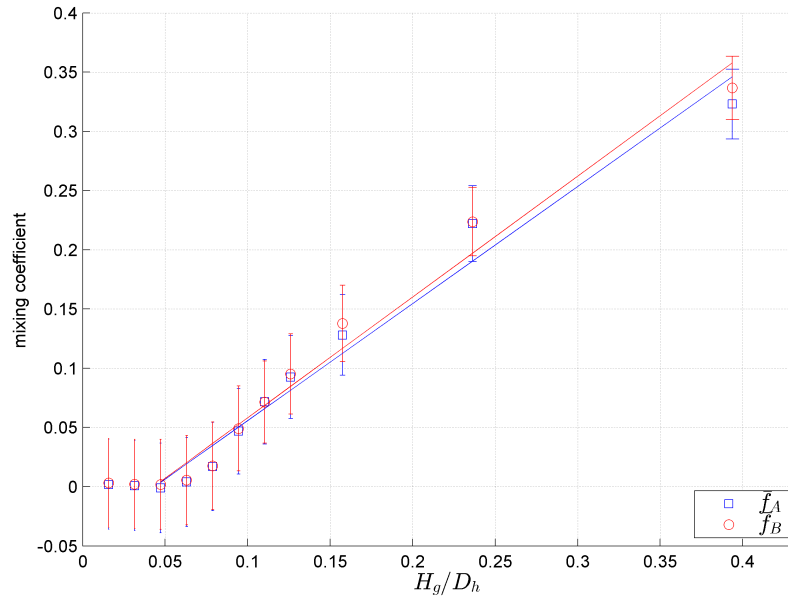


Figure 7.5: Mixing coefficients \bar{f}_A and \bar{f}_B for $Re = [40\ 40]k$. Circles and squares with bars represent the measured data of \bar{f}_A and \bar{f}_B and their uncertainties (bar) at each data point. Solid blue and red lines show the linear trend lines of f_A and y based on the results of the gap height from 6 mm to 50 mm.

Table 7.4: Mixing coefficients \bar{f}_A and \bar{f}_B for $Re = [40\ 40]k$.

h_g	\bar{f}_A	$\delta\bar{f}_A$	\bar{f}_B	$\delta\bar{f}_B$
2	0.0018	0.0379	0.0031	0.0376
4	0.0009	0.0380	0.0022	0.0378
6	-0.0010	0.0378	0.0020	0.0379
8	0.0040	0.0377	0.0055	0.0377
10	0.0170	0.0373	0.0177	0.0370
12	0.0468	0.0362	0.0491	0.0358
14	0.0716	0.0358	0.0714	0.0347
16	0.0925	0.0348	0.0952	0.0339
20	0.1280	0.0339	0.1379	0.0323
30	0.2221	0.0320	0.2238	0.0290
50	0.3230	0.0295	0.3366	0.0268

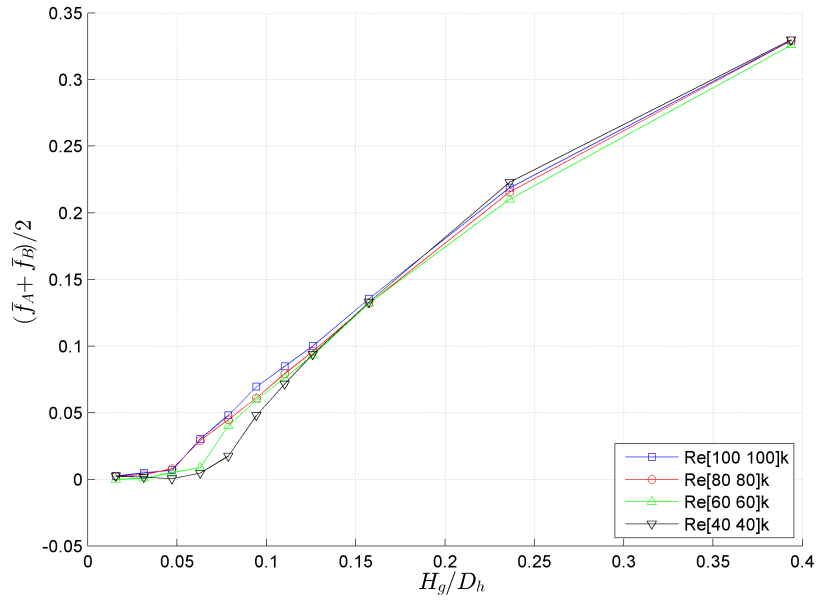


Figure 7.6: Comparison of average mixing coefficients of the balanced flows plotted against the axis H_g/D_h .

7.2.2 Unbalanced Flow

Fig. 7.7 to 7.9 show the result of \bar{f}_A and \bar{f}_B and their uncertainties for Re[80 100]k, Re[60 100]k, and Re[40 100]k, respectively. Unlike balanced flows, a steady mixing due to the pressure gradient occurs in the unbalanced flow. If mixing was due to purely one-way mass transfer from channel B to channel A, and flow balanced perfectly by the end of the test section, then by definition,

$$x = 0, \text{ and } y = \frac{1}{2} \left(1 - \frac{\dot{m}_{AI}}{\dot{m}_{BI}} \right). \quad (7.20)$$

As the flow velocity difference between two channel increases, the effect of the coherent structure to the mixing decreases, and the mixing tends to follow the pressure-induced steady mixing. As one can see later in §8.6, the coherent structure gets stronger when two vorticity sources at the tips of the gap have the same strength. If one vorticity source is dominantly stronger than the other, the flow pattern is governed by a steady flow.

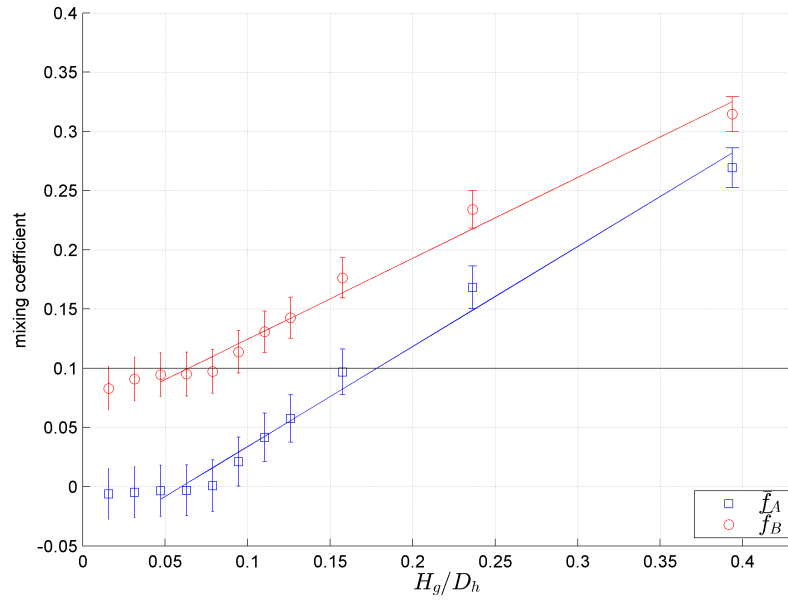


Figure 7.7: Mixing coefficients \bar{f}_A and \bar{f}_B for $Re = [80\ 100]k$. Circles and squares with bars represent the measured data of \bar{f}_A and \bar{f}_B and their uncertainties (bar) at each data point. Solid blue and red lines show the linear trend lines of f_A and y based on the results of the gap height from 6 mm to 50 mm. Solid black line shows the mixing coefficient y with steady mixing assumption as shown in (7.20).

Table 7.5: Mixing coefficients \bar{f}_A and \bar{f}_B for $Re = [80\ 100]k$.

h_g	\bar{f}_A	$\delta\bar{f}_A$	\bar{f}_B	$\delta\bar{f}_B$
2	-0.0060	0.0216	0.0830	0.0184
4	-0.0048	0.0214	0.0909	0.0183
6	-0.0035	0.0216	0.0946	0.0184
8	-0.0032	0.0215	0.0951	0.0185
10	0.0008	0.0217	0.0974	0.0184
12	0.0212	0.0207	0.1137	0.0179
14	0.0417	0.0204	0.1308	0.0176
16	0.0575	0.0200	0.1426	0.0174
20	0.0968	0.0193	0.1763	0.0169
30	0.1683	0.0181	0.2342	0.0159
50	0.2693	0.0167	0.3145	0.0147

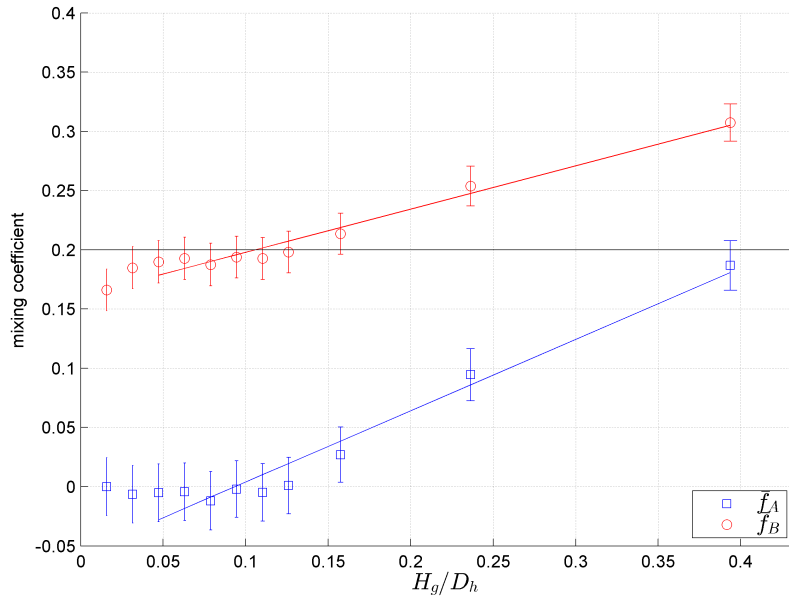


Figure 7.8: Mixing coefficients \bar{f}_A and \bar{f}_B for $\text{Re} = [60\ 100]\text{k}$. Circles and squares with bars represent the measured data of \bar{f}_A and \bar{f}_B and their uncertainties (bar) at each data point. Solid blue and red lines show the linear trend lines of f_A and y based on the results of the gap height from 6 mm to 50 mm. Solid black line shows the mixing coefficient y with steady mixing assumption as shown in (7.20).

Table 7.6: Mixing coefficients \bar{f}_A and \bar{f}_B for $\text{Re} = [60\ 100]\text{k}$.

h_g	\bar{f}_A	$\delta\bar{f}_A$	\bar{f}_B	$\delta\bar{f}_B$
2	0.0000	0.0246	0.1661	0.0176
4	-0.0064	0.0242	0.1848	0.0177
6	-0.0052	0.0244	0.1898	0.0178
8	-0.0042	0.0242	0.1928	0.0178
10	-0.0120	0.0247	0.1875	0.0179
12	-0.0021	0.0238	0.1938	0.0177
14	-0.0049	0.0243	0.1926	0.0177
16	0.0010	0.0238	0.1981	0.0177
20	0.0270	0.0232	0.2135	0.0174
30	0.0945	0.0219	0.2537	0.0168
50	0.1868	0.0210	0.3074	0.0157

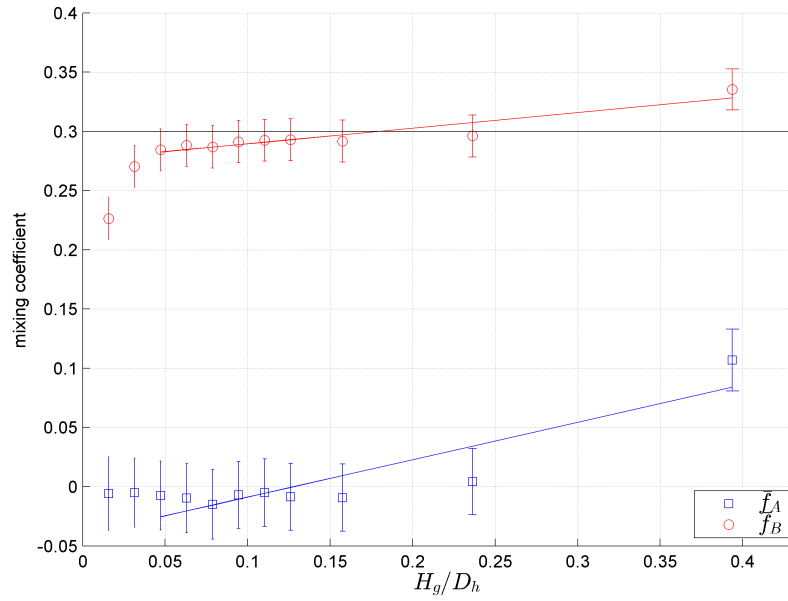


Figure 7.9: Mixing coefficients \bar{f}_A and \bar{f}_B for $Re = [40\ 100]k$. Circles and squares with bars represent the measured data of \bar{f}_A and \bar{f}_B and their uncertainties (bar) at each data point. Solid blue and red lines show the linear trend lines of f_A and y based on the results of the gap height from 6 mm to 50 mm. Solid black line shows the mixing coefficient y with steady mixing assumption as shown in (7.20).

Table 7.7: Mixing coefficients \bar{f}_A and \bar{f}_B for $Re = [40\ 100]k$.

h_g	\bar{f}_A	$\delta\bar{f}_A$	\bar{f}_B	$\delta\bar{f}_B$
2	-0.0059	0.0311	0.2264	0.0180
4	-0.0051	0.0290	0.2704	0.0177
6	-0.0074	0.0290	0.2844	0.0177
8	-0.0095	0.0290	0.2881	0.0178
10	-0.0150	0.0293	0.2868	0.0178
12	-0.0069	0.0282	0.2912	0.0178
14	-0.0051	0.0285	0.2924	0.0177
16	-0.0085	0.0282	0.2929	0.0177
20	-0.0093	0.0284	0.2918	0.0178
30	0.0043	0.0280	0.2960	0.0177
50	0.1069	0.0262	0.3353	0.0172

CHAPTER 8

Visualization of the Coherent Structures within the Mixing Gap Flow Fields by Proper Orthogonal Decomposition

8.1 Introduction

In this chapter, we discuss how to extract the coherent structure from the velocity field data of the gap measured by the Particle Image Velocimetry (PIV) using the Proper Orthogonal Decomposition (POD) method, and provide four most energetic coherent structures of the gap mixing flow extracted by POD.

A coherent structure in fluid mechanics is defined as ‘a connected, large-scale turbulent fluid mass with a phase-correlated vorticity over its spatial extent [1].’ A coherent structure differs from random (incoherent) turbulence in that it has a periodic (if not, at least quasi-periodic) structure, and creates large area of mixing which transports mass, heat, and momentum. Study of coherent structures has been an important topic in turbulent mechanics to understand the mixing mechanism. Furthermore, because it is periodic, a resonance with the external force can occur which may bring a critical damage to the enclosing body.

In the experimental study of turbulent flow, phase-averaging has been widely used to separate time periodic coherent structures from random turbulence [3]. Phase-averaging is the ensemble average of any property of fluid at a particular phase [1] of a predefined frequency. With sufficiently large size of data, any phase-random structure is canceled during the averaging process, which leaves only the periodic structures with the chosen frequency and its harmonics. Here, we are going to use the classical phase-averaging that requires time-resolved measurement data.

Another relatively modern approach is the Proper Orthogonal Decomposition (POD). Unlike the frequency based method such as Fourier transform where the basis functions are

predefined as sine and cosine functions, POD extracts the set of basis functions from the data structure. POD has been introduced to the fluid community by Lumley as a continuous form in 1967 [4,5], but the same concept has been developed outside the fluid community since 1901 [6] under a different name, Principal Component Analysis (PCA) and Singular Value Decomposition (SVD). POD has two benefits analyzing the flow pattern: 1) it is insensitive to the outliers, i.e., it can extract the mode (or a pattern) even when the data is noise-corrupted, not periodic, or missing frames, 2) it decomposes the data into spatial and temporal basis, which helps understand the structure of the coherent mode. We will show how the POD can outperform the phase-averaging in §8.4.3.

8.2 Particle Image Velocimetry

We obtained the velocity field data which are used to evaluate the coherent structure by Particle Image Velocimetry (PIV). PIV is a flow visualization technique by tracking the seeded particles in the fluid. The particles are preferably small, $O(10 - 100) \mu\text{m}$, and neutrally buoyant enough so that it follows the flow motion with minimum interference. At each time step, two images of the particles are taken consecutively using camera with the light source from a sheet of laser. Raw images are first filtered to reduce noise, then, velocity vectors are computed based on the cross-correlation of multiple subset windows of two consecutive images. As a result, the PIV generates a time series of 2D velocity vector fields. Generally, there are missing data due to noise or 3D flow effect. In those cases, the software applies low pass spatial filtering to reduce noise, and fills the missing data using a interpolator.

Because of the large size of the gap, and the obstructing structures designed to adjust the gap height, all gap area cannot be fit into a single field of view (FOV) with a desirable resolution. Thus, the particle images are taken in three separated FOVs. Those data with different FOV are not time-synchronized as we use one camera moving up and down manually to have three different FOVs. Fig. 8.1 shows the location of the FOVs in the gap window with respect to the origin at the center bottom of the gap. Since we fixed the laser sheet at the center of the gap height, all particle images are acquired at the center of the gap height as well as 2D velocity fields.

8.2.1 Instrumentation

We used the following hardware/software instruments for PIV recording/processing:

- Recording software: DaVis 7.2.2.470, Windows XP (32 bit).

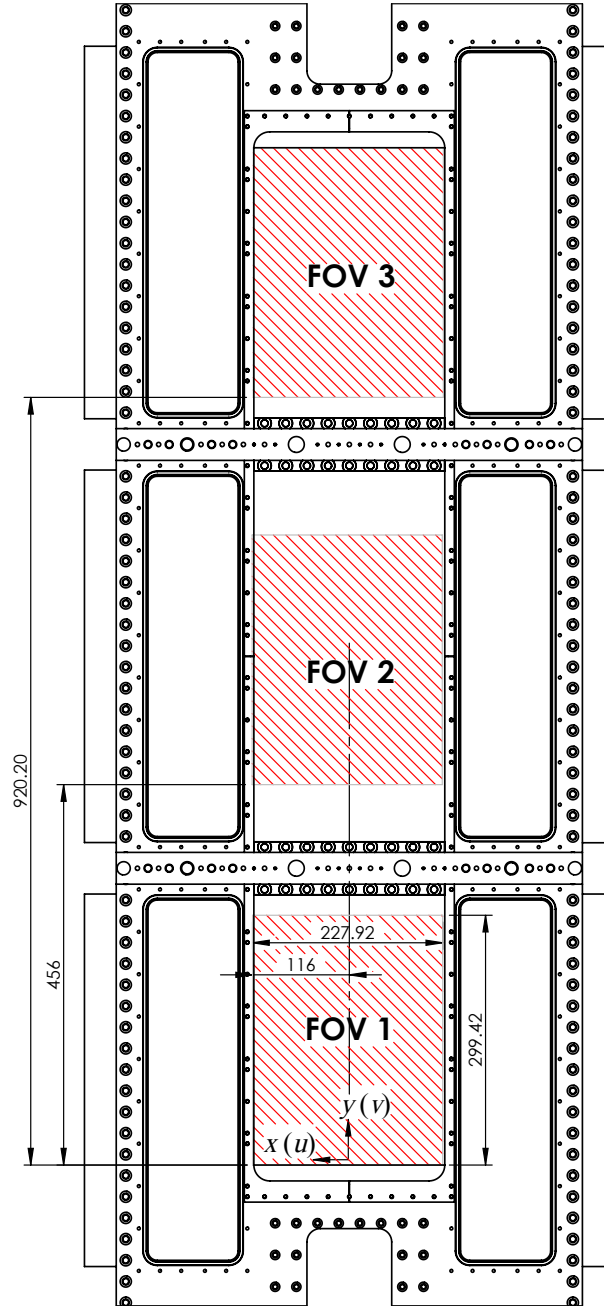


Figure 8.1: Locations of the three Fields Of View (FOV) that has been used for PIV and its coordinate system. Origin ($x = y = 0$) is defined at the center, bottom plane of the gap. Hatched area shows the location where the particle image was taken. Note that the coordinate system of PIV is different from that of LDV shown in Fig. 6.2. Also, note that the FOVs are not exactly centered on the gap width. All dimensions are in millimeters, and accurate within ± 2 mm.

- Processing software: DaVis 8.1.4.36762, Windows 7 (64 bit).
- Seeding particles: Potters LCC 110P8, nominal size 11.7 microns.
- ImagerPro camera, S/N VC04-0025 EN: 04000006, 1600x1200 pixels, 12bit
- Lens: Nikon 28mm, 1:2.8D, AF Nikkor.
- Laser: Nd:YAG Dual Cavity pulsed laser - Quantel Evergreen PIV 200, 2 x 200 mJ/pulse at 532 nm, 15 Hz pulse rate, single power supply.
- Light arm.
- Traverse: manually traversed on Linos-rails.

All other instruments that are not shown here are identical with §6.2.3.

8.2.2 Data Processing

We used the following settings for data processing to extract the flow velocity vectors from the raw particle images using DaVis 8.1.4.36762:

- Subtract time filter
 - Subtract Gaussian average
 - Filter length: 3 images
 - Output format: same as input format
- Subtract sliding background, scale length: 8 pixels
- Masking
 - Geometric mask, enable inside, shapes saved in `masksettings_FOVx_xxmm.set` where x is the FOV number, xx is the gap height.
- Vector calculations
 - Use GPU
 - Multi-pass (decreasing size) cross-correlation
 - * Pass 1: 128×128 , square, 25% overlap, maximum shift: 30 pixels
 - * Pass 2: 64×64 , square, 25% overlap, maximum shift: 16 pixels
 - * Pass 3: 32×32 , square, 25% overlap, maximum shift: 8 pixels

- * Pass 4: 32×32 , square, 25% overlap, maximum shift: 4 pixels
- * High-accuracy mode for final passes
- Multi-pass options: initial shift 0, symmetric shift
- Multipass post processing
 - * 1 pass median filter: remove if $> 2 \times \text{r.m.s}$ of neighbor pixels
 - * 1 pass smooth filter 3×3

PIV generates massive amount of velocity field data for each flow condition. Those data cannot be directly compared with other data generated by different methods, for example, numerical simulations, due to its large size and randomness. Thus, we need to process/compress the data to analyze the behavior of the flow or to compare with other data. In the following sections, we will discuss how we can extract the meaningful data, such as the dominant frequency and the coherent modes, from the raw velocity data.

8.3 Frequency Analysis of the Coherent Structures

Predicting the frequency of the vortex shedding is crucial for preventing structural damages. Generally, the vortex shedding has more than one frequency mode. In fact, every frequency mode has non-zero energy due to the random turbulence. Thus, we need to find a way to characterize the vortex shedding in a single number. To characterize the frequency of the vortex shedding, we define the dominant period as follows. Denote $u(i, j, t)$ and $v(i, j, t)$ be the transverse and vertical flow velocity data, respectively, where i and j are 2D spatial axis indices, and k is the time index. The peak frequency f_p of each velocity component at every position (i, j) is defined as the frequency component that has the maximum amplitude:

$$f_p^{(u)}(i, j) = \arg \max_f \left| \mathcal{F}_k \{ u(i, j, k) \} (f) \right|, \quad (8.1)$$

$$f_p^{(v)}(i, j) = \arg \max_f \left| \mathcal{F}_k \{ v(i, j, k) \} (f) \right|, \quad (8.2)$$

where $\mathcal{F}_k \{ \cdot \}$ denotes 1D Discrete-Time Fourier Transform (DTFT), and f is the frequency. Then, the dominant peak frequency f_d is defined as the most frequent peak frequency.

$$f_d = \text{mode}[\mathbf{f}_p], \quad (8.3)$$

where $\mathbf{f}_p = \{ f \mid f = f_p^{(u)}(i, j) \text{ or } f = f_p^{(v)}(i, j) \text{ for all } 1 \leq i \leq N_y \text{ and } 1 \leq j \leq N_x \}$. As we have finite size of discretized data, we cannot find true f_d based on the discrete data.

Thus, we use Discrete Fourier Transform (DFT) instead of DTFT, i.e., f_d is chosen from a finite set of discretized frequency.

Strouhal discovered that the frequency of the vortex shedding around a circular cylinder varies linearly with the nominal flow velocity, and proposed the following non-dimensional number that describes the vortex shedding frequency called Strouhal number:

$$\text{St} = \frac{f_d L}{V}, \quad (8.4)$$

where f_d is the dominant peak frequency defined in Eqn. (8.3), L is the characteristic length, and V is the characteristic flow velocity. For our study, we use the gap width W_g for the characteristic length, and nominal velocity at the channel inlet for the characteristic flow velocity.

While the vortex shedding in a balanced flow has a distinctive dominant peak frequency, the vortex shedding behavior in a unbalanced flow is more chaotic, and the energy is distributed to a wide range of frequency. For this reason, we could only obtain the Strouhal number for balanced flows. Fig. 8.2 shows the Strouhal number of each balanced flow condition. Here, we can see that the Strouhal number is less dependent on the Reynolds number, compared with the gap height.

To verify that the PIV data obtained is plausible, we compare the Strouhal numbers based on the dominant frequency described in Eqn. (8.3) with other existing studies. Unfortunately, there were not many studies regarding the gap mixing between two rectangular channels which specified Strouhal numbers and the flow entrance conditions clearly. Meyer and Rehme [7] studied Strouhal number for the vortex shedding in the mixing gap between two rectangular channels, but their test section has no gap end, extending the identical sectional shape from the start to the end of the channel, which inherently differs from our test section that has the gap ends on both upstream and downstream. When there is no gap end, the velocity difference between the gap and the channel is generated entirely by the development of boundary layer in the gap, and the shear layers start to form parallel to the gap edge. In this case, the vortex shedding frequency strictly depends on the Reynolds number as the main source of the shear flow is the effect of the boundary layer. On the other hand, when the gap is blocked at the end, the flow velocity at the gap starts from zero at the gap which is the main source of the velocity difference between the gap and channels. The shear layers start from the tip of the gap end, and form two converging diagonal lines, then merged at the center of the gap. The influence of the Reynolds number to the St is relatively low as the main source of the shear flow is the abrupt change of the flow velocity at the gap end.

Consequently, instead of gap-channel experiments with no gap end, we find the geometric similarity from the flow around the flat plate with a semi-circle leading edge by Parker and Welsh [8]. Assume the boundary layer starts after the contraction, we can compare the aspect ratio of the entrance length/gap width with the aspect ratio of the plate length/plate thickness ratio of the flat plate. Fig. 8.2 shows the area where the St of the mixing gap lies on the flat plate experiments. The flat plate experiment was carried out in an open channel, so the result cannot be exactly same, but the Strouhal number of the semi-circular leading edge plate with similar aspect ratio matches within the range of mixing gap Strouhal numbers.

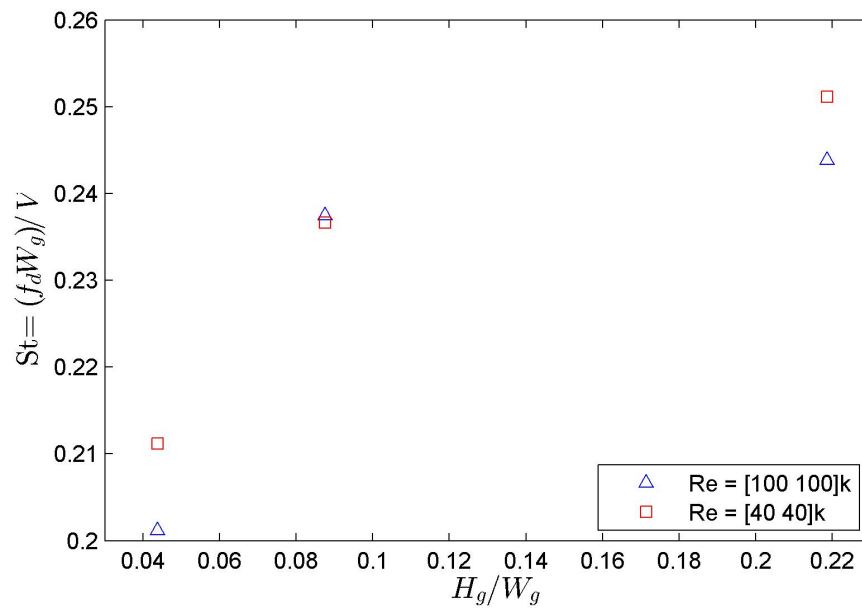


Figure 8.2: Strouhal number of the balanced flows $Re[100 \ 100]k$ (blue triangle) and $Re[40 \ 40]k$ (red square) plotted against the gap height/gap width ratio.

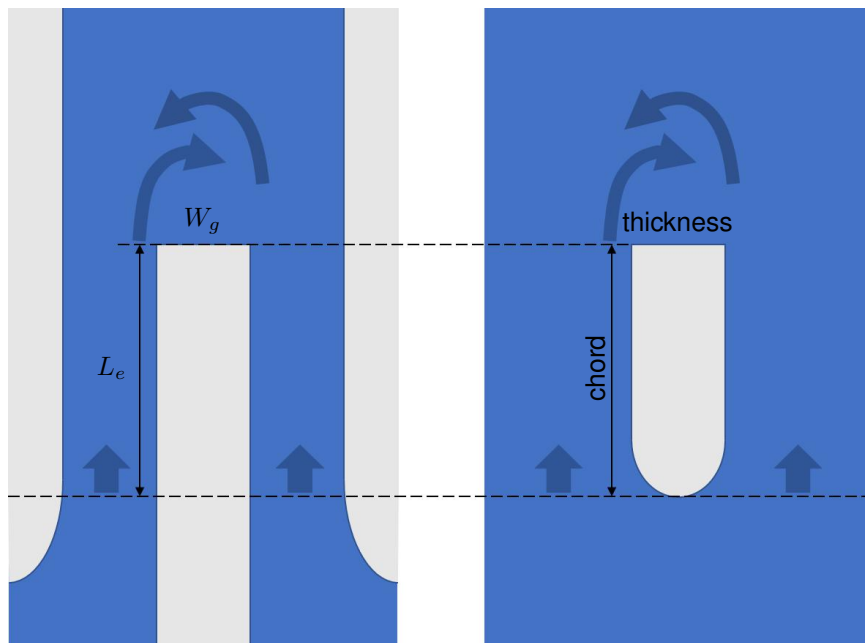


Figure 8.3: Geometric similarity between the contracted channel flow with a gap and the flow around the semi-circular leading edge plate. Dotted line indicates the assumed starting points of the boundary layers.

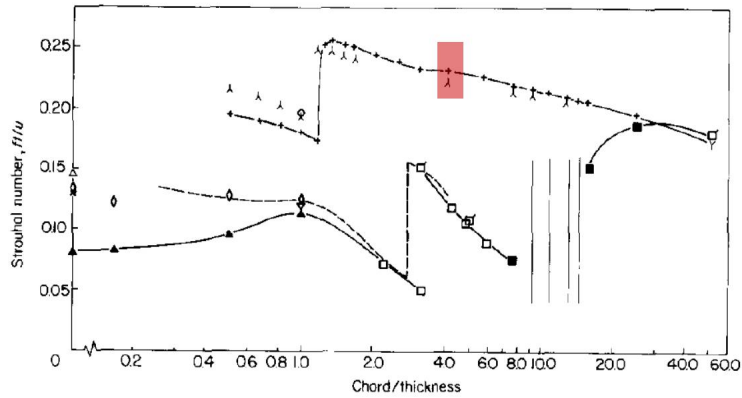


Fig 2 Vortex shedding Strouhal number for flat plates at zero incidence without sound applied. $Re = 14\,800$ to $31\,100$

- ▲ square leading edge narrow spectral peak without end plates $t = 12$
 - ◇ square leading edge narrow spectral peak with end plates $t = 12$
 - square leading edge narrow spectral peak with and without end plates $t = 12$
 - ◻ square leading edge narrow spectral peak with and without end plates $t \cong 6$
 - square leading edge broad spectral peak with and without end plates $t = 12$
 - ! square leading edge no spectral peak with and without end plates $t = 12$
 - + semi-circular leading edge without end plates $t = 12$
 - λ semi-circular leading edge with end plates $t = 12$
 - γ semi-circular leading edge with and without end plates $t \cong 6$
 - circular cylinder with end plates $t = 12$
- Nakaguchi et al ---; Roshko ×; Fage & Johansen, △; Vickery, ▽

Figure 8.4: Vortex shedding Strouhal number for flat plates at zero incidence (excerpted from Parker and Welsh 1983 [8]). Filled red box on the graph shows the range where the current gap mixing Sts of the balanced flows are bounded in, $St = 0.201$ to 0.253 at $L_e/W_g \cong 4$, where L_e is the entrance length defined in Fig. 8.3.

8.4 Methods to Identify Coherent Structures and Mixing Coefficients from the Particle Image Velocimetry Data

8.4.1 Phase-averaging

Phase-averaged image is obtained by averaging a set of data points at the same phase (ensembles) based on the predefined frequency. In our case we use the dominant peak frequency described in (8.3). Here, we chose two-period interval ($2/f_d$) to include the possible subharmonic mode by doubling the frequency resolution.

$$\hat{u}(i, j, p) = \frac{1}{N_q} \sum_{q=0}^{N_q} u \left(i, j, \frac{(q + p/N_p)f_s}{f_d/2} \right), \quad (8.5)$$

$$\hat{v}(i, j, p) = \frac{1}{N_q} \sum_{q=0}^{N_q} v \left(i, j, \frac{(q + p/N_p)f_s}{f_d/2} \right). \quad (8.6)$$

where p is the discrete phase index, f_s is the sampling frequency, N_q is the number of complete two periods in the dataset $N_q = \lfloor N_t \Delta t f_d/2 \rfloor$, $\lfloor \cdot \rfloor$ is the round off operator, and N_p is the number of phase angles to be evaluated in the given interval. In this study, 2D velocity field data are measured for 4000 time steps with the frequency of 12 Hz, and total phase angle of 720 degrees are equally divided into 64 phase steps ($N_p = 64$) for phase-averaging.

Generally, measurement data at the exact phases for (8.5) and (8.6) are not available as the measurement data are recorded in discrete time. The data at the exact phase are estimated by the Piecewise Cubic Hermite Interpolating Polynomials (PCHIP) provided in Matlab.

Phase-averaging does not give a quantitative data such as true energy and the results can even give a false impression that every mode is exactly periodic. We will discuss the drawback of the phase-averaging further in §8.4.3 with some examples.

8.4.2 Proper Orthogonal Decomposition

The Proper Orthogonal Decomposition (POD) is a method to extract a set of basis functions (vectors) that have the most energetic modes sequentially. Let two functions f and g are defined on a interval Ω . An inner product of two functions (f, g) and a norm of a function

$\|f\|$ are defined as

$$(f, g) = \int_{\Omega} f(x)g^*(x)dx, \quad (8.7)$$

$$\|f\| = (f, f)^{1/2}. \quad (8.8)$$

In a continuous function space, POD of a function ψ can be defined as the following optimization problem [9]:

$$\phi = \arg \max_{\phi} \frac{\langle(\psi, \phi)\rangle}{\|\phi\|^2}, \quad (8.9)$$

where $\langle \cdot \rangle$ is an averaging operator. However, the continuous function ψ for the experimental data of turbulent flows is not usually available. Instead, we have a set of discrete time - discrete space data, so we use discrete data method which is called as Singular Value Decomposition (SVD). Assuming data is represented by a matrix $A \in \mathbb{R}^{M \times N}$ that has spatial domain as rows and time domain as columns, SVD theorem states that there exist matrices \mathbf{L} , $\mathbf{\Sigma}$, and \mathbf{R} such that

$$\mathbf{A} = \mathbf{L}\mathbf{\Sigma}\mathbf{R}^T, \quad (8.10)$$

$\mathbf{L} = [l_1 l_2 \cdots l_M]$ and $\mathbf{R} = [r_1 r_2 \cdots r_N]$ are orthogonal matrices, i.e., all its columns are orthonormal to each other, and $\mathbf{\Sigma}$ is a diagonal matrix with all its diagonal elements greater than or equal to zero. The diagonal elements of $\mathbf{\Sigma}$ are sorted in descending order, $\sigma_1 \geq \sigma_2 \geq \cdots \geq \sigma_L \geq 0$, where L is the minimum between M and N .

The most energetic temporal basis vector R_1 which corresponds to σ_1 is obtained by solving the following optimization problem:

$$r_1 = \arg \max_{r_1} \frac{\|\mathbf{A}r_1\|_2}{\|r_1\|_2} = \arg \max_{r_1} \frac{r_1^T \mathbf{A}^T \mathbf{A} r_1}{r_1^T r_1}. \quad (8.11)$$

Since every column of \mathbf{R} is orthonormal to each other, the second most energetic temporal basis vector r_2 can be obtained by imposing additional constraint:

$$r_2 = \arg \max_{r_2} \frac{\|\mathbf{A}r_2\|_2}{\|r_2\|_2} = \arg \max_{r_2} \frac{r_2^T \mathbf{A}^T \mathbf{A} r_2}{r_2^T r_2}. \quad (8.12)$$

such that $r_1^T r_2 = 0$ such that $r_1^T r_2 = 0$

One can find that the optimization problem shown above is identical with the principal component analysis (PCA), and \mathbf{R} is the eigenvector matrix of $\mathbf{A}^T \mathbf{A}$ [10, 11]. Similarly, the most energetic spatial basis vector l_1 can be obtained by transposing the data matrix A :

$$l_1 = \arg \max_{l_1} \frac{\|\mathbf{A}^T l_1\|_2}{\|l_1\|_2} = \arg \max_{l_1} \frac{l_1^T \mathbf{A} \mathbf{A}^T l_1}{l_1^T l_1}, \quad (8.13)$$

and \mathbf{L} is the eigenvector matrix of $\mathbf{A} \mathbf{A}^T$.

SVD is a linear decomposition which does not necessarily reveal the underlying physics of coherent structures. Coherent structures are nonlinear phenomena, and they cannot be superimposed. However, SVD compresses data so that they can be easily compared with other results.

SVD requires centering the data by subtracting the mean value of $u \in \mathbb{R}^{N_y \times N_x \times N_t}$ and $v \in \mathbb{R}^{N_y \times N_x \times N_t}$ so that SVD can only deal with the fluctuation:

$$u'(i, j, k) = u(i, j, k) - \bar{u}(i, j), \quad (8.14)$$

$$v'(i, j, k) = v(i, j, k) - \bar{v}(i, j), \quad (8.15)$$

where \bar{u} and \bar{v} are the sample mean of u and v , respectively. Then, we need to reorder the 3D data u and v into 2D matrix $\mathbf{A}_u \in \mathbb{R}^{2N_y N_x \times N_t}$:

$$\mathbf{A}_u = \begin{bmatrix} v'(1, 1, 1) & v'(1, 1, 2) & \dots & v'(1, 1, N_t) \\ v'(1, 2, 1) & v'(1, 2, 2) & \dots & v'(1, 2, N_t) \\ \vdots & \vdots & \ddots & \vdots \\ v'(1, N_x, 1) & v'(1, N_x, 2) & \dots & v'(1, N_x, N_t) \\ v'(2, 1, 1) & v'(2, 1, 2) & \dots & v'(2, 1, N_t) \\ v'(2, 2, 1) & v'(2, 2, 2) & \dots & v'(2, 2, N_t) \\ \vdots & \vdots & \ddots & \vdots \\ v'(N_y, N_x, 1) & v'(N_y, N_x, 2) & \dots & v'(N_y, N_x, N_t) \\ \hline u'(1, 1, 1) & u'(1, 1, 2) & \dots & u'(1, 1, N_t) \\ u'(1, 2, 1) & u'(1, 2, 2) & \dots & u'(1, 2, N_t) \\ \vdots & \vdots & \ddots & \vdots \\ u'(1, N_x, 1) & u'(1, N_x, 2) & \dots & u'(1, N_x, N_t) \\ u'(2, 1, 1) & u'(2, 1, 2) & \dots & u'(2, 1, N_t) \\ u'(2, 2, 1) & u'(2, 2, 2) & \dots & u'(2, 2, N_t) \\ \vdots & \vdots & \ddots & \vdots \\ u'(N_y, N_x, 1) & u'(N_y, N_x, 2) & \dots & u'(N_y, N_x, N_t) \end{bmatrix} \quad (8.16)$$

The sequence of the u and v , and their spatial indices i and j do not affect the uniqueness of the solution as long as they are converted to actual domain correspondingly after the SVD

is performed.

After SVD is performed, each column vector of \mathbf{L} (left singular vector) and \mathbf{R} (right singular vector) represents the spatial and temporal basis vector, respectively. To have the basis vector in 2D, column vectors of \mathbf{L} must be reordered back to 2D velocity fields according to the scheme shown in (8.16).

Total of eight most energetic modes are obtained for the velocity field data of each field of view (FOV). In most cases, partial energy sum up to eight most energetic modes exceed 90 % of the total energy. Energy ratio of each modes are shown separately in §8.6 for each specific flow condition.

8.4.3 Comparison between SVD modes after phase-averaging and without phase-averaging

As mentioned earlier, coherent structures are only quasi-periodic, and they keep interacting with the random turbulence and slightly change their dominant peak frequency. When we use the frequency-based method such as phase-averaging, there is high possibility that we actually filter out some valuable information, because the only frequency components that survive after phase-averaging are the set of harmonics of the frequency that was used for phase-averaging.

Even when the coherent structure is strongly periodic, while the amplitude of the first harmonic may be well-preserved, but the higher harmonics are still vulnerable to the error. Because we use DFT to find the dominant peak frequency, there is a discretization error between the estimated and actual dominant peak frequency. As we move up to the higher harmonics, this error is amplified and the harmonic frequency of the discretized dominant peak frequency deviates significantly from the actual harmonics of the dominant peak frequency.

Fig. 8.5 and 8.6 show the first left and right singular vectors of the velocity data without phase-averaging and with phase-averaging, respectively. Fig. 8.7 and 8.8 show the first left and right singular vectors of the velocity data without phase-averaging and with phase-averaging, respectively. The flow condition $Re[100\ 100]k$ is symmetric, thus we can expect that the corresponding modes are either symmetric, or anti-symmetric. SVD results without phase-averaging in Fig. 8.5 and 8.7 show that the coherent structures of $Re[100\ 100]k$ are truly symmetric or anti-symmetric. While the first harmonic mode in the SVD results with phase-averaging in Fig. 8.6 conforms the symmetry, the second harmonic mode in the SVD results with PIV in Fig. 8.8 have a deformed shaped that is not symmetric. To explain why the phase-averaging is erroneous, we need to see the Fourier transform of

each temporal singular vector. Fig. 8.9 show the power spectral densities of the first six right (temporal) singular vectors, and Fig. 8.10 show the detailed power spectral densities of the squared areas in Fig. 8.9. One can see that the actual dominant peak frequency does not lie on the discrete frequency grid, and the energy is split into two discrete frequency modes. Phase-averaging only saves the exact frequency mode, which means that half of the actual fluctuation energy. Even worse, the second harmonic mode of the estimated dominant frequency is one step off from the actual second harmonic mode, and almost all its energy is lost during the phase-averaging.

In summary, phase-averaging does not preserve the energy quantity, and it can produce substantial error especially for the higher harmonic modes. In this study, we will only use the SVD data without applying phase-averaging due to the observed deterioration of data when phase-averaging is applied. Computing the entire set of SVD without phase-averaging can take large computational resources, but we only need a few (six) highest modes to account for more than 80% of the total fluctuation energy.

8.5 Implementation

8.5.1 Matlab codes

Matlab is used to process the phase-averaging, vorticity calculation, and then SVD. Corresponding m files and result files are explained below.

1. `create2DVec_SJ.m` Parse the raw data stored in the Matlab structure 'Frames' and extract velocity fields and grid information.
2. `getTimeStamp.m` Parse the raw data stored in the Matlab structure 'Frames' and extract time stamp information.
3. `vc7_read_v8.m` Core routine, read velocity vectors from vc7 binary files and perform the singular value decomposition.
4. `batch_copy_file.m` Copy all processed data to the designated folder.
5. `batch_read_PA_SVD.m` Read folder locations where the data sets are stored, adjust the image grid based on the fields of view, then call `vc7_read_v6.m` for each dataset.
6. `ListOfFolderPaths_5b_SJ.m` List the folder location where raw dataset is stored for each case number.

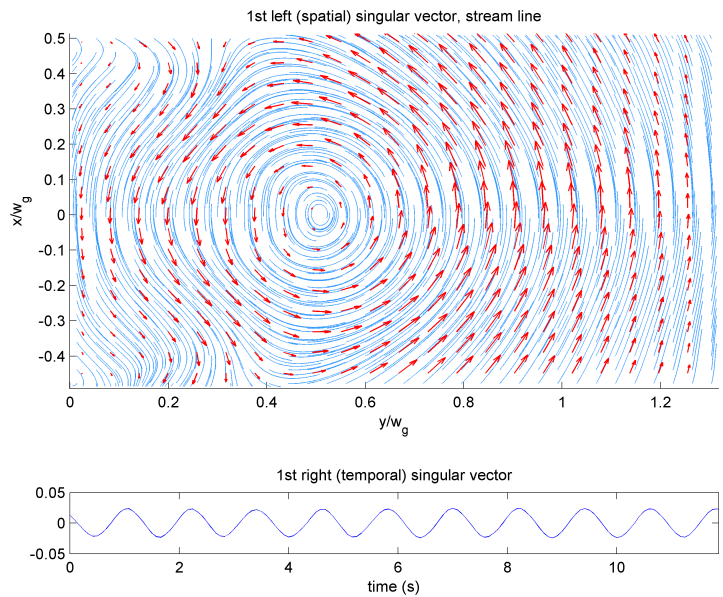


Figure 8.5: First left and right singular vectors of the velocity data of the flow condition $Re[100, 100]k$, gap size 50 mm, FOV 1. The first and second singular modes correspond to the dominant frequency.

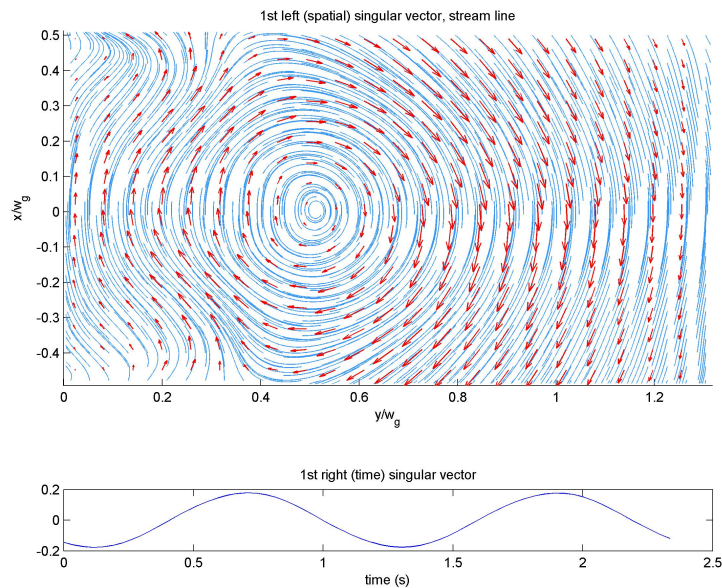


Figure 8.6: First left and right singular vectors of the phase-averaged velocity data of the flow condition $Re[100, 100]k$, $H_g = 50$ mm, FOV 1.

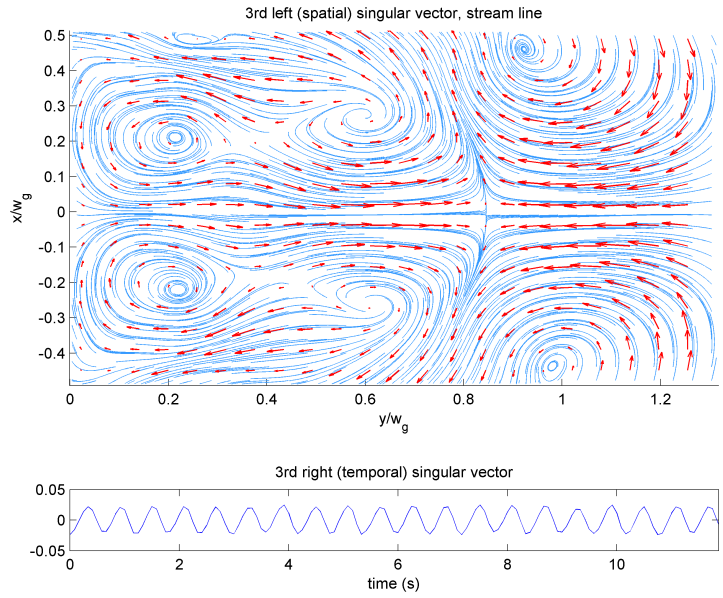


Figure 8.7: Third left and right singular vectors of the original velocity data of the flow condition $Re[100, 100]k$, $H_g = 50$ mm, FOV 1. The third and fourth singular modes correspond to the second harmonic of the dominant frequency. The streamline shows symmetric coherent structure.

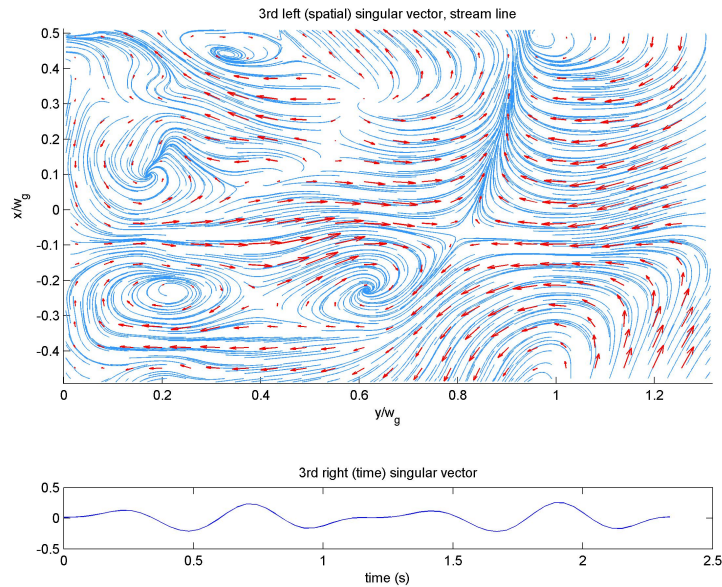


Figure 8.8: Third left and right singular vectors of the phase-averaged velocity data of the flow condition $Re[100, 100]k$, $H_g = 50$ mm, FOV 1. The symmetric structure shown in 8.7 is broken during the phase-averaging process.

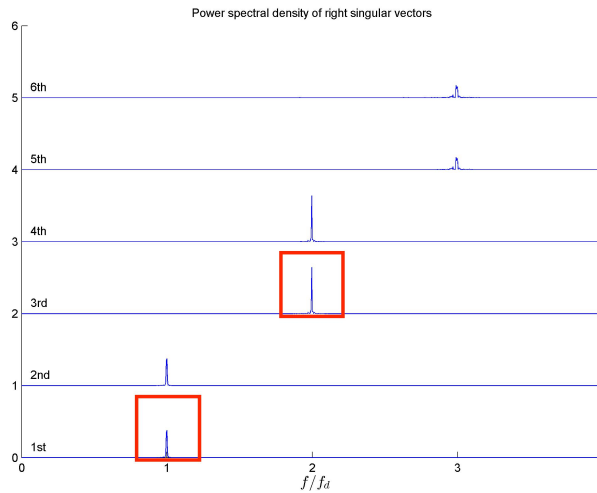


Figure 8.9: Power spectral densities of the first six right singular vectors of the flow condition $\text{Re}[100, 100]\text{k}$, $H_g = 50$ mm, FOV 1. Each set of Fourier coefficients are shifted by $i - 1$ upward, where i is the order of each mode in terms of the magnitude of singular values. Red squares show the location where the detailed images in Fig. 8.10 are taken.

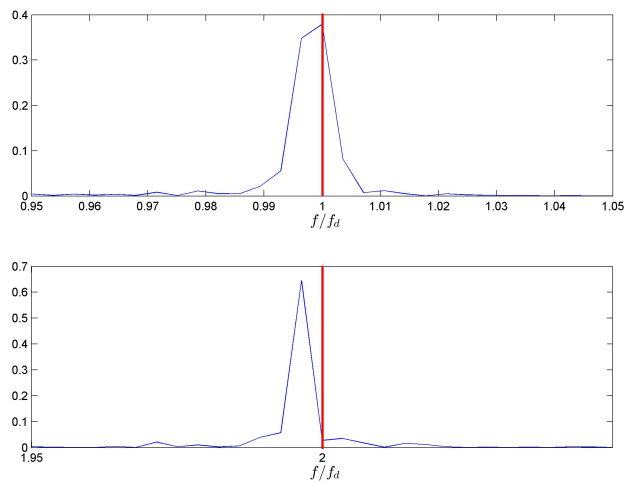


Figure 8.10: Detailed power spectral densities of the 1st (up) and 3rd (down) right singular vectors of the flow condition $\text{Re}[100, 100]\text{k}$, $H_g = 50$ mm, FOV 1. The dominant peak frequency does not lie on the discrete frequency grid exactly, which makes the estimated dominant peak frequency deviates from the actual dominant frequency slightly. As the phase-averaging only leaves the exact harmonics of the discrete dominant peak frequency, the third singular modes, which corresponds to the second harmonic, lost most of its data due to the offset of the actual second harmonic frequency.

7. `process_Strouhal.m` obtain Strouhal number from the frequency information

8.5.2 Data files

Processed data are stored in the following formats.

Matlab data files

1. `raw_data_v3.mat` raw data in Matlab format
 - (a) `U_dat` raw data stored in cell array, vertical velocity in `U_dat{1}` and transverse velocity in `U_dat{2}`
 - (b) `t_stamp` acquisition time stamps (note: time stamp data has not been used because of the possible error, and time steps are assumed to be constant. It needs further verification).
2. `SVD_Ns=XX.mat` Singular value decomposition results for the velocity field and vorticity field. `XX` denotes the number of highest energetic modes acquired.
 - (a) `grd_X, grd_Y` grid information of the spatial domain
 - (b) `grd_T` grid information of the time domain
 - (c) `grd_F` grid information of the frequency domain
 - (d) `U_dat_mean` time mean of the velocity data in cell array
 - (e) `C_dat_mean` time mean of the vorticity data
 - (f) `freq_dom` dominant peak frequency
 - (g) `U_L_svd` left (spatial) singular vector of the velocity data
 - (h) `U_S_svd` singular value matrix of the velocity data
 - (i) `U_R_svd` right (temporal) singular vector for the velocity data
 - (j) `energy_ratio_vel` accumulated energy ratio of the velocity singular modes, i.e.,

$$\text{energy_ratio_vel}(n) = (\sum_{i=1}^n \sigma_i^2) / (\sum_{i=1}^L \sigma_i^2)$$

PNG files

1. `freq_analysis_XX.png` Frequency analysis result of
 - (a) `XX=1` Map of peak frequency for the vertical velocity

- (b) $XX=2$ Map of peak frequency for the transverse velocity
- 2. VEL_time_avg_1.png Time-averaged velocity field, shown as streamlines.
- 3. VTC_time_avg_1.png Time-averaged vorticity field.
- 4. SVD_XXX_sval_Y.png Singular values,
 - (a) XXX 'vel' for velocity field, 'vtc' for vorticity field
 - (b) Y '1' for singular value plot, '2' for partial sum energy ratio
- 5. SVD_XXX_svec_YYY.png Left and right singular vectors,
 - (a) XXX 'vel' for velocity field, 'vtc' for vorticity field
 - (b) YYY 'contour' for contour plots, 'stream' for streamline plots
- 6. SVD_XXX_svec_FFT_1.png Power spectral density of the right singular vectors. XXX denotes 'vel' for velocity field, 'VTC' for vorticity field. (note: By convention of SVD, all left and right singular vectors are normalized. Amplitude does not have a physical meaning, but one can see which harmonic is dominant in each mode.)

8.6 Mean, Singular values, and Singular Vectors of Each Flow Condition

In this section, we summarize the SVD results in the following manner:

1. Time-averaged velocity field
2. Normalized singular values, and the energy proportion of each singular mode to the total fluctuation energy. We define the normalized singular value as

$$\hat{\sigma}_s = \frac{\sigma_s}{\sqrt{N_x N_y N_t}}, \quad (8.17)$$

and the energy proportion as

$$\hat{E}_s = \frac{\sigma_s^2}{\sum_{r=1}^{N_s} \sigma_r^2}. \quad (8.18)$$

Note that the normalized singular value is equivalent to the root mean squared deviation of the mode. Identifying all singular modes are not only time-consuming, but also not required to compute $\sum_{r=1}^{N_s} \sigma_r^2$. Instead, we can use the identity of Frobenius norm.

$$\sum_r \sigma_r^2 = \|\mathbf{A}_u\|_F^2 = \sum_m \sum_n a_{m,n}^2. \quad (8.19)$$

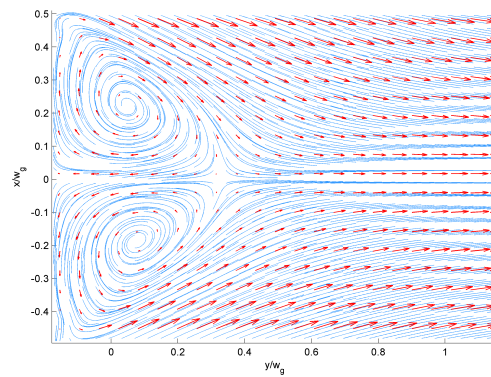
3. Four largest left and right singular vectors.
4. Power spectral density of the first six right singular vectors. We define the power spectral density as

$$\Phi_r(s, w) = \begin{cases} \frac{2}{N_k} |\mathcal{R}(s, l)|^2 & \text{if } l = 2, 3, \dots, N_k/2, \\ \frac{1}{N_k} |\mathcal{R}(s, l)|^2 & \text{if } l = 1 \text{ or } N_k/2 + 1, \\ 0 & \text{otherwise} \end{cases} \quad (8.20)$$

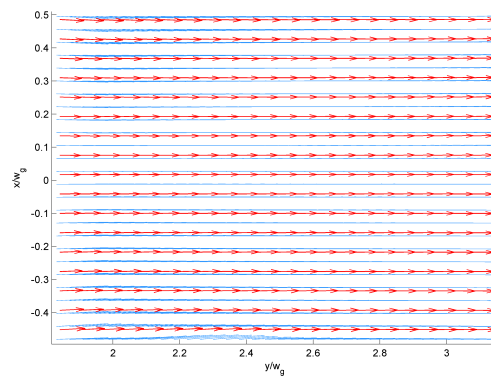
where $\mathcal{R}(s, w)$ is the DFT of the s^{th} right singular vector $r_s(k)$. w is the frequency index. All DFT conventions including indices in Eqn. (8.20) follow the Matlab R2014a FFT(\cdot) conventions. By parseval's theorem, $\sum_w \Phi_r(s, w) = 1$.

5. Detailed power spectral densities of the first and third right singular vectors.

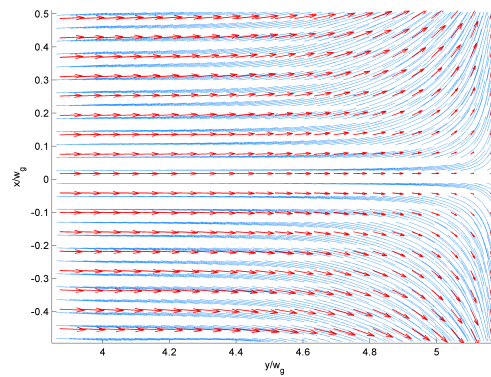
8.6.1 $\text{Re}[100\ 100]\mathbf{k}$, $H_g = 10\text{mm}$



(a)



(b)



(c)

Figure 8.11: Time-averaged velocity field of $\text{Re}[100\ 100]\mathbf{k}$, $H_g = 10\text{ mm}$; FOV 1 (a), FOV 2 (b), and FOV 3 (C). Red arrows indicate velocity vectors, and blue lines indicate streamlines.

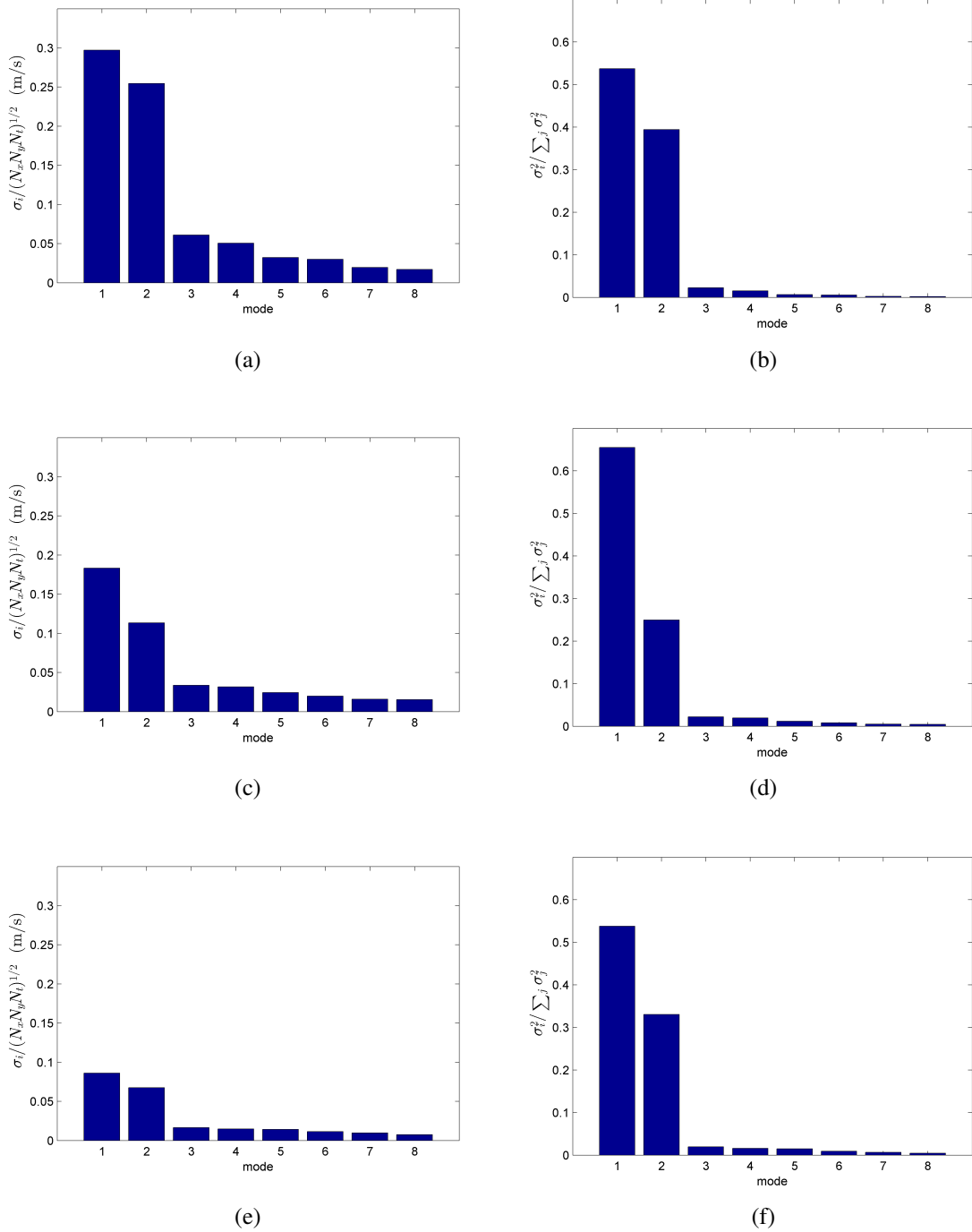


Figure 8.12: Normalized singular values (left) and their energy proportions (right) of the first eight modes, $\text{Re}[100\ 100]_k$, $H_g = 10$ mm; FOV 1: (a) and (b), FOV 2: (c) and (d), FOV 3: (e) and (f).

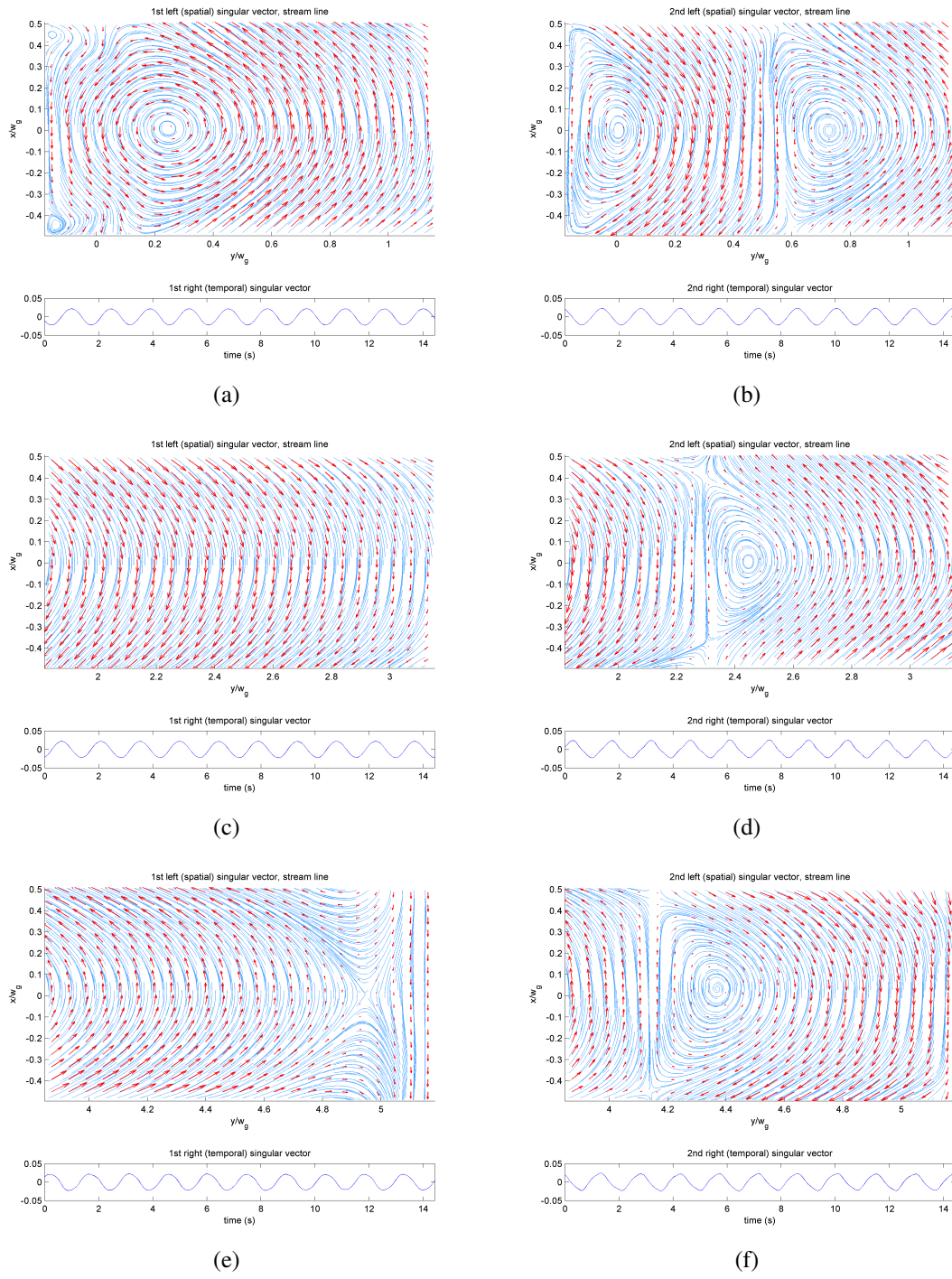


Figure 8.13: Singular vectors of the first (left) and the second (right) modes, $Re[100\ 100]k$, $H_g = 10\text{ mm}$; FOV1: (a) and (b), FOV2: (c) and (d), FOV3: (e) and (f). Red arrows are velocity vectors, and blue lines are streamlines.

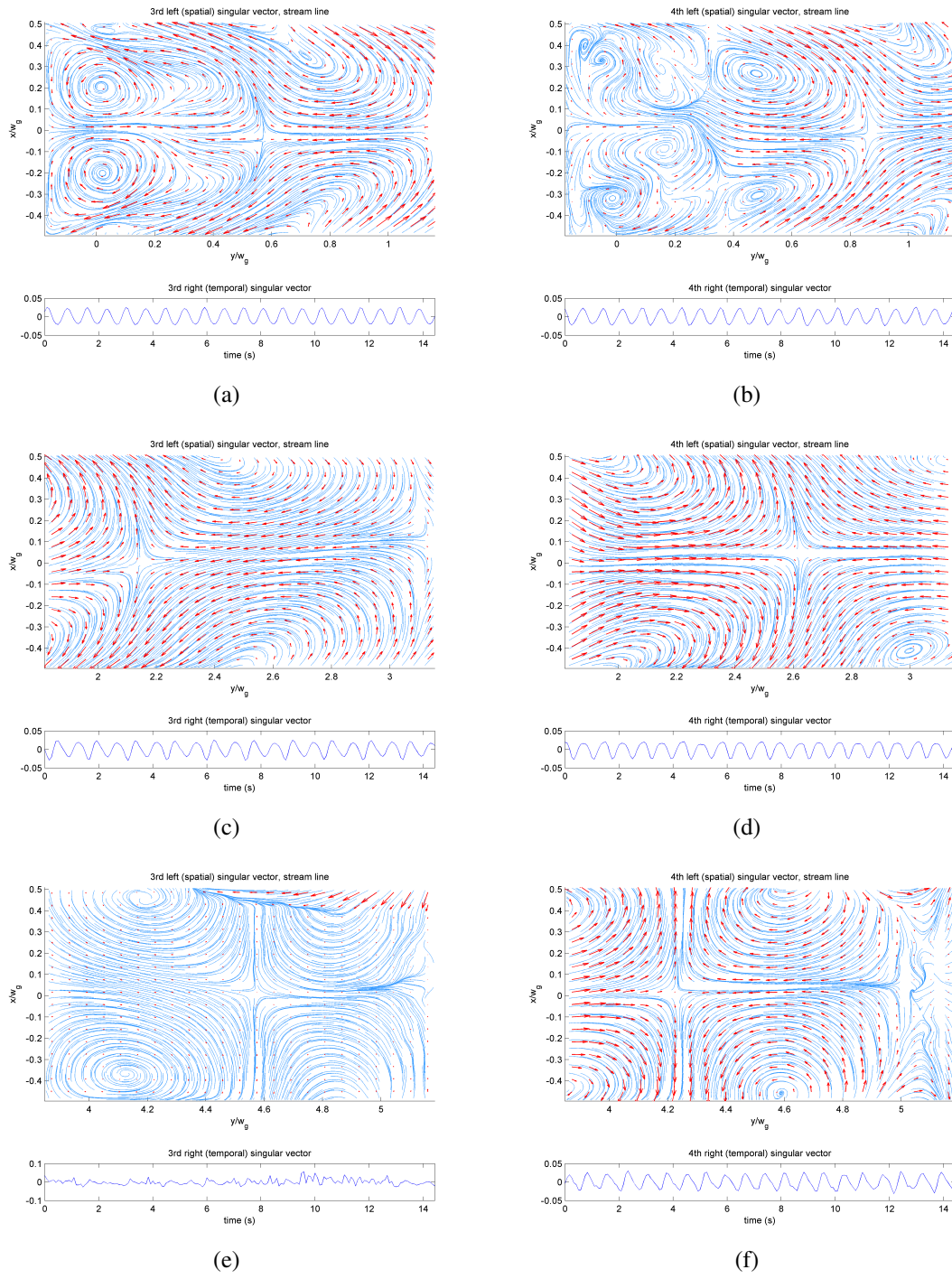


Figure 8.14: Singular vectors of the third (left) and the fourth (right) modes, $\text{Re}[100\ 100]k$, $H_g = 10\text{ mm}$; FOV1: (a) and (b), FOV2: (c) and (d), FOV3: (e) and (f). Red arrows are velocity vectors, and blue lines are streamlines.

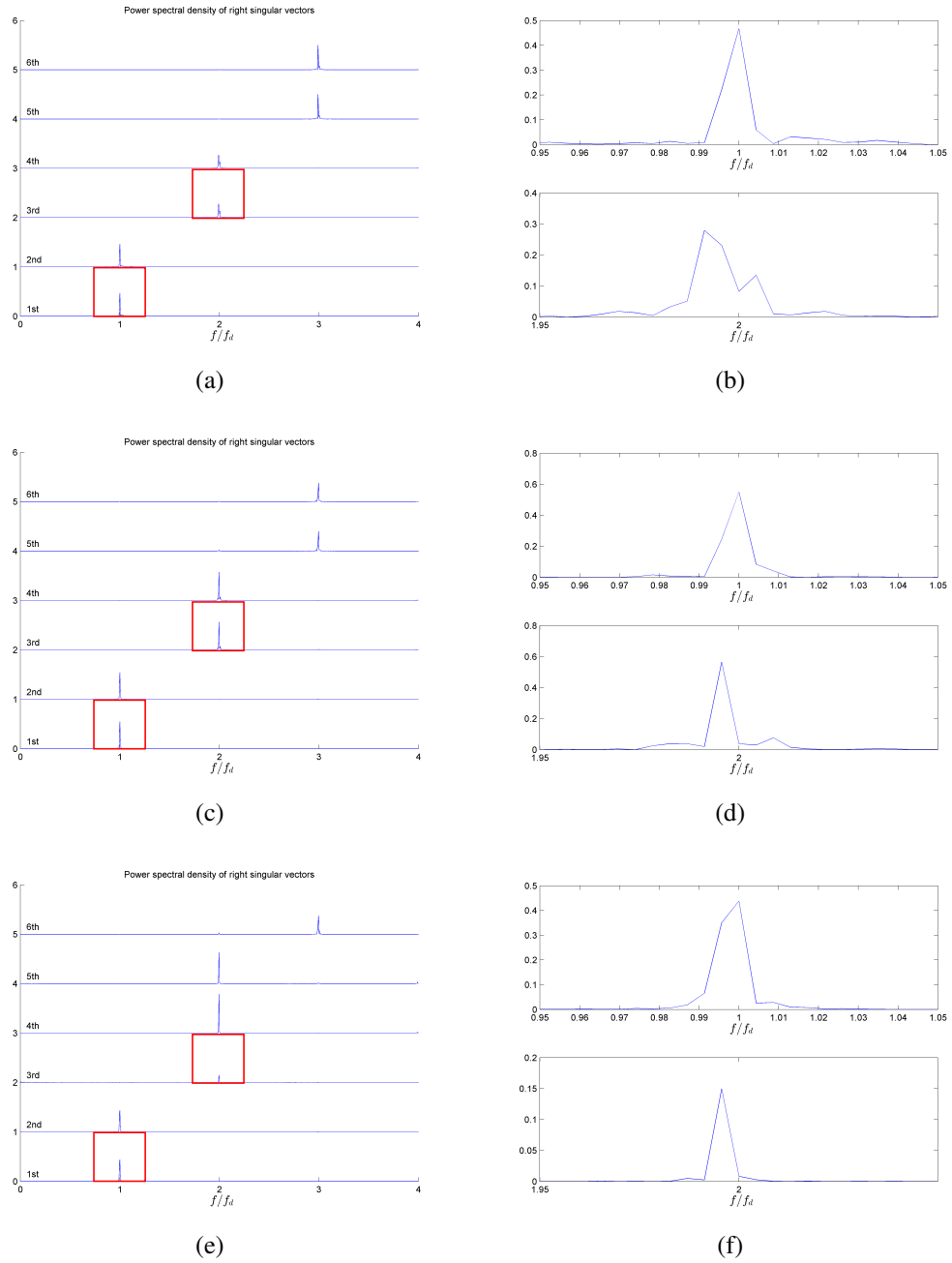
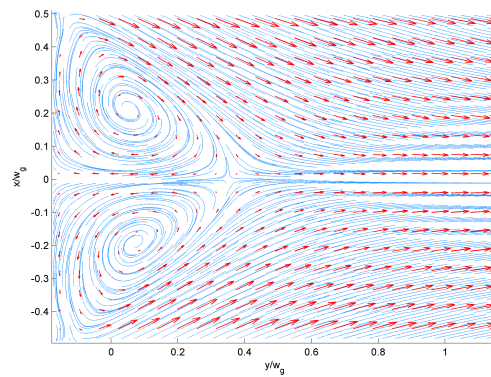
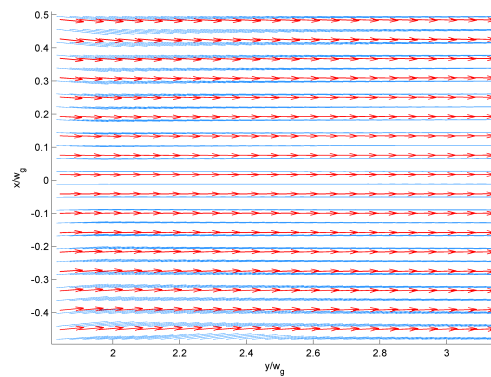


Figure 8.15: Power spectral densities of the first four right singular vectors (a), (c), (e), and the enlarged images of the power spectral densities of the first (top) and the third (bottom) right singular vectors (b), (d), (f), $\text{Re}[100\ 100]k$, $H_g = 10$ mm; FOV 1: (a) and (b), FOV 2: (c) and (d), and FOV 3: (e) and (f). Red squares on (a), (c), and (e) show the areas where (b), (d), and (f) are taken, respectively.

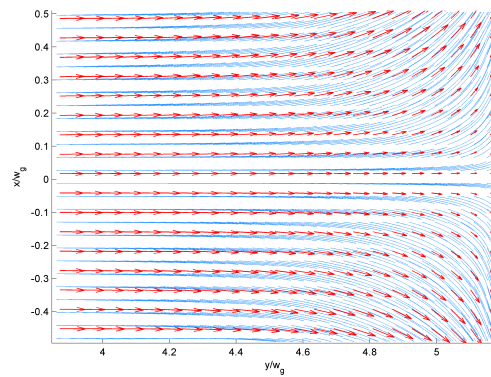
8.6.2 $\text{Re}[100\ 100]\mathbf{k}$, $H_g = 20\text{mm}$



(a)



(b)



(c)

Figure 8.16: Time-averaged velocity field of $\text{Re}[100\ 100]\mathbf{k}$, $H_g = 20\text{ mm}$; FOV 1 (a), FOV 2 (b), and FOV 3 (C). Red arrows indicate velocity vectors, and blue lines indicate streamlines.

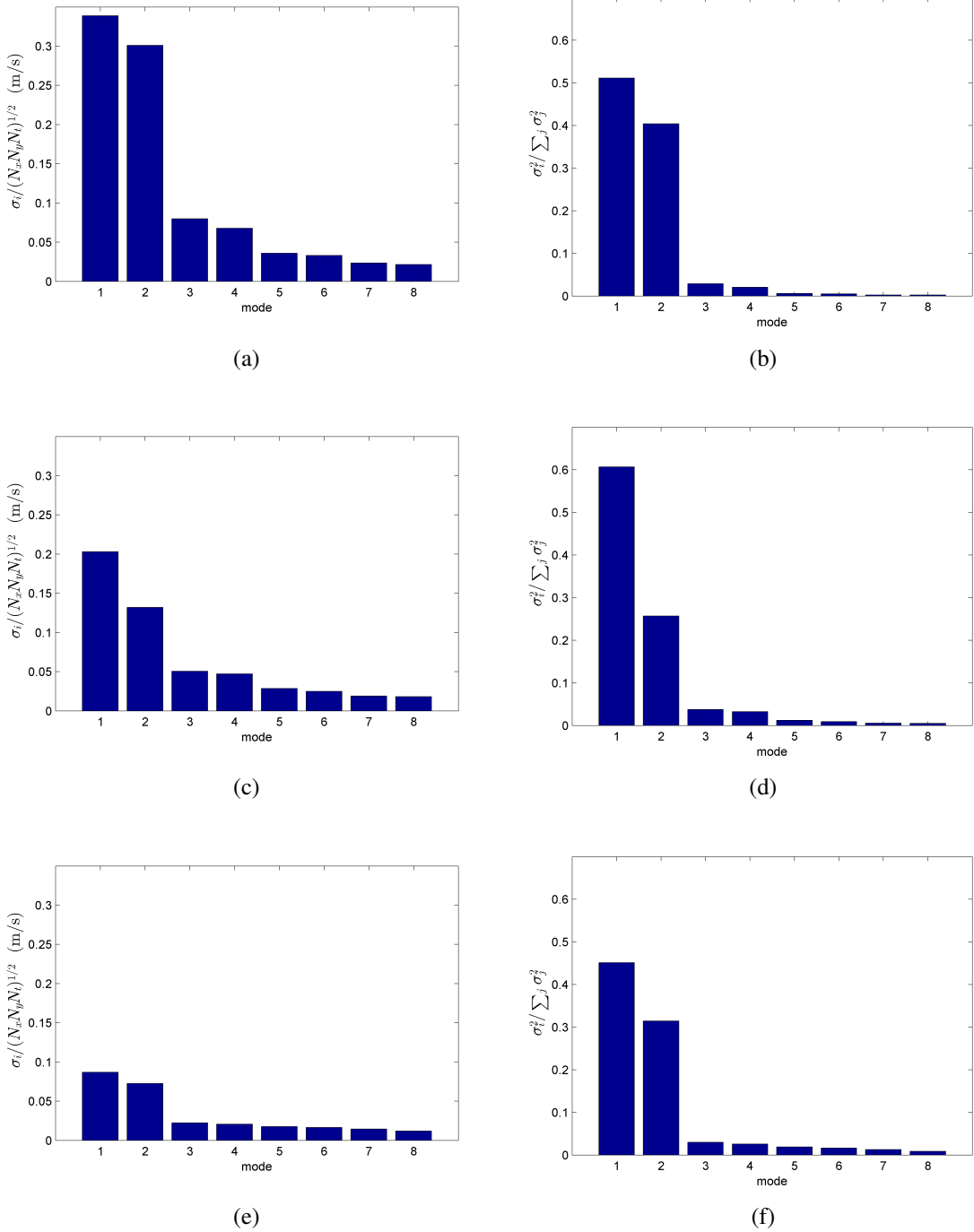


Figure 8.17: Normalized singular values (left) and their energy proportions (right) of the first eight modes, $\text{Re}[100\ 100]_k$, $H_g = 20$ mm; FOV 1: (a) and (b), FOV 2: (c) and (d), FOV 3: (e) and (f).

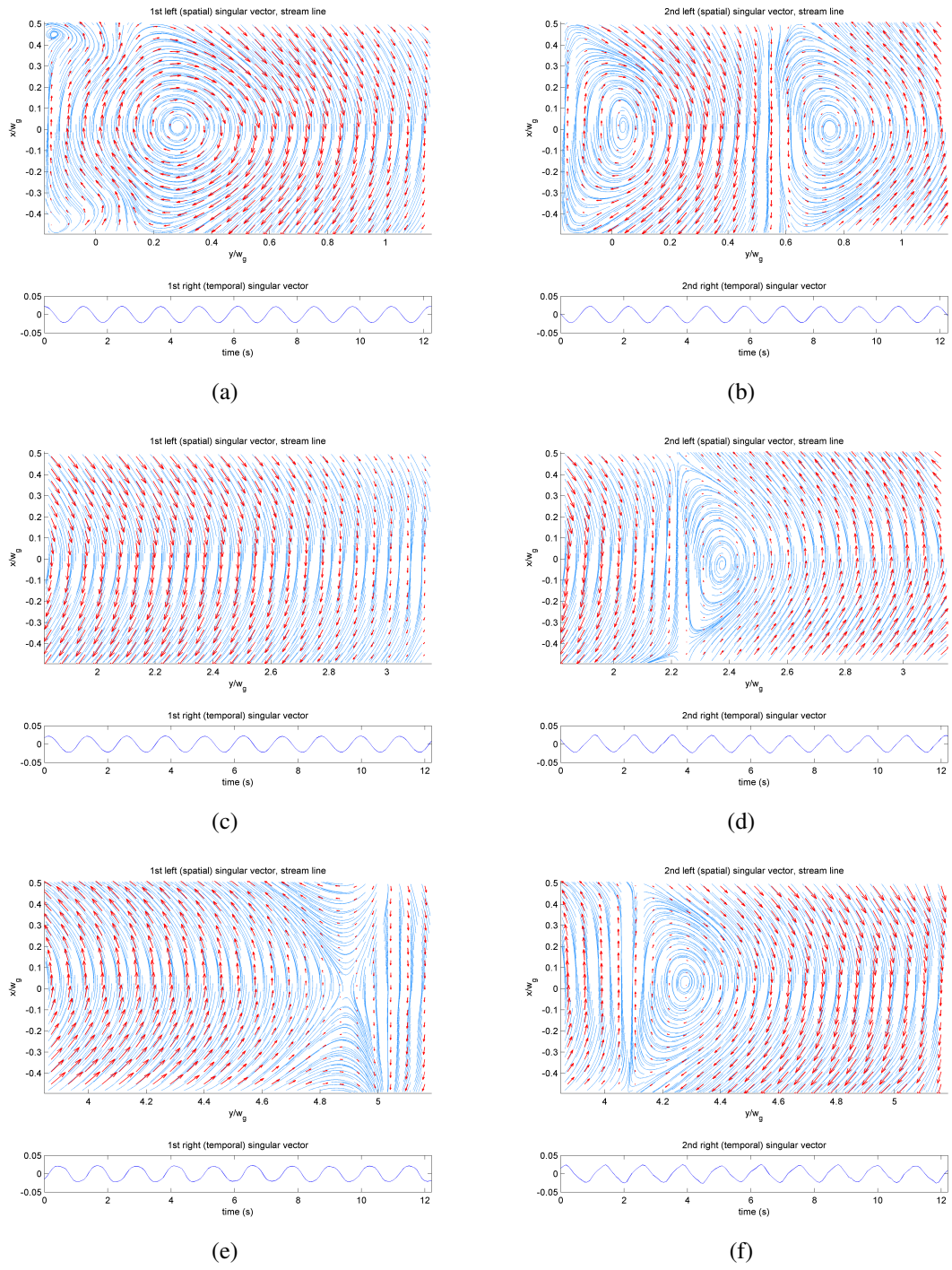


Figure 8.18: Singular vectors of the first (left) and the second (right) modes, $\text{Re}[100\ 100]k$, $H_g = 20\text{ mm}$; FOV1: (a) and (b), FOV2: (c) and (d), FOV3: (e) and (f). Red arrows are velocity vectors, and blue lines are streamlines.

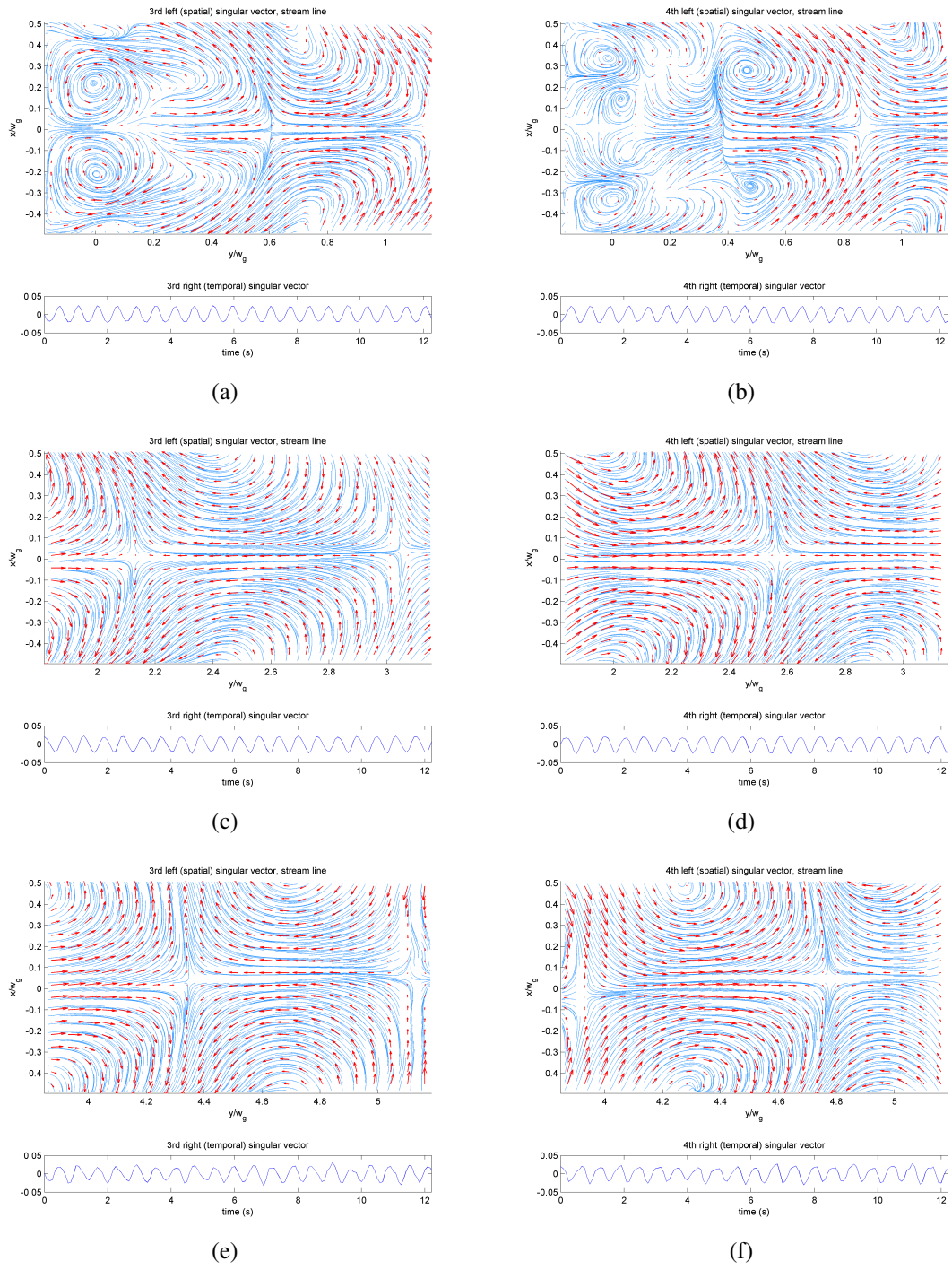


Figure 8.19: Singular vectors of the third (left) and the fourth (right) modes, $\text{Re}[100\ 100]k$, $H_g = 20\text{ mm}$; FOV1: (a) and (b), FOV2: (c) and (d), FOV3: (e) and (f). Red arrows are velocity vectors, and blue lines are streamlines.

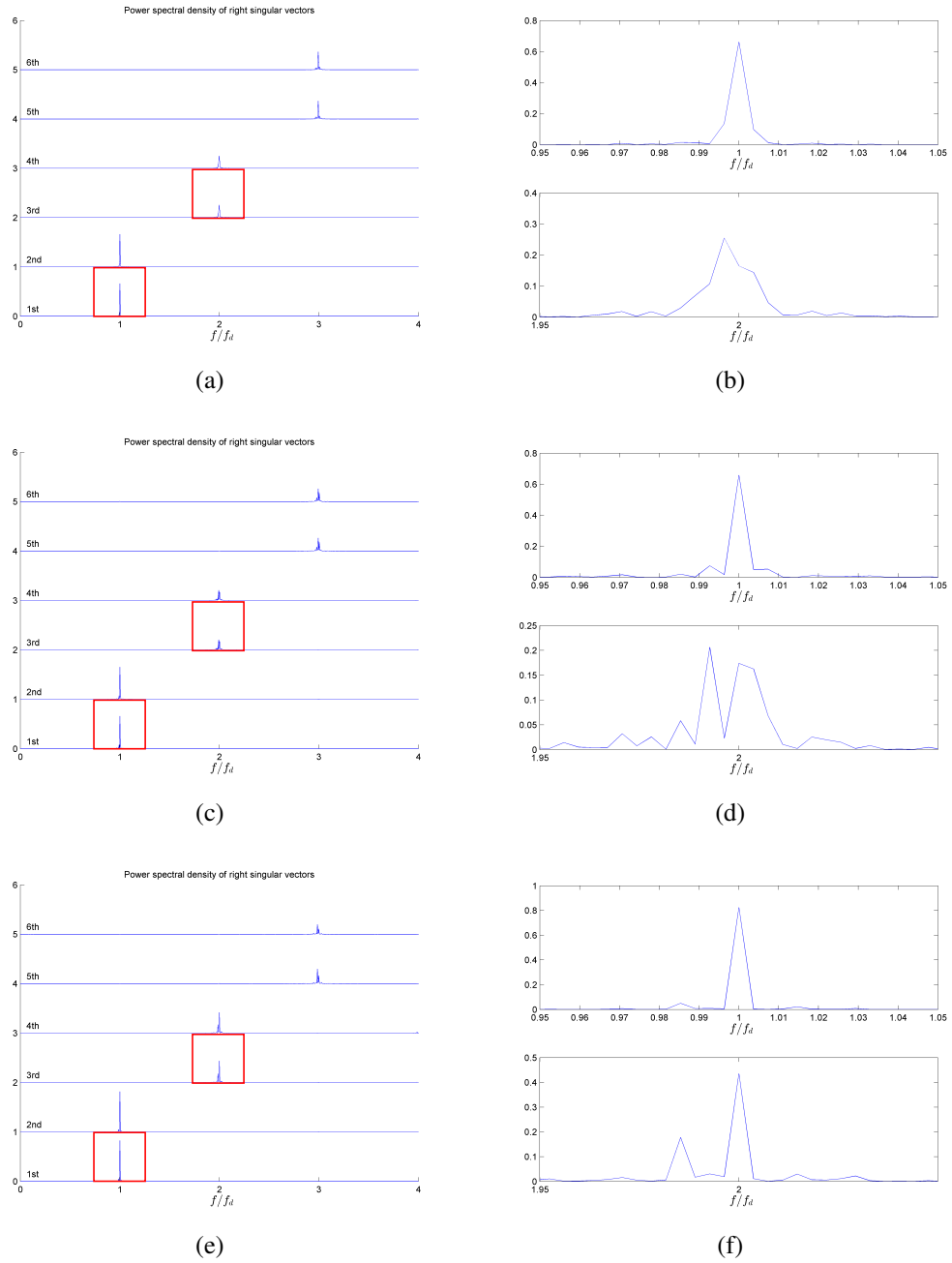
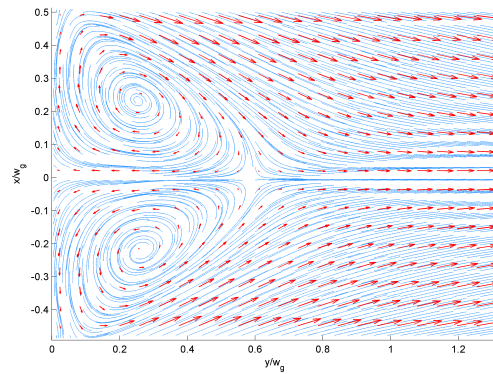
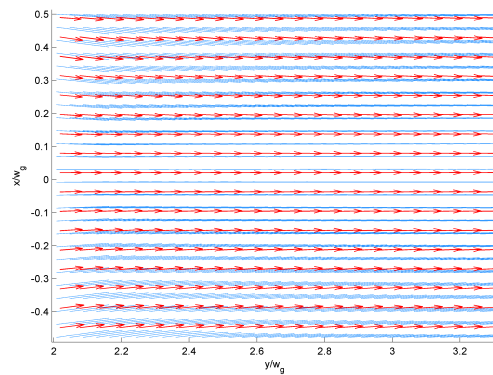


Figure 8.20: Power spectral densities of the first four right singular vectors (a), (c), (e), and the enlarged images of the power spectral densities of the first (top) and the third (bottom) right singular vectors (b), (d), (f), $\text{Re}[100\ 100]_k$, $H_g = 20$ mm; FOV 1: (a) and (b), FOV 2: (c) and (d), and FOV 3: (e) and (f). Red squares on (a), (c), and (e) show the areas where (b), (d), and (f) are taken, respectively.

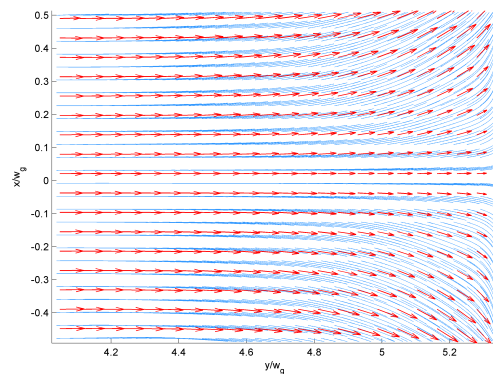
8.6.3 $\text{Re}[100\ 100]\mathbf{k}$, $H_g = 50\text{mm}$



(a)



(b)



(c)

Figure 8.21: Time-averaged velocity field of $\text{Re}[100\ 100]\mathbf{k}$, $H_g = 50\text{ mm}$; FOV 1 (a), FOV 2 (b), and FOV 3 (C). Red arrows indicate velocity vectors, and blue lines indicate streamlines.

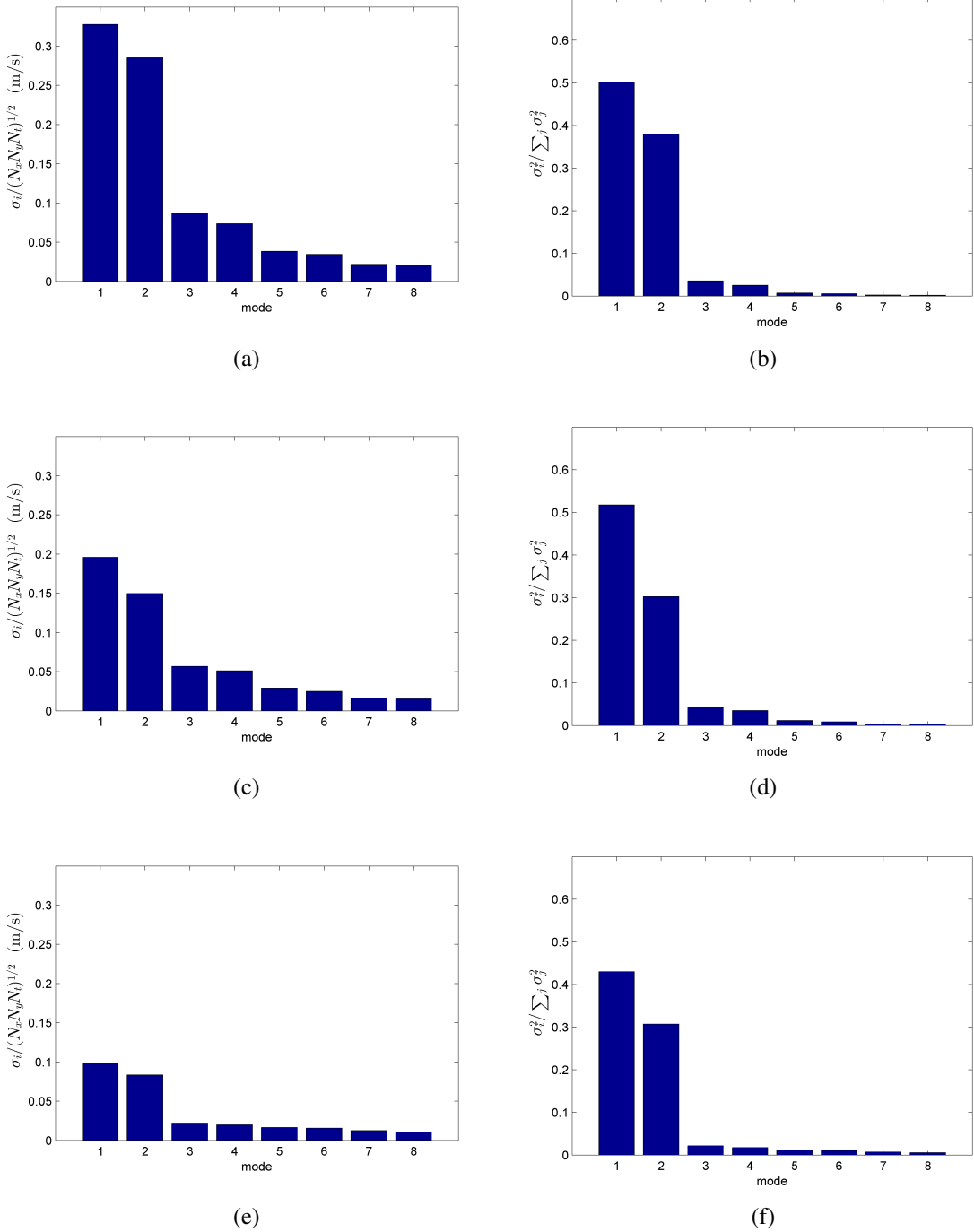


Figure 8.22: Normalized singular values (left) and their energy proportions (right) of the first eight modes, $\text{Re}[100\ 100]_k$, $H_g = 50$ mm; FOV 1: (a) and (b), FOV 2: (c) and (d), FOV 3: (e) and (f).

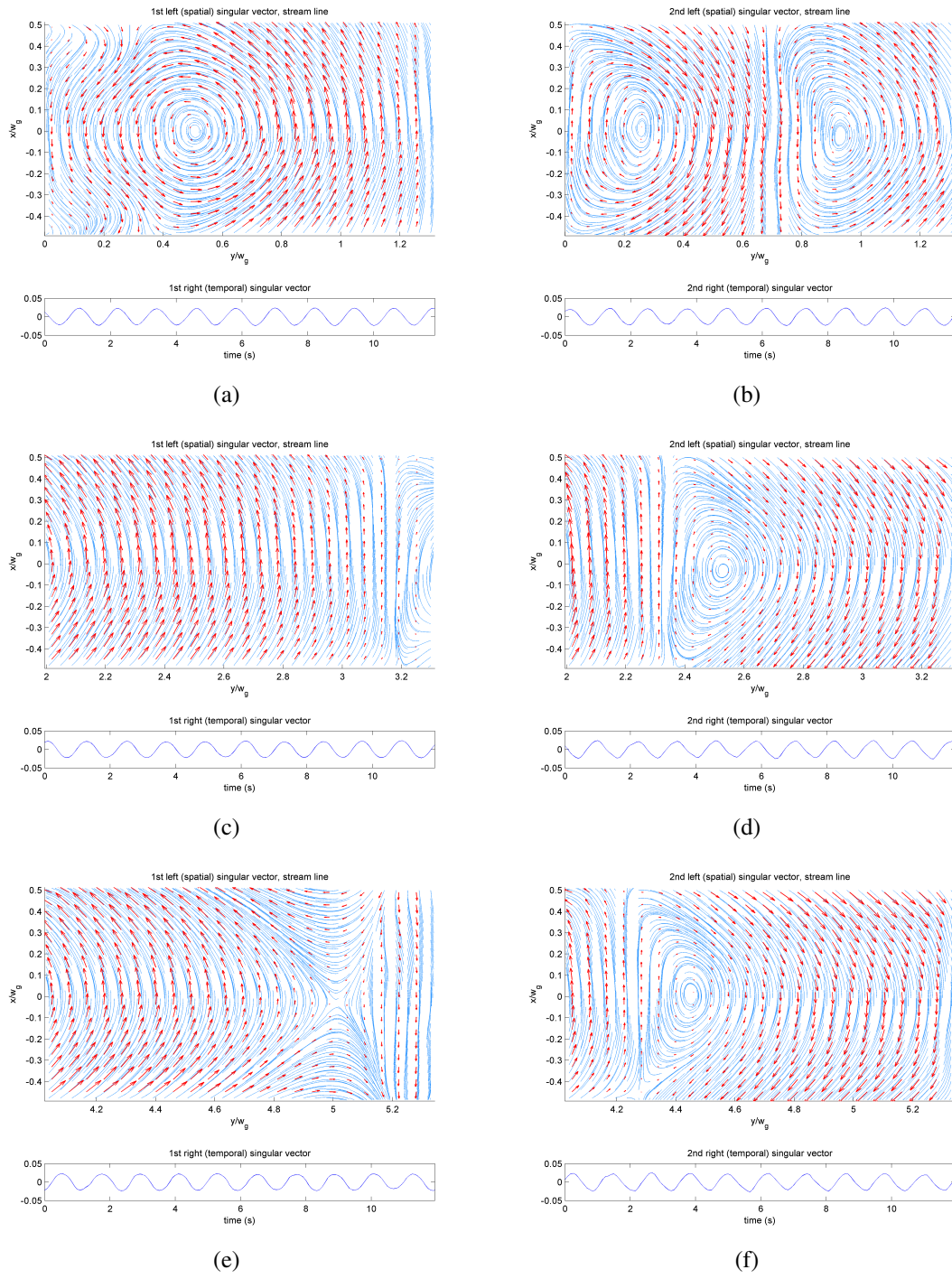


Figure 8.23: Singular vectors of the first (left) and the second (right) modes, $\text{Re}[100\ 100]k$, $H_g = 50\text{ mm}$; FOV1: (a) and (b), FOV2: (c) and (d), FOV3: (e) and (f). Red arrows are velocity vectors, and blue lines are streamlines.

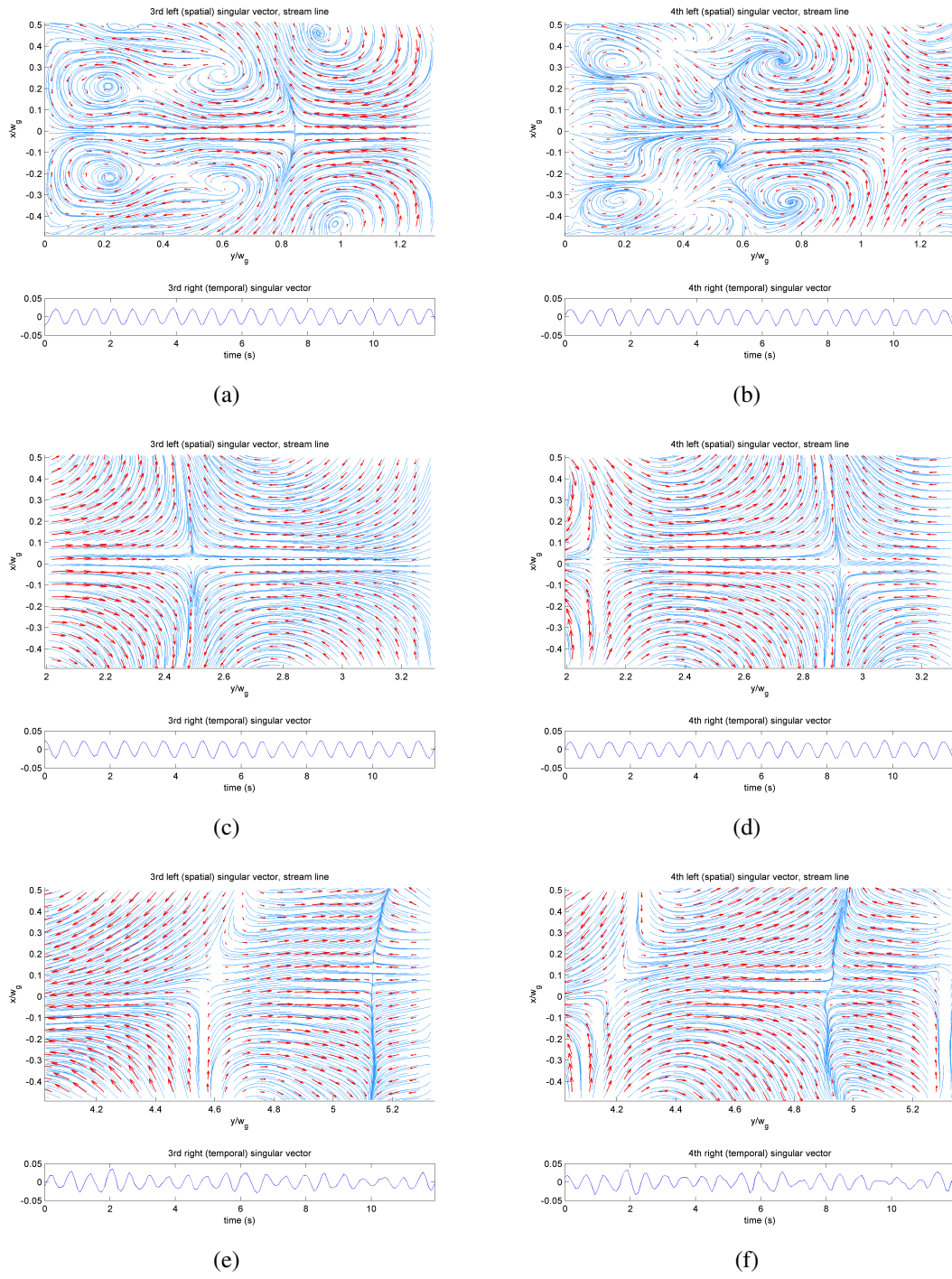


Figure 8.24: Singular vectors of the third (left) and the fourth (right) modes, $\text{Re}[100\ 100]k$, $H_g = 50\text{ mm}$; FOV1: (a) and (b), FOV2: (c) and (d), FOV3: (e) and (f). Red arrows are velocity vectors, and blue lines are streamlines.

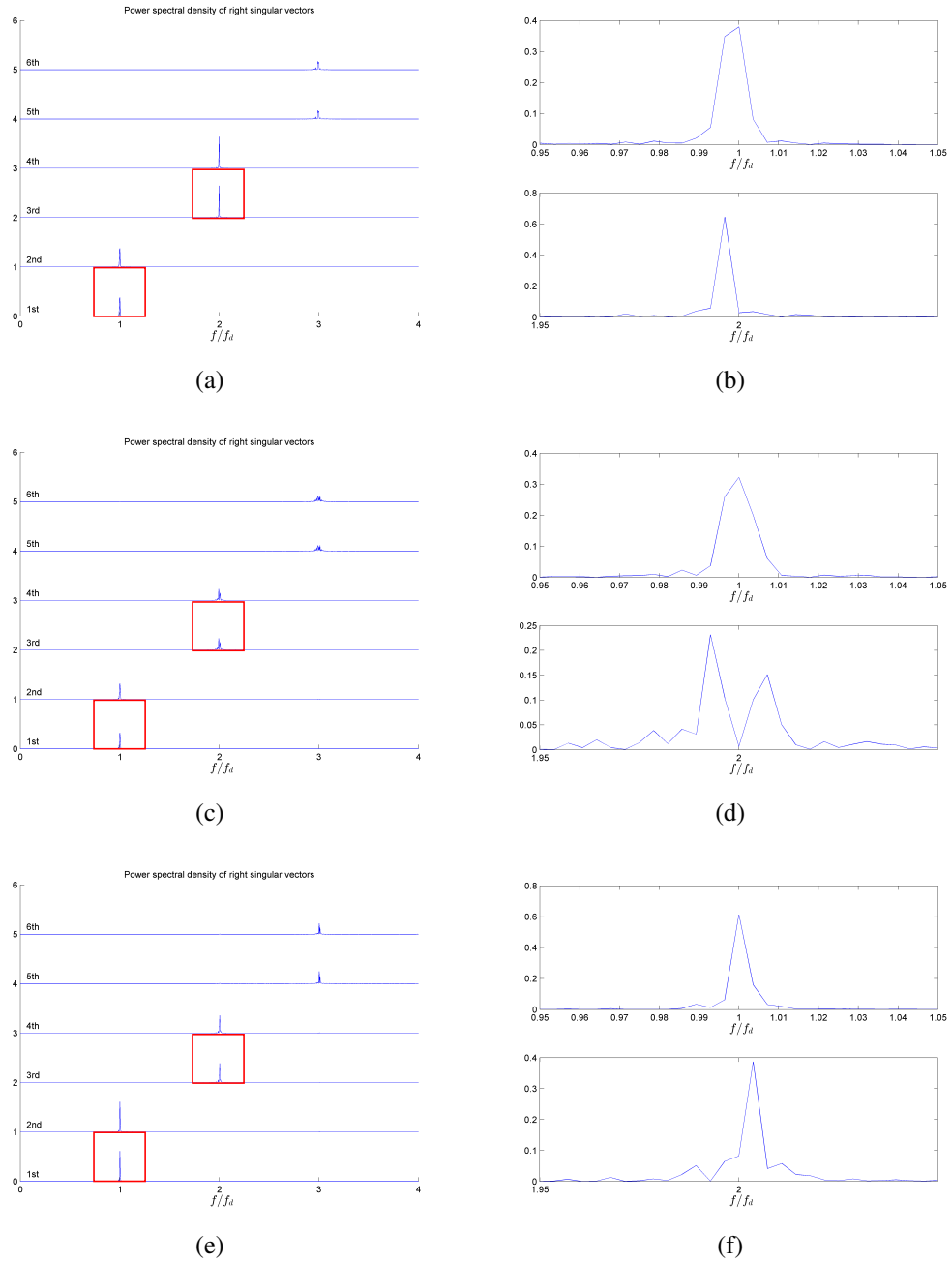
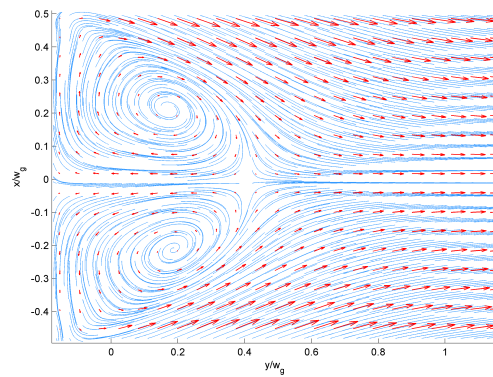
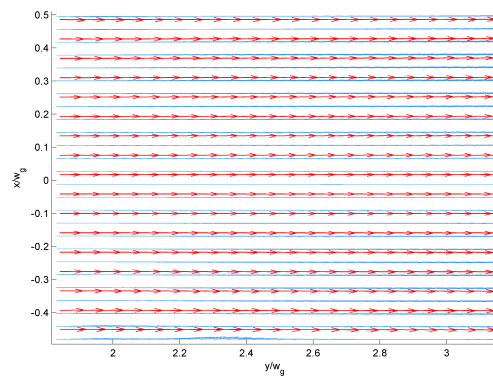


Figure 8.25: Power spectral densities of the first four right singular vectors (a), (c), (e), and the enlarged images of the power spectral densities of the first (top) and the third (bottom) right singular vectors (b), (d), (f), $\text{Re}[100\ 100]k$, $H_g = 50$ mm; FOV 1: (a) and (b), FOV 2: (c) and (d), and FOV 3: (e) and (f). Red squares on (a), (c), and (e) show the areas where (b), (d), and (f) are taken, respectively.

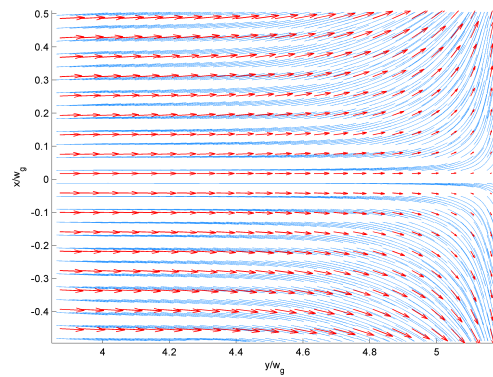
8.6.4 $\text{Re}[40\ 40]\mathbf{k}$, $H_g = 10\text{mm}$



(a)



(b)



(c)

Figure 8.26: Time-averaged velocity field of $\text{Re}[40\ 40]\mathbf{k}$, $H_g = 10\text{ mm}$; FOV 1 (a), FOV 2 (b), and FOV 3 (C). Red arrows indicate velocity vectors, and blue lines indicate streamlines.

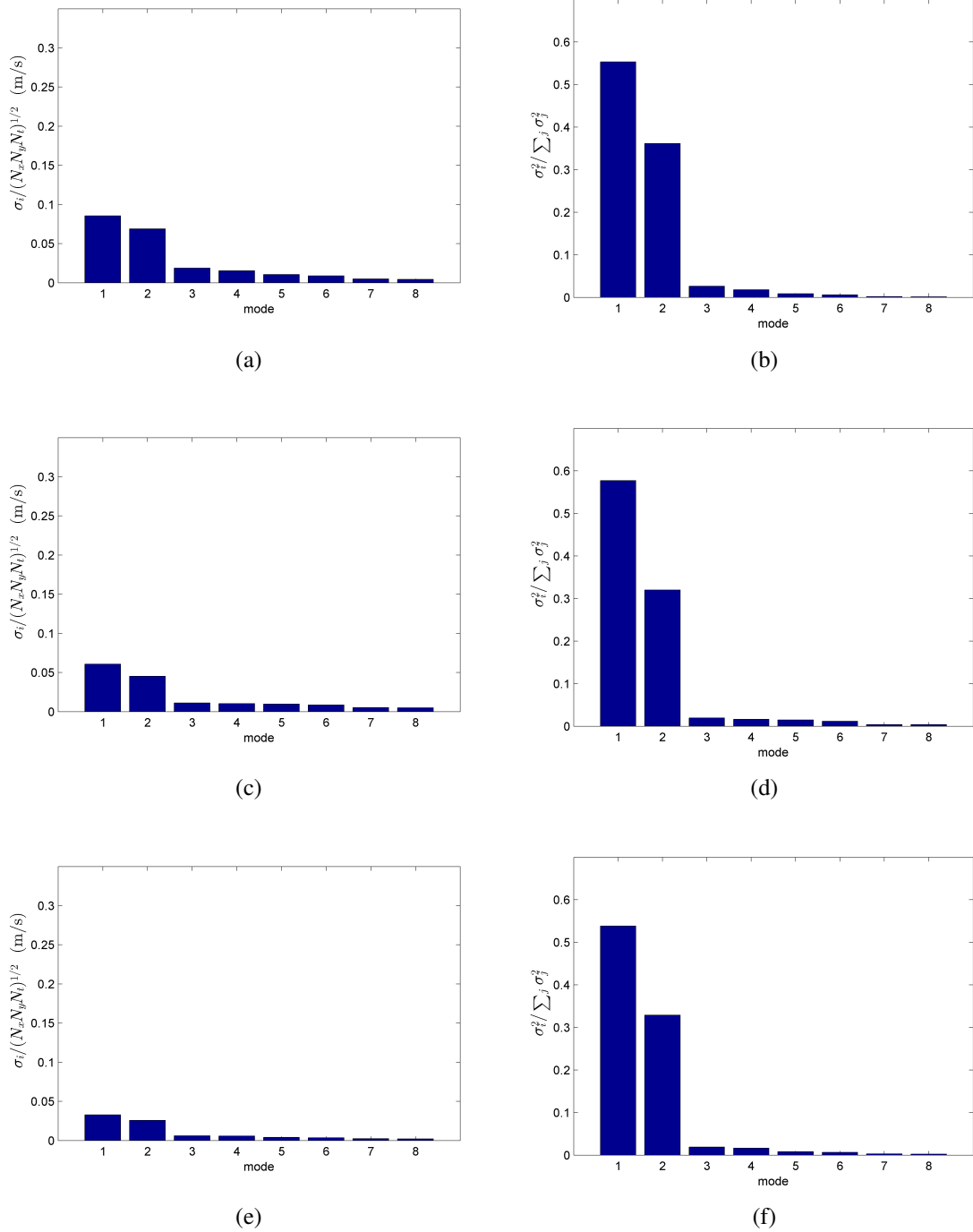


Figure 8.27: Normalized singular values (left) and their energy proportions (right) of the first eight modes, $\text{Re}[40\ 40]\text{k}$, $H_g = 10\ \text{mm}$; FOV 1: (a) and (b), FOV 2: (c) and (d), FOV 3: (e) and (f).

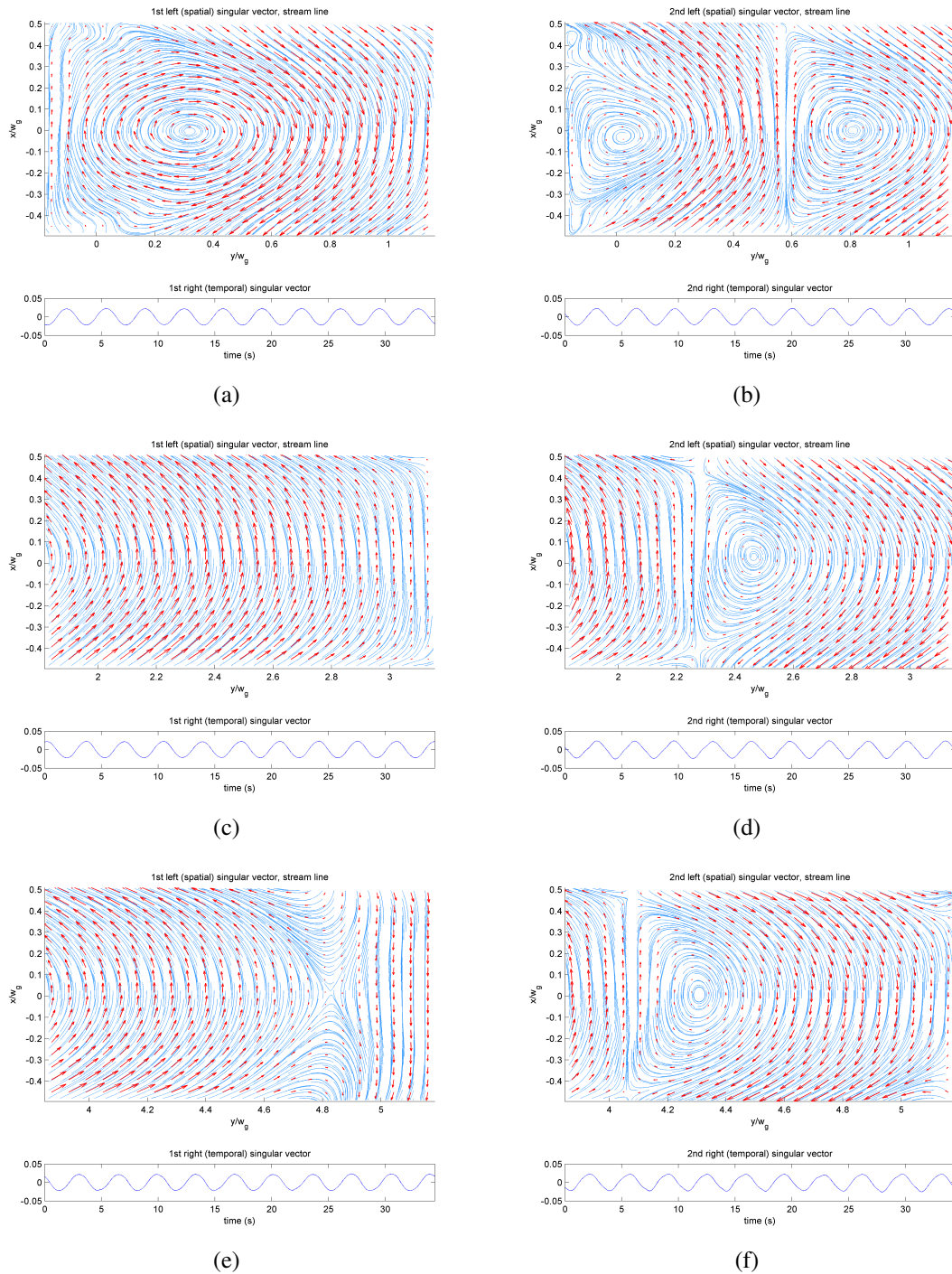


Figure 8.28: Singular vectors of the first (left) and the second (right) modes, $\text{Re}[40\ 40]k$, $H_g = 10\text{ mm}$; FOV1: (a) and (b), FOV2: (c) and (d), FOV3: (e) and (f). Red arrows are velocity vectors, and blue lines are streamlines.

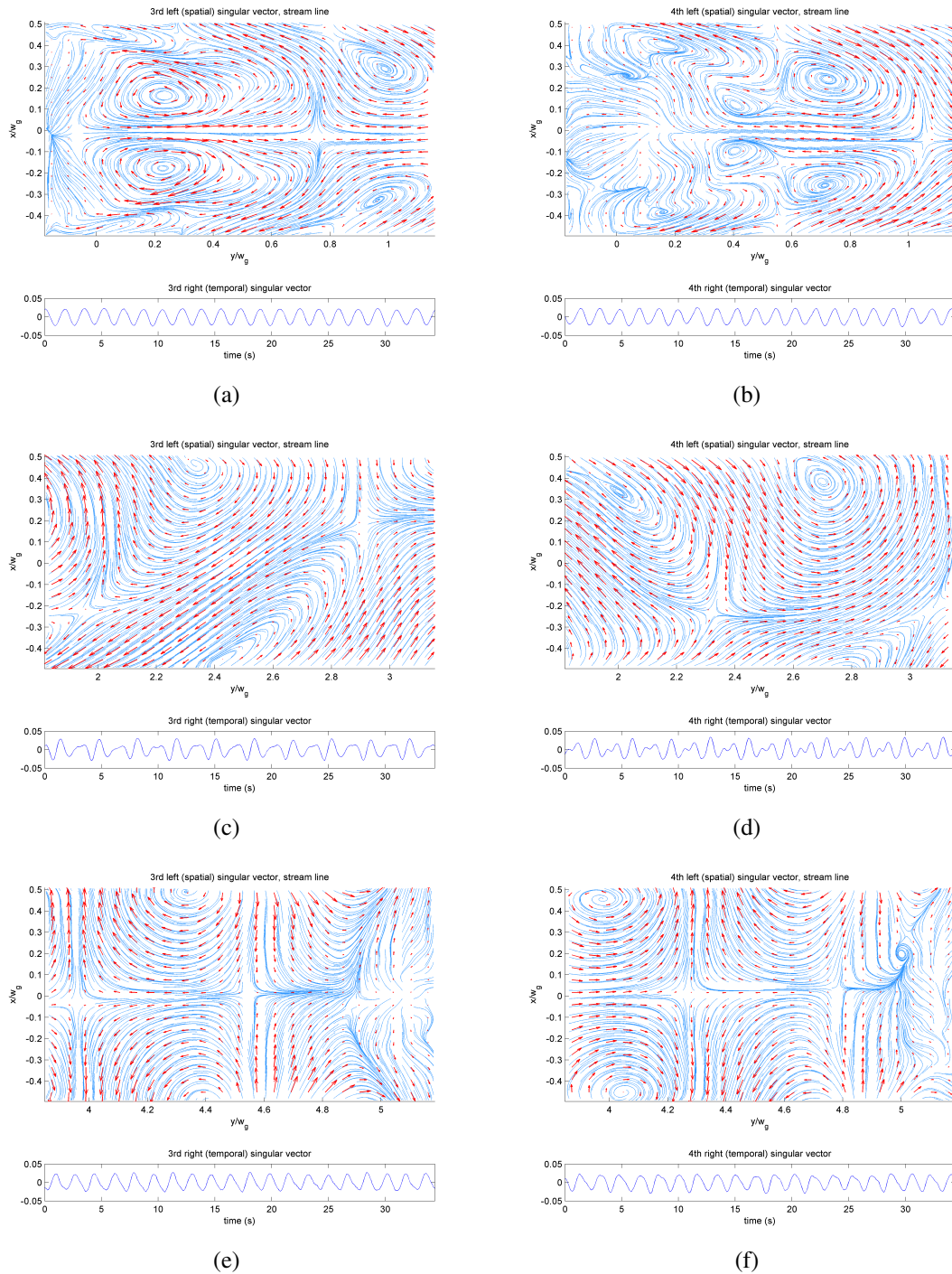


Figure 8.29: Singular vectors of the third (left) and the fourth (right) modes, $\text{Re}[40\ 40]_k$, $H_g = 10\text{ mm}$; FOV1: (a) and (b), FOV2: (c) and (d), FOV3: (e) and (f). Red arrows are velocity vectors, and blue lines are streamlines.

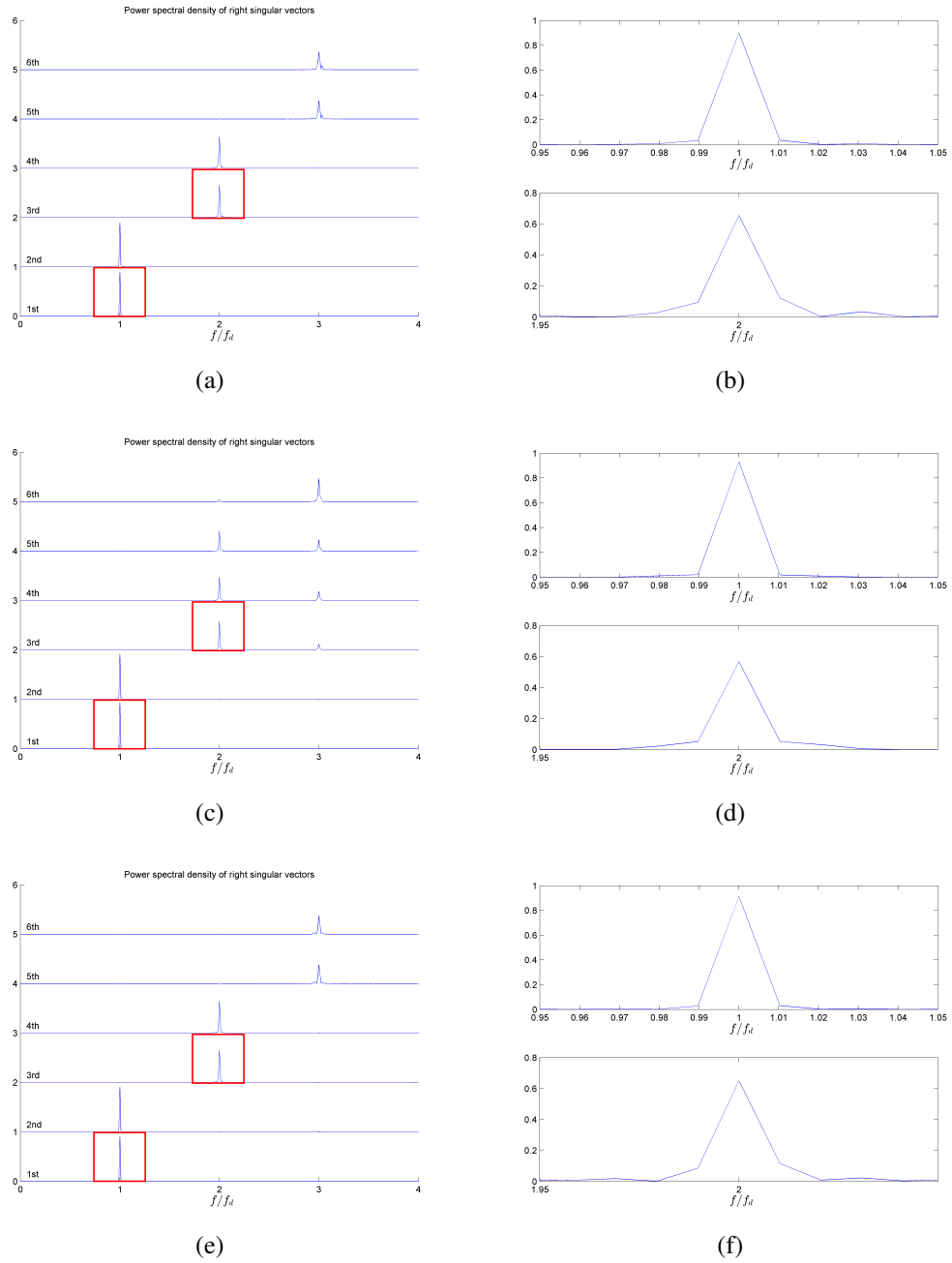
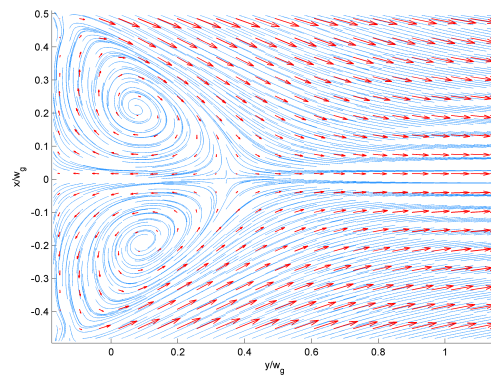
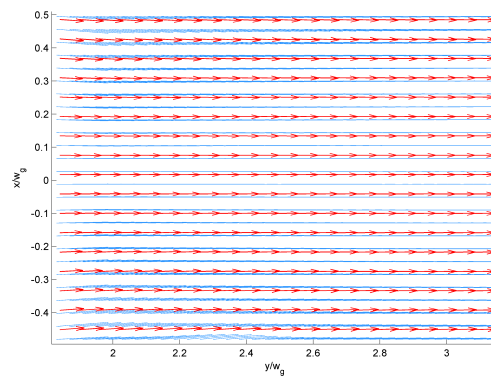


Figure 8.30: Power spectral densities of the first four right singular vectors (a), (c), (e), and the enlarged images of the power spectral densities of the first (top) and the third (bottom) right singular vectors (b), (d), (f), $\text{Re}[40\ 40]\text{k}$, $H_g = 10\text{ mm}$; FOV 1: (a) and (b), FOV 2: (c) and (d), and FOV 3: (e) and (f). Red squares on (a), (c), and (e) show the areas where (b), (d), and (f) are taken, respectively.

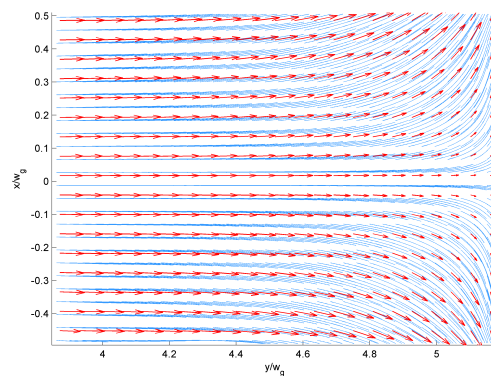
8.6.5 $\text{Re}[40\ 40]\mathbf{k}$, $H_g = 20\text{mm}$



(a)



(b)



(c)

Figure 8.31: Time-averaged velocity field of $\text{Re}[40\ 40]\mathbf{k}$, $H_g = 20\text{ mm}$; FOV 1 (a), FOV 2 (b), and FOV 3 (C). Red arrows indicate velocity vectors, and blue lines indicate streamlines.

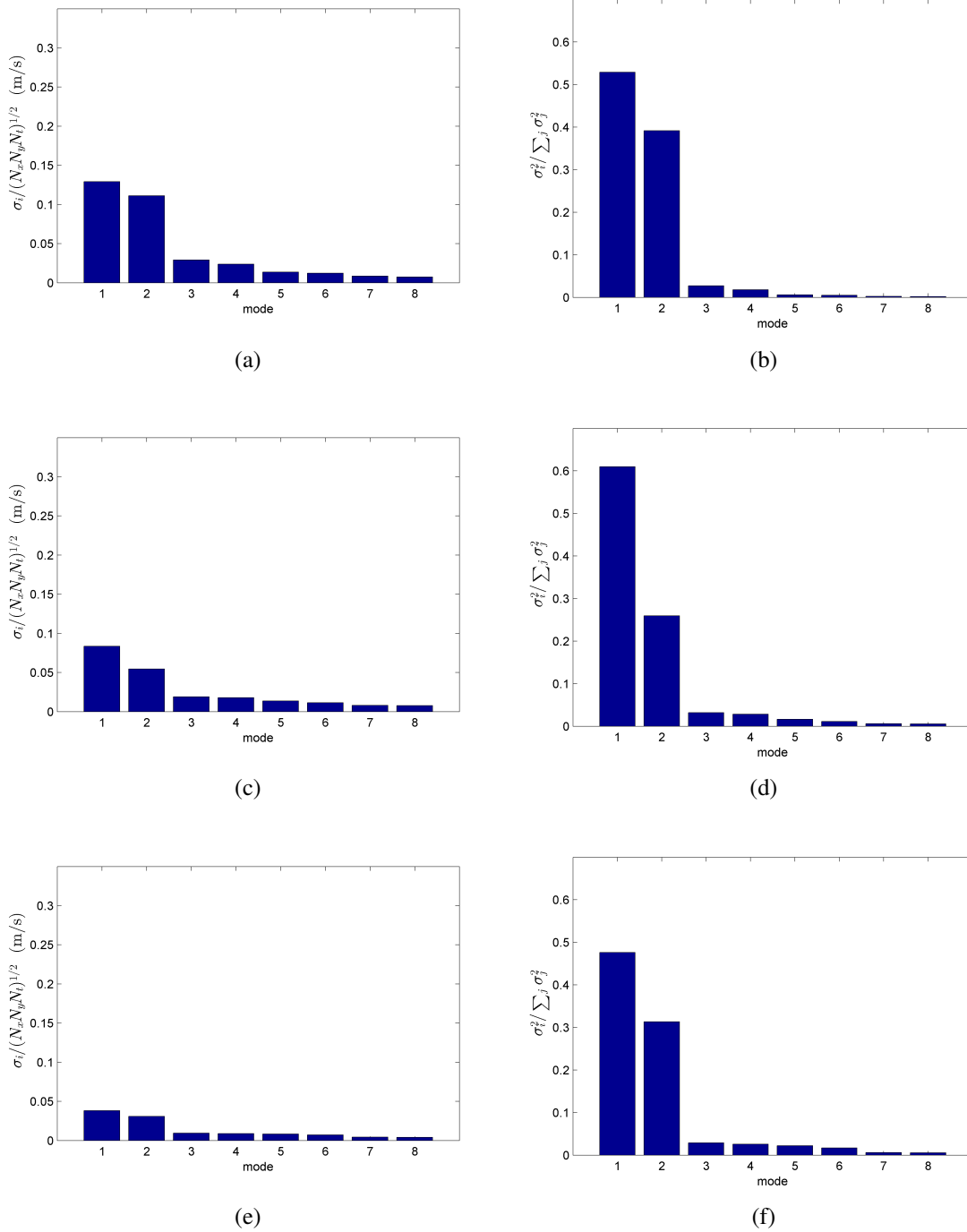


Figure 8.32: Normalized singular values (left) and their energy proportions (right) of the first eight modes, $\text{Re}[40\ 40]\text{k}$, $H_g = 20\ \text{mm}$; FOV 1: (a) and (b), FOV 2: (c) and (d), FOV 3: (e) and (f).

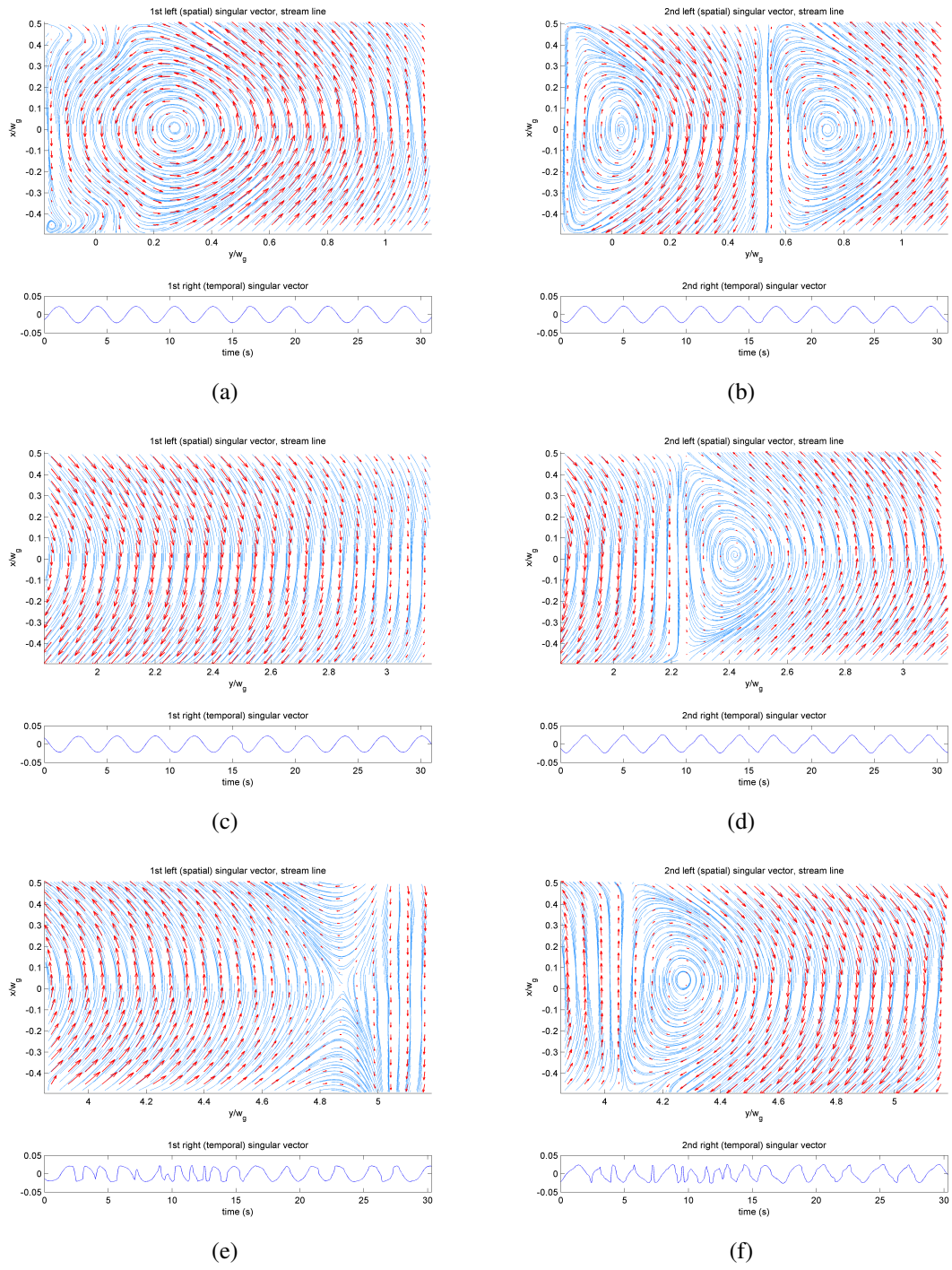


Figure 8.33: Singular vectors of the first (left) and the second (right) modes, $\text{Re}[40\ 40]k$, $H_g = 20\text{ mm}$; FOV1: (a) and (b), FOV2: (c) and (d), FOV3: (e) and (f). Red arrows are velocity vectors, and blue lines are streamlines.

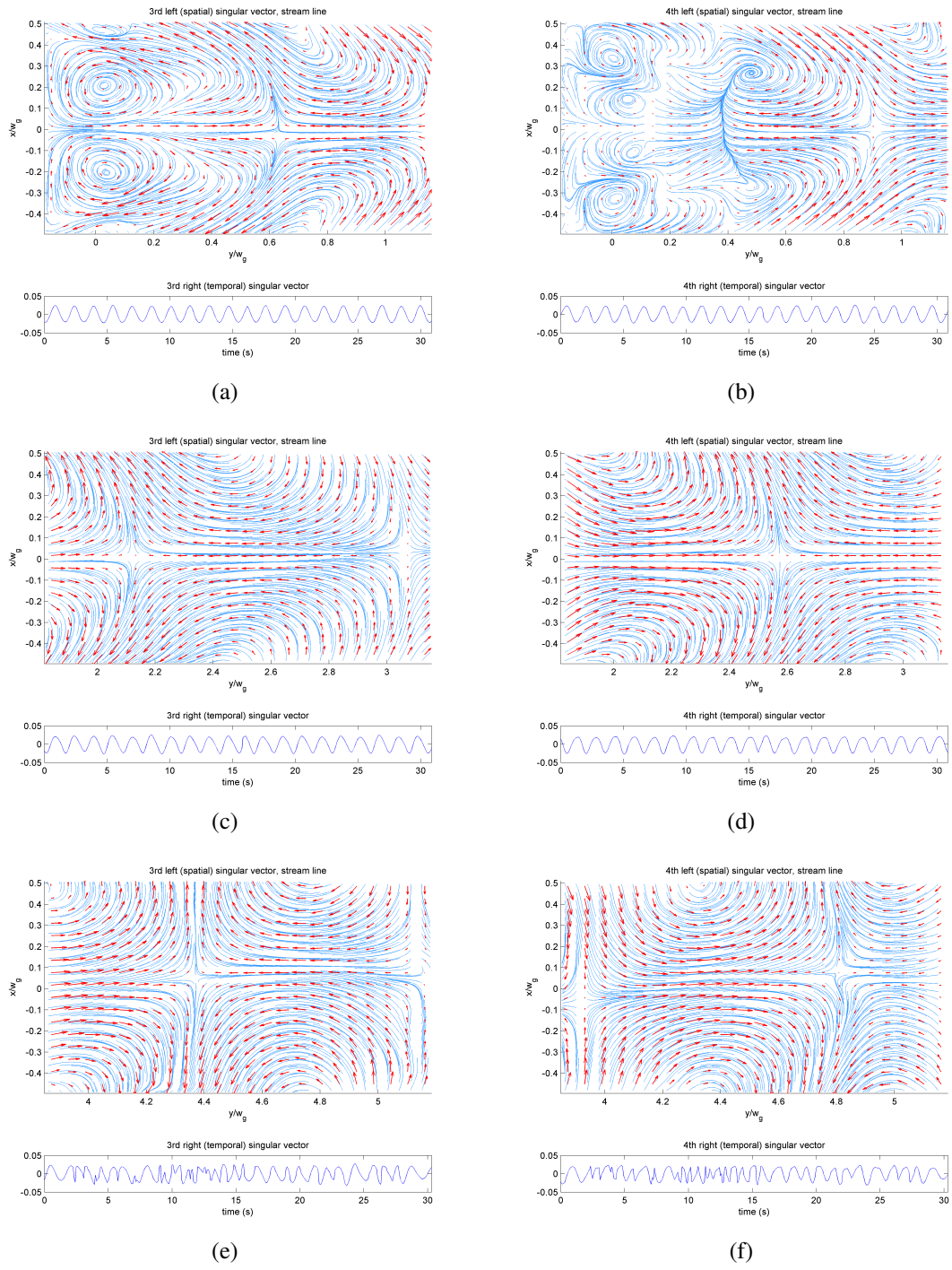


Figure 8.34: Singular vectors of the third (left) and the fourth (right) modes, $\text{Re}[40\ 40]k$, $H_g = 20$ mm; FOV1: (a) and (b), FOV2: (c) and (d), FOV3: (e) and (f). Red arrows are velocity vectors, and blue lines are streamlines.

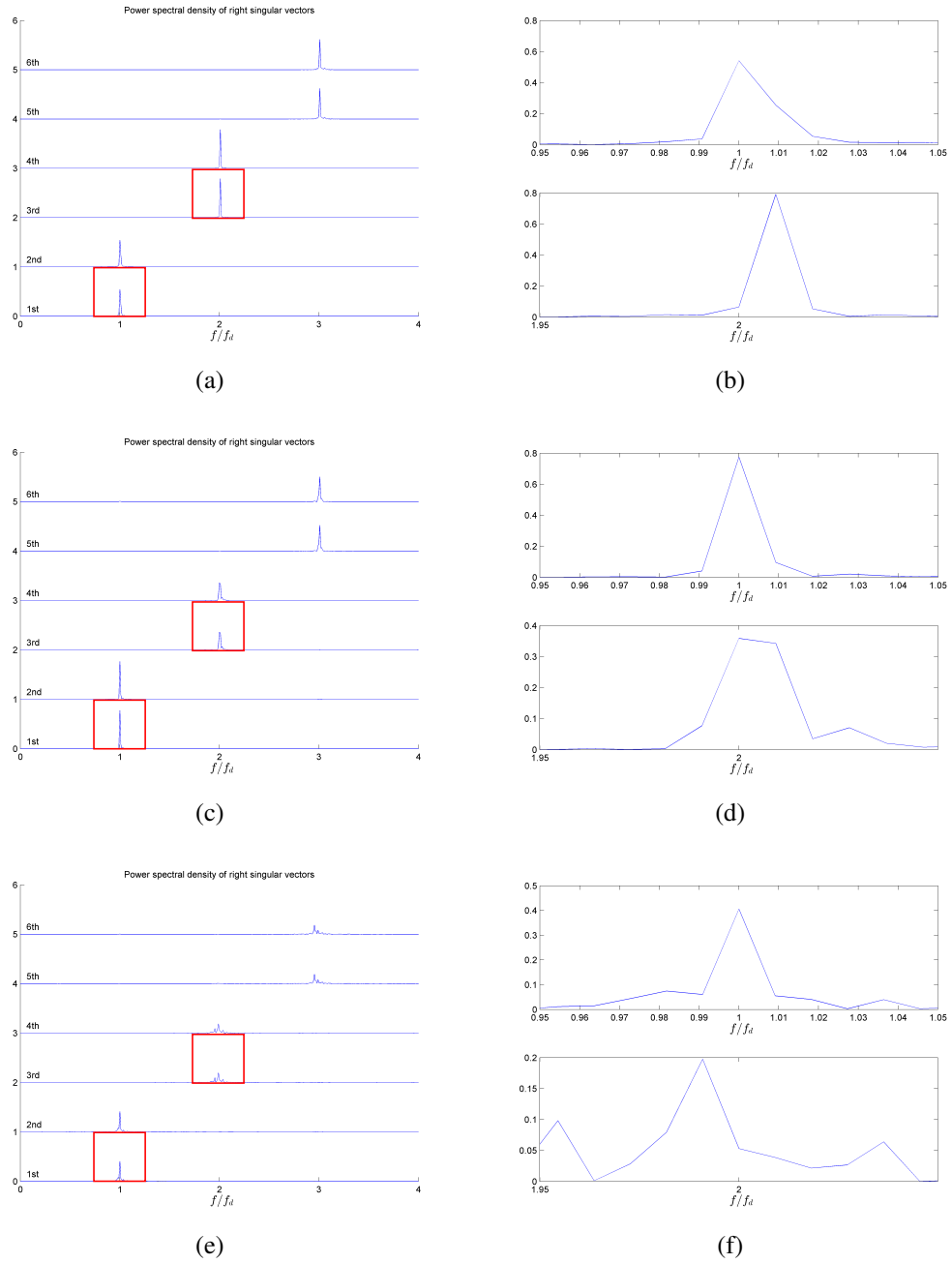
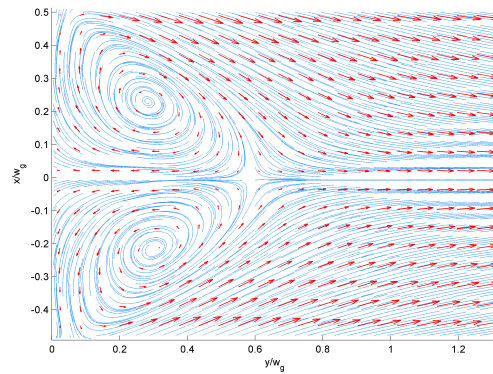
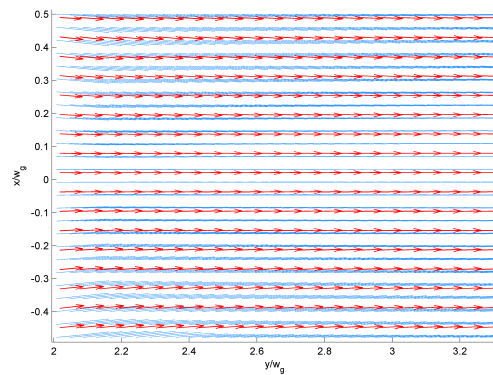


Figure 8.35: Power spectral densities of the first four right singular vectors (a), (c), (e), and the enlarged images of the power spectral densities of the first (top) and the third (bottom) right singular vectors (b), (d), (f), $\text{Re}[40\ 40]\text{k}$, $H_g = 20\text{ mm}$; FOV 1: (a) and (b), FOV 2: (c) and (d), and FOV 3: (e) and (f). Red squares on (a), (c), and (e) show the areas where (b), (d), and (f) are taken, respectively.

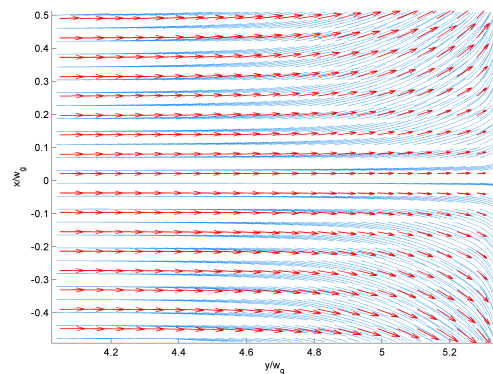
8.6.6 $\text{Re}[40\ 40]\mathbf{k}$, $H_g = 50\text{mm}$



(a)



(b)



(c)

Figure 8.36: Time-averaged velocity field of $\text{Re}[40\ 40]\mathbf{k}$, $H_g = 50\text{ mm}$; FOV 1 (a), FOV 2 (b), and FOV 3 (C). Red arrows indicate velocity vectors, and blue lines indicate streamlines.

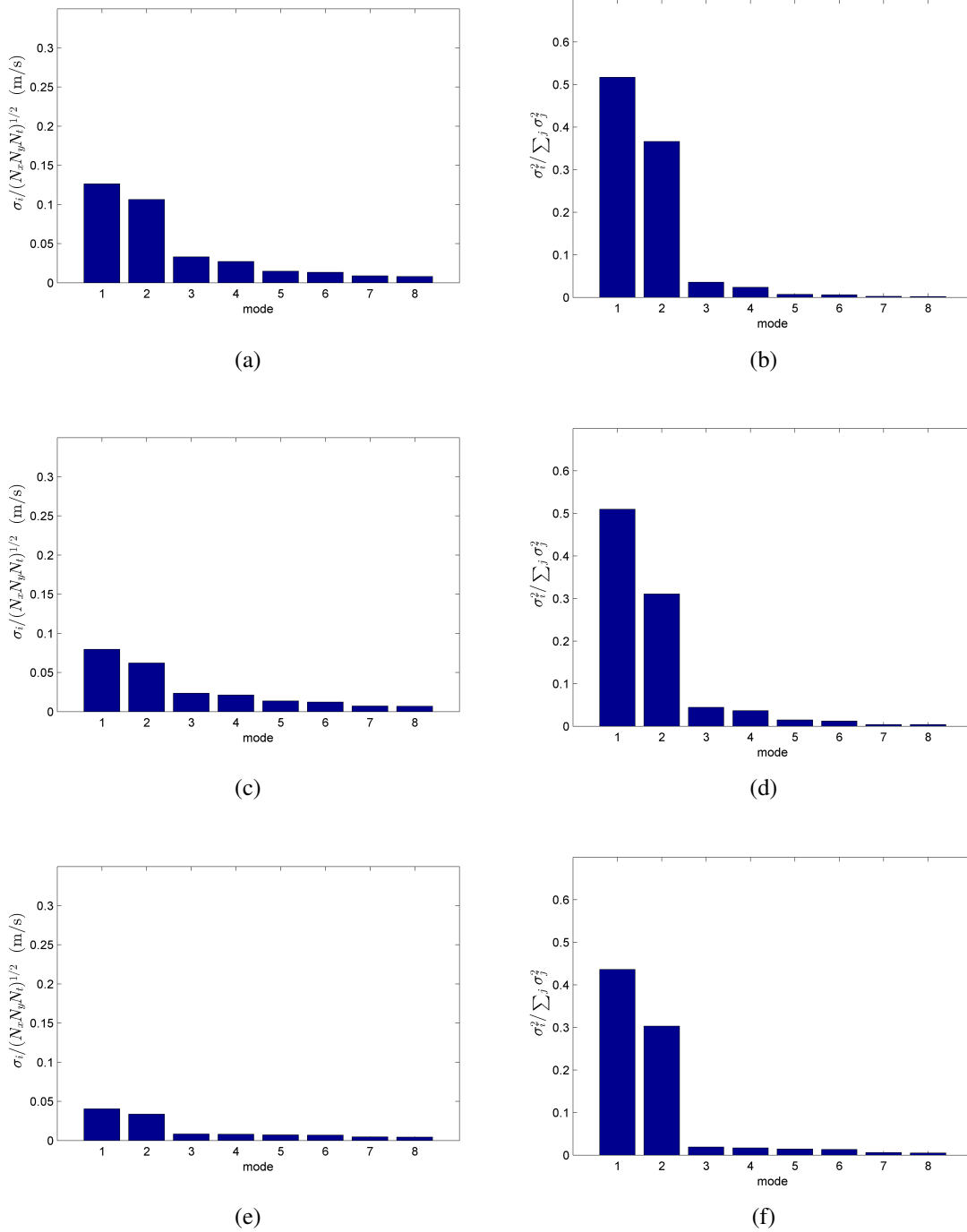


Figure 8.37: Normalized singular values (left) and their energy proportions (right) of the first eight modes, $\text{Re}[40\ 40]\text{k}$, $H_g = 50\ \text{mm}$; FOV 1: (a) and (b), FOV 2: (c) and (d), FOV 3: (e) and (f).

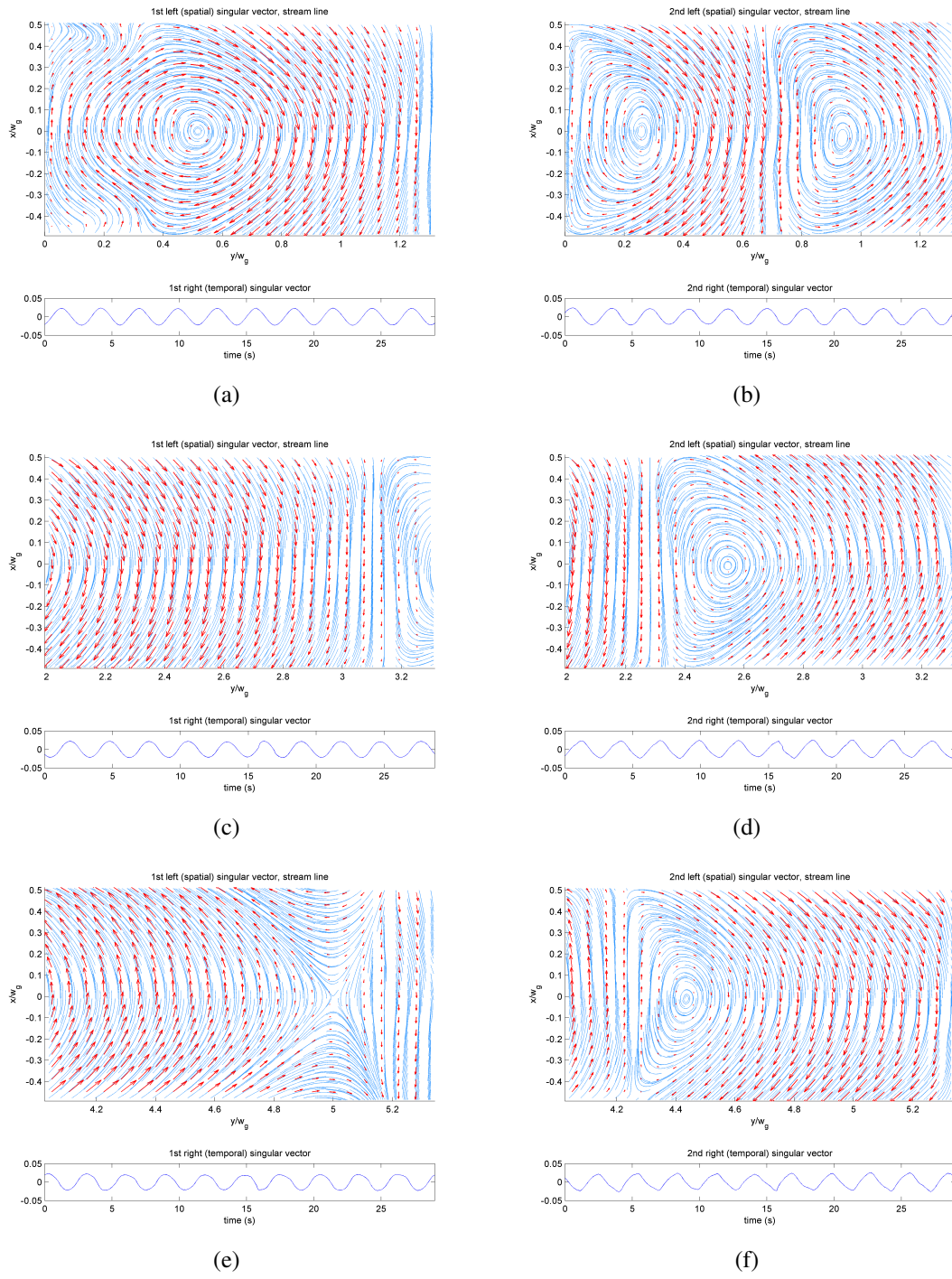


Figure 8.38: Singular vectors of the first (left) and the second (right) modes, $\text{Re}[40\ 40]k$, $H_g = 50\text{ mm}$; FOV1: (a) and (b), FOV2: (c) and (d), FOV3: (e) and (f). Red arrows are velocity vectors, and blue lines are streamlines.

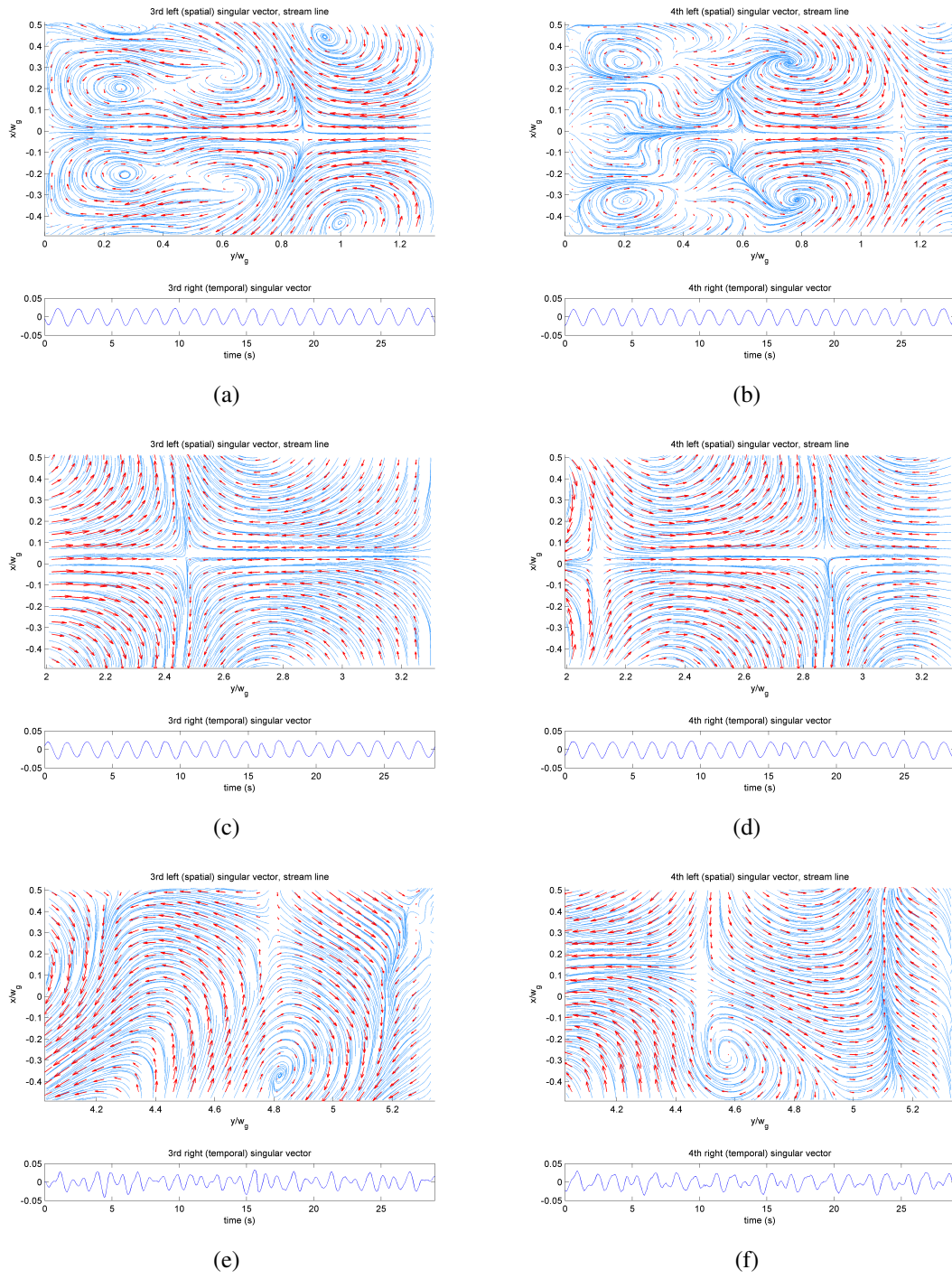


Figure 8.39: Singular vectors of the third (left) and the fourth (right) modes, $\text{Re}[40\ 40]_k$, $H_g = 50$ mm; FOV1: (a) and (b), FOV2: (c) and (d), FOV3: (e) and (f). Red arrows are velocity vectors, and blue lines are streamlines.

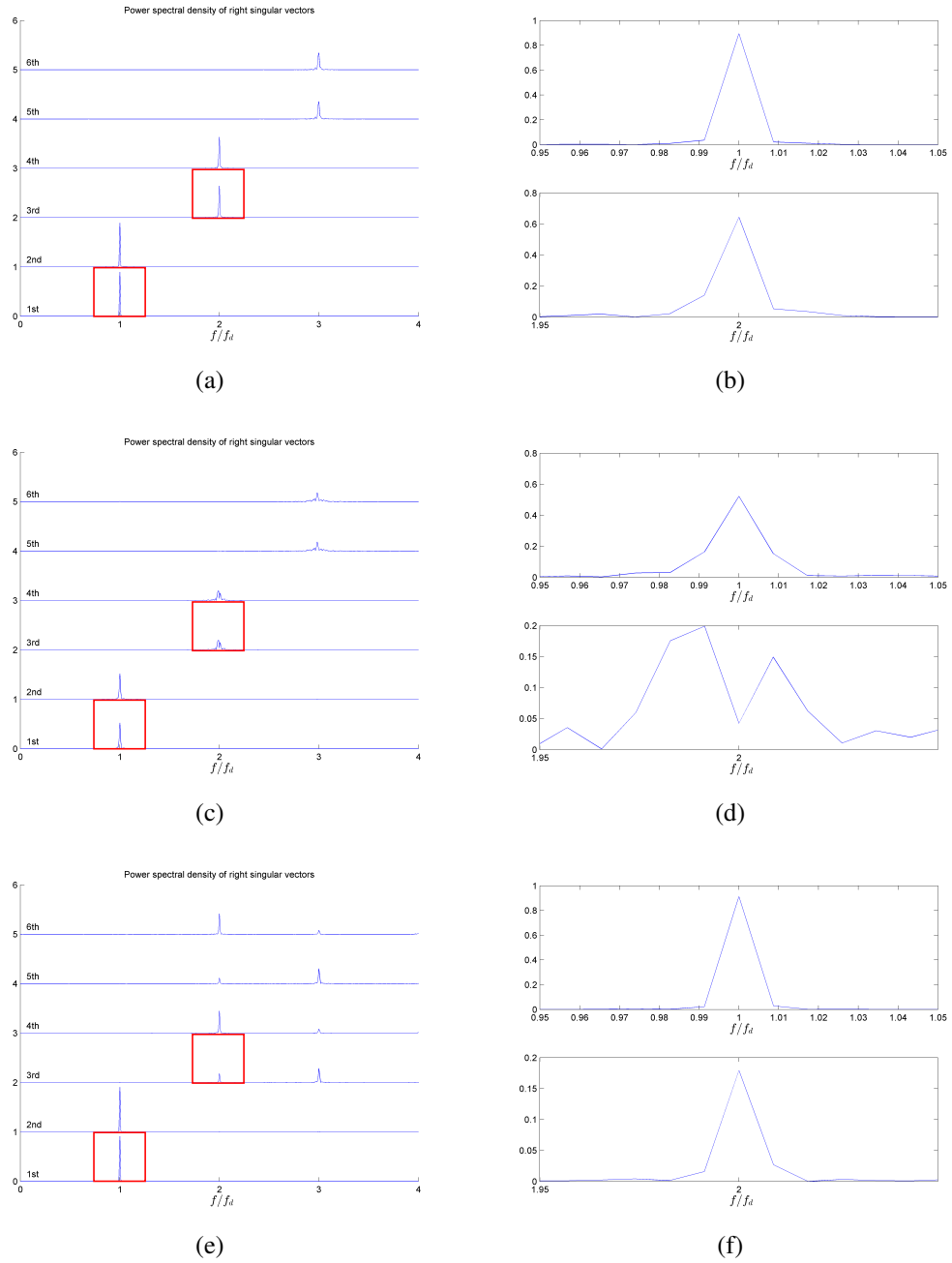
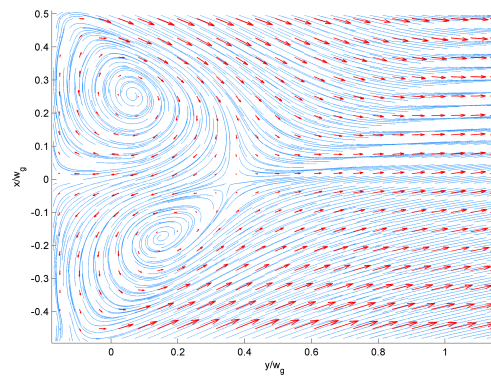
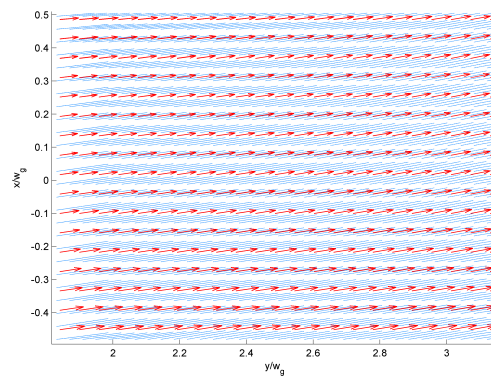


Figure 8.40: Power spectral densities of the first four right singular vectors (a), (c), (e), and the enlarged images of the power spectral densities of the first (top) and the third (bottom) right singular vectors (b), (d), (f), $\text{Re}[40\ 40]\text{k}$, $H_g = 50$ mm; FOV 1: (a) and (b), FOV 2: (c) and (d), and FOV 3: (e) and (f). Red squares on (a), (c), and (e) show the areas where (b), (d), and (f) are taken, respectively.

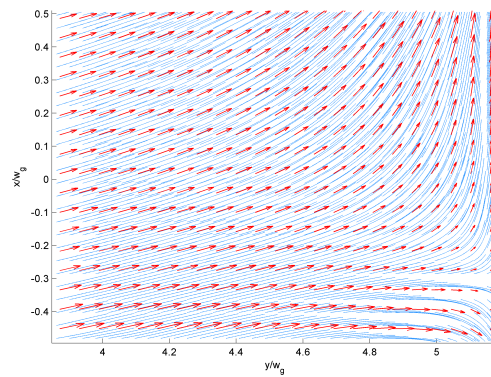
8.6.7 $\text{Re}[80\ 100]\mathbf{k}$, $H_g = 10\text{mm}$



(a)



(b)



(c)

Figure 8.41: Time-averaged velocity field of $\text{Re}[80\ 100]\mathbf{k}$, $H_g = 10\text{ mm}$; FOV 1 (a), FOV 2 (b), and FOV 3 (C). Red arrows indicate velocity vectors, and blue lines indicate streamlines.

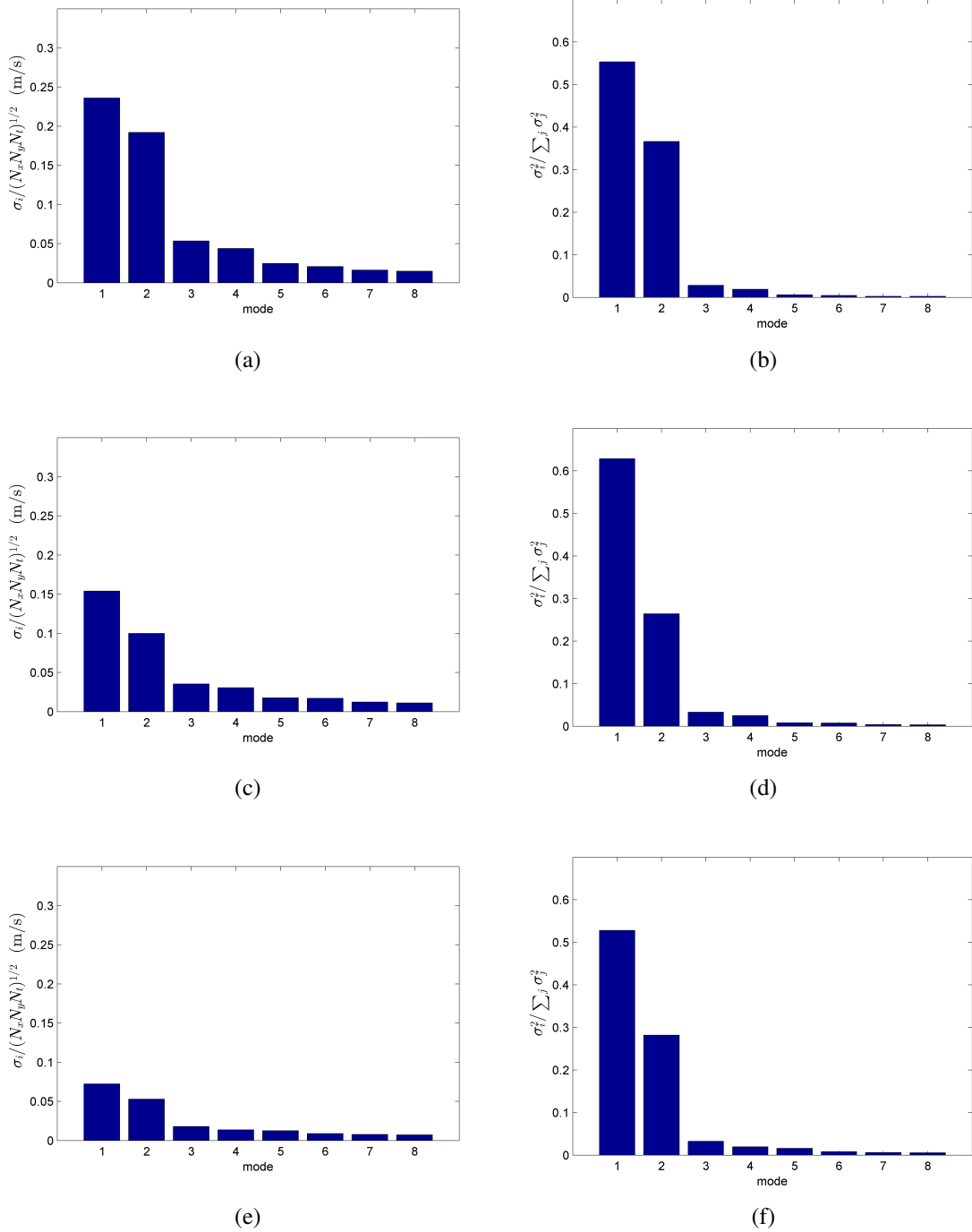


Figure 8.42: Normalized singular values (left) and their energy proportions (right) of the first eight modes, $\text{Re}[80\ 100]\text{k}$, $H_g = 10\text{ mm}$; FOV 1: (a) and (b), FOV 2: (c) and (d), FOV 3: (e) and (f).

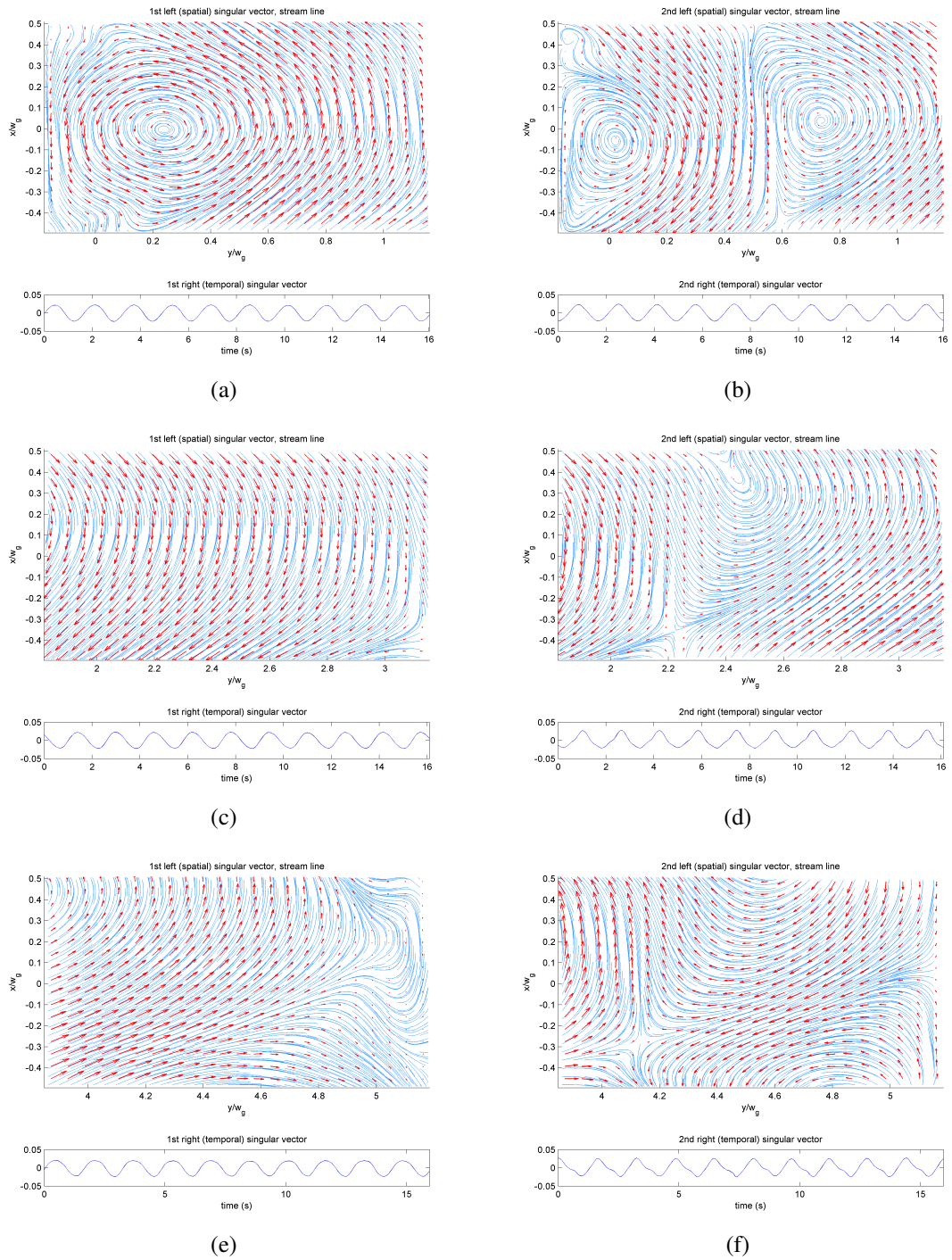


Figure 8.43: Singular vectors of the first (left) and the second (right) modes, $\text{Re}[80\ 100]k$, $H_g = 10\text{ mm}$; FOV1: (a) and (b), FOV2: (c) and (d), FOV3: (e) and (f). Red arrows are velocity vectors, and blue lines are streamlines.

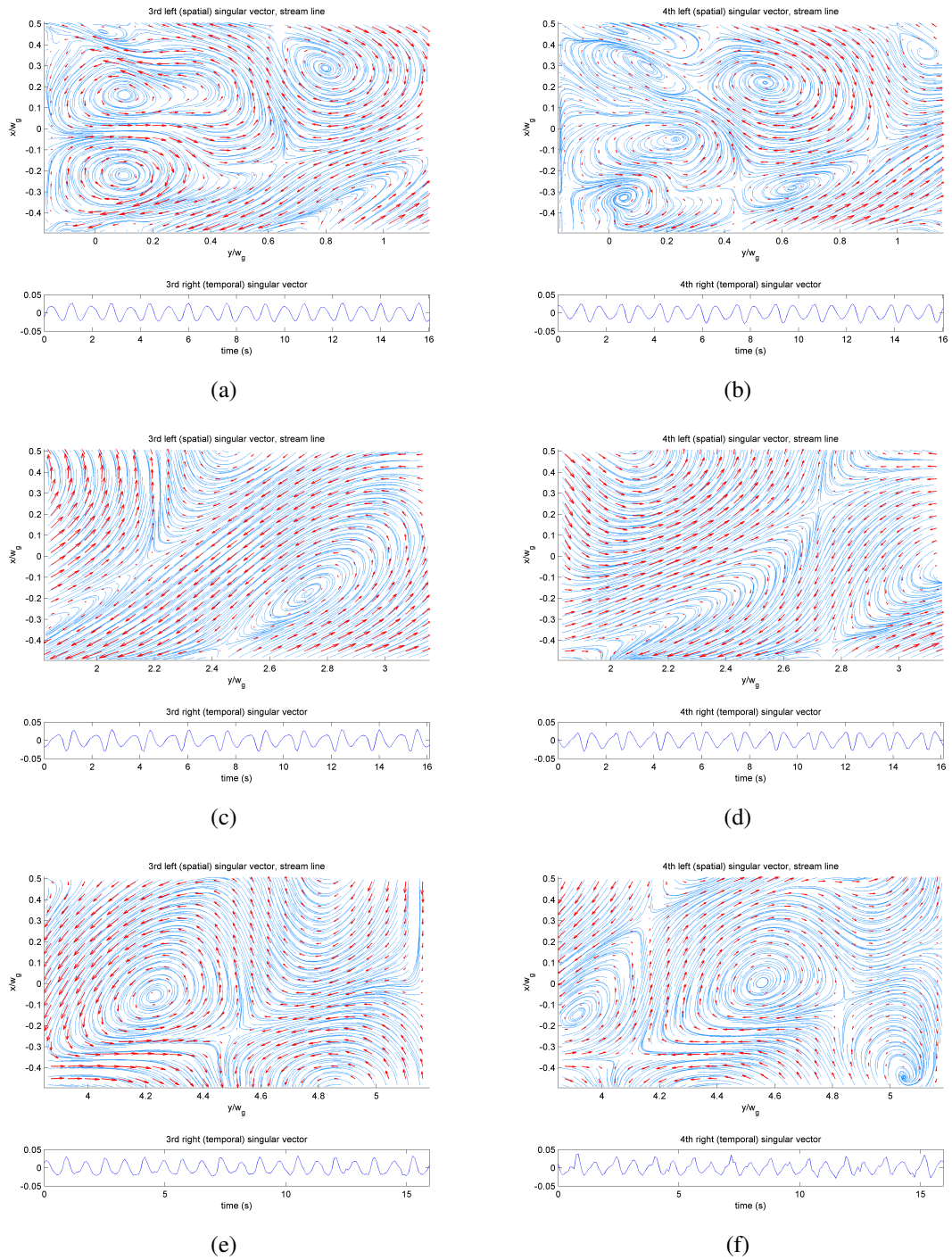


Figure 8.44: Singular vectors of the third (left) and the fourth (right) modes, $\text{Re}[80\ 100]k$, $H_g = 10\text{ mm}$; FOV1: (a) and (b), FOV2: (c) and (d), FOV3: (e) and (f). Red arrows are velocity vectors, and blue lines are streamlines.

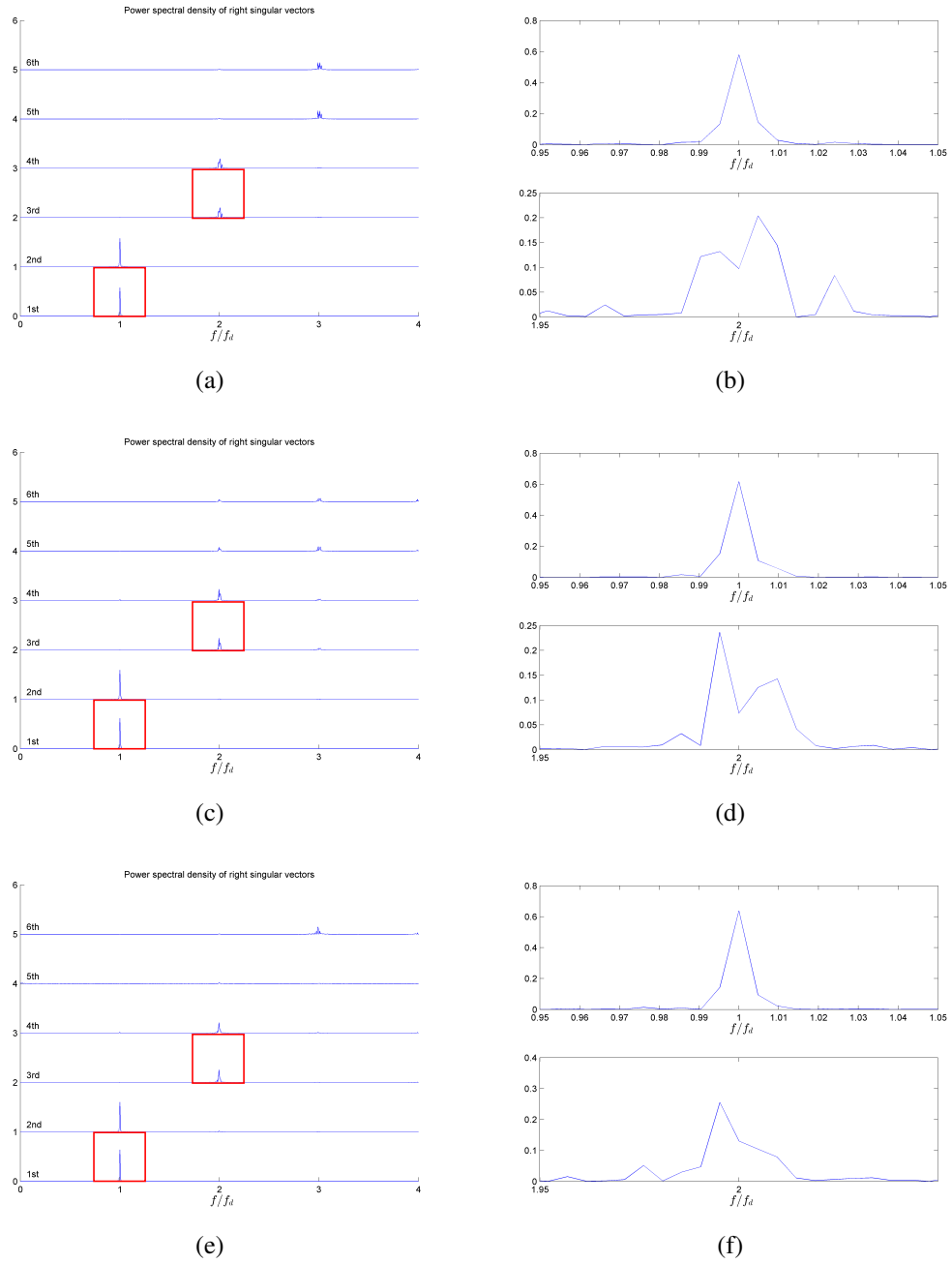
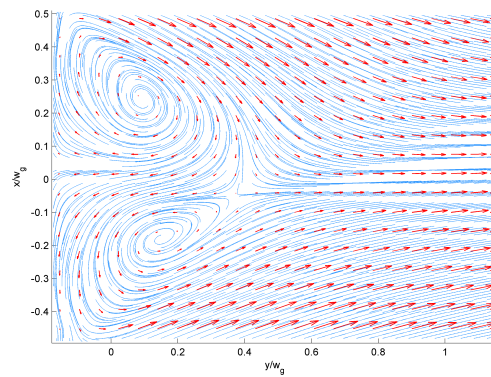
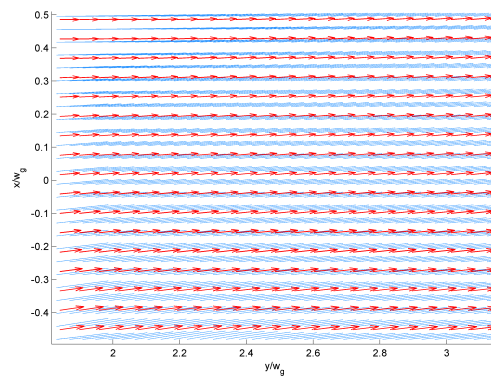


Figure 8.45: Power spectral densities of the first four right singular vectors (a), (c), (e), and the enlarged images of the power spectral densities of the first (top) and the third (bottom) right singular vectors (b), (d), (f), $\text{Re}[80\ 100]\text{k}$, $H_g = 10\text{ mm}$; FOV 1: (a) and (b), FOV 2: (c) and (d), and FOV 3: (e) and (f). Red squares on (a), (c), and (e) show the areas where (b), (d), and (f) are taken, respectively.

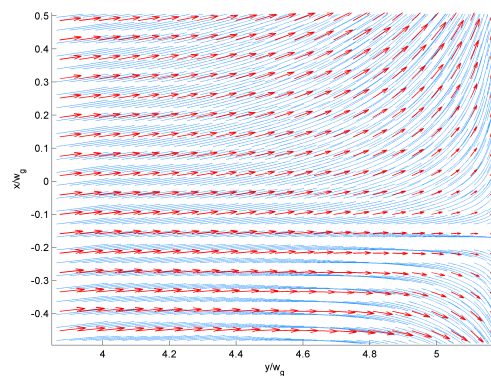
8.6.8 $\text{Re}[80\ 100]k$, $H_g = 20\text{mm}$



(a)



(b)



(c)

Figure 8.46: Time-averaged velocity field of $\text{Re}[80\ 100]k$, $H_g = 20\text{ mm}$; FOV 1 (a), FOV 2 (b), and FOV 3 (C). Red arrows indicate velocity vectors, and blue lines indicate streamlines.

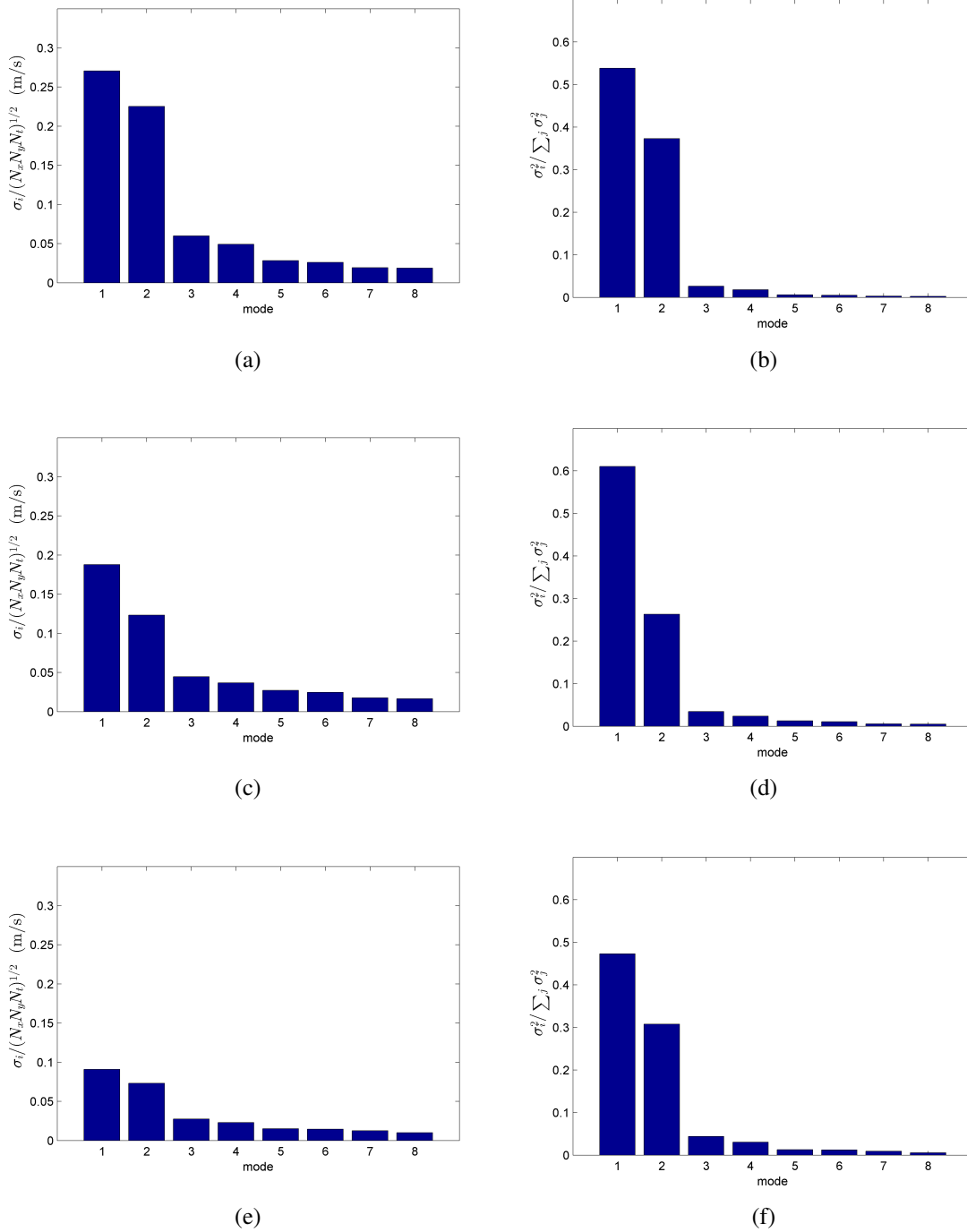


Figure 8.47: Normalized singular values (left) and their energy proportions (right) of the first eight modes, $\text{Re}[80\ 100]\text{k}$, $H_g = 20\text{ mm}$; FOV 1: (a) and (b), FOV 2: (c) and (d), FOV 3: (e) and (f).

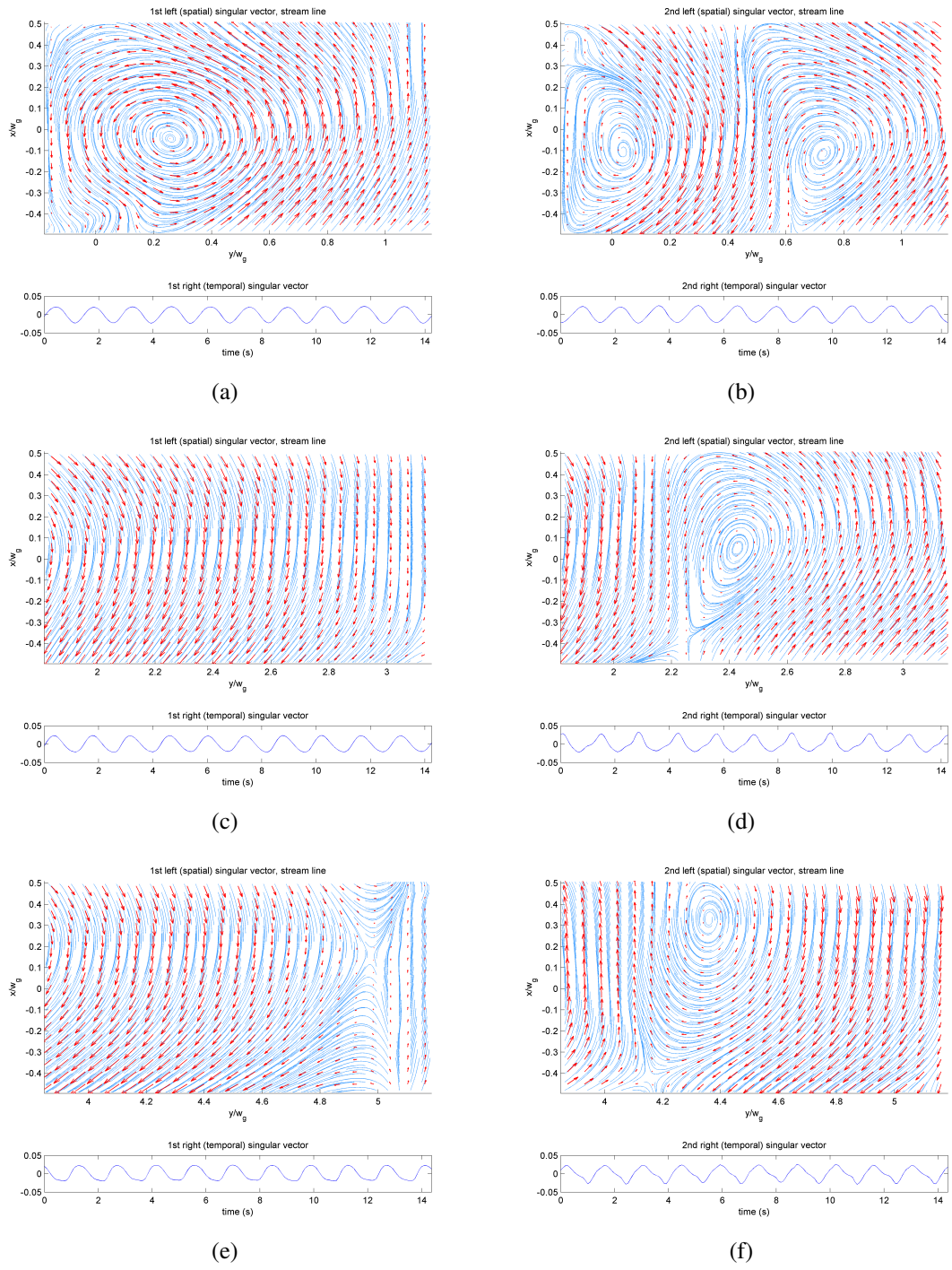


Figure 8.48: Singular vectors of the first (left) and the second (right) modes, $\text{Re}[80\ 100]k$, $H_g = 20\text{ mm}$; FOV1: (a) and (b), FOV2: (c) and (d), FOV3: (e) and (f). Red arrows are velocity vectors, and blue lines are streamlines.

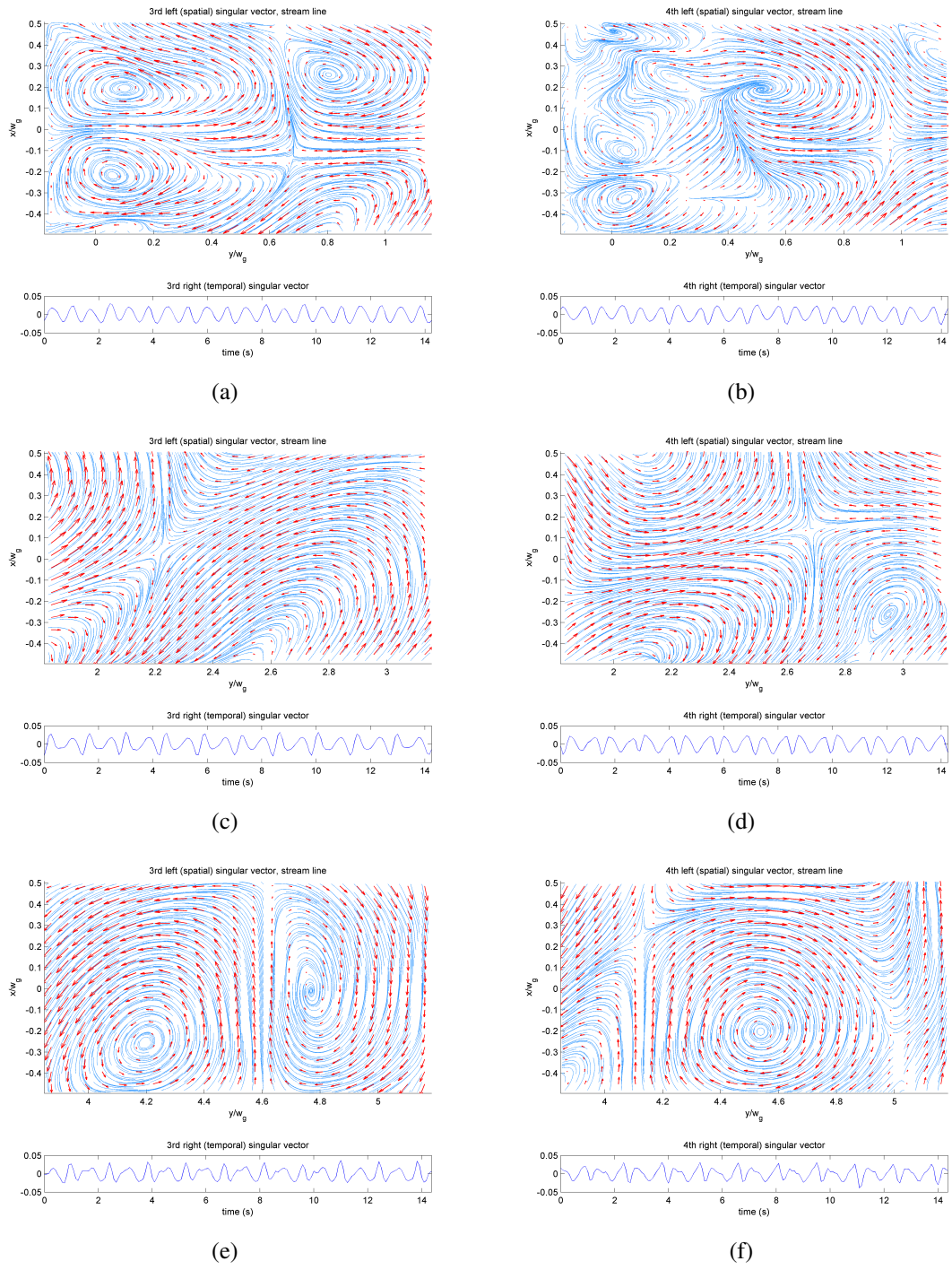


Figure 8.49: Singular vectors of the third (left) and the fourth (right) modes, $\text{Re}[80\ 100]k$, $H_g = 20\text{ mm}$; FOV1: (a) and (b), FOV2: (c) and (d), FOV3: (e) and (f). Red arrows are velocity vectors, and blue lines are streamlines.

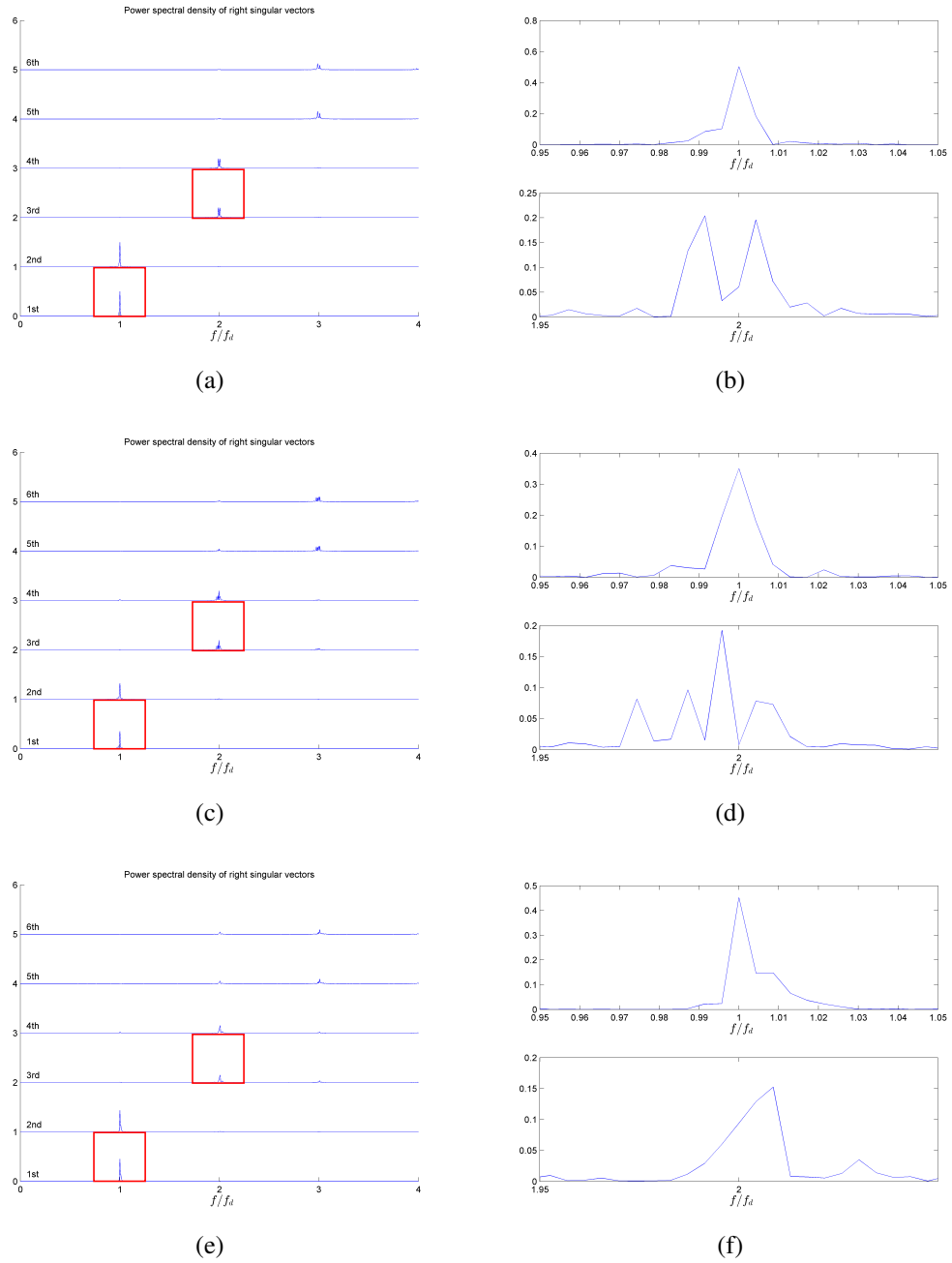
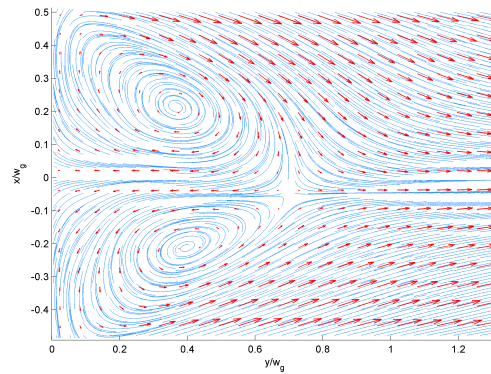
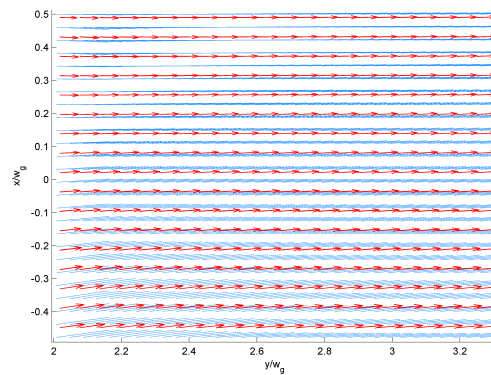


Figure 8.50: Power spectral densities of the first four right singular vectors (a), (c), (e), and the enlarged images of the power spectral densities of the first (top) and the third (bottom) right singular vectors (b), (d), (f), $\text{Re}[80\ 100]\text{k}$, $H_g = 20\text{ mm}$; FOV 1: (a) and (b), FOV 2: (c) and (d), and FOV 3: (e) and (f). Red squares on (a), (c), and (e) show the areas where (b), (d), and (f) are taken, respectively.

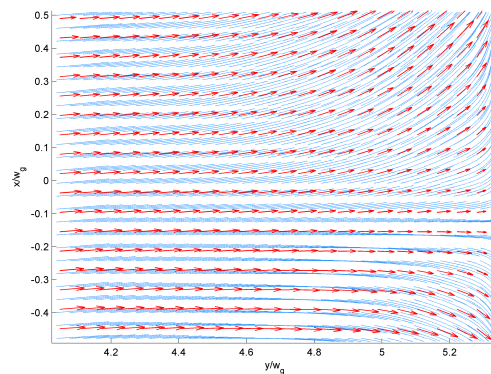
8.6.9 $\text{Re}[80\ 100]\mathbf{k}$, $H_g = 50\text{mm}$



(a)



(b)



(c)

Figure 8.51: Time-averaged velocity field of $\text{Re}[80\ 100]\mathbf{k}$, $H_g = 50\text{ mm}$; FOV 1 (a), FOV 2 (b), and FOV 3 (C). Red arrows indicate velocity vectors, and blue lines indicate streamlines.

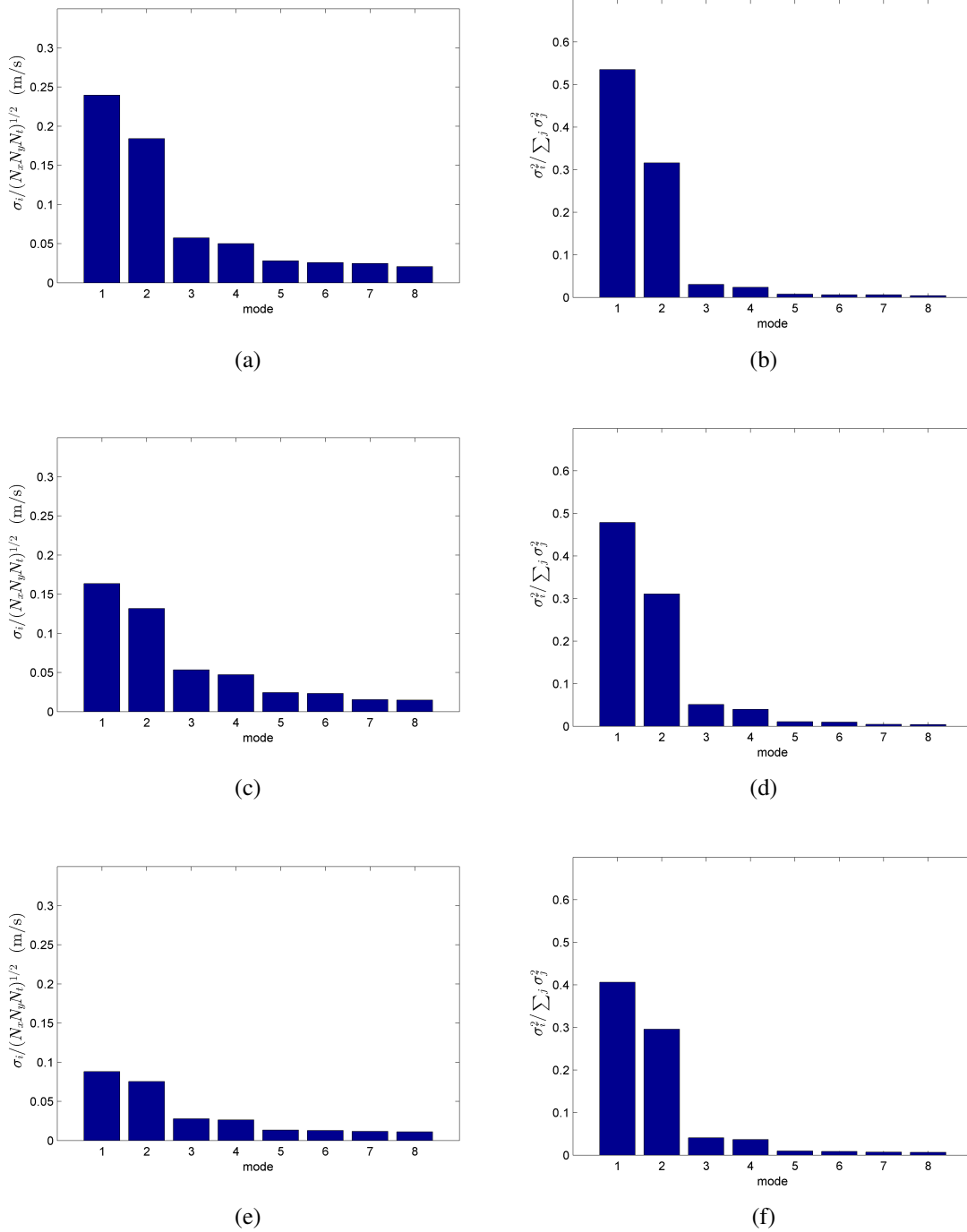


Figure 8.52: Normalized singular values (left) and their energy proportions (right) of the first eight modes, $\text{Re}[80\ 100]\text{k}$, $H_g = 50\ \text{mm}$; FOV 1: (a) and (b), FOV 2: (c) and (d), FOV 3: (e) and (f).

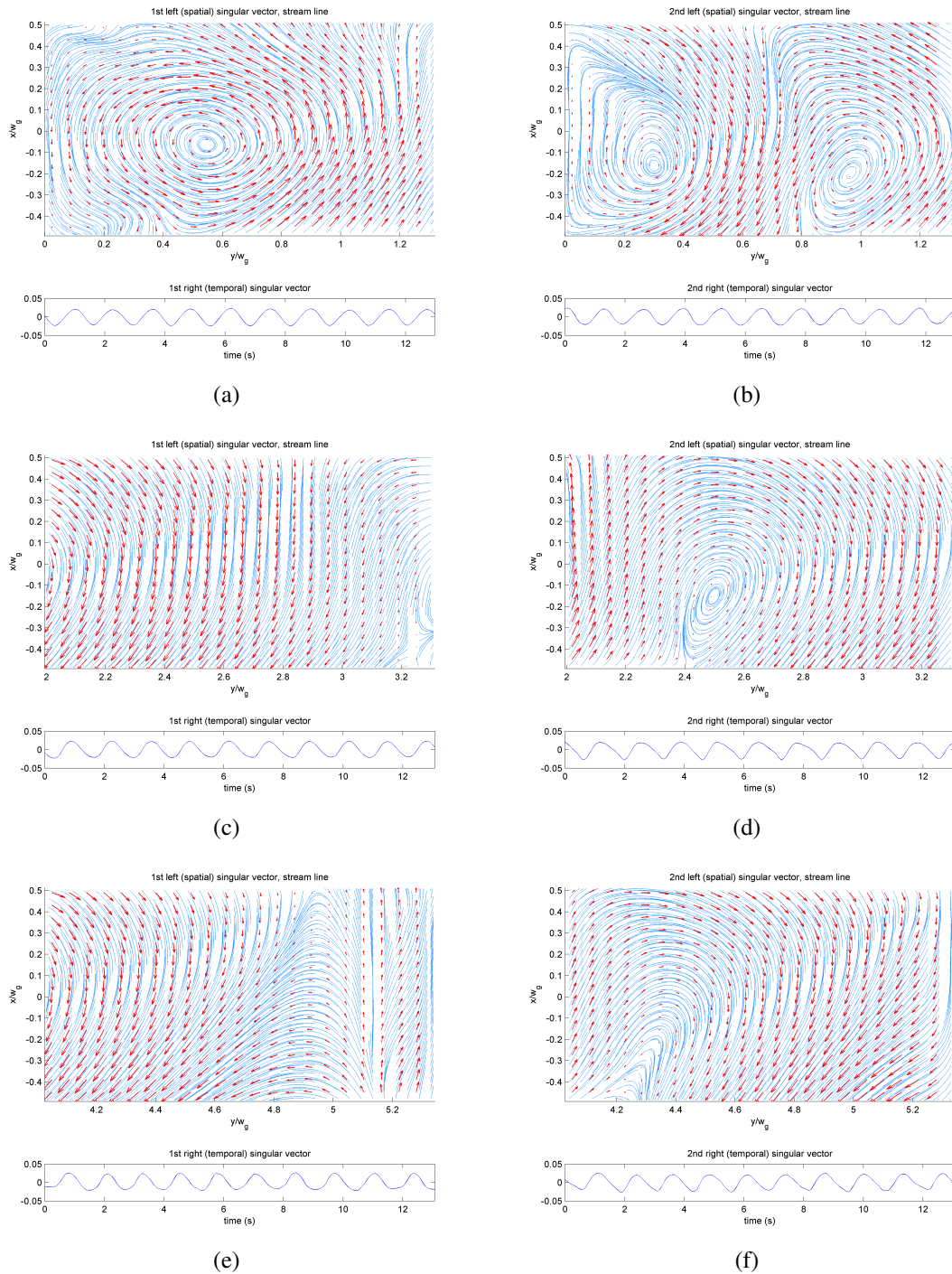


Figure 8.53: Singular vectors of the first (left) and the second (right) modes, $\text{Re}[80\ 100]k$, $H_g = 50\text{ mm}$; FOV1: (a) and (b), FOV2: (c) and (d), FOV3: (e) and (f). Red arrows are velocity vectors, and blue lines are streamlines.

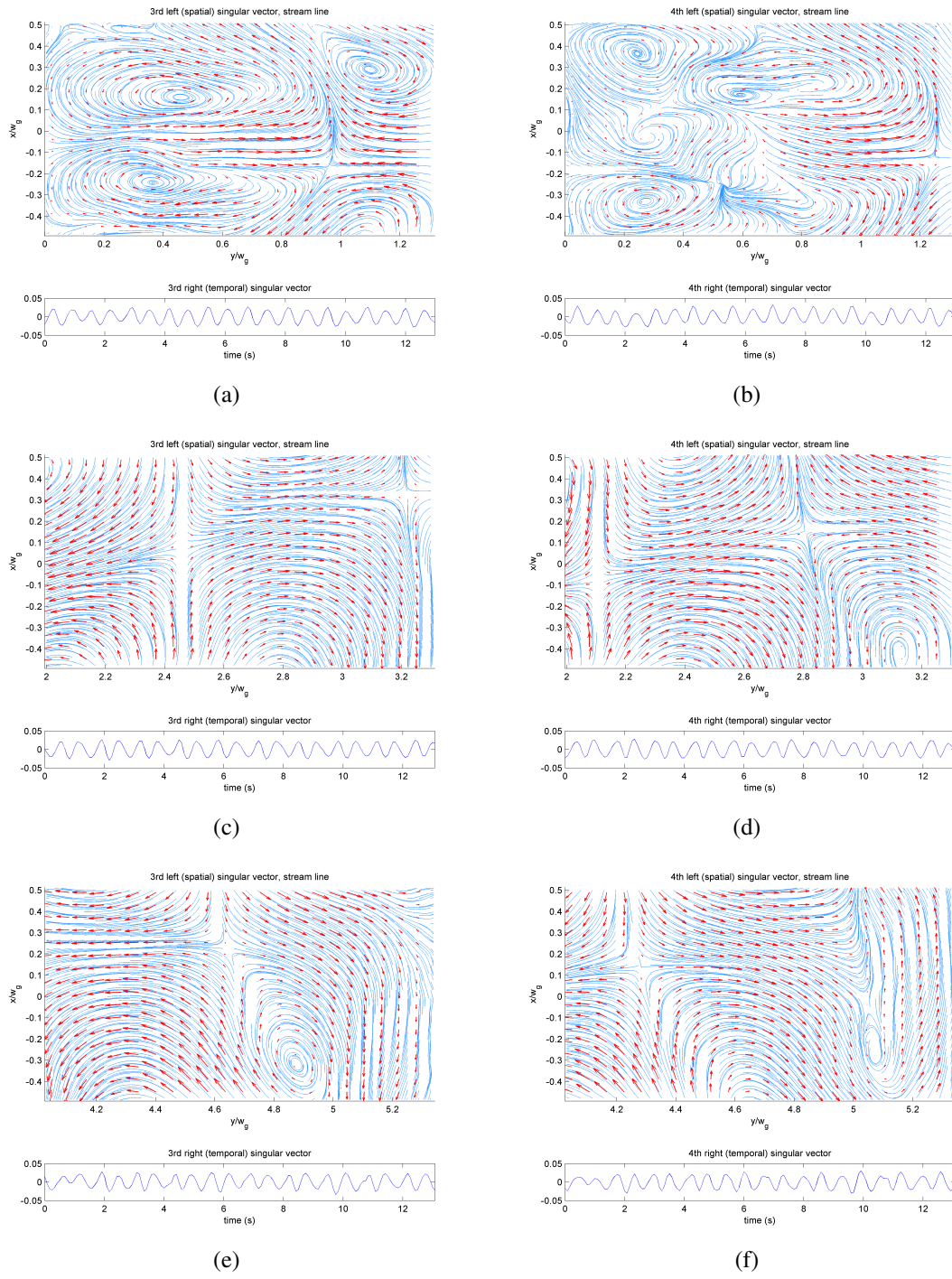


Figure 8.54: Singular vectors of the third (left) and the fourth (right) modes, $\text{Re}[80\ 100]k$, $H_g = 50\text{ mm}$; FOV1: (a) and (b), FOV2: (c) and (d), FOV3: (e) and (f). Red arrows are velocity vectors, and blue lines are streamlines.

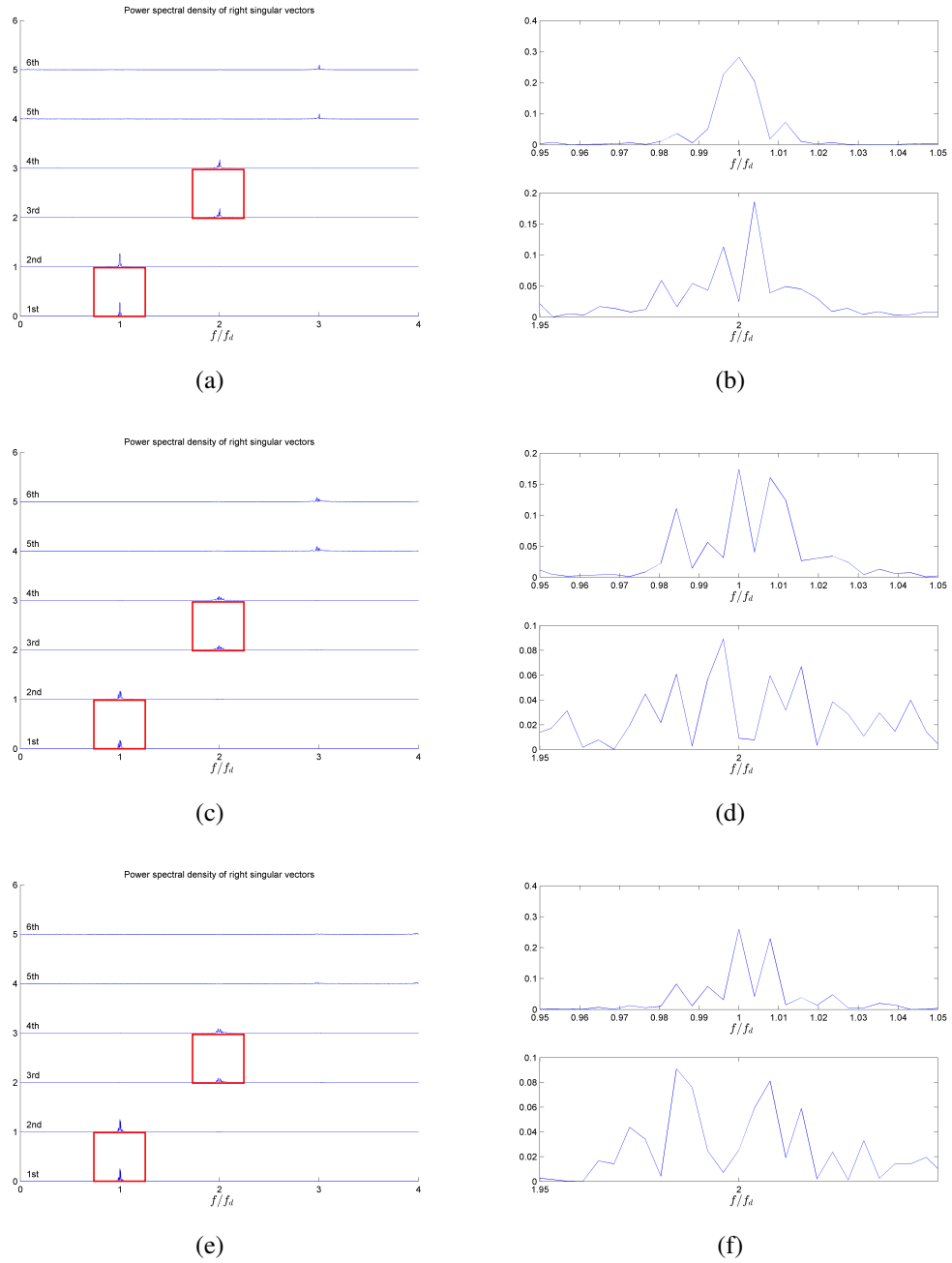
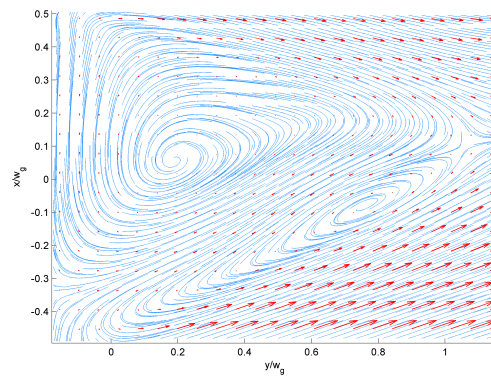
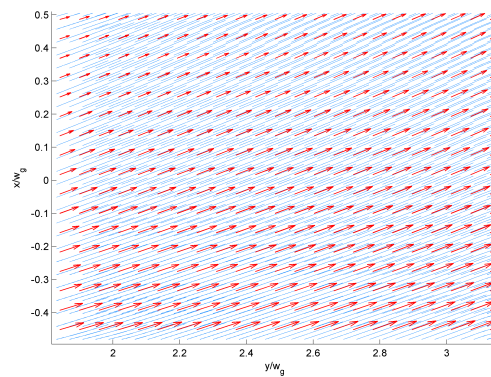


Figure 8.55: Power spectral densities of the first four right singular vectors (a), (c), (e), and the enlarged images of the power spectral densities of the first (top) and the third (bottom) right singular vectors (b), (d), (f), $\text{Re}[80\ 100]\text{k}$, $H_g = 50\text{ mm}$; FOV 1: (a) and (b), FOV 2: (c) and (d), and FOV 3: (e) and (f). Red squares on (a), (c), and (e) show the areas where (b), (d), and (f) are taken, respectively.

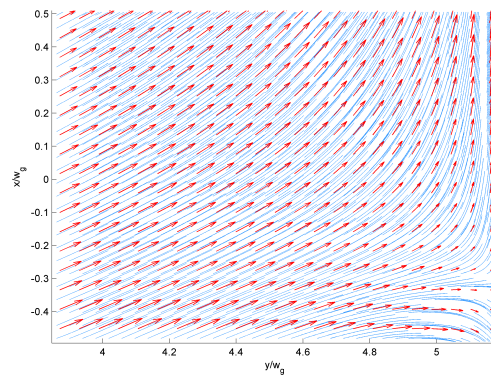
8.6.10 $\text{Re}[60\ 100]_k, H_g = 10\text{mm}$



(a)



(b)



(c)

Figure 8.56: Time-averaged velocity field of $\text{Re}[60\ 100]_k, H_g = 10\text{ mm}$; FOV 1 (a), FOV 2 (b), and FOV 3 (C). Red arrows indicate velocity vectors, and blue lines indicate streamlines.

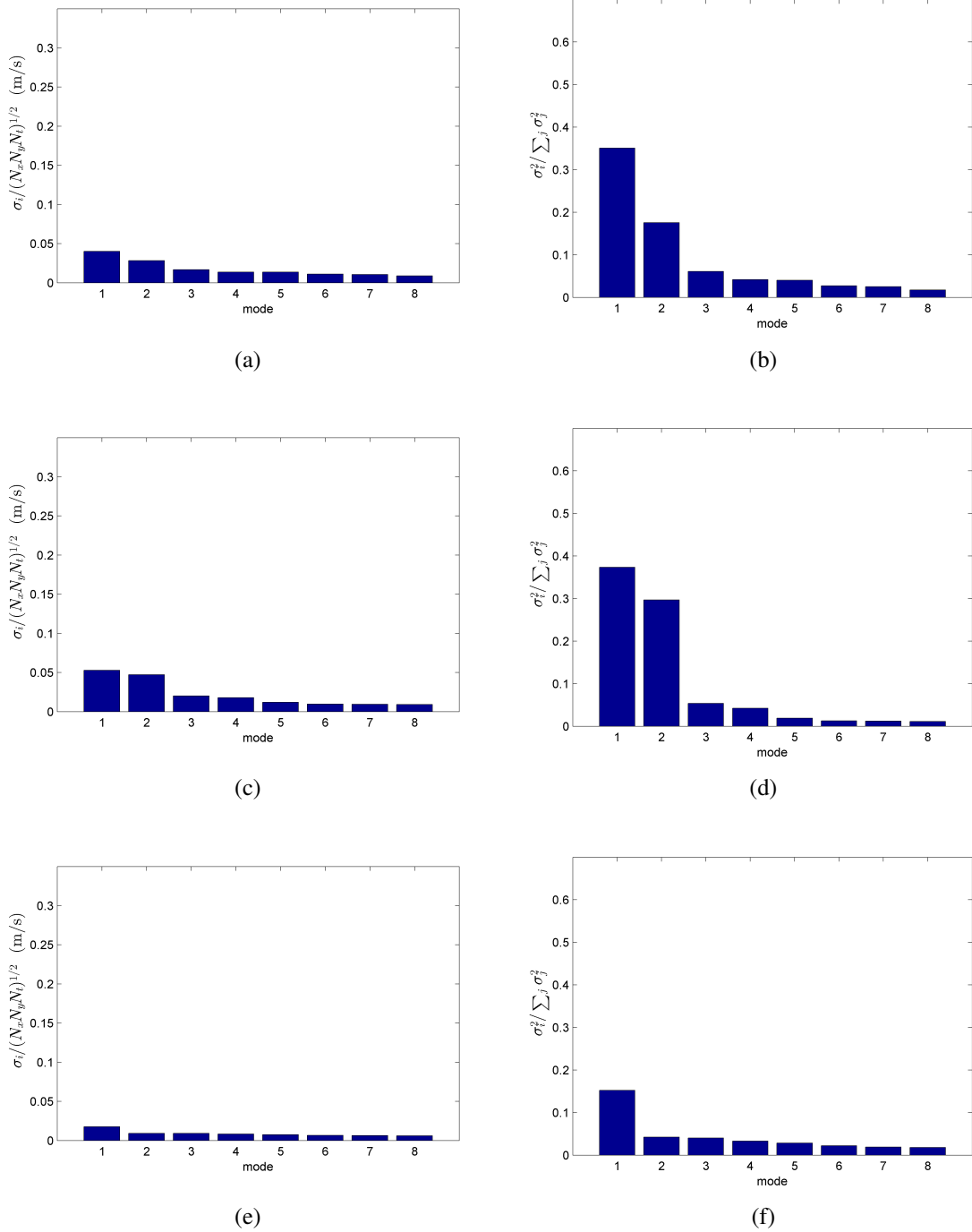


Figure 8.57: Normalized singular values (left) and their energy proportions (right) of the first eight modes, Re[60 100]k, $H_g = 10$ mm; FOV 1: (a) and (b), FOV 2: (c) and (d), FOV 3: (e) and (f).

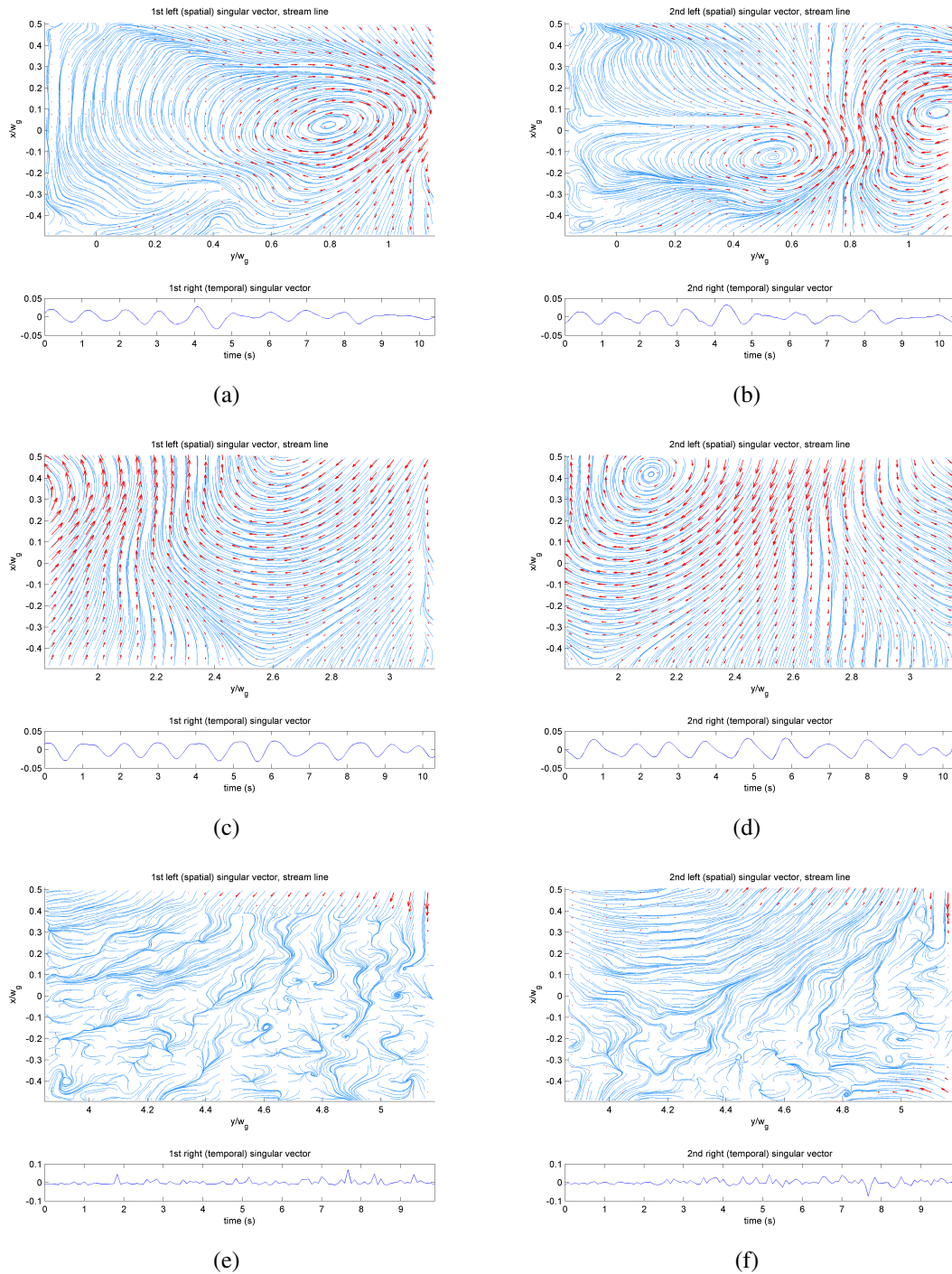


Figure 8.58: Singular vectors of the first (left) and the second (right) modes, $\text{Re}[60\ 100]k$, $H_g = 10\text{ mm}$; FOV1: (a) and (b), FOV2: (c) and (d), FOV3: (e) and (f). Red arrows are velocity vectors, and blue lines are streamlines.

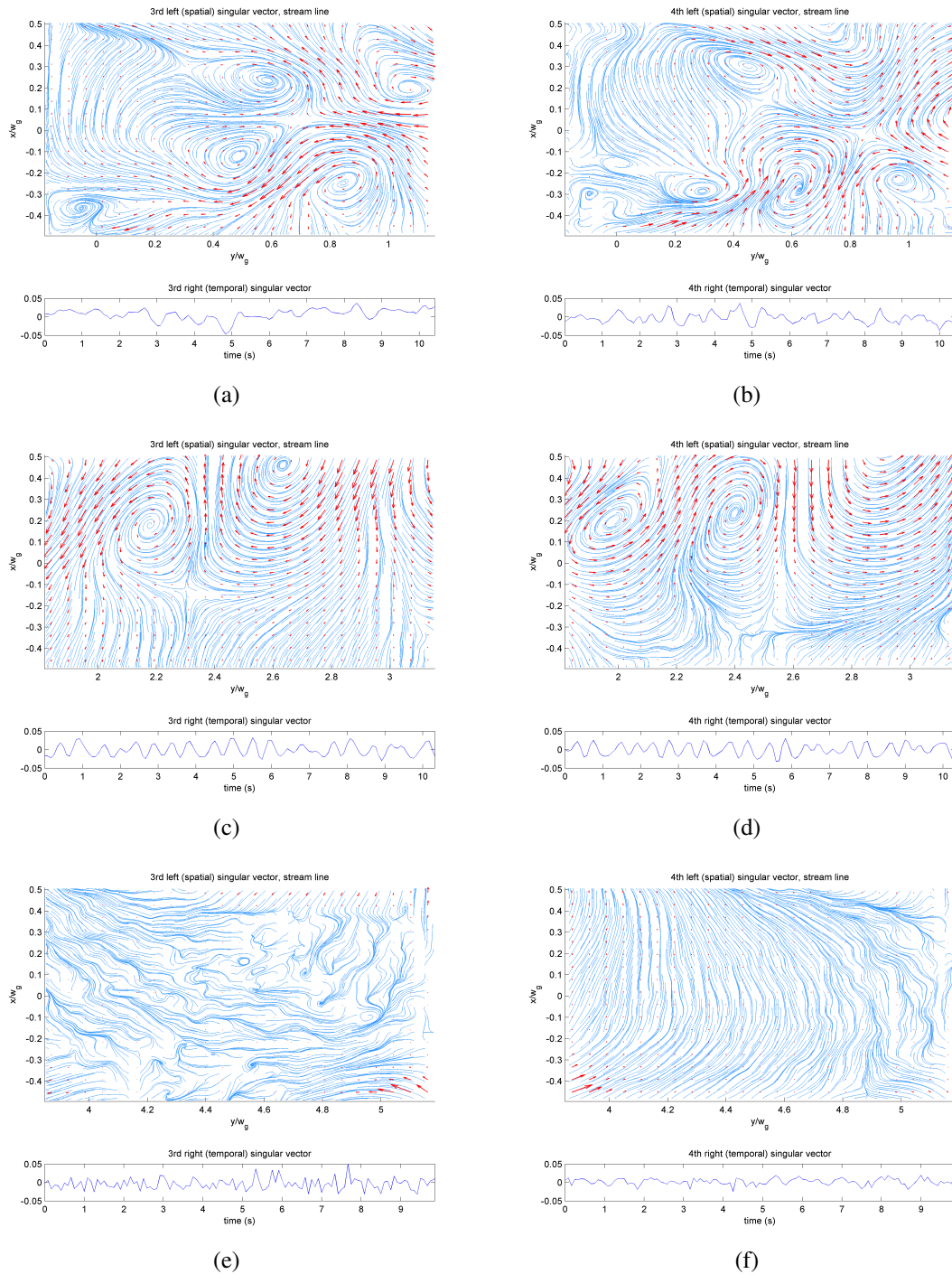
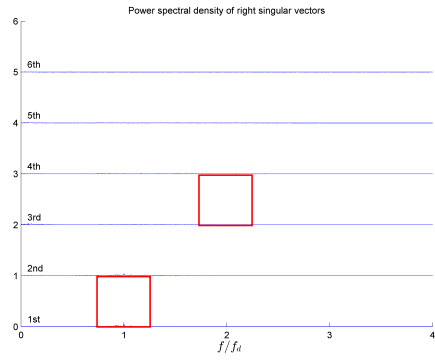
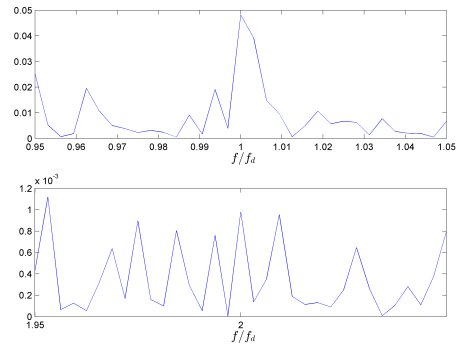


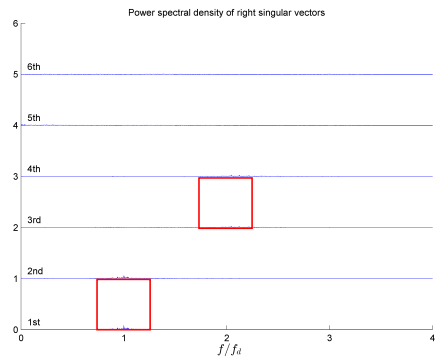
Figure 8.59: Singular vectors of the third (left) and the fourth (right) modes, $\text{Re}[60\ 100]k$, $H_g = 10\text{ mm}$; FOV1: (a) and (b), FOV2: (c) and (d), FOV3: (e) and (f). Red arrows are velocity vectors, and blue lines are streamlines.



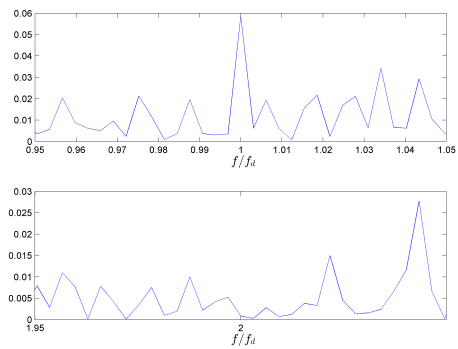
(a)



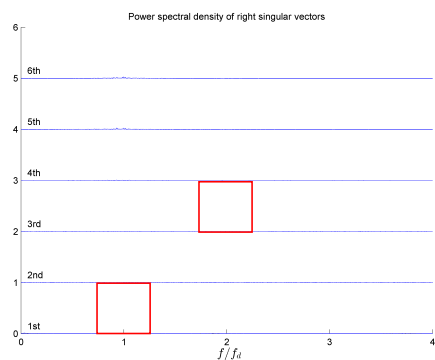
(b)



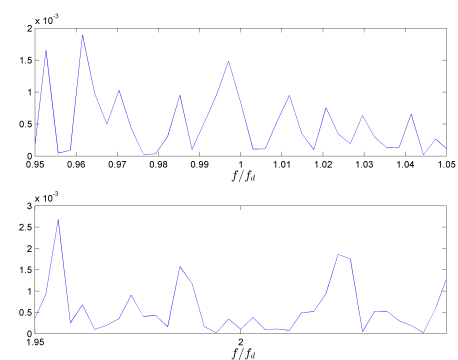
(c)



(d)



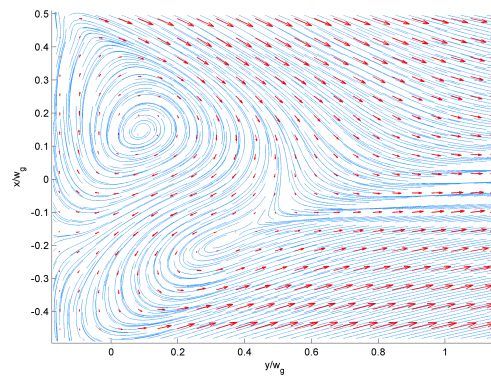
(e)



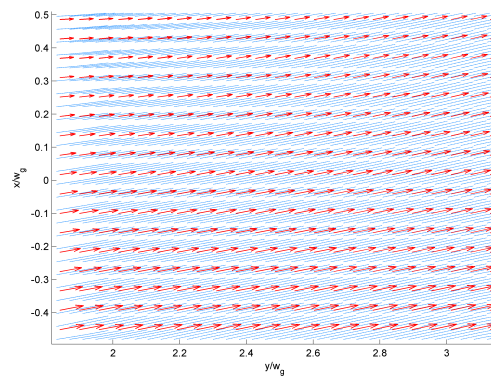
(f)

Figure 8.60: Power spectral densities of the first four right singular vectors (a), (c), (e), and the enlarged images of the power spectral densities of the first (top) and the third (bottom) right singular vectors (b), (d), (f), $\text{Re}[60\ 100]k$, $H_g = 10\text{ mm}$; FOV 1: (a) and (b), FOV 2: (c) and (d), and FOV 3: (e) and (f). Red squares on (a), (c), and (e) show the areas where (b), (d), and (f) are taken, respectively.

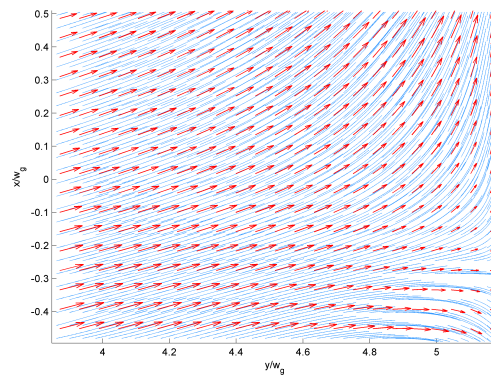
8.6.11 $\text{Re}[60\ 100]_k, H_g = 20\text{mm}$



(a)

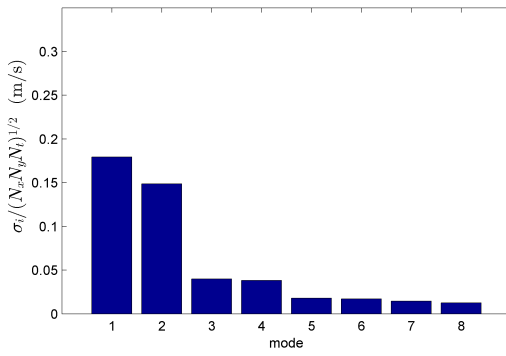


(b)

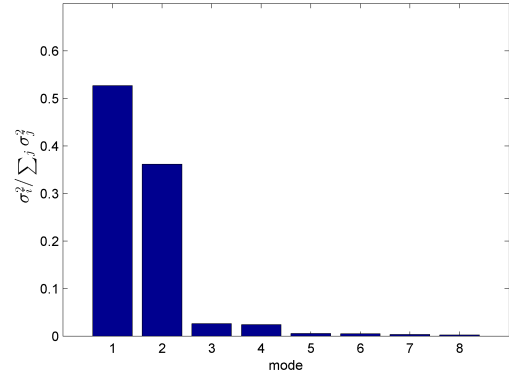


(c)

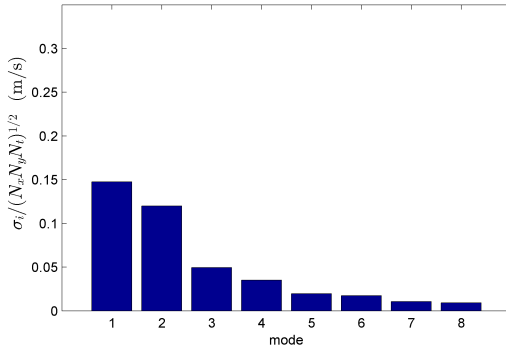
Figure 8.61: Time-averaged velocity field of $\text{Re}[60\ 100]_k, H_g = 20\text{ mm}$; FOV 1 (a), FOV 2 (b), and FOV 3 (c). Red arrows indicate velocity vectors, and blue lines indicate streamlines.



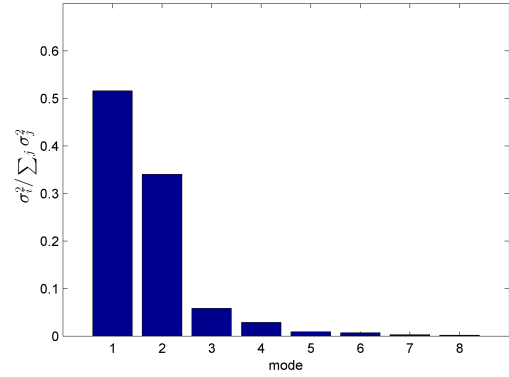
(a)



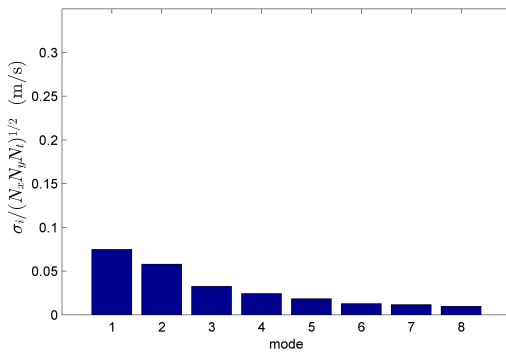
(b)



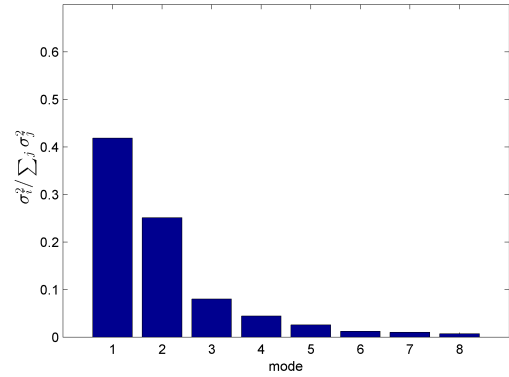
(c)



(d)



(e)



(f)

Figure 8.62: Normalized singular values (left) and their energy proportions (right) of the first eight modes, $\text{Re}[60\ 100]\text{k}$, $H_g = 20\text{ mm}$; FOV 1: (a) and (b), FOV 2: (c) and (d), FOV 3: (e) and (f).

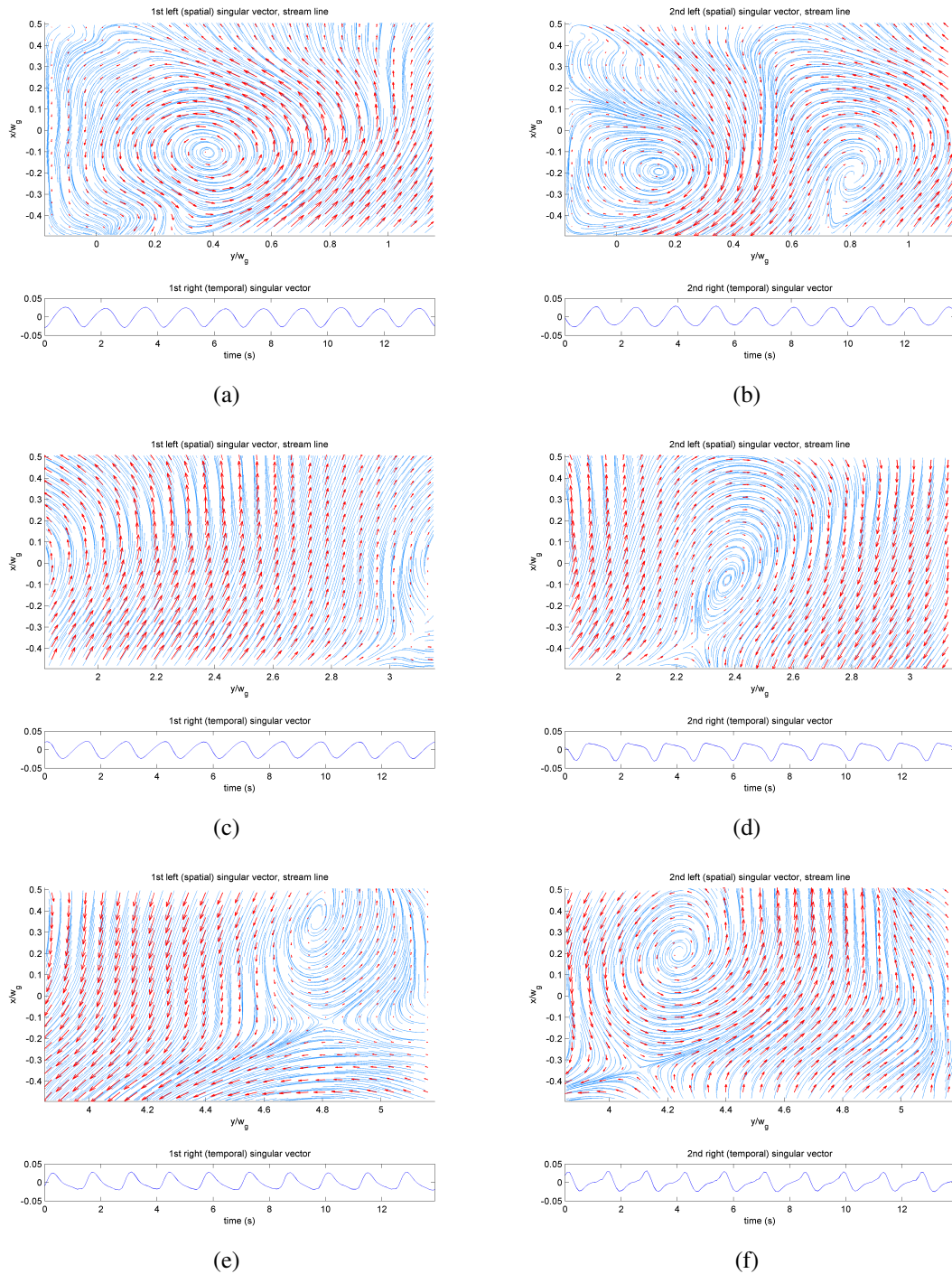


Figure 8.63: Singular vectors of the first (left) and the second (right) modes, $\text{Re}[60\ 100]k$, $H_g = 20\text{ mm}$; FOV1: (a) and (b), FOV2: (c) and (d), FOV3: (e) and (f). Red arrows are velocity vectors, and blue lines are streamlines.

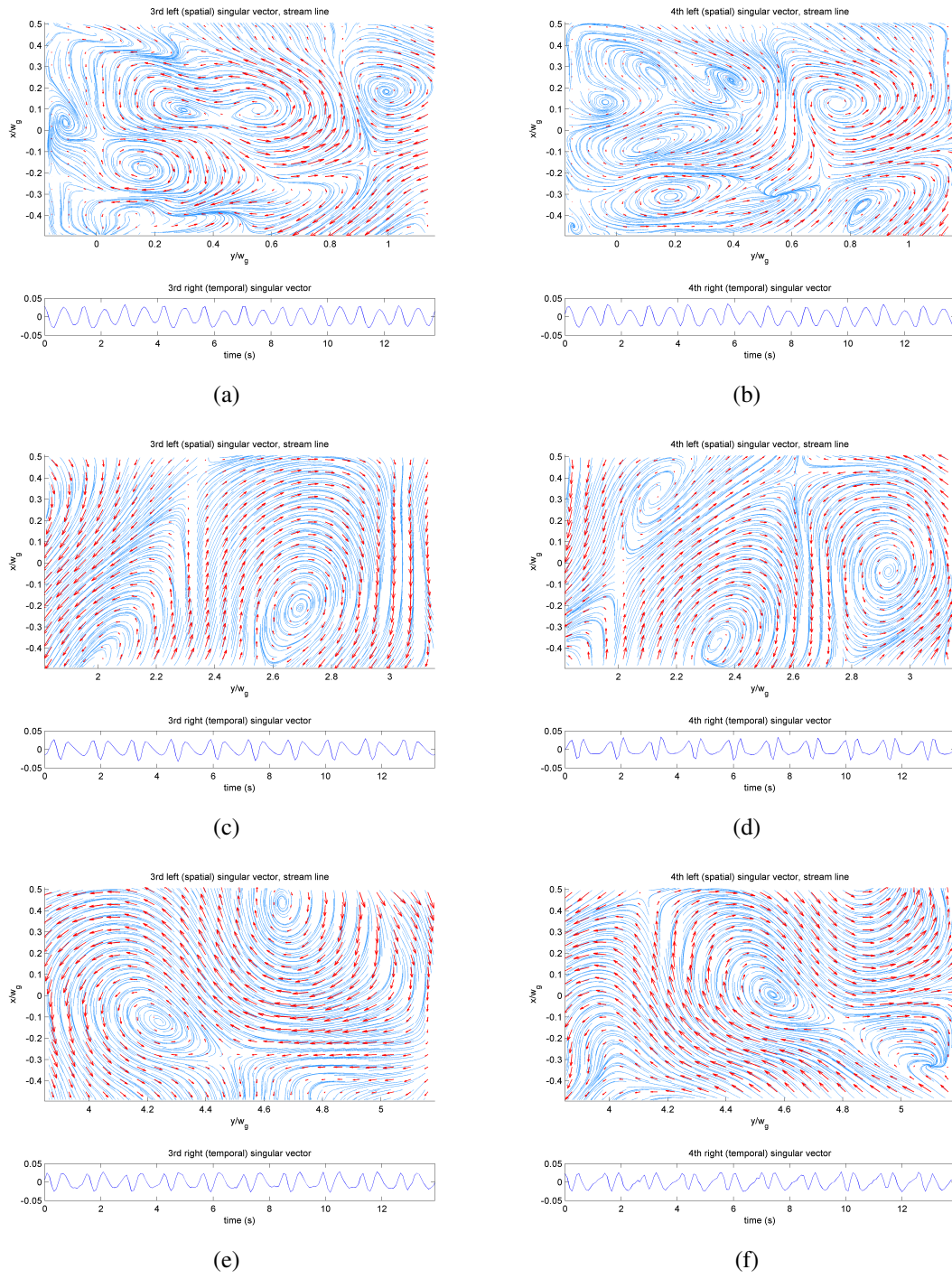


Figure 8.64: Singular vectors of the third (left) and the fourth (right) modes, $\text{Re}[60\ 100]k$, $H_g = 20\text{ mm}$; FOV1: (a) and (b), FOV2: (c) and (d), FOV3: (e) and (f). Red arrows are velocity vectors, and blue lines are streamlines.

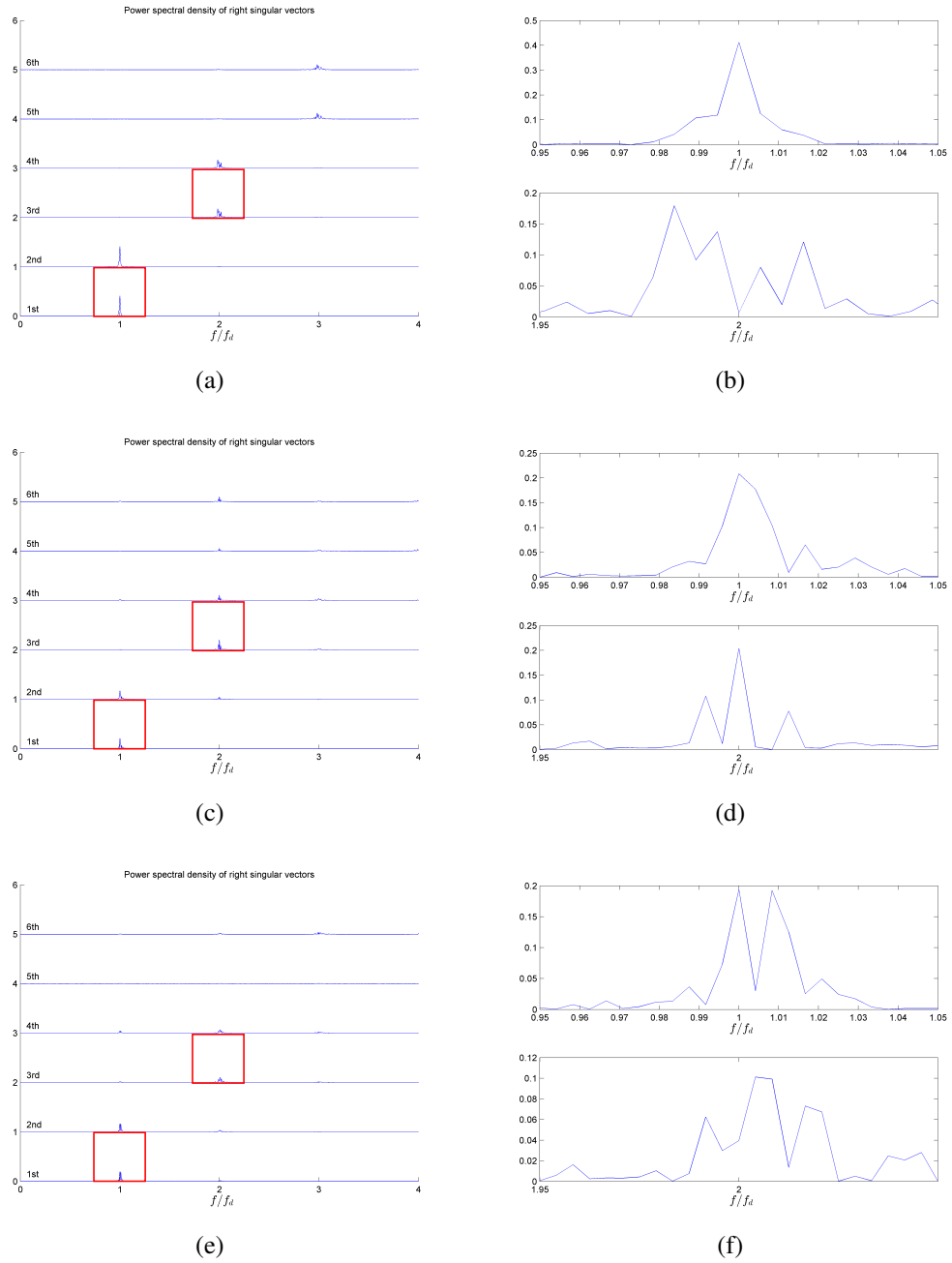
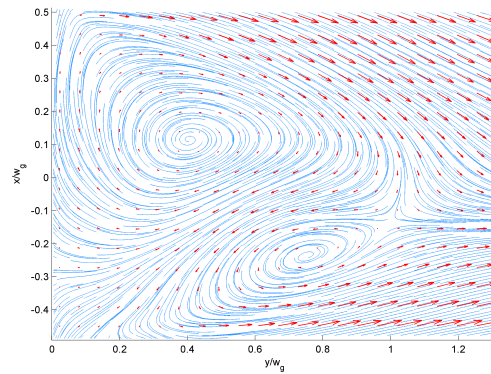
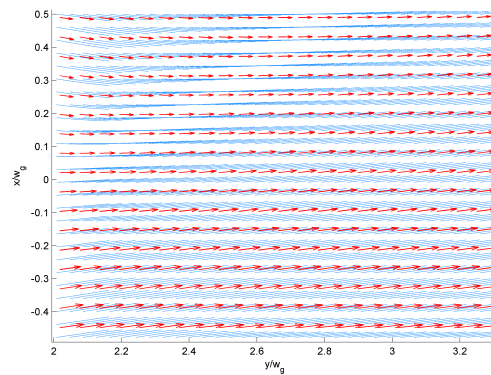


Figure 8.65: Power spectral densities of the first four right singular vectors (a), (c), (e), and the enlarged images of the power spectral densities of the first (top) and the third (bottom) right singular vectors (b), (d), (f), $\text{Re}[60\ 100]\text{k}$, $H_g = 20\text{ mm}$; FOV 1: (a) and (b), FOV 2: (c) and (d), and FOV 3: (e) and (f). Red squares on (a), (c), and (e) show the areas where (b), (d), and (f) are taken, respectively.

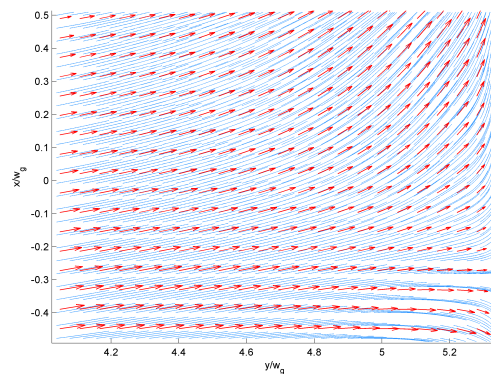
8.6.12 $\text{Re}[60\ 100]_k$, $H_g = 50\text{mm}$



(a)



(b)



(c)

Figure 8.66: Time-averaged velocity field of $\text{Re}[60\ 100]_k$, $H_g = 50\text{ mm}$; FOV 1 (a), FOV 2 (b), and FOV 3 (C). Red arrows indicate velocity vectors, and blue lines indicate streamlines.

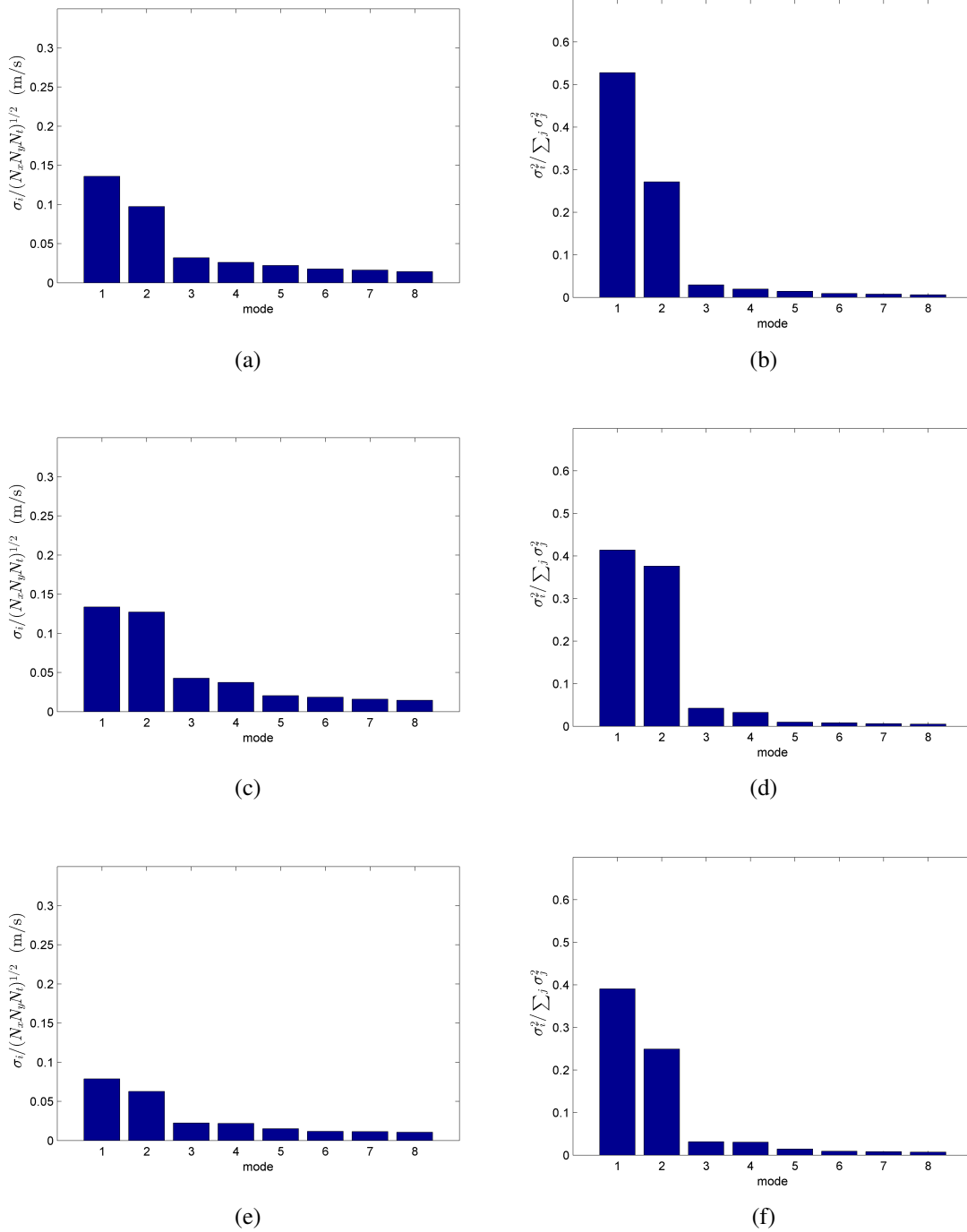


Figure 8.67: Normalized singular values (left) and their energy proportions (right) of the first eight modes, $\text{Re}[60\ 100]\text{k}$, $H_g = 50\ \text{mm}$; FOV 1: (a) and (b), FOV 2: (c) and (d), FOV 3: (e) and (f).

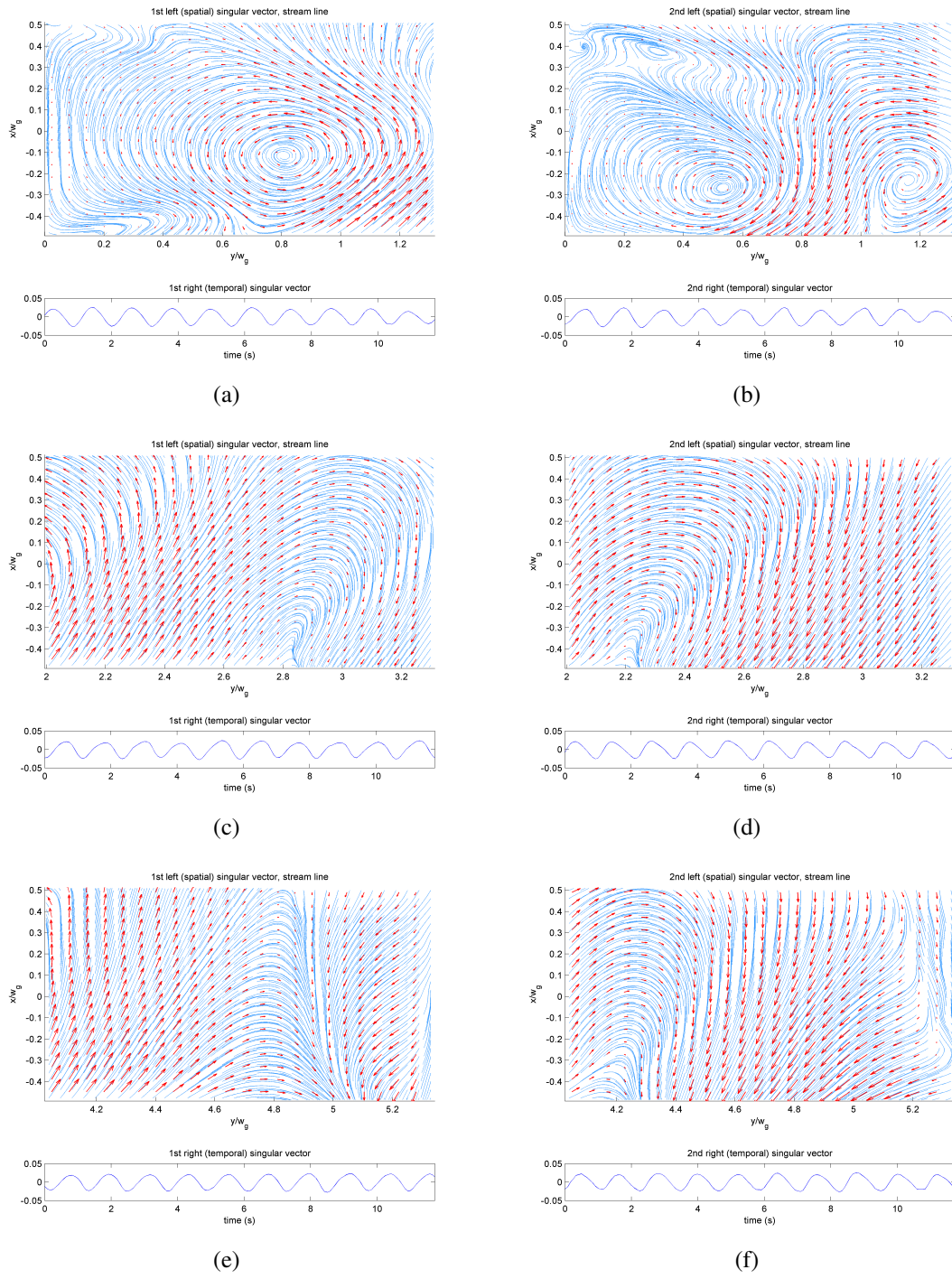


Figure 8.68: Singular vectors of the first (left) and the second (right) modes, $\text{Re}[60\ 100]k$, $H_g = 50$ mm; FOV1: (a) and (b), FOV2: (c) and (d), FOV3: (e) and (f). Red arrows are velocity vectors, and blue lines are streamlines.

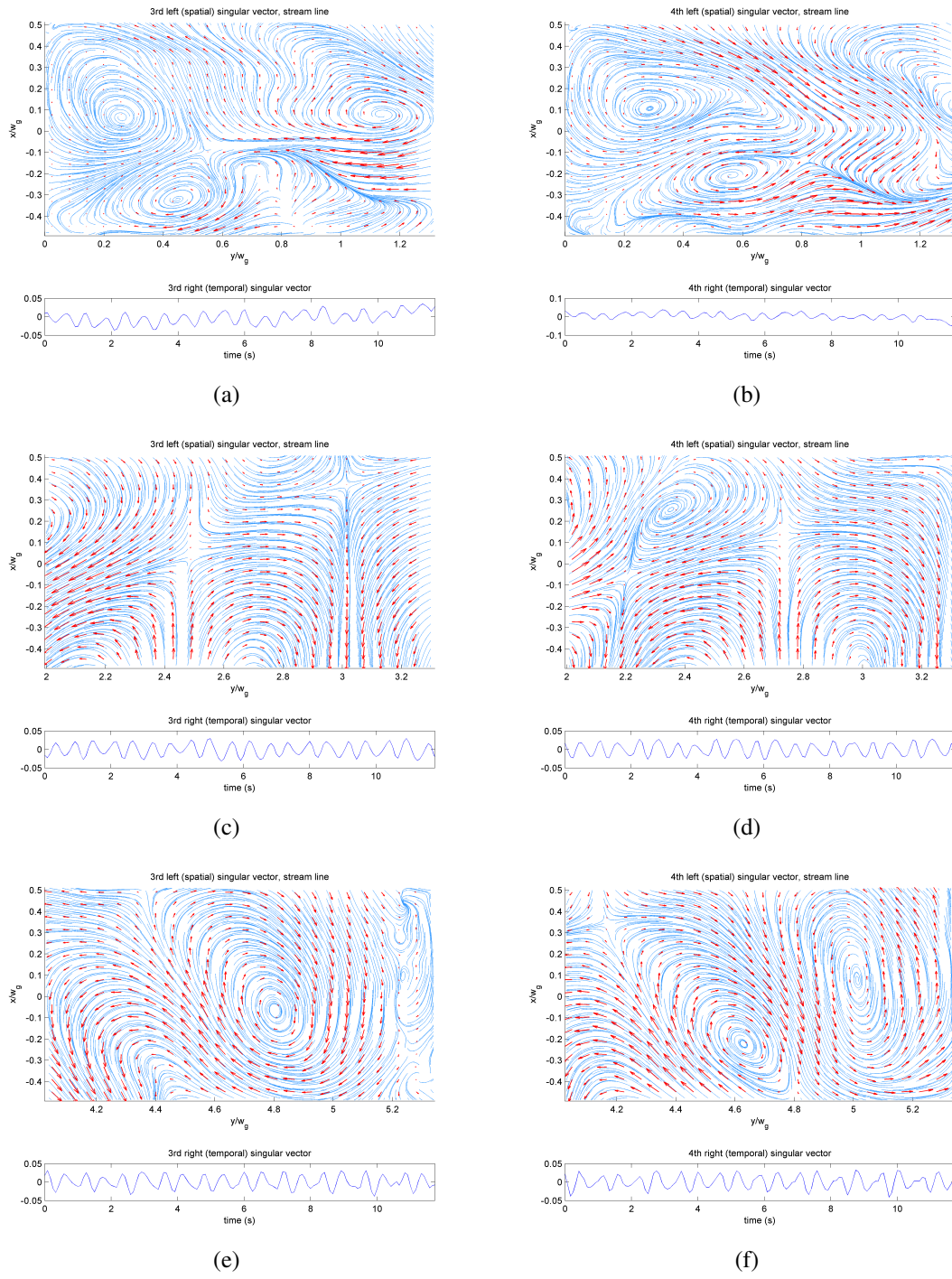


Figure 8.69: Singular vectors of the third (left) and the fourth (right) modes, $\text{Re}[60\ 100]k$, $H_g = 50\text{ mm}$; FOV1: (a) and (b), FOV2: (c) and (d), FOV3: (e) and (f). Red arrows are velocity vectors, and blue lines are streamlines.

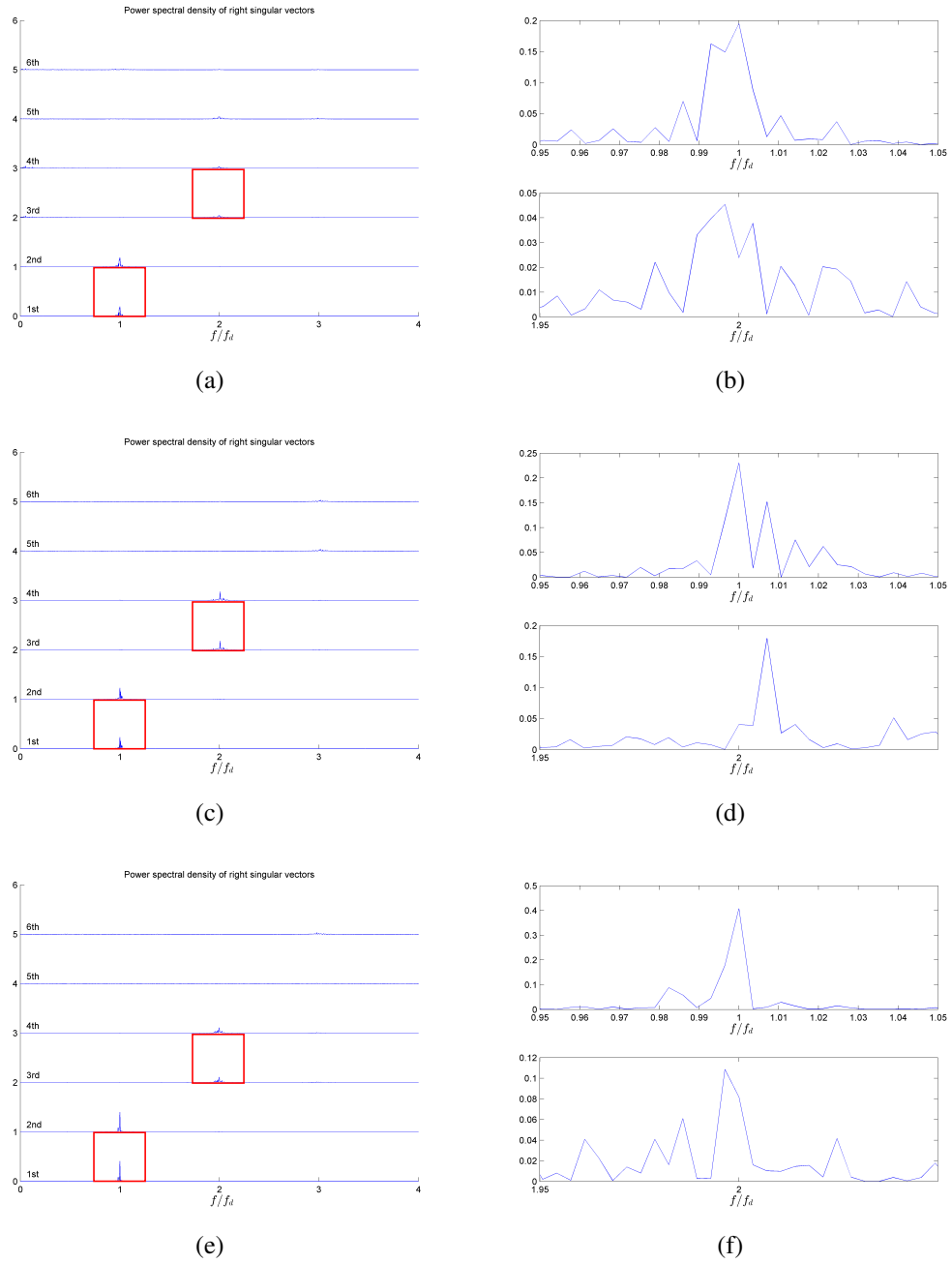
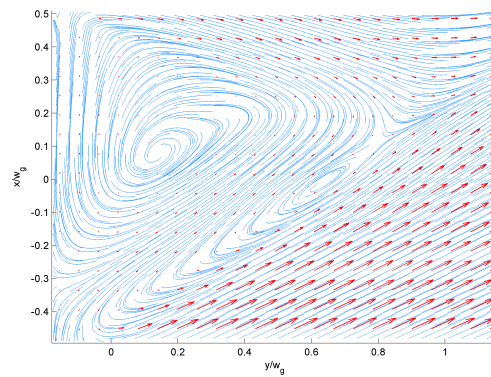
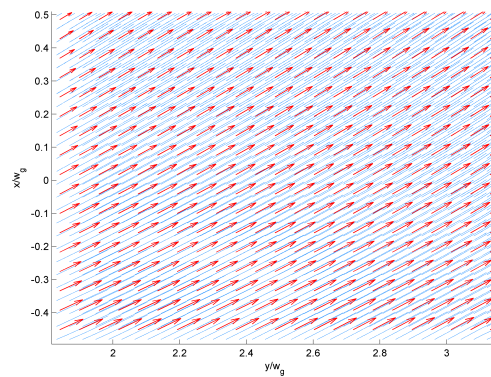


Figure 8.70: Power spectral densities of the first four right singular vectors (a), (c), (e), and the enlarged images of the power spectral densities of the first (top) and the third (bottom) right singular vectors (b), (d), (f), $\text{Re}[60\ 100]\text{k}$, $H_g = 50\text{ mm}$; FOV 1: (a) and (b), FOV 2: (c) and (d), and FOV 3: (e) and (f). Red squares on (a), (c), and (e) show the areas where (b), (d), and (f) are taken, respectively.

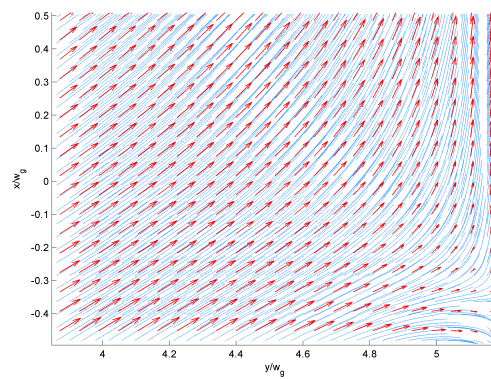
8.6.13 $\text{Re}[40\ 100]k$, $H_g = 10\text{mm}$



(a)

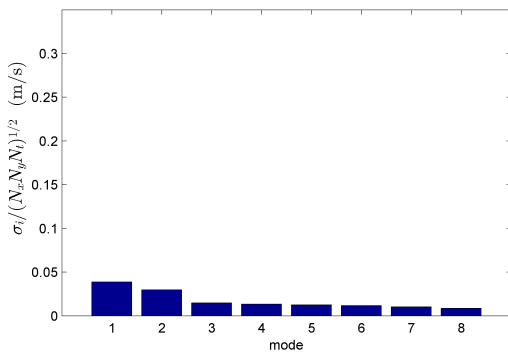


(b)

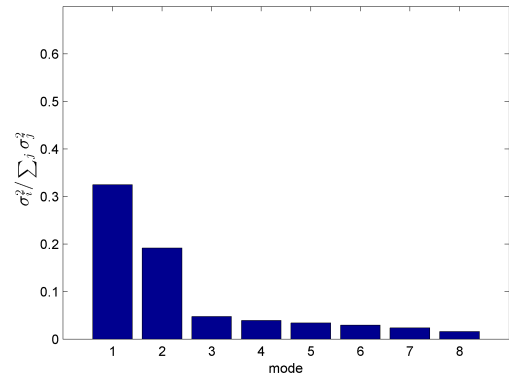


(c)

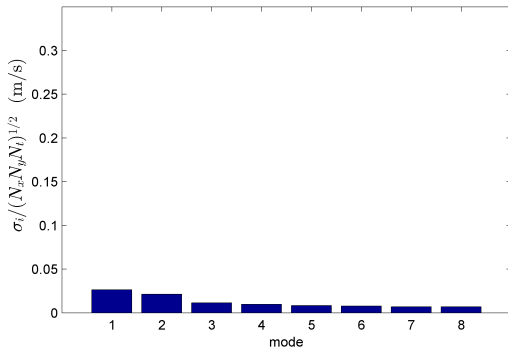
Figure 8.71: Time-averaged velocity field of $\text{Re}[40\ 100]k$, $H_g = 10\text{ mm}$; FOV 1 (a), FOV 2 (b), and FOV 3 (C). Red arrows indicate velocity vectors, and blue lines indicate streamlines.



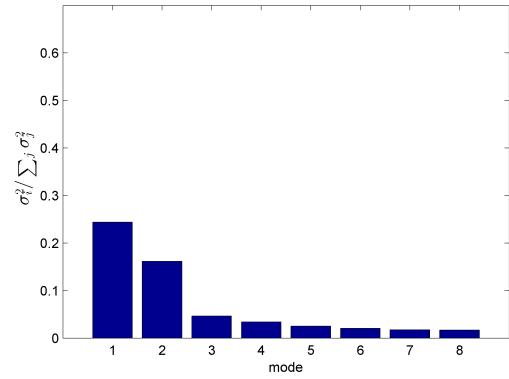
(a)



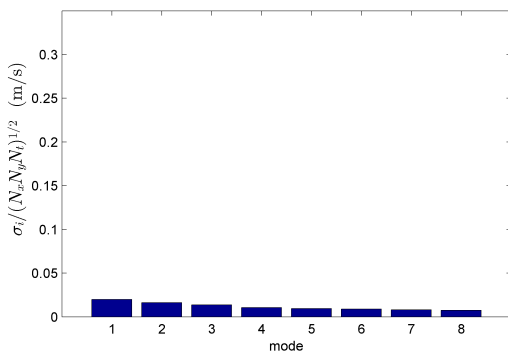
(b)



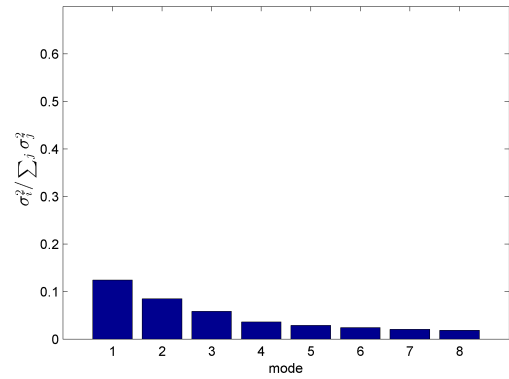
(c)



(d)



(e)



(f)

Figure 8.72: Normalized singular values (left) and their energy proportions (right) of the first eight modes, $\text{Re}[40\ 100]\text{k}$, $H_g = 10\text{ mm}$; FOV 1: (a) and (b), FOV 2: (c) and (d), FOV 3: (e) and (f).

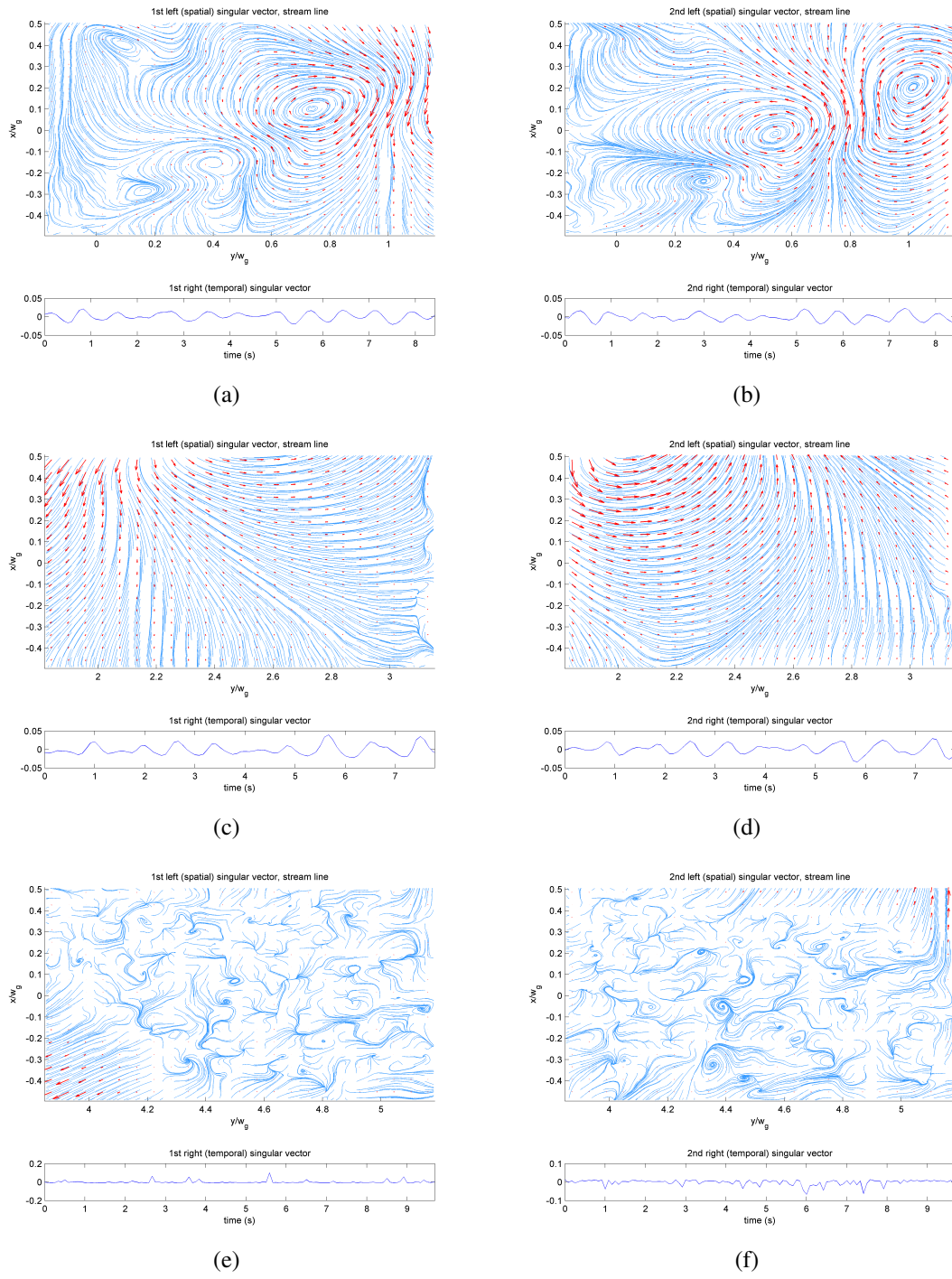


Figure 8.73: Singular vectors of the first (left) and the second (right) modes, $\text{Re}[40\ 100]k$, $H_g = 10\text{ mm}$; FOV1: (a) and (b), FOV2: (c) and (d), FOV3: (e) and (f). Red arrows are velocity vectors, and blue lines are streamlines.

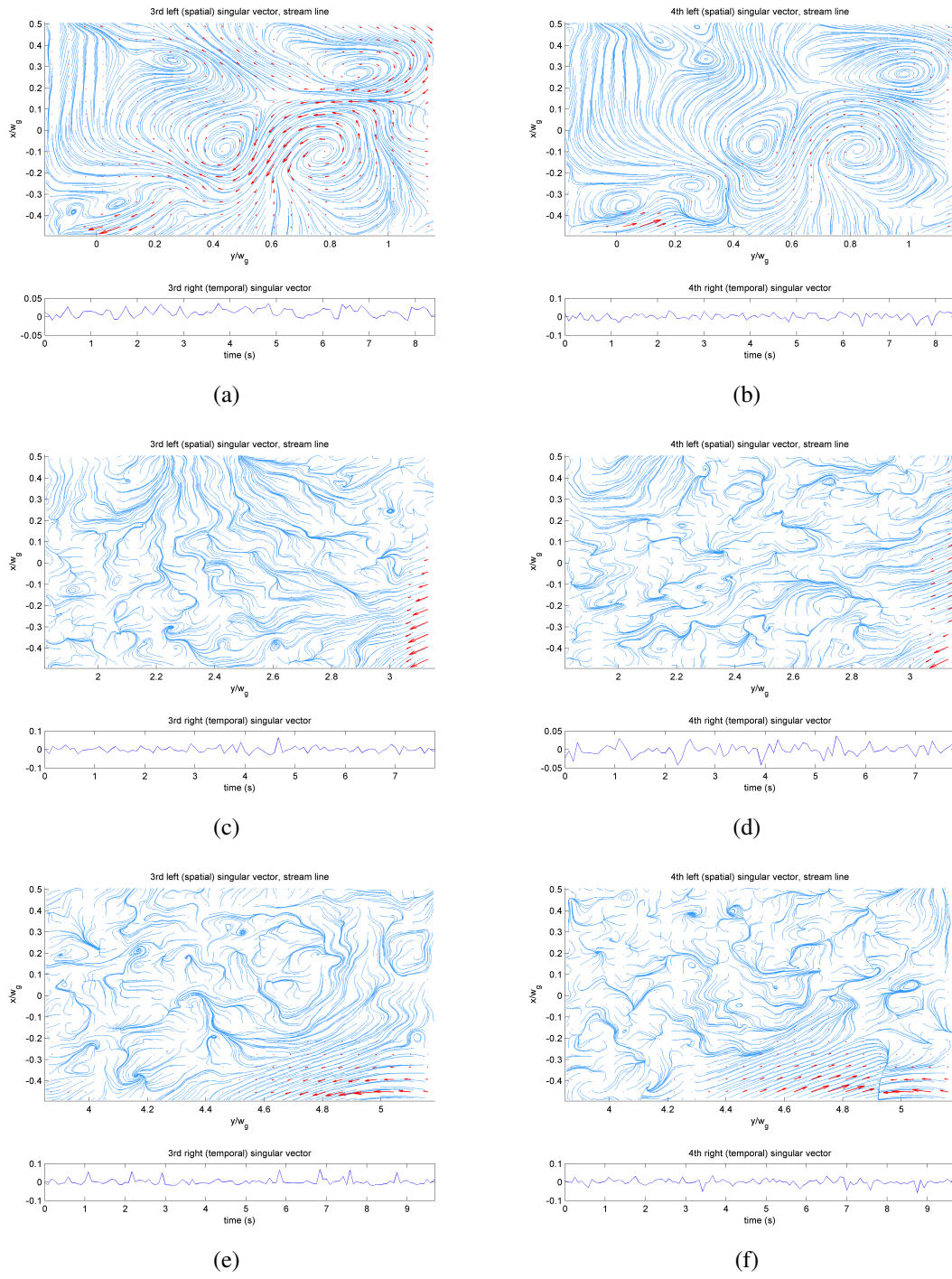


Figure 8.74: Singular vectors of the third (left) and the fourth (right) modes, $\text{Re}[40\ 100]k$, $H_g = 10\text{ mm}$; FOV1: (a) and (b), FOV2: (c) and (d), FOV3: (e) and (f). Red arrows are velocity vectors, and blue lines are streamlines.

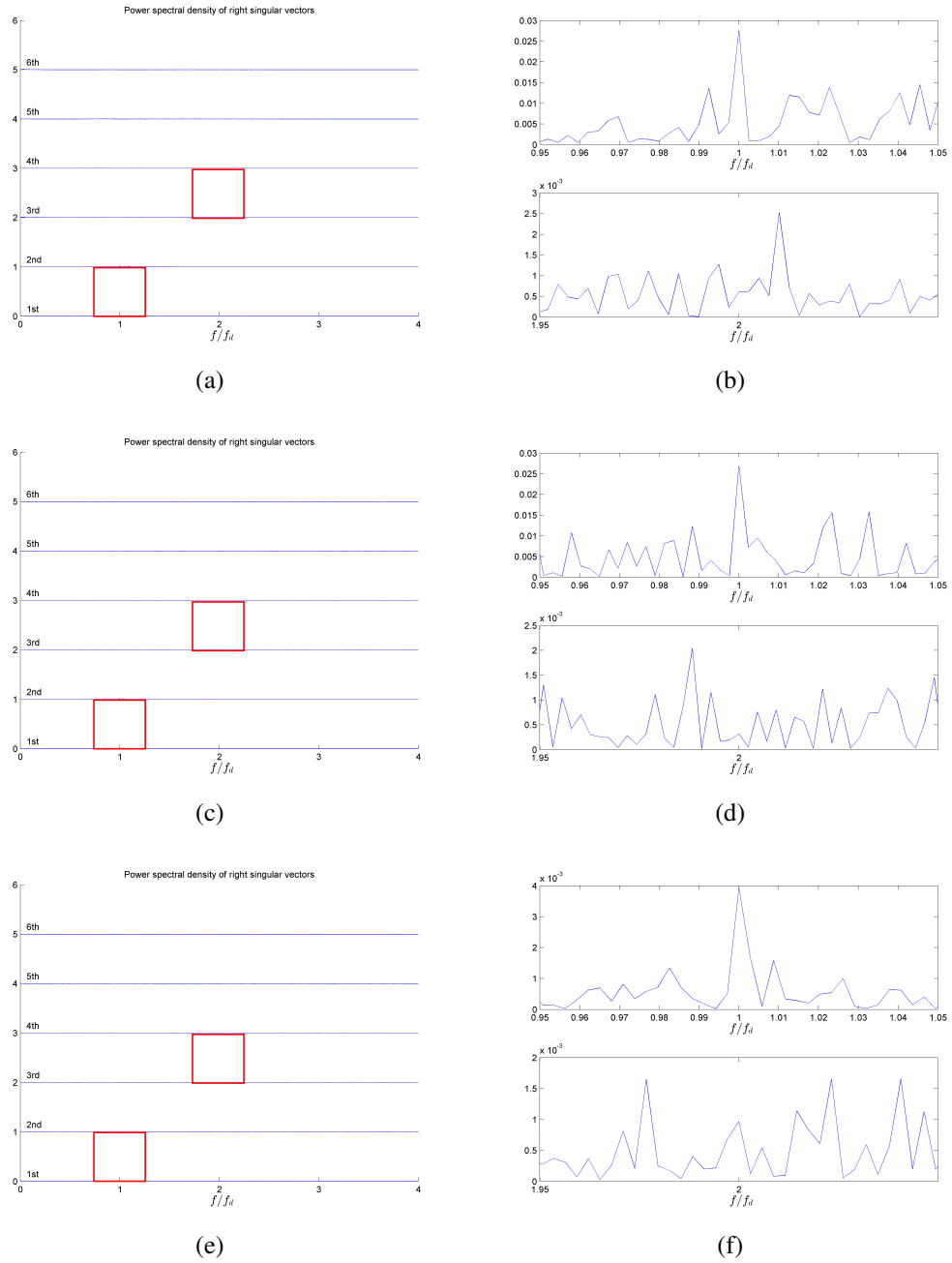
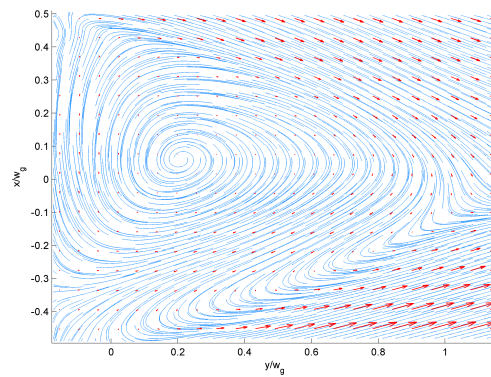
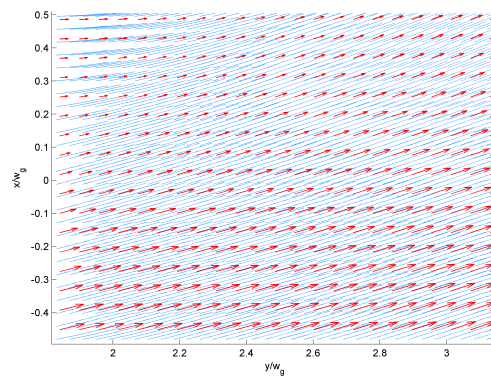


Figure 8.75: Power spectral densities of the first four right singular vectors (a), (c), (e), and the enlarged images of the power spectral densities of the first (top) and the third (bottom) right singular vectors (b), (d), (f), $\text{Re}[40\ 100]\text{k}$, $H_g = 10\text{ mm}$; FOV 1: (a) and (b), FOV 2: (c) and (d), and FOV 3: (e) and (f). Red squares on (a), (c), and (e) show the areas where (b), (d), and (f) are taken, respectively.

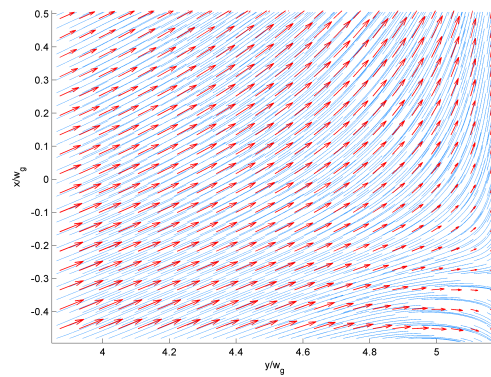
8.6.14 $\text{Re}[40\ 100]_k$, $H_g = 20\text{mm}$



(a)



(b)



(c)

Figure 8.76: Time-averaged velocity field of $\text{Re}[40\ 100]_k$, $H_g = 20\text{ mm}$; FOV 1 (a), FOV 2 (b), and FOV 3 (C). Red arrows indicate velocity vectors, and blue lines indicate streamlines.

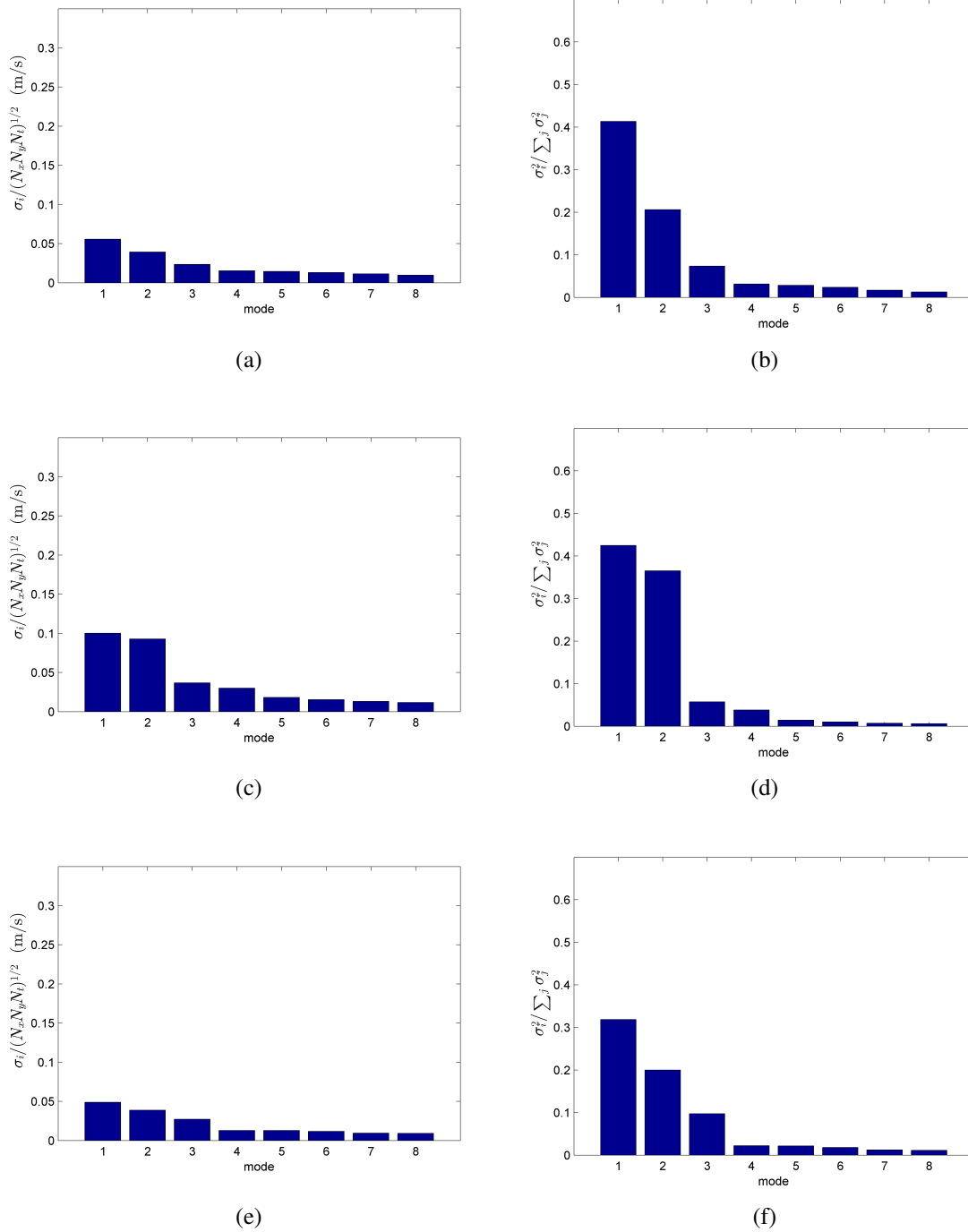


Figure 8.77: Normalized singular values (left) and their energy proportions (right) of the first eight modes, Re[40 100]k, $H_g = 20$ mm; FOV 1: (a) and (b), FOV 2: (c) and (d), FOV 3: (e) and (f).

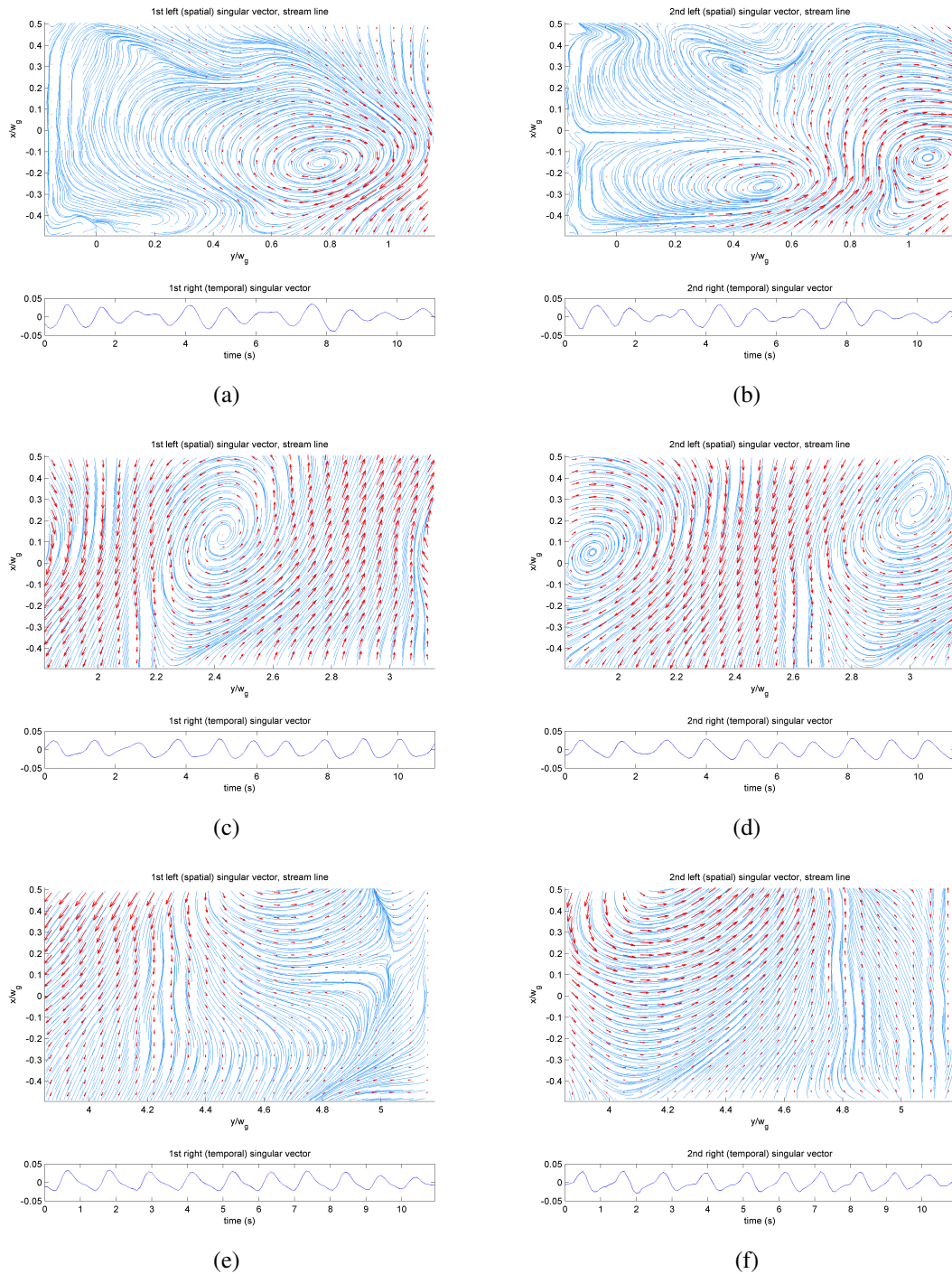


Figure 8.78: Singular vectors of the first (left) and the second (right) modes, $\text{Re}[40\ 100]k$, $H_g = 20\text{ mm}$; FOV1: (a) and (b), FOV2: (c) and (d), FOV3: (e) and (f). Red arrows are velocity vectors, and blue lines are streamlines.

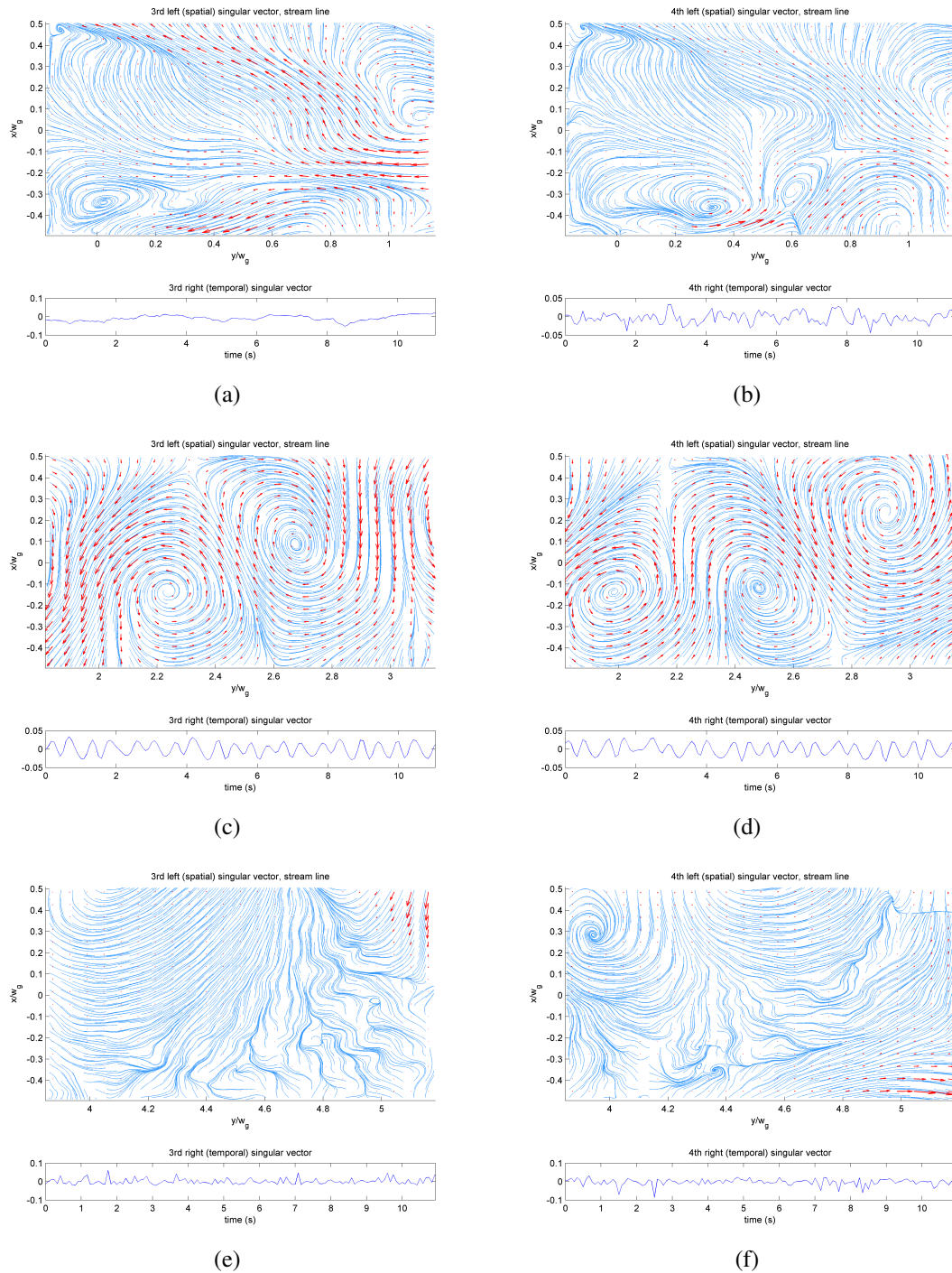


Figure 8.79: Singular vectors of the third (left) and the fourth (right) modes, $\text{Re}[40\ 100]k$, $H_g = 20\text{ mm}$; FOV1: (a) and (b), FOV2: (c) and (d), FOV3: (e) and (f). Red arrows are velocity vectors, and blue lines are streamlines.

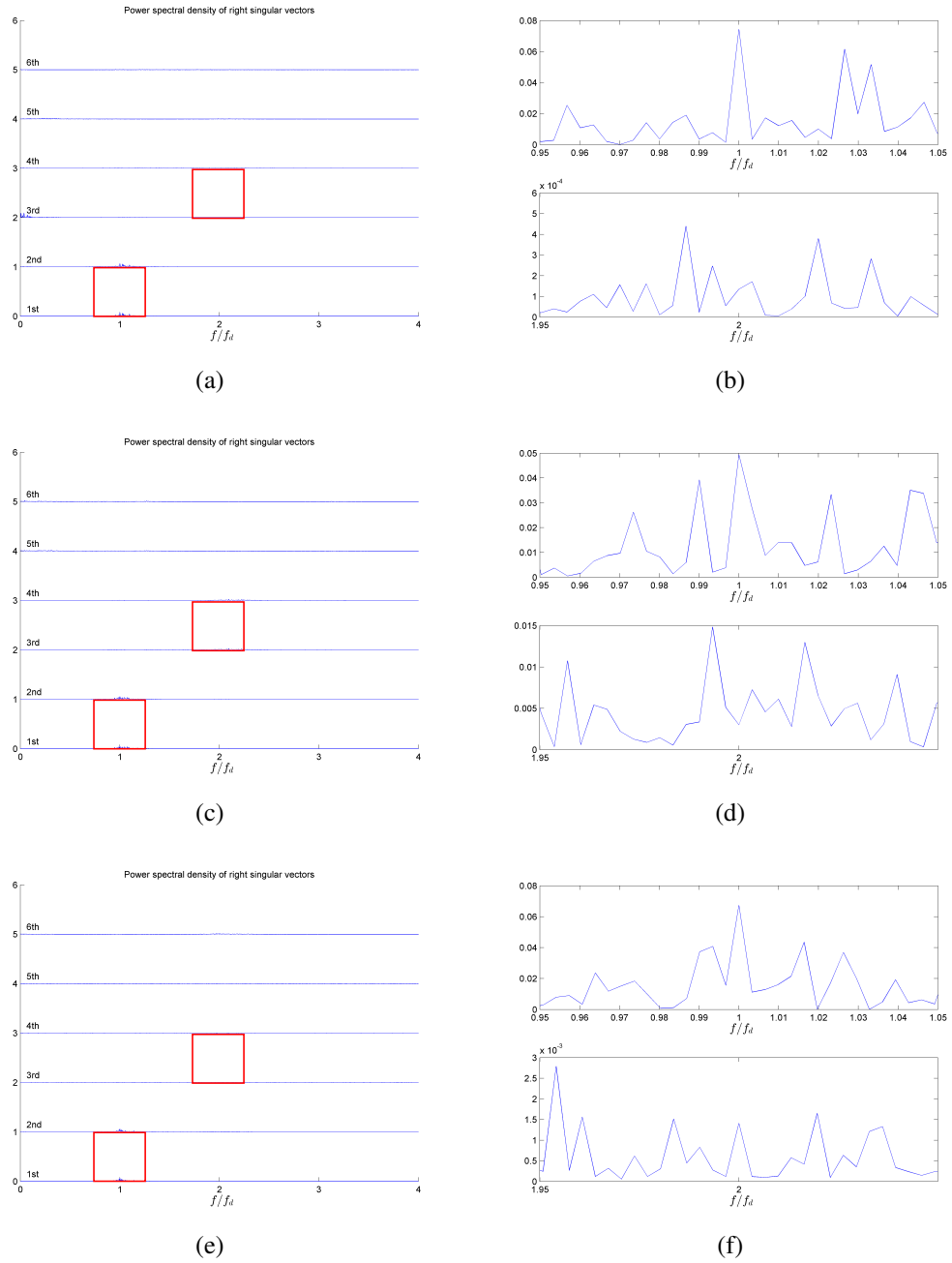
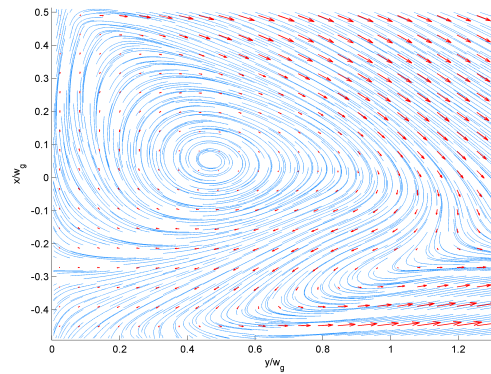
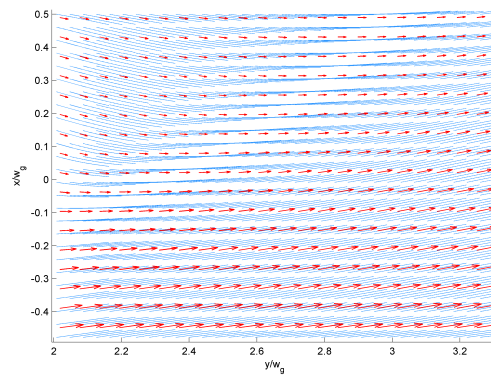


Figure 8.80: Power spectral densities of the first four right singular vectors (a), (c), (e), and the enlarged images of the power spectral densities of the first (top) and the third (bottom) right singular vectors (b), (d), (f), $\text{Re}[40\ 100]\text{k}$, $H_g = 20\text{ mm}$; FOV 1: (a) and (b), FOV 2: (c) and (d), and FOV 3: (e) and (f). Red squares on (a), (c), and (e) show the areas where (b), (d), and (f) are taken, respectively.

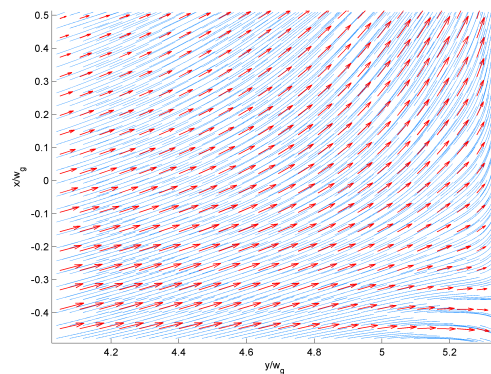
8.6.15 $\text{Re}[40\ 100]_k$, $H_g = 50\text{mm}$



(a)



(b)



(c)

Figure 8.81: Time-averaged velocity field of $\text{Re}[40\ 100]_k$, $H_g = 50\text{ mm}$; FOV 1 (a), FOV 2 (b), and FOV 3 (C). Red arrows indicate velocity vectors, and blue lines indicate streamlines.

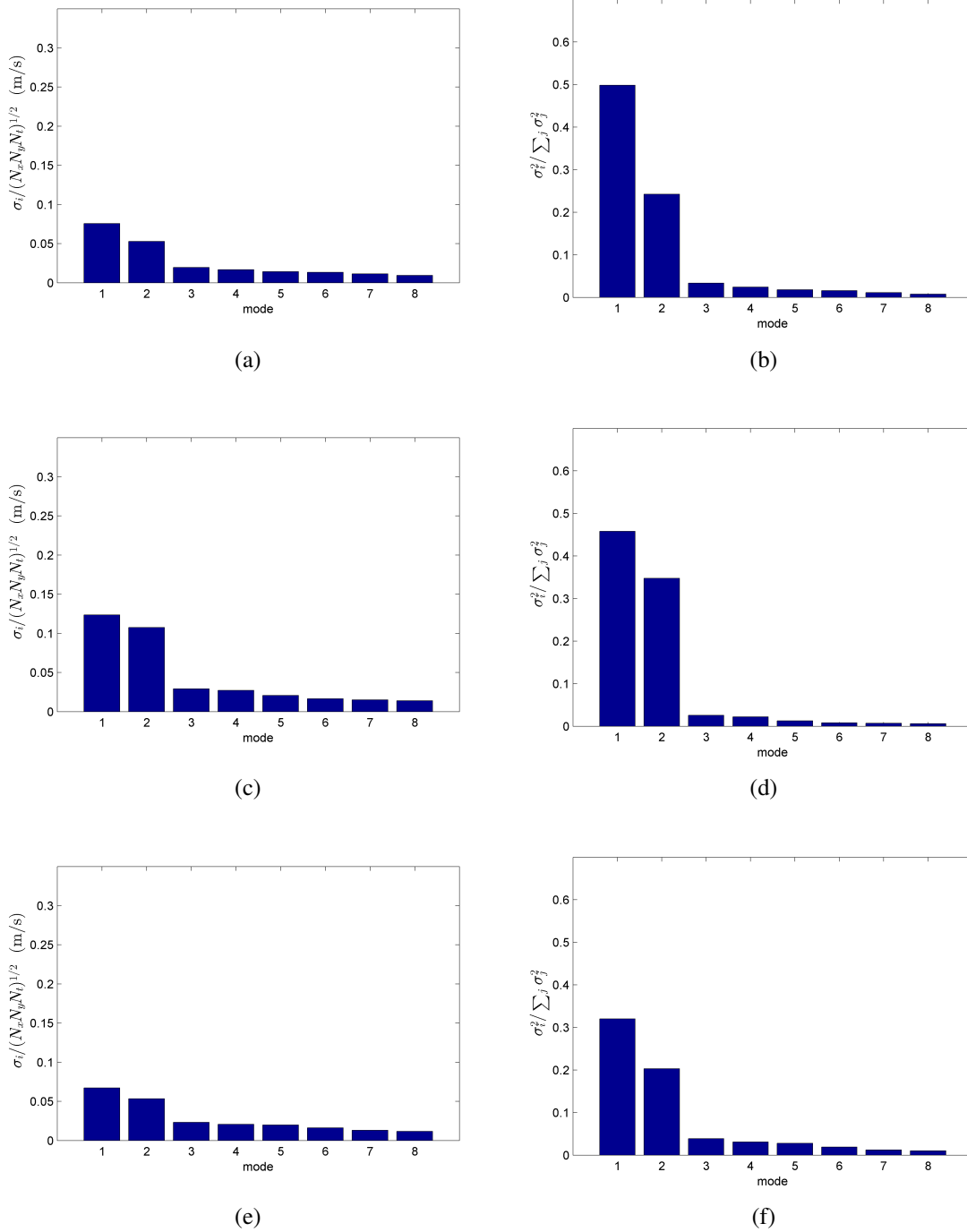


Figure 8.82: Normalized singular values (left) and their energy proportions (right) of the first eight modes, Re[40 100]k, $H_g = 50$ mm; FOV 1: (a) and (b), FOV 2: (c) and (d), FOV 3: (e) and (f).

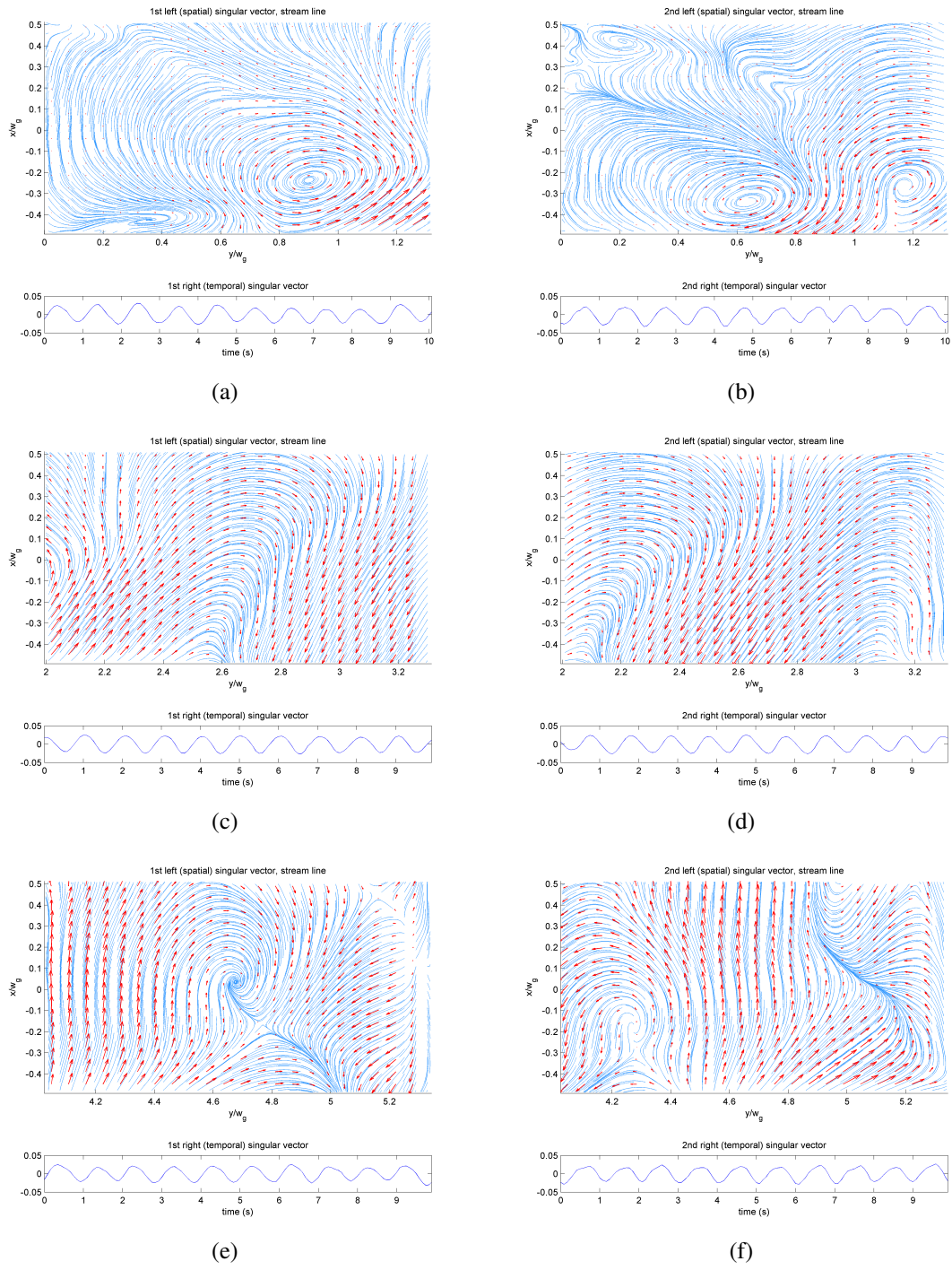


Figure 8.83: Singular vectors of the first (left) and the second (right) modes, $\text{Re}[40\ 100]k$, $H_g = 50\text{ mm}$; FOV1: (a) and (b), FOV2: (c) and (d), FOV3: (e) and (f). Red arrows are velocity vectors, and blue lines are streamlines.

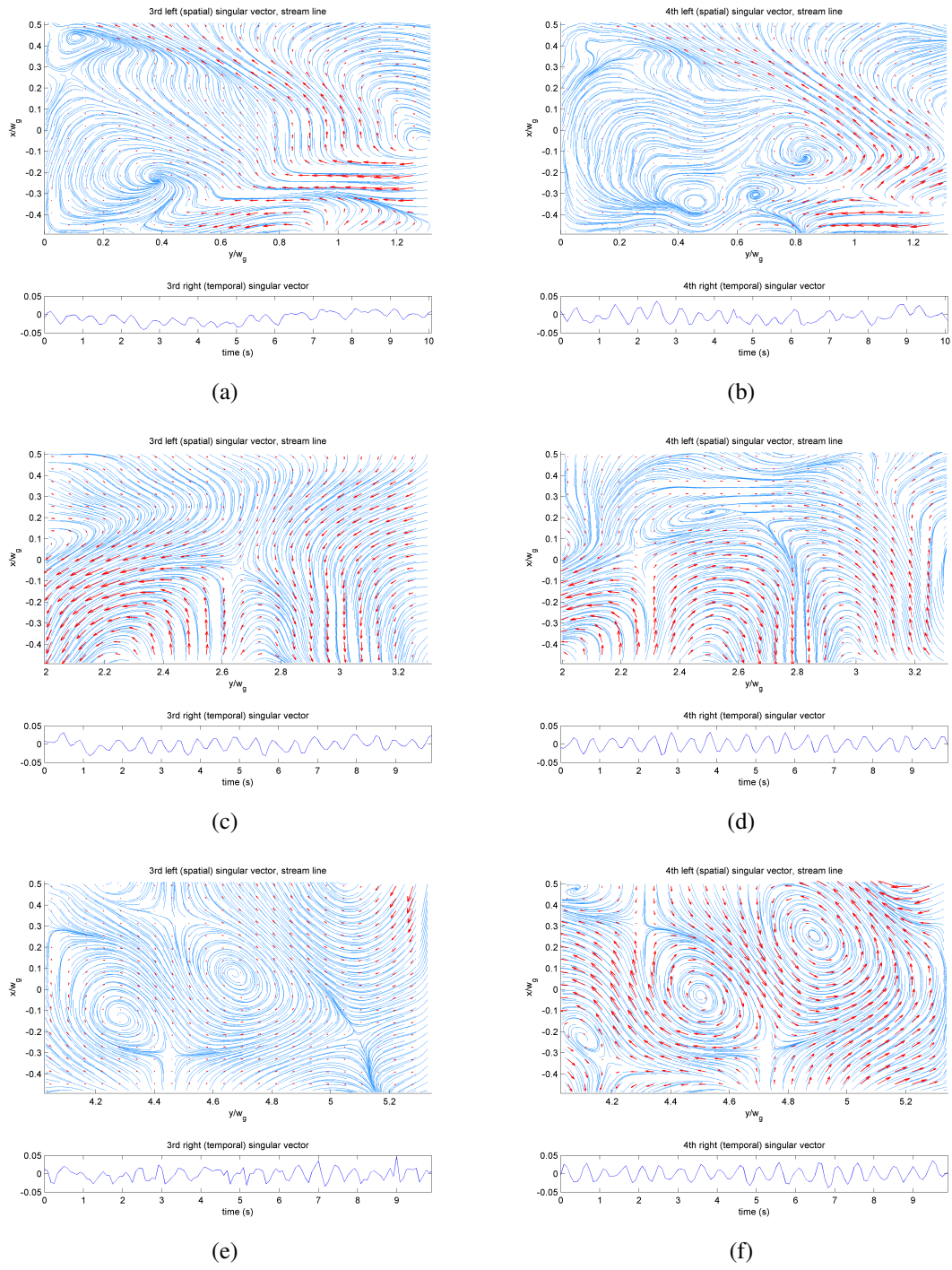


Figure 8.84: Singular vectors of the third (left) and the fourth (right) modes, $\text{Re}[40\ 100]k$, $H_g = 50\text{ mm}$; FOV1: (a) and (b), FOV2: (c) and (d), FOV3: (e) and (f). Red arrows are velocity vectors, and blue lines are streamlines.

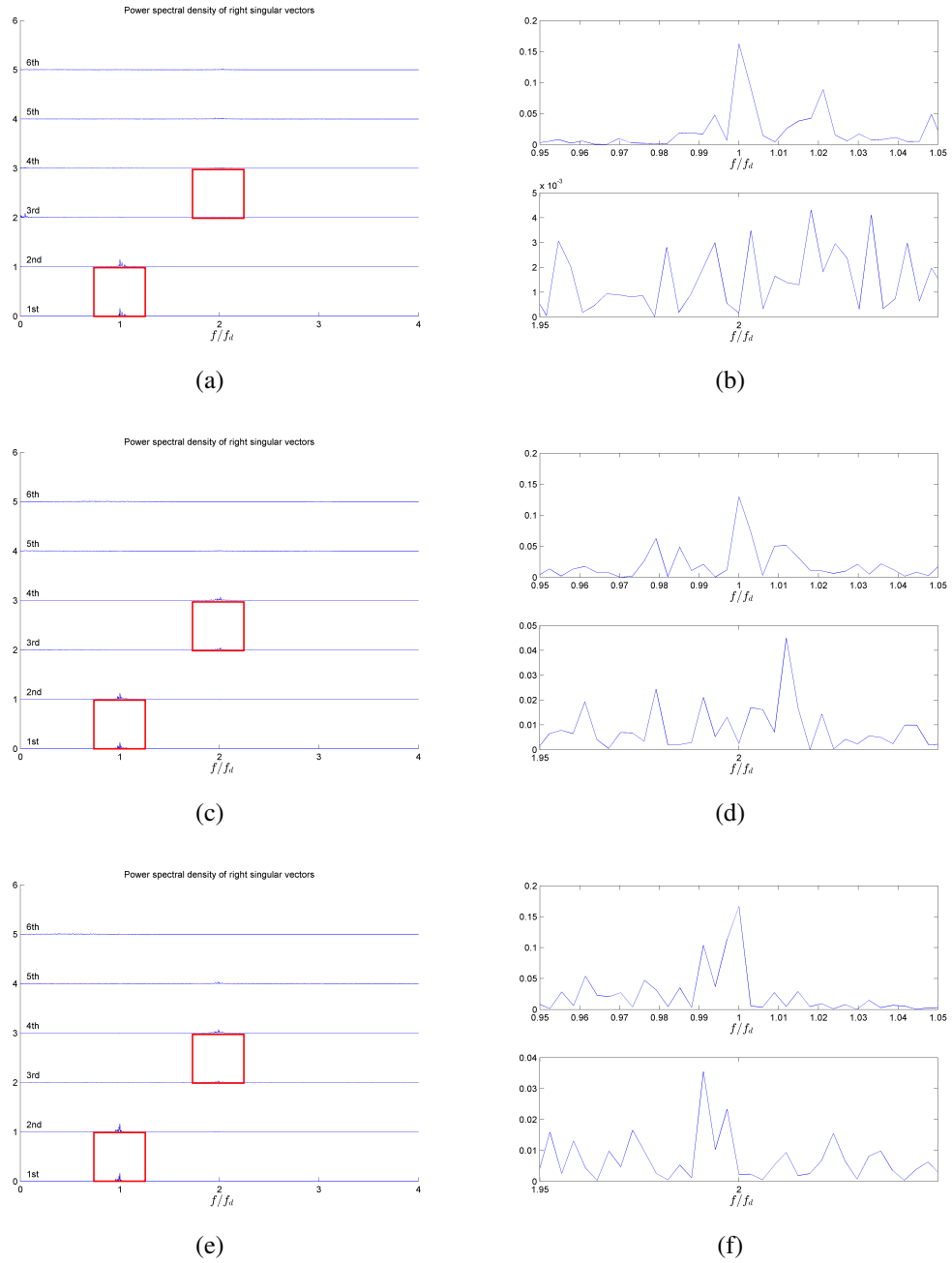


Figure 8.85: Power spectral densities of the first four right singular vectors (a), (c), (e), and the enlarged images of the power spectral densities of the first (top) and the third (bottom) right singular vectors (b), (d), (f), $\text{Re}[40\ 100]\text{k}$, $H_g = 50$ mm; FOV 1: (a) and (b), FOV 2: (c) and (d), and FOV 3: (e) and (f). Red squares on (a), (c), and (e) show the areas where (b), (d), and (f) are taken, respectively.

BIBLIOGRAPHY

- [1] A. K. M. F. Hussain, “Coherent structures - reality and myth,” *Phys. Fluids*, vol. 26, no. 10, p. 2816, 1983.
- [2] M. M. Bernitsas, K. Raghavan, Y. Ben-Simon, and E. M. H. Garcia, “VIVACE (vortex induced vibration aquatic clean energy): A new concept in generation of clean and renewable energy from fluid flow,” *J. Offshore Mech. Arct. Eng. Asme*, vol. 130, no. 4, pp. –, 2008.
- [3] R. Sonnenberger, K. Graichen, and P. Erk, “Fourier averaging: a phase-averaging method for periodic flow,” *Exp. Fluids*, vol. 28, no. 3, pp. 217–224, 2000.
- [4] J. L. Lumley, “The structure of inhomogeneous turbulent flows,” *Atmospheric turbulence and radio wave propagation*, vol. 790, pp. 166–178, 1967.
- [5] ———, “The state of turbulence research,” *Advances in Turbulence*, pp. 1–10, 1989.
- [6] K. Pearson, “On lines and planes of closest fit to systems of point in space,” *Philosophical Magazine*, vol. 2, no. 11, pp. 559–572, 1901.
- [7] L. Meyer and K. Rehme, “Large-Scale Turbulence Phenomena in Compound Rectangular Channels,” *Exp. Therm. Fluid Sci.*, vol. 8, no. 4, pp. 286–304, 1994.
- [8] R. Parker and M. C. Welsh, “Effects of sound on flow separation from blunt flat plates,” *Int. J. Heat Fluid Flow*, vol. 4, no. 2, pp. 113–127, 1983.
- [9] G. Berkooz, P. Holmes, and J. Lumley, “The Proper Orthogonal Decomposition in the Analysis of Turbulent Flows,” *Ann. Rev. Fluid Mech.*, vol. 25, no. 1971, pp. 539–575, 1993.
- [10] I. Jolliffe, *Principal Component Analysis*. Elsevier B.V., 1986.
- [11] A. Chatterjee, “An introduction to the proper orthogonal decomposition,” *Computational Science*, vol. 78, no. 7, 2000.

CHAPTER 9

Estimation of the Mixing Coefficients Based on Particle Image Velocimetry data

9.1 Introduction

In §7, we estimated the time-averaged mixing rate, represented by the ratio between the volume transfer flow rate and the nominal inlet flow rate, based on the fluorescein dye concentration. While mixing estimation based on the dye concentration gives us valuable information of total mixing rate, it does not provide what is causing the mixing, for example, whether the driving force of the mixing is the steady flow or the unsteady flow. In this chapter, we will re-estimate the mixing coefficients using the data based on the singular value decomposition (SVD) of the velocity field obtained by the Particle Image Velocimetry (PIV) shown in §8. To use SVD, we first assume that the mixing can be linearly decomposed. By checking each singular mode, we identify how each singular mode contribute to the mass transfer between Channel A and B. Then, we calculate the global mixing coefficient of each singular mode that contribute to the global mixing, and add them together to have the total mixing coefficient. Due to the gap areas where PIV data is not available, we provide some rough approximation methods to fill the missing flow information based on the characteristics of the coherent modes. §9.2 explains how to compute the mixing coefficients for steady and unsteady flows separately, and §9.3 shows comparisons between the mixing coefficient obtained by the dye concentration and the SVD based predictions.

9.2 Method to estimate the mixing coefficients from the SVD data

Following the classification of the turbulence flow described in §8, we divide the gap mixing mechanism into three categories: steady mixing, coherent mixing, and local turbulent mixing. Steady mixing is the mass transfer induced by the mean flow velocity. If there is no velocity fluctuation, the liquid flows from higher flow velocity channel to lower flow velocity channel with constant flow rate. As a consequence, the steady mixing appears as a one-sided mass transfer. Coherent mixing is the global mixing (mass transfer between two channels) driven by periodic, large coherent turbulence structures consisted of multiple vortices. Unlike steady mixing, coherent mixing changes direction of flow each time, so the mixing can happen both way regardless of the flow velocity of each channel. Local turbulent mixing is a mixing induced by non-periodic turbulence. The local turbulent does not contribute the global mass transfer directly as it forms relatively smaller mixing structure. However, it helps the global mixing by agitating the flow entered into the gap, makes the mixing more evenly spread, without breaking the large coherent structure. We assume that mixing can be linearly decomposed and then superimposed so that we can utilize the SVD data to compute the mixing coefficients.

$$f_A = f_A^{(s)} + f_A^{(c)}, \quad (9.1)$$

$$f_B = f_B^{(s)} + f_B^{(c)}, \quad (9.2)$$

where $f_A^{(s)}$ is the steady mixing coefficient, and $f_A^{(c)}$ is the coherent mixing coefficient. There is no local turbulence mixing coefficient as it does not directly cause the global mixing.

Not all coherent modes contribute to the global mixing. For example, we can see Fig. 9.1 and 9.2 which are the third and fourth singular modes of the flow $\text{Re}[100 \ 100]k$, $H_g = 50$. The streamlines form a symmetric structure with the transverse velocity at the center line being zero. In this case, there is no flow crossing the center line, i.e., it does not cause the global mixing by itself. In general, if a spatial singular vector is divided by a set of nodal lines with transverse velocity being zero, mixing cannot occur, unless more than two modes are combined. For the sake of global mixing computation, we choose the first two modes, which correspond to the first harmonic modes, as coherent structures, and the rest are considered as local turbulences which are not directly involved in the global mixing.

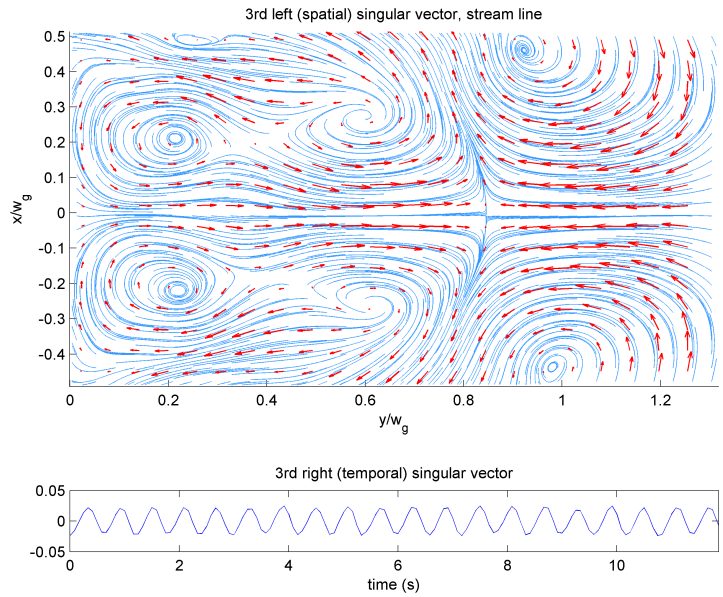


Figure 9.1: Singular vectors of the third mode, $\text{Re}[100\ 100]k$, $H_g = 50$ mm, FOV 1. Note that the formation of the nodal line at the center of the gap, so there is no flow crossing the center line of the gap.

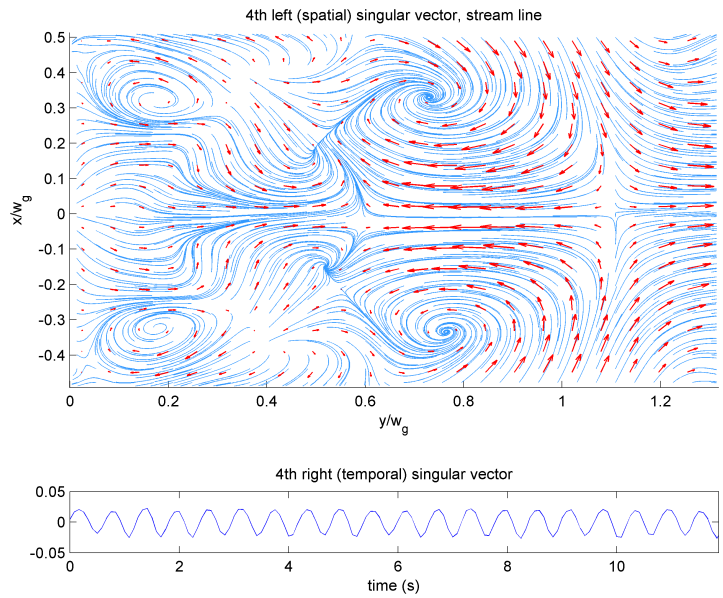


Figure 9.2: Singular vectors of the fourth mode, $\text{Re}[100\ 100]k$, $H_g = 50$ mm, FOV 1. Note that the formation of the nodal line at the center of the gap, so there is no flow crossing the center line of the gap.

9.2.1 Steady mixing

Let u , v , w denote the flow velocity in the transverse, the vertical, and the depth direction, respectively, as shown in Fig. 8.1. We assume the flow in the gap is two-dimensional, i.e., there is no flow in the depth direction and the 2D velocity field of u and v is identical along the depth of the gap. We consider the entire gap as a control volume. Because there is no flow from top and bottom of the gap, we only need to consider the transverse flow from side edges. Let \bar{F}_A and \bar{F}_B be the total steady volume flow rates at the side edges of the gap adjacent to Channel A and Channel B, respectively.

$$\bar{F}_A = H_g \int_0^{L_g} \bar{u}(y, W_g/2) dy, \quad (9.3)$$

$$\bar{F}_B = H_g \int_0^{L_g} \bar{u}(y, -W_g/2) dy, \quad (9.4)$$

where \bar{u} is the time-averaged transverse velocity, H_g is the gap height, L_g is the gap vertical length, W_g is the gap width. (Note: x and y are the local coordinates with the origin at the center bottom of the gap, while f_A and f_B are the mixing coefficients.)

We need to discretize Eqn. (9.3) and (9.4) and write them as functions of velocity fields obtained at three FOVs. Unfortunately, those three FOVs do not cover the entire gap, so we need to estimate the flow in the missing FOV based on the data from the available FOVs. By inspecting the time-average velocity fields shown in §8.6, we can see that most of the transverse flow at the edges of the gap occurs at the start (inflow) and the end (outflow) of the gap, and the flow rapidly converges to the vertical flow around the middle of the gap. Thus, instead of weighting the integrated flow rate of each FOV evenly, we can say that the flow around the missing FOV is similar to the flow at the middle of the gap. To do this, we introduce a factor β as follows:

$$\beta_p = \begin{cases} 1 & \text{if } p = 1 \text{ or } 3, \\ 2.114 & \text{if } p = 2, \end{cases} \quad (9.5)$$

where the factor 2.114 at the FOV 2 is obtained from the ratio between the total area of FOV 2 plus missing FOVs and the area of FOV 2. After discretization, the corrected flow

rates including the entire area of the gap are given by:

$$\bar{F}_A = H_g \sum_{p=1}^3 \left(\beta_p \sum_{i=1}^{N_y} \bar{u}^{(p)}(i, 1) \Delta y \right), \quad (9.6)$$

$$\bar{F}_B = H_g \sum_{p=1}^3 \left(\beta_p \sum_{i=1}^{N_y} \bar{u}^{(p)}(i, N_x) \Delta y \right), \quad (9.7)$$

where p is the FOV index, i is the y index, N_y and N_x are the total number of pixels in y axis and x axis, respectively. $\bar{u}^{(p)}(i, j)$ is the time-average of the transverse velocity u at (i, j) location in FOV p .

The mass conservation in a control volume (entire gap) requires $\bar{F}_A = \bar{F}_B$. The actual PIV data does not satisfy the mass conservation exactly (tilted, uncentered camera location), so we use the average value of \bar{F}_A and \bar{F}_B to compute the steady mixing coefficients. Finally, we can calculate the steady mixing coefficients as

$$\begin{cases} f_A^{(s)} = \frac{|\bar{F}_A + \bar{F}_B|}{2\bar{V}_{Ai}}, f_B^{(s)} = 0 & \text{if } \bar{F}_A + \bar{F}_B < 0 \\ f_A^{(s)} = 0, f_B^{(s)} = \frac{|\bar{F}_A + \bar{F}_B|}{2\bar{V}_{Bi}} & \text{if } \bar{F}_A + \bar{F}_B \geq 0, \end{cases} \quad (9.8)$$

where \bar{V}_{Ai} and \bar{V}_{Bi} are the nominal volume flow rates at the inlet of Channel A and Channel B, respectively.

9.2.2 Coherent mixing

Coherent mixing is induced by the periodic fluctuation of the velocity field. Unlike the steady mixing, we need to track the transition of the flow on both direction, Channel A to Channel B and Channel B to Channel A. Thus, instead of integrating the transverse flow rate entirely, we split the inlet and outlet flows first, and then integrate them separately. We

first calculate the absolute volume flow rate after the time average velocity is subtracted.

$$F_{A_{in}}(t) = -H_g \int_0^{L_g} \min \{u'(y, W_g/2, t), 0\} dy, \quad (9.9)$$

$$F_{A_{out}}(t) = H_g \int_0^{L_g} \max \{u'(y, W_g/2, t), 0\} dy, \quad (9.10)$$

$$F_{B_{in}}(t) = H_g \int_0^{L_g} \max \{u'(y, -W_g/2, t), 0\} dy, \quad (9.11)$$

$$F_{B_{out}}(t) = -H_g \int_0^{L_g} \min \{u'(y, -W_g/2, t), 0\} dy. \quad (9.12)$$

Discretizing Eqn. (9.9) to (9.12) for p^{th} FOV yields

$$F_{A_{in}}^{(p)}(k) = -H_g \sum_{i=1}^{N_y} \min \{u^{(p)}(i, 1, k), 0\} \Delta y, \quad (9.13)$$

$$F_{A_{out}}^{(p)}(k) = H_g \sum_{i=1}^{N_y} \max \{u^{(p)}(i, 1, k), 0\} \Delta y, \quad (9.14)$$

$$F_{B_{in}}^{(p)}(k) = H_g \sum_{i=1}^{N_y} \max \{u^{(p)}(i, N_x, k), 0\} \Delta y, \quad (9.15)$$

$$F_{B_{out}}^{(p)}(k) = -H_g \sum_{i=1}^{N_y} \min \{u^{(p)}(i, N_x, k), 0\} \Delta y. \quad (9.16)$$

For the coherent mixing, we need two additional assumptions:

1. There is no re-entry of flow to the gap, i.e., $F_{A_{in}}^{(p)}(t)$ is purely from the source of Channel A, and $F_{B_{in}}^{(p)}(t)$ is purely from Channel B.
2. For each FOV, fluids from two different source are fully mixed by the local turbulence so that the composition of outgoing flow is uniformly proportional to the incoming flow rates of Channel A and Channel B.

Then, we can derive the flow rate between Channel A and B as follows:

$$F_{A \rightarrow B}^{(p)}(k) = \left(\frac{F_{A_{in}}^{(p)}(k)}{F_{A_{in}}^{(p)}(k) + F_{B_{in}}^{(p)}(k)} \right) F_{B_{out}}^{(p)}(k), \quad (9.17)$$

$$F_{B \rightarrow A}^{(p)}(k) = \left(\frac{F_{B_{in}}^{(p)}(k)}{F_{A_{in}}^{(p)}(k) + F_{B_{in}}^{(p)}(k)} \right) F_{A_{out}}^{(p)}(k). \quad (9.18)$$

Note that Eqn. (9.17) and (9.18) are time dependent. To compress the data into a

quantitatively comparable measures, we need to get the time-averaged flow exchanging rate. SVD decomposes the data into spatial (left singular vectors) and temporal (right singular vectors) bases along with their intensity (singular values). Using the SVD results, we can easily find the time-averaged coherent mixing.

Denote $l^{(p,s)}$, $\sigma^{(p,s)}$, and $r^{(p,s)}$ as the left singular vector, the singular value, and the right singular vector of the s^{th} mode taken at p^{th} FOV. Let $\hat{u}_{(i,j)}^{(p,s)}$ be the reordered matrix of the transverse velocity part of the p^{th} FOV, s^{th} left singular vector.

$$\hat{u}_{(i,j)}^{(p,s)} = l^{(p,s)}(N_x N_y + N_x i + j), \quad (9.19)$$

where $l^{(p,s)}$ is the s^{th} left singular vector of p^{th} FOV data. Then, we can rewrite the centered transverse flow velocity of s^{th} mode $u_{(i,j,k)}^{(p,s)}$ in terms of $\hat{u}_{(i,j)}^{(p,s)}$, singular value, and right singular vector.

$$u_{(i,j,k)}^{(p,s)} = \hat{u}_{(i,j)}^{(p,s)} \sigma^{(p,s)} r_{(k)}^{(p,s)}. \quad (9.20)$$

In the right hand side of Eqn. 9.20, only $r_{(k)}^{(p,s)}$ depends on time, so we can find the time-average of $u_{(i,j,k)}^{(p,s)}$ by just time-averaging $r_{(k)}^{(p,s)}$. However, we only get zero if we just taking time-average of $r_{(k)}^{(p,s)}$. Instead, we need to split $r_{(k)}^{(p,s)}$ into positive and negative phase.

$$\{r^{(p,s)}\}^+ = \frac{\sum_{k=1}^{N_k} \max\{r_{(k)}^{(p,s)}, 0\}}{N_k}, \quad (9.21)$$

$$\{r^{(p,s)}\}^- = -\frac{\sum_{k=1}^{N_k} \min\{r_{(k)}^{(p,s)}, 0\}}{N_k}, \quad (9.22)$$

where N_k is the total number of the temporal sampling points. One can see that $\{r^{(p,s)}\}^+ = \{r^{(p,s)}\}^-$ as time-average of $r_{(k)}^{(p,s)}$ is zero. Using Eqn. (9.21), we can obtain the absolute valued time-average flow rate as

$$\{F_{A_{\text{in}}}^{(p,s)}\}^+ = -H_g \left(\sum_{i=1}^{N_i} \min\{\hat{u}_{(i,1)}^{(p,s)}, 0\} \Delta y \right) \sigma^{(p,s)} \{r_{(k)}^{(p,s)}\}^+, \quad (9.23)$$

$$\{F_{A_{\text{out}}}^{(p,s)}\}^+ = H_g \left(\sum_{i=1}^{N_i} \max\{\hat{u}_{(i,1)}^{(p,s)}, 0\} \Delta y \right) \sigma^{(p,s)} \{r_{(k)}^{(p,s)}\}^+, \quad (9.24)$$

$$\{F_{B_{\text{in}}}^{(p,s)}\}^+ = H_g \left(\sum_{i=1}^{N_i} \max\{\hat{u}_{(i,N_x)}^{(p,s)}, 0\} \Delta y \right) \sigma^{(p,s)} \{r_{(k)}^{(p,s)}\}^+, \quad (9.25)$$

$$\{F_{B_{\text{out}}}^{(p,s)}\}^+ = -H_g \left(\sum_{i=1}^{N_i} \min\{\hat{u}_{(i,N_x)}^{(p,s)}, 0\} \Delta y \right) \sigma^{(p,s)} \{r_{(k)}^{(p,s)}\}^+, \quad (9.26)$$

$$\{F_{A_{in}}^{(p,s)}\}^- = \{F_{A_{out}}^{(p,s)}\}^+, \quad (9.27)$$

$$\{F_{A_{out}}^{(p,s)}\}^- = \{F_{A_{in}}^{(p,s)}\}^+, \quad (9.28)$$

$$\{F_{B_{in}}^{(p,s)}\}^- = \{F_{B_{out}}^{(p,s)}\}^+, \quad (9.29)$$

$$\{F_{B_{out}}^{(p,s)}\}^- = \{F_{B_{in}}^{(p,s)}\}^+. \quad (9.30)$$

Applying Eqn. (9.23)-(9.30) to Eqn. (9.17) and (9.18), we can compute the time-averaged coherent mixing coefficients as follows:

$$f_A^{(c)} = \sum_{p=1}^3 \sum_{s=1}^{N_s} \frac{\{F_{A \rightarrow B}^{(p)}\}^+ + \{F_{B \rightarrow A}^{(p)}\}^-}{\bar{V}_{A_i}}, \quad (9.31)$$

$$f_B^{(c)} = \sum_{p=1}^3 \sum_{s=1}^{N_s} \frac{\{F_{B \rightarrow A}^{(p)}\}^+ + \{F_{A \rightarrow B}^{(p)}\}^-}{\bar{V}_{B_i}}, \quad (9.32)$$

$$\{F_{A \rightarrow B}^{(p)}\}^* = \left(\frac{\{F_{A_{in}}^{(p)}\}^*}{\{F_{A_{in}}^{(p)}\}^* + \{F_{B_{in}}^{(p)}\}^*} \right) \{F_{B_{out}}^{(p)}\}^*, \quad (9.33)$$

$$\{F_{B \rightarrow A}^{(p)}\}^* = \left(\frac{\{F_{B_{in}}^{(p)}\}^*}{\{F_{A_{in}}^{(p)}\}^* + \{F_{B_{in}}^{(p)}\}^*} \right) \{F_{A_{out}}^{(p)}\}^*, \quad (9.34)$$

where * denotes the sign, + or -.

9.2.3 Correction for the vertical edge flows with unknown sources

So far, we have only considered flows in/out from side edges of the gap, which is sufficient if we have entire flow field of the gap. However, our FOVs do not cover the entire gap, and there are flows in/out from the top and bottom of each FOV, which we do not know the source of the flow as described in Fig. 9.3. While those unknown source flow is only 5 to 15% of the total absolute volume flow rate for balanced flow conditions, it amounts to 30% of the total absolute volume flow rate when the flow is unbalanced. Predicting those source of vertical flows is essential to estimate the coherent mixing.

Because the coherent structures are periodic, and the vorticity of the flow field must be conserved, we can assume that there is a counter-rotating vortex outside the FOV that compensates the imbalance between in/out flow rates in the FOV. Also, centers of vortices form along the shear boundary in unbalanced flow, so we can assume that the strength of the incoming (outgoing) flow induced by the counter vortex is proportional to the outgoing (incoming) flow induced by the original vortex in the FOV. The total amount of the flow rate due to the counter vortices must match with the imbalance of the flow rate obtained by integrating the flow rate on both side of the gap to satisfy the mass conservation. Let

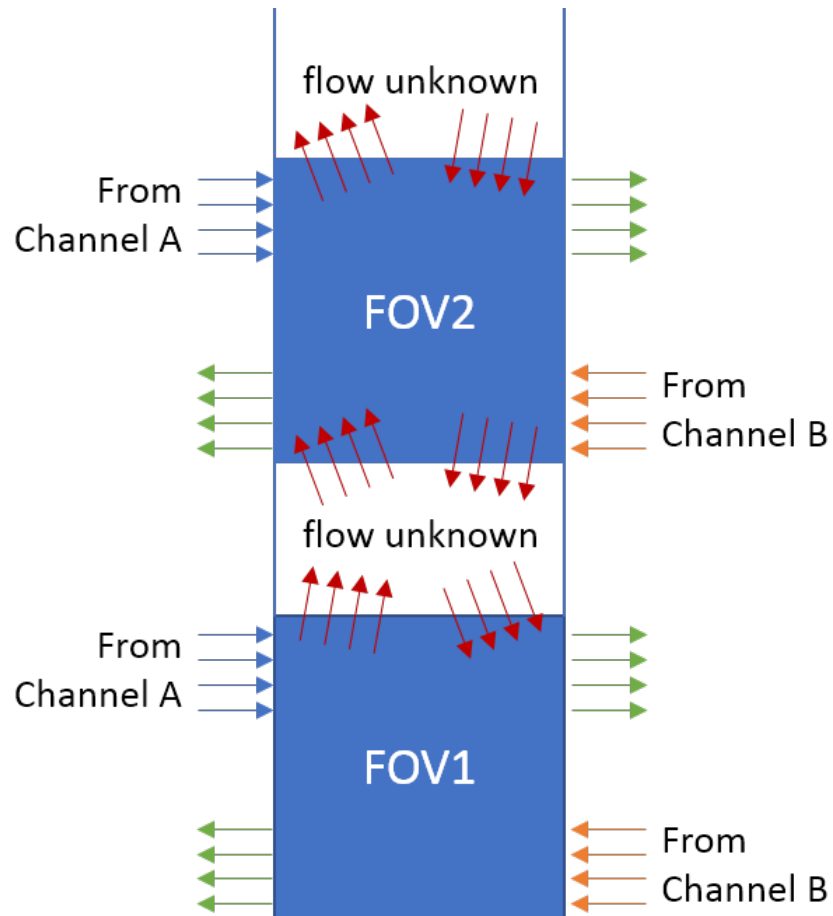


Figure 9.3: Explanation of the unknown source of incoming flow to FOV 1 and 2. Because the flow field around the area between FOV 1 and 2 is unknown, we cannot estimate the source of the inlet flow marked in red arrows, and therefore the total inlet flow rate of Channel A and B to the gap.

$F_{\text{in}}^{(p,s)}$ and $F_{\text{out}}^{(p,s)}$ be the total flow rates of the s^{th} singular mode incoming/outgoing from both sides of the gap in p^{th} FOV, respectively.

$$F_{\text{in}}^{(p,s)} = F_{A_{\text{in}}}^{(p,s)} + F_{B_{\text{in}}}^{(p,s)}, \quad (9.35)$$

$$F_{\text{out}}^{(p,s)} = F_{A_{\text{out}}}^{(p,s)} + F_{B_{\text{out}}}^{(p,s)}, \quad (9.36)$$

Then, we calculate the corrected flow rates as follows:

$$\text{If } F_{\text{in}}^{(p,s)} > F_{\text{out}}^{(p,s)} \quad \left\{ \begin{array}{l} \tilde{F}_{A_{\text{in}}}^{(p,s)} = F_{A_{\text{in}}}^{(p,s)} \\ \tilde{F}_{B_{\text{in}}}^{(p,s)} = F_{B_{\text{in}}}^{(p,s)} \\ \tilde{F}_{A_{\text{out}}}^{(p,s)} = F_{A_{\text{out}}}^{(p,s)} + \left(F_{\text{in}}^{(p,s)} - F_{\text{out}}^{(p,s)} \right) \frac{F_{A_{\text{in}}}^{(p,s)}}{F_{\text{in}}^{(p,s)}} \\ \tilde{F}_{B_{\text{out}}}^{(p,s)} = F_{B_{\text{out}}}^{(p,s)} + \left(F_{\text{in}}^{(p,s)} - F_{\text{out}}^{(p,s)} \right) \frac{F_{B_{\text{in}}}^{(p,s)}}{F_{\text{in}}^{(p,s)}} \end{array} \right. , \quad (9.37)$$

$$\text{otherwise} \quad \left\{ \begin{array}{l} \tilde{F}_{A_{\text{in}}}^{(p,s)} = F_{A_{\text{in}}}^{(p,s)} + \left(F_{\text{out}}^{(p,s)} - F_{\text{in}}^{(p,s)} \right) \frac{F_{A_{\text{out}}}^{(p,s)}}{F_{\text{out}}^{(p,s)}} \\ \tilde{F}_{B_{\text{in}}}^{(p,s)} = F_{B_{\text{in}}}^{(p,s)} + \left(F_{\text{out}}^{(p,s)} - F_{\text{in}}^{(p,s)} \right) \frac{F_{B_{\text{out}}}^{(p,s)}}{F_{\text{out}}^{(p,s)}} \\ \tilde{F}_{A_{\text{out}}}^{(p,s)} = F_{A_{\text{out}}}^{(p,s)} \\ \tilde{F}_{B_{\text{out}}}^{(p,s)} = F_{B_{\text{out}}}^{(p,s)} \end{array} \right. . \quad (9.38)$$

Then, we substitute the original flow rates in Eqn. (9.33)-(9.34) with the corrected flow rates in Eqn (9.37)-(9.38).

Since we brought in the in/out flow from the outside of the FOV to satisfy the mass conservation, there will be overlapped flows between FOVs. With the overlapped flows, the mixing rate can be double counted. To avoid it, we multiply the corrected flow rate by a factor α_p so that we only consider the flow in/out for each FOV in terms of average values.

$$\alpha_p = \frac{\min \left\{ F_{\text{in}}^{(p,s)}, F_{\text{out}}^{(p,s)} \right\}}{\max \left\{ F_{\text{in}}^{(p,s)}, F_{\text{out}}^{(p,s)} \right\}}. \quad (9.39)$$

Then, we also need to add the effect of missing FOVs. The coherent mixing pattern is quite different from the steady mixing. While most of the steady mixing happens at the start and the end of the gap, the coherent mixing occurs every part of the gap. So, we evenly divide the areas of missing FOVs, assume the flow pattern in each missing FOV follows the flow pattern of the nearest known FOV. As a result, we multiply the following area ratio to the

flow rate of each FOV:

$$\gamma_p = \begin{cases} 1.275 & \text{if } p=1, \\ 1.537 & \text{if } p=2, \\ 1.328 & \text{if } p=3. \end{cases} \quad (9.40)$$

Finally, we compute the corrected coherent mixing coefficients as follows:

$$f_A^{(c)} = \sum_{p=1}^3 \left(\alpha_p \gamma_p \sum_{s=1}^{N_s} \frac{\{F_{A \rightarrow B}^{(p)}\}^+ + \{F_{B \rightarrow A}^{(p)}\}^-}{\bar{V}_{Ai}} \right), \quad (9.41)$$

$$f_B^{(c)} = \sum_{p=1}^3 \left(\alpha_p \gamma_p \sum_{s=1}^{N_s} \frac{\{F_{B \rightarrow A}^{(p)}\}^+ + \{F_{A \rightarrow B}^{(p)}\}^-}{\bar{V}_{Bi}} \right). \quad (9.42)$$

9.3 Results

Total of 5 flow conditions with 3 different gap sizes are investigated. Same as §7.2, flow conditions are defined by the Reynolds numbers of the nominal inlet flows, defined based on the hydraulic diameter of the channels, i.e.,

$$\text{Re}_{A \text{ (or B)}} = \frac{\bar{V}_{A \text{ (or B)}} D_h}{\nu} \quad (9.43)$$

where $\bar{V}_{A \text{ (or Channel B)}}$ is the nominal inlet velocity of Channel A (or Channel B), D_h is the hydraulic diameter of Channel A and Channel B, ν is the kinematic viscosity of water. For balanced flow, the following 2 cases of flow conditions are considered: Re[100 100]k and Re[40 40]k. For unbalanced flow, the following 3 cases of flow conditions are considered: Re[80 100]k, Re[60 100]k, and Re[40 100]k. For each inlet condition, total of 3 gap heights are considered: 10, 20, and 50 mm.

9.3.1 Balanced flows

Fig. 9.4 and 9.5, and Table 9.1 and 9.2 show the comparisons between mixing coefficients obtained by the dye concentration and the SVD for Re[100 100]k and Re[40 40]k, respectively. The coherent structures of balanced flows are always symmetrical, and the effect of the vertical flow is low, which makes the source of the incoming flow is mostly accounted for. We can also verify the linear dependency between the mixing and the gap for the balanced flow from the mixing coefficient estimation results.

For both Re[100 100]k and Re[40 40]k, the mixing coefficients based on SVD follow the same pattern of the mixing coefficients based on the dye concentration, but

overestimated by 15 to 220%. Because we estimate the mixing coefficient based on the 2D data taken at the midplane of the gap, flow velocity near the wall can be much lower than the midplane velocity due to the flow separations. Eventually, it is natural that the actual mixing coefficient is much less than the estimated value based on the 2D PIV data.

Also, we can see that the maximum error occurs at $Re[40\ 40]k$, $H_g = 10\text{mm}$. As the gap height decreases, the effect of the flow separation in the gap becomes relatively significant. Thus, smaller gap has more deviation than the larger gap. As mentioned in §7.2, turbulence delays the flow separation, so we expect that the sudden contraction at the entrance of the gap affects the velocity field more on the laminar flow $Re[40\ 40]k$ than the turbulent flow $Re[100\ 100]k$.

Fig. 9.6 and 9.7 show the time-averaged velocity fields for $Re[100\ 100]k$ at FOV 1 with the gap height 50 mm and 10 mm, respectively. Because the transverse flow velocity u is anti-symmetric everywhere with the nodal line at the center, there is no steady mixing in this case. This applies to $Re[40\ 40]k$ as well. There was a small amount of flow moving from Channel B to A with mixing coefficient f_B less than 0.01. This could be due to the misalignment of the camera, or the flowmeter error.

Fig. 9.8 and 9.9 show the 8 largest singular values of the velocity fields for $Re[100\ 100]k$ at FOV 1 with the gap height 50 mm and 10 mm, respectively, and Fig. 9.10 and 9.11 show the first singular vectors of the same flow condition. In the first singular vectors, $H_g = 10\text{mm}$ has slightly smaller structures than $H_g = 50\text{mm}$, and its singular values are also slightly less than $H_g = 50\text{mm}$. However, the patterns of streamlines are almost identical in general, which makes the mixing flow rate linearly dependent on the gap height (if the pressure drop at the entrance of the gap is not considered).

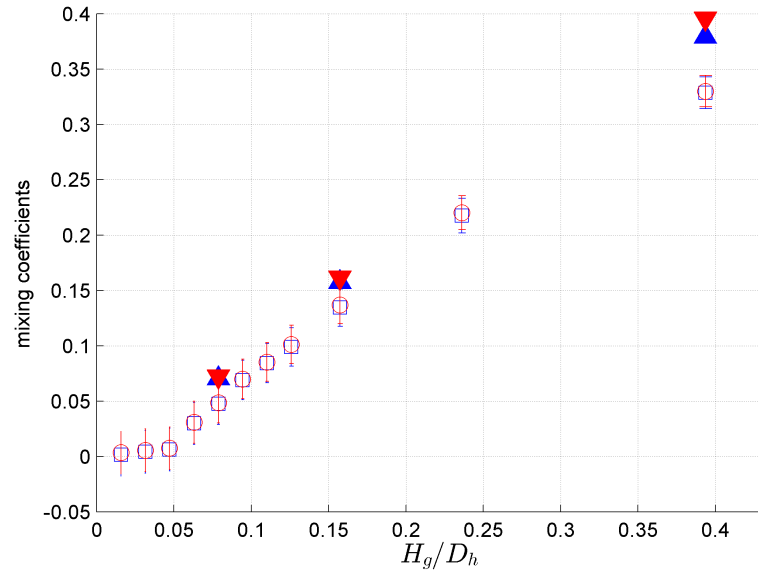


Figure 9.4: Comparison of mixing coefficients f_A and f_B of Re[100, 100]k based on the dye concentration and the SVD of the PIV data; blue square: f_A based on the dye concentration, red circle: f_B based on the dye concentration, blue triangle: f_A based on the SVD of the PIV data, red circle: f_B based on the SVD of the PIV data.

Table 9.1: Summary of the mixing coefficients of Re[100 100]k

H_g	mixing Coeff.	steady	coherent				total	dye	$\frac{\text{total}}{\text{dye}}$
			FOV 1	FOV 2	FOV 3	$\sum_p \gamma_p(\cdot)_p$			
10	f_A	0.000	0.025	0.020	0.007	0.071	0.071	0.047	1.49
	f_B	0.002	0.025	0.020	0.007	0.071	0.072	0.049	1.49
20	f_A	0.000	0.056	0.041	0.017	0.157	0.157	0.134	1.17
	f_B	0.004	0.056	0.041	0.017	0.157	0.162	0.137	1.18
50	f_A	0.000	0.116	0.104	0.054	0.379	0.379	0.329	1.15
	f_B	0.017	0.116	0.104	0.054	0.379	0.396	0.330	1.20

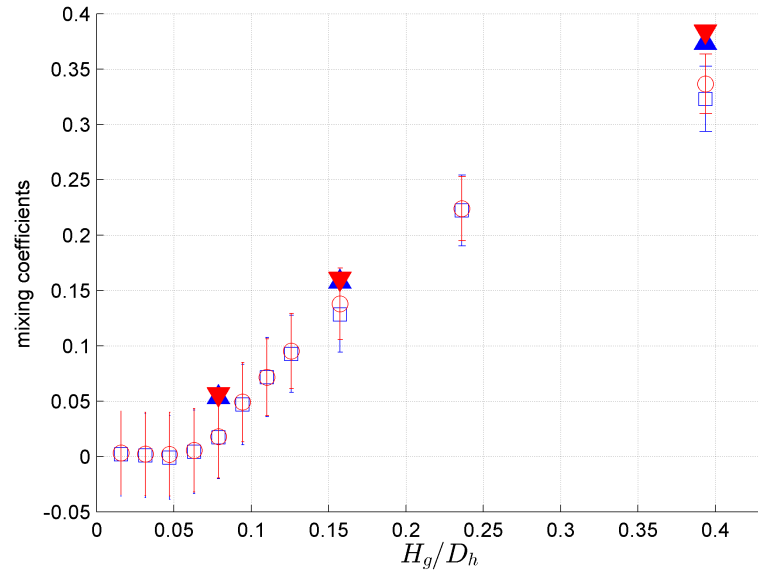


Figure 9.5: Comparison of mixing coefficients f_A and f_B of Re[40, 40]k based on the dye concentration and the SVD of the PIV data; blue square: f_A based on the dye concentration, red circle: f_B based on the dye concentration, blue triangle: f_A based on the SVD of the PIV data, red circle: f_B based on the SVD of the PIV data.

Table 9.2: Summary of the mixing coefficients of Re[40 40]k

H_g	mixing Coeff.	steady	coherent				total	dye	total dye
			FOV 1	FOV 2	FOV 3	$\sum_p \gamma_p(\cdot)_p$			
10	f_A	0.000	0.015	0.016	0.007	0.054	0.054	0.017	3.15
	f_B	0.003	0.015	0.016	0.007	0.054	0.056	0.018	3.18
20	f_A	0.000	0.052	0.043	0.019	0.158	0.158	0.128	1.23
	f_B	0.003	0.052	0.043	0.019	0.158	0.161	0.138	1.17
50	f_A	0.000	0.108	0.106	0.055	0.373	0.373	0.323	1.16
	f_B	0.011	0.108	0.106	0.055	0.373	0.384	0.337	1.14

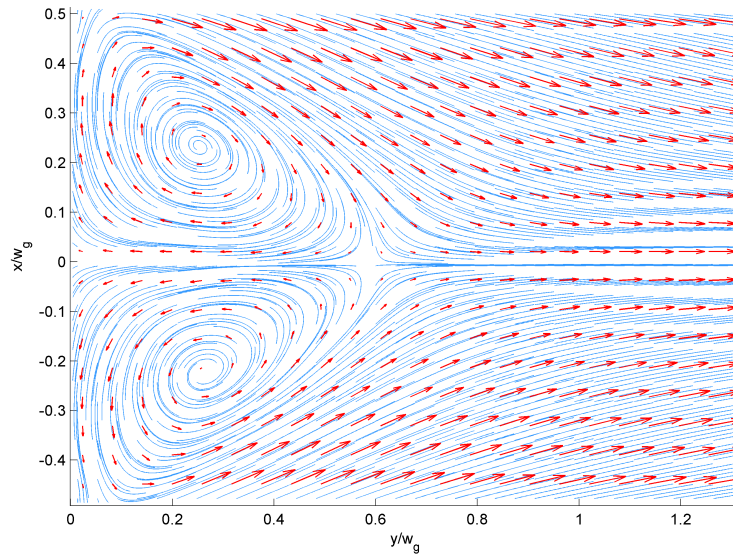


Figure 9.6: Mean velocity of the velocity field data for the flow condition $Re[100, 100]k$, gap size 50 mm, FOV 1

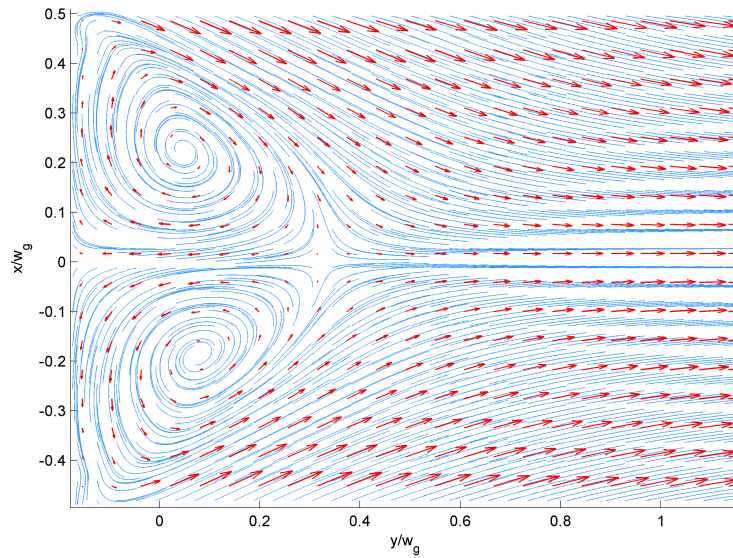


Figure 9.7: Mean velocity of the velocity field data for the flow condition $Re[100, 100]k$, gap size 10 mm, FOV 1

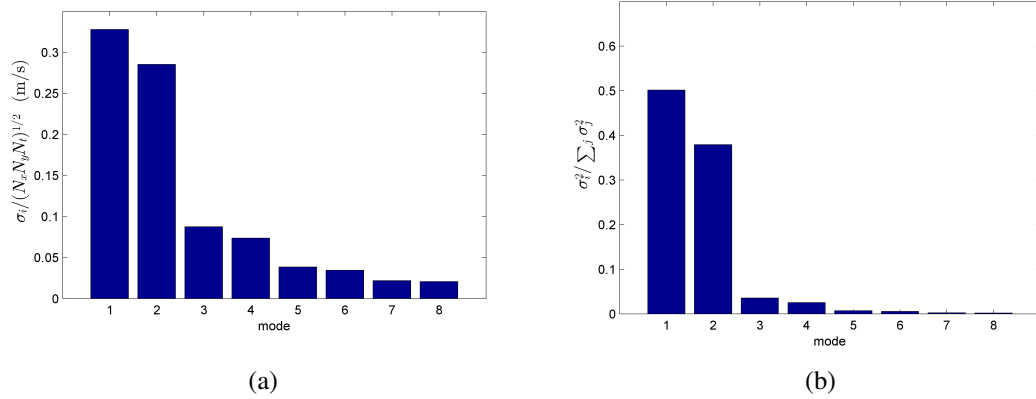


Figure 9.8: 8 largest singular values of the velocity field data for the flow condition $Re[100, 100]k$, gap size 50 mm, FOV 1; (a) singular values normalized by $\sqrt{N_x N_y N_z}$ equivalent to the RMSE of the velocity field in each mode, (b) ratio of energy in each mode to the total fluctuation energy.

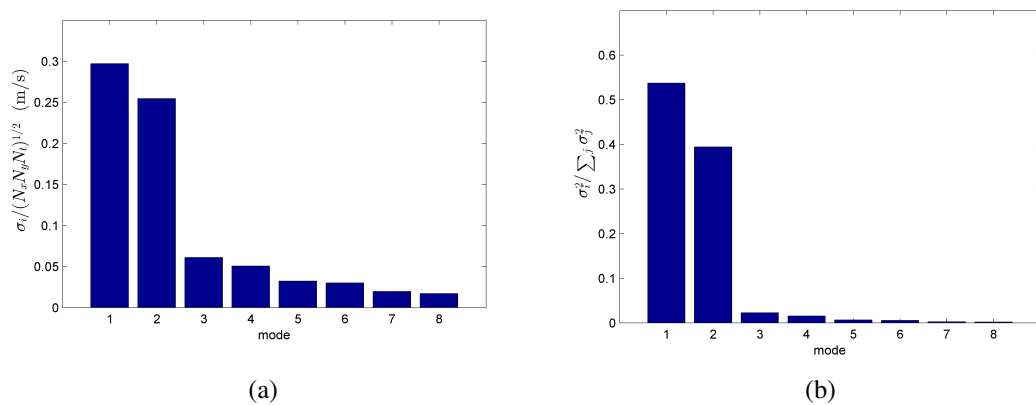


Figure 9.9: 8 largest singular values of the velocity field data for the flow condition $Re[100, 100]k$, gap size 10 mm, FOV 1; (a) singular values normalized by $\sqrt{N_x N_y N_z}$ equivalent to the RMSE of the velocity field in each mode, (b) ratio of energy in each mode to the total fluctuation energy.

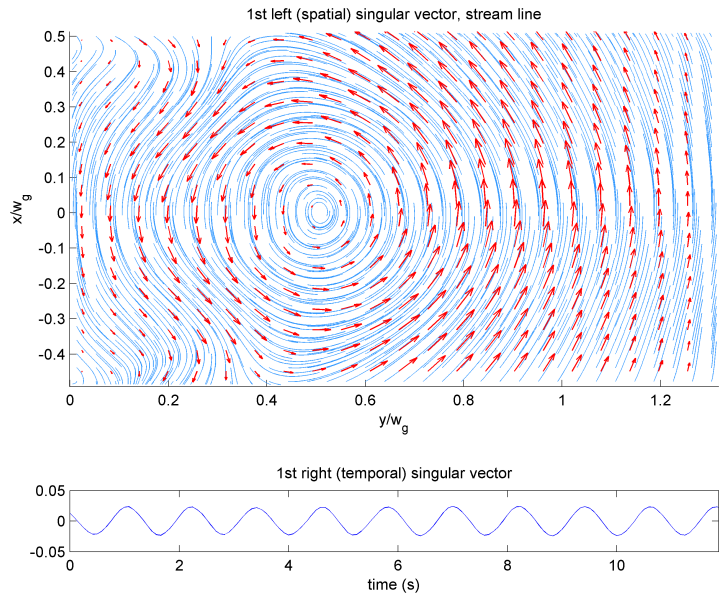


Figure 9.10: First left and right singular vectors of the velocity field data for the flow condition $Re[100, 100]k$, gap size 50 mm, FOV 1

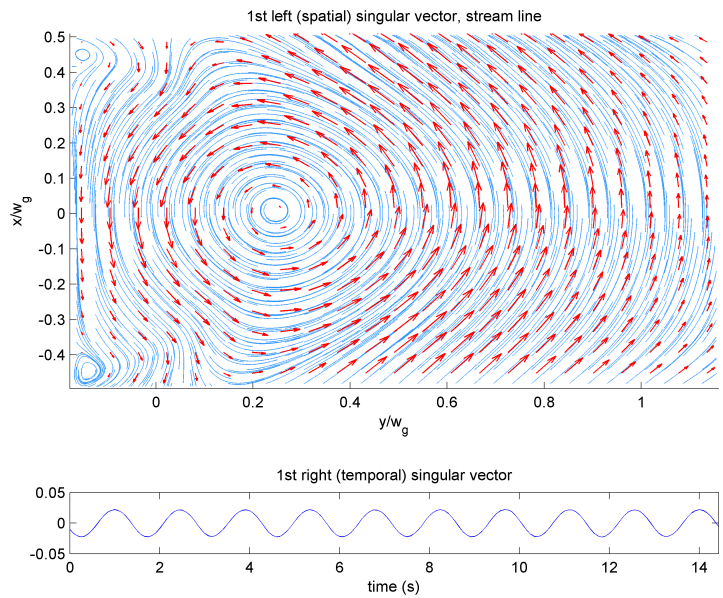


Figure 9.11: First left and right singular vectors of the velocity field data for the flow condition $Re[100, 100]k$, gap size 10 mm, FOV 1

9.3.2 Unbalanced flows

Fig. 9.15, 9.16, and 9.17 show the time-averaged velocity fields for $Re[40\ 100]k$ at FOV 1 with the gap height 50 mm, 20 mm and 10 mm, respectively. Time-averaged velocity fields are not symmetric any more, as the flow condition is unbalanced. A shear layer is formed at the Channel B side starting from the bottom of the gap. By observing this shear layer, we can qualitatively estimate how much flow is moving from Channel B to Channel A in 2D. As the gap height is being narrower, the shear layer formed at Channel B is getting thicker, which means more 2D flow from Channel B is moving towards Channel A. This effect offsets the decrement of the gap height in 3D, makes the steady mixing coefficient almost independent of the gap height.

Table 9.3, 9.4, and 9.5 show the steady, coherent, and total mixing coefficients for $Re[80\ 100]k$, $Re[60\ 100]k$, and $Re[40\ 100]k$, respectively. We can see that the steady mixing coefficients are almost, but not entirely, constant in each flow condition regardless of the gap thickness. The estimated steady mixing coefficients are mostly 5 to 10% higher than the ideal steady mixing coefficients shown in Eqn. (7.20).

Fig. 9.18 and 9.20 show the first singular vectors of the velocity fields for $Re[40\ 100]k$ at FOV 1 with the gap height 50 mm, 20 mm, and 10 mm, respectively. As the gap height is becoming narrower, the coherent structure represented by streamlines in the first singular vector is getting more chaotic as one can see in Fig. 9.18, 9.19, and 9.20. Even worse, the temporal singular vectors shown in the same figures are not the form of single frequency wave, which illustrates that the coherent structure may not be even periodic any more.

Fig. 9.12, 9.13, and 9.14 show the comparisons between the mixing coefficients based on the dye concentration and the SVD of the PIV data, for $Re[80\ 100]k$, $Re[60\ 100]k$, and $Re[40\ 100]k$, respectively. The mixing coefficient estimation results based on the dye concentration and the SVD do not match very well in the unbalanced flow as they were in the balanced flow. This could be due to the rough approximation of the unknown source from the top and bottom of the FOV as described in §9.2.3. Also, the assumption that the mixing can be linearly decomposed is not entirely true. There can be interactions between the steady mixing and the coherent mixing. While it did not affect the result of balanced flows because there was little steady mixing, the steady mixing and coherent mixing coexist in unbalanced flow. The flow conditions with the gap height 20 mm have typically the most discrepancy between mixing coefficients obtained by two different method. We could not explain why $H_g = 20\text{mm}$ has the biggest error at this point, but we suspect that $H_g = 20\text{mm}$ is where the interaction between the steady mixing and the coherent mixing is stronger than the other conditions.

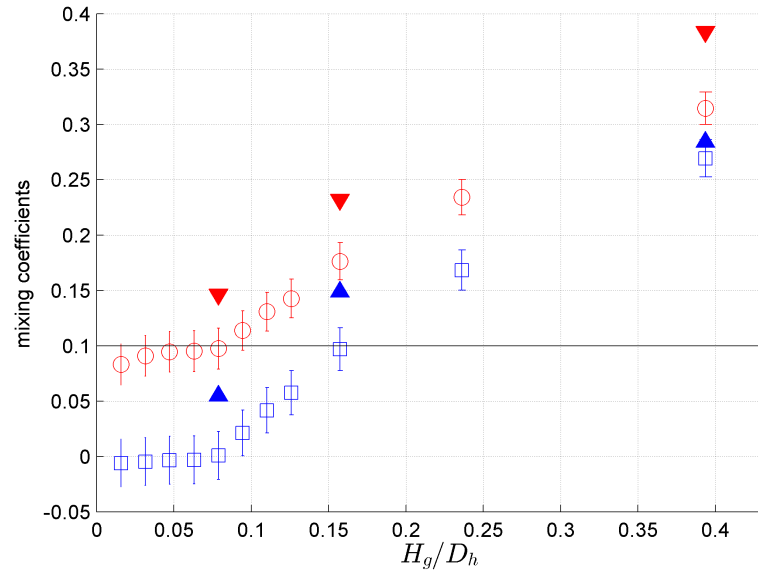


Figure 9.12: Comparison of mixing coefficients f_A and f_B of Re[80, 100]k based on the dye concentration and the SVD of the PIV data; blue square: f_A based on the dye concentration, red circle: f_B based on the dye concentration, blue triangle: f_A based on the SVD of the PIV data, red circle: f_B based on the SVD of the PIV data.

Table 9.3: Summary of the mixing coefficients of Re[80 100]k

H_g	mixing Coeff.	steady	coherent				total	dye	$\frac{\text{total}}{\text{dye}}$
			FOV 1	FOV 2	FOV 3	$\sum_p \gamma_p(\cdot)_p$			
10	f_A	0.000	0.024	0.014	0.003	0.055	0.055	0.001	68.38
	f_B	0.103	0.019	0.011	0.002	0.044	0.146	0.097	1.50
20	f_A	0.000	0.045	0.044	0.018	0.149	0.149	0.097	1.54
	f_B	0.113	0.036	0.035	0.015	0.119	0.232	0.176	1.32
50	f_A	0.000	0.062	0.095	0.045	0.284	0.284	0.269	1.06
	f_B	0.157	0.049	0.076	0.036	0.227	0.384	0.315	1.22

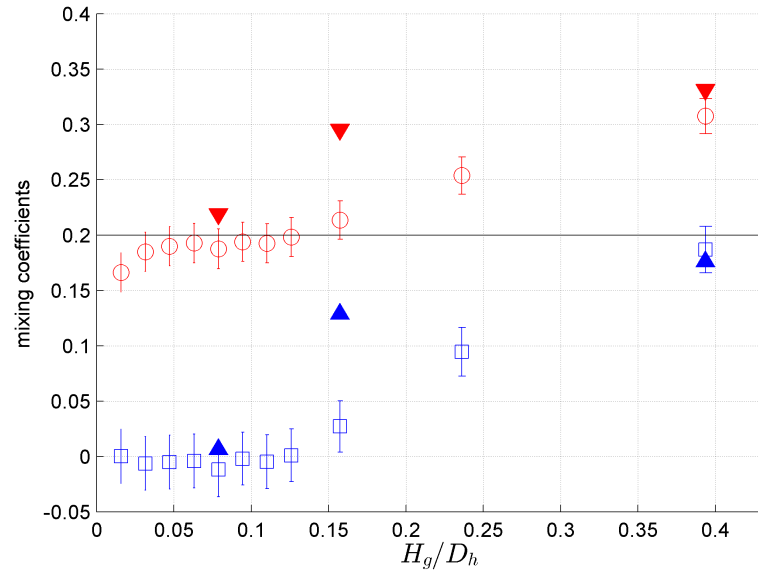


Figure 9.13: Comparison of mixing coefficients f_A and f_B of Re[60, 100]k based on the dye concentration and the SVD of the PIV data; blue square: f_A based on the dye concentration, red circle: f_B based on the dye concentration, blue triangle: f_A based on the SVD of the PIV data, red circle: f_B based on the SVD of the PIV data.

Table 9.4: Summary of the mixing coefficients of Re[60 100]k

H_g	mixing Coeff.	steady	coherent				total	dye	total dye
			FOV 1	FOV 2	FOV 3	$\sum_p \gamma_p(\cdot)_p$			
10	f_A	0.000	0.002	0.003	0.000	0.007	0.007	-0.012	-0.55
	f_B	0.216	0.001	0.002	0.000	0.004	0.220	0.188	1.17
20	f_A	0.000	0.023	0.051	0.017	0.129	0.129	0.027	4.78
	f_B	0.218	0.014	0.030	0.010	0.077	0.296	0.214	1.39
50	f_A	0.000	0.017	0.060	0.047	0.176	0.176	0.187	0.94
	f_B	0.226	0.010	0.036	0.028	0.106	0.332	0.307	1.08

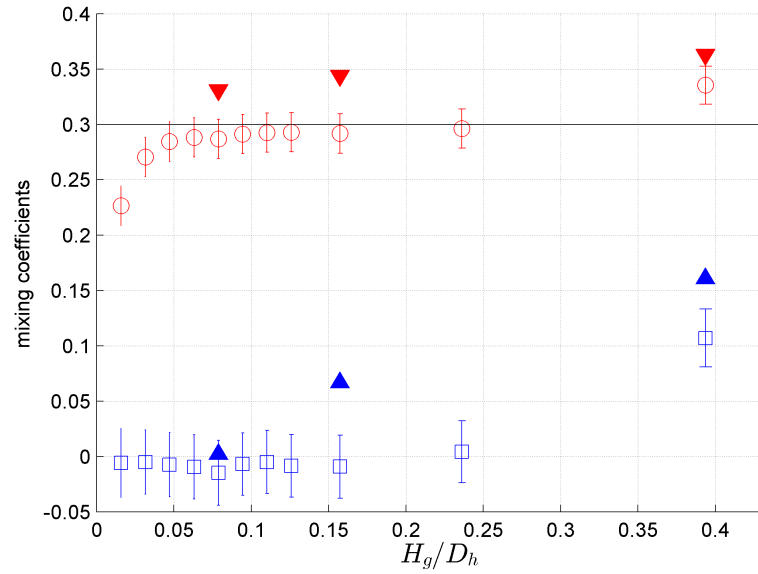


Figure 9.14: Comparison of mixing coefficients f_A and f_B of Re[40, 100]k based on the dye concentration and the SVD of the PIV data; blue square: f_A based on the dye concentration, red circle: f_B based on the dye concentration, blue triangle: f_A based on the SVD of the PIV data, red circle: f_B based on the SVD of the PIV data.

Table 9.5: Summary of the mixing coefficients of Re[40 100]k

H_g	mixing Coeff.	steady	coherent				total	dye	$\frac{\text{total}}{\text{dye}}$
			FOV 1	FOV 2	FOV 3	$\sum_p \gamma_p(\cdot)_p$			
10	f_A	0.000	0.000	0.001	0.001	0.002	0.002	-0.015	-0.15
	f_B	0.331	0.000	0.000	0.000	0.001	0.332	0.287	1.16
20	f_A	0.000	0.003	0.036	0.006	0.067	0.067	0.009	7.18
	f_B	0.318	0.001	0.014	0.002	0.027	0.345	0.292	1.18
50	f_A	0.000	0.004	0.047	0.063	0.161	0.161	0.107	1.51
	f_B	0.299	0.002	0.019	0.025	0.064	0.363	0.335	1.08

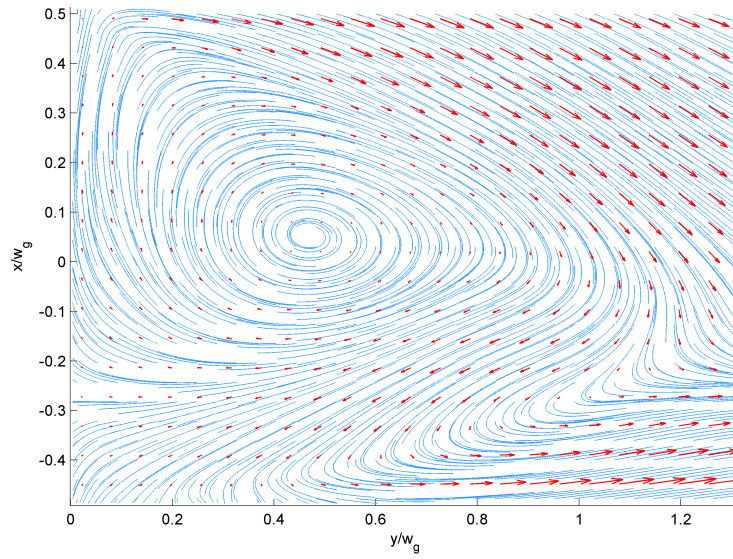


Figure 9.15: Mean velocity of the velocity field data for the flow condition $Re[40, 100]k$, gap size 50 mm, FOV 1

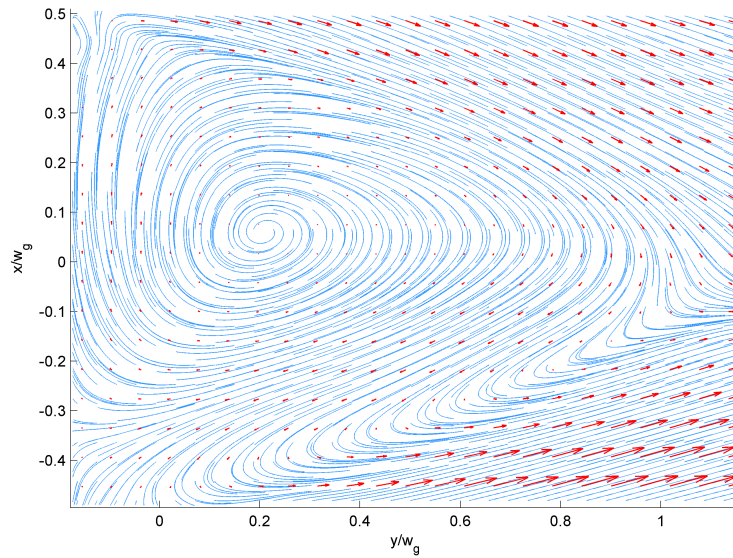


Figure 9.16: Mean velocity of the velocity field data for the flow condition $Re[40, 100]k$, gap size 20 mm, FOV 1

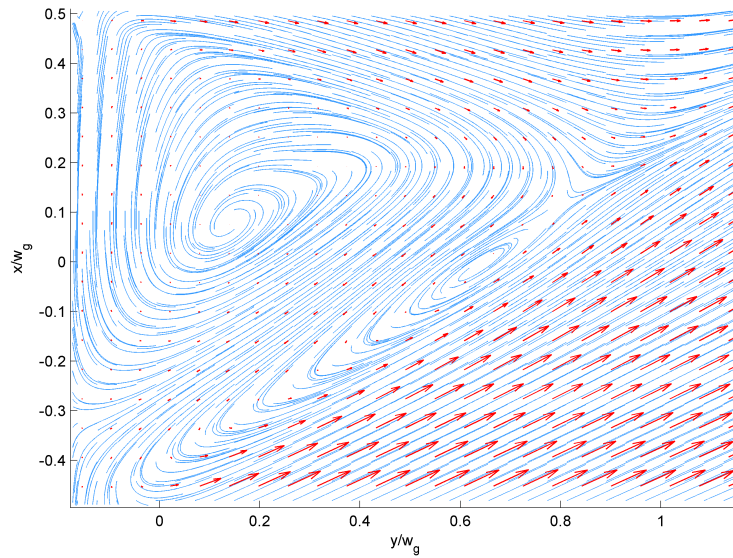


Figure 9.17: Mean velocity of the velocity field data for the flow condition $Re[40, 100]k$, gap size 10 mm, FOV 1

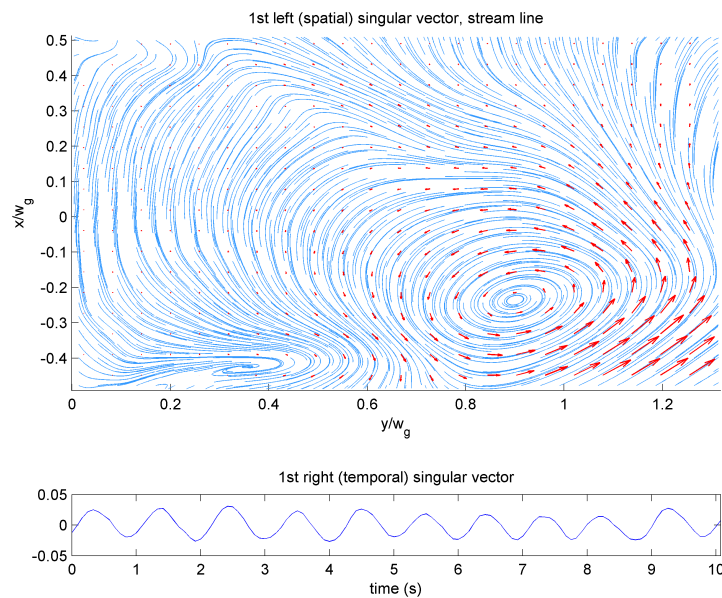


Figure 9.18: First left and right singular vectors of the velocity field data for the flow condition $Re[40, 100]k$, gap size 50 mm, FOV 1

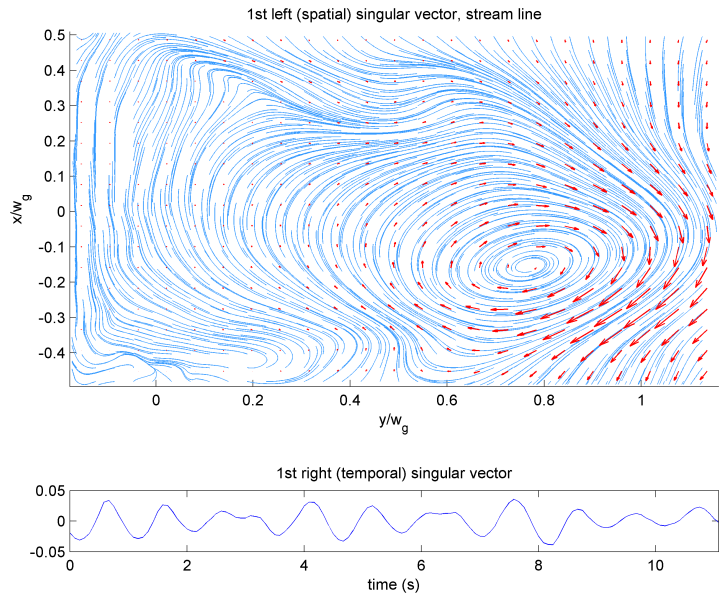


Figure 9.19: First left and right singular vectors of the velocity field data for the flow condition $Re[40, 100]k$, gap size 20 mm, FOV 1

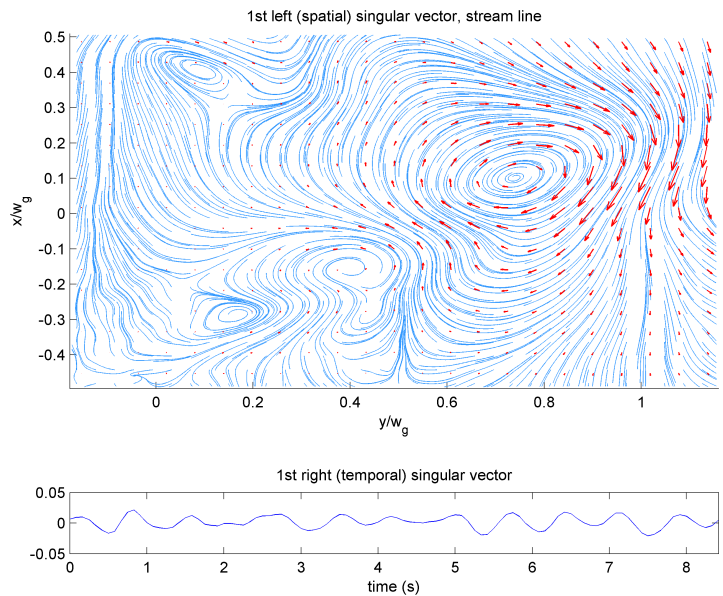


Figure 9.20: First left and right singular vectors of the velocity field data for the flow condition $Re[40, 100]k$, gap size 20 mm, FOV 1

CHAPTER 10

Conclusions: An Experimental Study of Inter-channel Mixing

We investigated the time-averaged mixing from the measurement data of inlet/outlet flow rates and dye concentrations. We calculated the total amount of mixing based on the conservation of mass of water and of the dye in a fixed control volume of each channel. To quantify the mixing, we defined a mixing coefficient as a fraction of inlet flow transferred from one channel to the other.

For the balanced flows, the mixing coefficients show weak dependency on the Reynolds number when the gap ratio H_g/D_h is larger than 0.06. However, when $H_g/D_h < 0.06$, mixing coefficients show some deviation depending on the Reynolds number, and there is no recognizable mixing in any flow velocity when $H_g/D_h < 0.025$. The deviation of mixing under $H_g/D_h < 0.06$ is within the range of the 68% confidence interval. The trend shows that the mixing coefficients are somewhat affected by changes in Reynolds number when the gap height is small. We expect that this is may be due to the fact that the gap width is on the order of the boundary layer thickness of the incoming flow. Also, it may be that effect of flow separation (3D flow) at the entry of the gap may be more important for smaller gap widths. Flow separation can cause blockage at the entrance of the cross-channel. This is a 3D effect, but our measurements in the gap were 2D. Therefore, either numerical simulations or experimental data will be required to examine the effect of the boundary layer in the gap to the mixing.

For unbalanced flow, the effect of the coherent structures on the mixing decreases, as the mixing due to pressure difference across the gap dominate. And, as the flow velocity difference between two channel increases, we see weaker large-scale structures. POD (SVD) results confirmed that the energy of the coherent structures, represented by the singular values, decreases when the flow velocities of two channels are different. Also, the right (temporal) singular values become less periodic as the velocity difference between two channels grows.

We estimated the mixing coefficients using the data based on the POD (SVD) of the velocity field obtained by the PIV. The POD (SVD) based mixing estimation provided us more insights into how both the steady (time averaged) and the unsteady components of the flow affect the overall mixing. While we made several important assumptions in order to compute the mixing, the computed mixing closely matched the experimentally determined values. The result of the estimated mixing coefficients based on SVD follow the same pattern of the mixing coefficients based on the dye concentration, but consistently overestimated in most of the case.

Because we estimated the mixing using a 2D PIV measurement of the 3D gap flow, it is natural that the actual mixing is less than estimated, due to the effect of the separation near the entrance and exit of the gap.

The mixing coefficient estimation results based on the dye concentration and the SVD match less well for the unbalanced flows compared to the balanced cases. There is not enough evidence to explain why this happened, but this could be due to the rough approximation of the unknown source from the top and bottom of the FOV.

In the future, a better estimate of mixing can be developed from three-dimensional measurements within the gap. Also, we can measure overlapping and additional FOVs within the gap. Also, we would repeat the PIV measurements for a wider range of flow conditions and gap widths. Finally, it would be of interest to repeat these experiments with a wider range of inlet Turbulent Boundary Layer (TBL) thicknesses in the incoming channel flow (possibly as a result of intentional TBL thickening). In this way we could further examine how changes in the TBL thickness alter the mixing when the TBL thickness is much smaller than or much larger than both the gap width and length.

APPENDIX A

CAD drawings for Phantom 0, 1, and 2

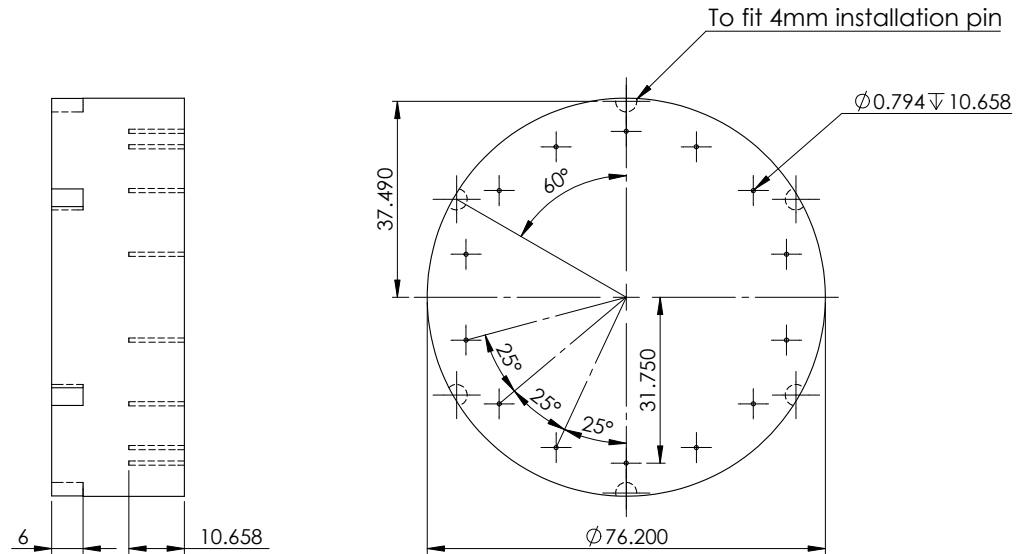


Figure A.1: 2D CAD drawing of Phantom 0. All dimensions are in millimeters, unless otherwise specified.

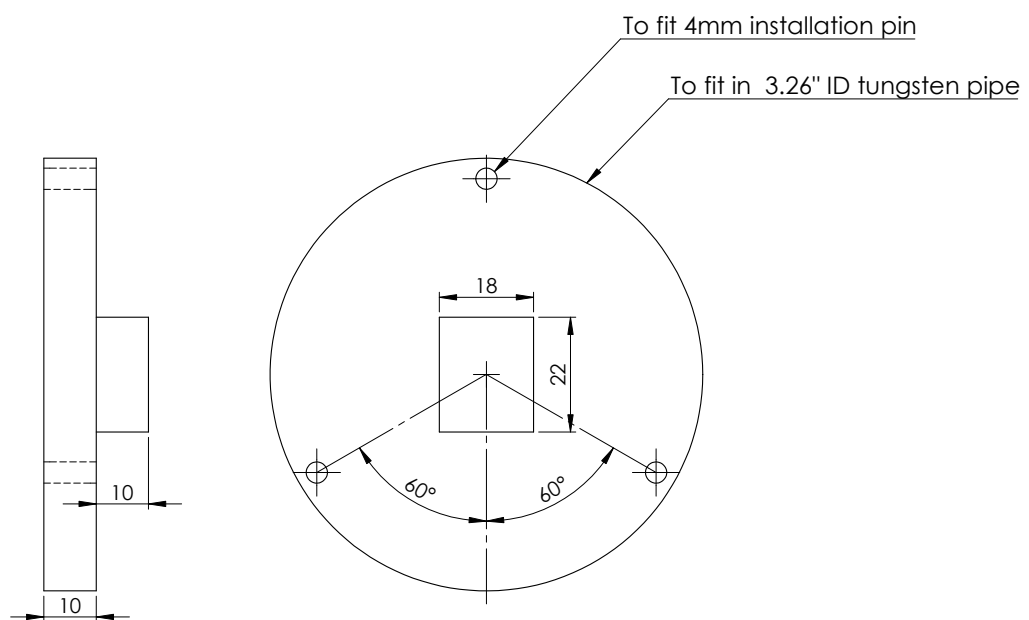


Figure A.2: 2D CAD drawing of Phantom 1. All dimensions are in millimeters, unless otherwise specified.

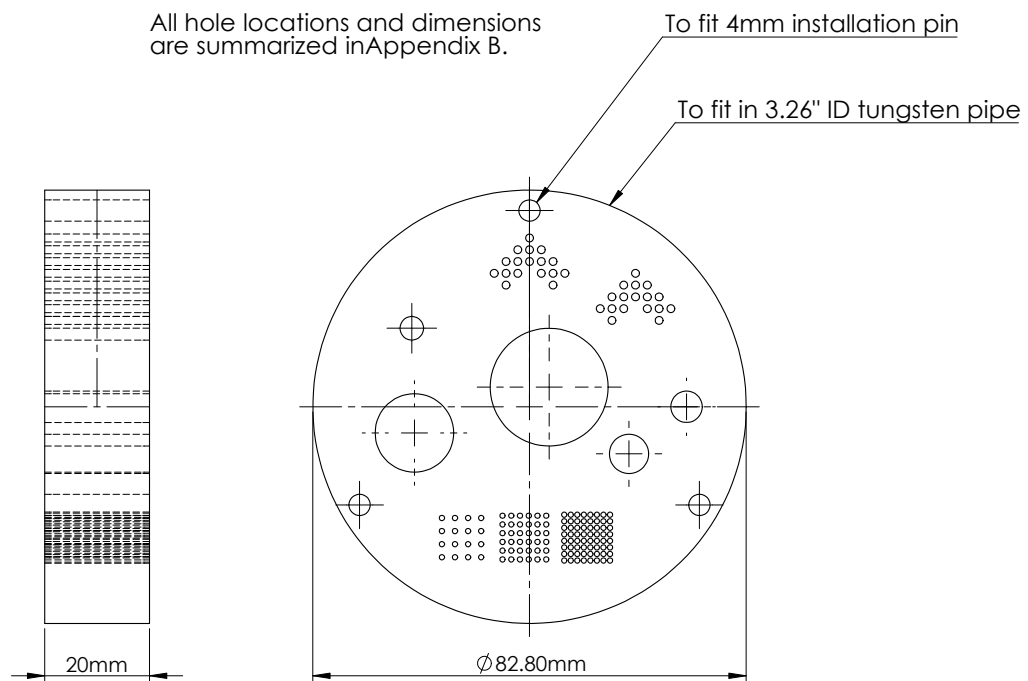


Figure A.3: 2D CAD drawing of Phantom 2. All dimensions are in millimeters, unless otherwise specified. All hole locations and sizes are specified in Appendix B.

APPENDIX B

Geometry of the phantom 2

This supplementary material contains the geometry of the phantom 2 used for simulations and experiments in §2.3 and §4. The synthetic phantom is filled with water-equivalent material except for the objects shown in Table B.1.

Table B.1: Object geometry and materials of the phantom 2 used in §2.3 and §4

Titanium pipe outer radius: 4.445 cm (1.75 inch)
Titanium pipe inner radius: 4.140 cm (1.63 inch)

Center x(cm)	Center y(cm)	Radius(cm)	Material
0.3750	0.3750	1.1250	air
-2.2000	-0.5000	0.7500	air
1.9000	-0.9000	0.3750	air
3.0000	0.0000	0.3000	air
-2.2500	1.5000	0.2250	air
0.0000	2.7750	0.0750	air
0.0000	3.0000	0.0750	air
0.2250	3.0000	0.0750	air
-0.2250	3.0000	0.0750	air
0.0000	3.2250	0.0750	air

Continued on next page

Table B.1 – *Continued from previous page*

Center x(cm)	Center y(cm)	Radius(cm)	Material
0.2250	2.7750	0.0750	air
0.4500	2.3250	0.0750	air
0.4500	2.5500	0.0750	air
0.6750	2.5500	0.0750	air
0.2250	2.5500	0.0750	air
0.4500	2.7750	0.0750	air
-0.2250	2.7750	0.0750	air
-0.4500	2.3250	0.0750	air
-0.4500	2.5500	0.0750	air
-0.6750	2.5500	0.0750	air
-0.2250	2.5500	0.0750	air
-0.4500	2.7750	0.0750	air
2.0250	2.1000	0.0750	air
2.0250	2.3250	0.0750	air
2.2500	2.3250	0.0750	air
1.8000	2.3250	0.0750	air
2.0250	2.5500	0.0750	air
2.2500	2.1000	0.0750	air
2.4750	1.6500	0.0750	air
2.4750	1.8750	0.0750	air
2.7000	1.8750	0.0750	air
2.2500	1.8750	0.0750	air
2.4750	2.1000	0.0750	air
1.8000	2.1000	0.0750	air
1.5750	1.6500	0.0750	air
1.5750	1.8750	0.0750	air
1.3500	1.8750	0.0750	air
1.8000	1.8750	0.0750	air
1.5750	2.1000	0.0750	air
-1.6750	-2.8750	0.0500	air

Continued on next page

Table B.1 – *Continued from previous page*

Center x(cm)	Center y(cm)	Radius(cm)	Material
-1.4250	-2.8750	0.0500	air
-1.1750	-2.8750	0.0500	air
-0.9250	-2.8750	0.0500	air
-1.6750	-2.6250	0.0500	air
-1.4250	-2.6250	0.0500	air
-1.1750	-2.6250	0.0500	air
-0.9250	-2.6250	0.0500	air
-1.6750	-2.3750	0.0500	air
-1.4250	-2.3750	0.0500	air
-1.1750	-2.3750	0.0500	air
-0.9250	-2.3750	0.0500	air
-1.6750	-2.1250	0.0500	air
-1.4250	-2.1250	0.0500	air
-1.1750	-2.1250	0.0500	air
-0.9250	-2.1250	0.0500	air
-0.5165	-2.9165	0.0500	air
-0.3495	-2.9165	0.0500	air
-0.1825	-2.9165	0.0500	air
-0.0155	-2.9165	0.0500	air
0.1515	-2.9165	0.0500	air
0.3185	-2.9165	0.0500	air
-0.5165	-2.7495	0.0500	air
-0.3495	-2.7495	0.0500	air
-0.1825	-2.7495	0.0500	air
-0.0155	-2.7495	0.0500	air
0.1515	-2.7495	0.0500	air
0.3185	-2.7495	0.0500	air
-0.5165	-2.5825	0.0500	air
-0.3495	-2.5825	0.0500	air
-0.1825	-2.5825	0.0500	air

Continued on next page

Table B.1 – *Continued from previous page*

Center x(cm)	Center y(cm)	Radius(cm)	Material
-0.0155	-2.5825	0.0500	air
0.1515	-2.5825	0.0500	air
0.3185	-2.5825	0.0500	air
-0.5165	-2.4155	0.0500	air
-0.3495	-2.4155	0.0500	air
-0.1825	-2.4155	0.0500	air
-0.0155	-2.4155	0.0500	air
0.1515	-2.4155	0.0500	air
0.3185	-2.4155	0.0500	air
-0.5165	-2.2485	0.0500	air
-0.3495	-2.2485	0.0500	air
-0.1825	-2.2485	0.0500	air
-0.0155	-2.2485	0.0500	air
0.1515	-2.2485	0.0500	air
0.3185	-2.2485	0.0500	air
-0.5165	-2.0815	0.0500	air
-0.3495	-2.0815	0.0500	air
-0.1825	-2.0815	0.0500	air
-0.0155	-2.0815	0.0500	air
0.1515	-2.0815	0.0500	air
0.3185	-2.0815	0.0500	air
0.6625	-2.9375	0.0500	air
0.7875	-2.9375	0.0500	air
0.9125	-2.9375	0.0500	air
1.0375	-2.9375	0.0500	air
1.1625	-2.9375	0.0500	air
1.2875	-2.9375	0.0500	air
1.4125	-2.9375	0.0500	air
1.5375	-2.9375	0.0500	air
0.6625	-2.8125	0.0500	air

Continued on next page

Table B.1 – *Continued from previous page*

Center x(cm)	Center y(cm)	Radius(cm)	Material
0.7875	-2.8125	0.0500	air
0.9125	-2.8125	0.0500	air
1.0375	-2.8125	0.0500	air
1.1625	-2.8125	0.0500	air
1.2875	-2.8125	0.0500	air
1.4125	-2.8125	0.0500	air
1.5375	-2.8125	0.0500	air
0.6625	-2.6875	0.0500	air
0.7875	-2.6875	0.0500	air
0.9125	-2.6875	0.0500	air
1.0375	-2.6875	0.0500	air
1.1625	-2.6875	0.0500	air
1.2875	-2.6875	0.0500	air
1.4125	-2.6875	0.0500	air
1.5375	-2.6875	0.0500	air
0.6625	-2.5625	0.0500	air
0.7875	-2.5625	0.0500	air
0.9125	-2.5625	0.0500	air
1.0375	-2.5625	0.0500	air
1.1625	-2.5625	0.0500	air
1.2875	-2.5625	0.0500	air
1.4125	-2.5625	0.0500	air
1.5375	-2.5625	0.0500	air
0.6625	-2.4375	0.0500	air
0.7875	-2.4375	0.0500	air
0.9125	-2.4375	0.0500	air
1.0375	-2.4375	0.0500	air
1.1625	-2.4375	0.0500	air
1.2875	-2.4375	0.0500	air
1.4125	-2.4375	0.0500	air

Continued on next page

Table B.1 – *Continued from previous page*

Center x(cm)	Center y(cm)	Radius(cm)	Material
1.5375	-2.4375	0.0500	air
0.6625	-2.3125	0.0500	air
0.7875	-2.3125	0.0500	air
0.9125	-2.3125	0.0500	air
1.0375	-2.3125	0.0500	air
1.1625	-2.3125	0.0500	air
1.2875	-2.3125	0.0500	air
1.4125	-2.3125	0.0500	air
1.5375	-2.3125	0.0500	air
0.6625	-2.1875	0.0500	air
0.7875	-2.1875	0.0500	air
0.9125	-2.1875	0.0500	air
1.0375	-2.1875	0.0500	air
1.1625	-2.1875	0.0500	air
1.2875	-2.1875	0.0500	air
1.4125	-2.1875	0.0500	air
1.5375	-2.1875	0.0500	air
0.6625	-2.0625	0.0500	air
0.7875	-2.0625	0.0500	air
0.9125	-2.0625	0.0500	air
1.0375	-2.0625	0.0500	air
1.1625	-2.0625	0.0500	air
1.2875	-2.0625	0.0500	air
1.4125	-2.0625	0.0500	air
1.5375	-2.0625	0.0500	air
0.0000	3.7500	0.2032	air
3.2476	-1.8750	0.2032	air
-3.2476	-1.8750	0.2032	air

APPENDIX C

Matlab codes for the singular value decomposition (SVD) and the estimation of the mixing coefficients based on SVD data

This supplementary material contains the Matlab codes for the singular value decomposition (SVD) of the particle image velocimetry data shown in §8, and the mixing coefficient estimation based on the SVD data shown in §9.

C.1 Matlab codes for singular vector decomposition

C.1.1 `batch_read_PA_SVD.m`

```
% BATCH_READ_PA_SVD
% Define set ID, then call vc7_read_vxx.m for each set to read vc7 data
  and process SVD.
% Written by Seongjin Yoon, University of Michigan, 2017

%% load folder paths
clear variables; cls;
ListOfFolderPaths_5b_SJ % folders for raw data path

% data overwriting
force_overwrite = false;
% false: do not overwrite data, load the existing processed data
% true : overwrite all Matlab-formatted raw & SVD data (choose it when
  there were changes in the code)

%% data set definition

% standard sets
```

```

% set ID      1   2   3   4   5           6   7   8   9  10           11  12  13
              14  15
set_FOV1 = [ 1,  6,  5,  2,  3,           89, 92, 93, 90, 91,           63, 66, 67,
             64, 65]'; % FOV 1 (lower window)
set_FOV2 = [12, 15, 16, 13, 14,           84, 87, 88, 85, 86,           68, 71, 72,
             69, 70]'; % FOV 2 (middle window)
set_FOV3 = [ 7, 10, 11,  8,  9,           78, 81, 83, 79, 80,           73, 76, 77,
             74, 75]'; % FOV 3 (upper window)

% extra sets that are not specified in the list
% because different lenses are used to acquire data, etc.
% set_extra = [ 0, 0,82;...
%              0,88, 0;...
%              93, 0, 0;...
%              96, 0, 0];
% FOV for extra runs: 82:FOV3, 88:FOV2, 93:FOV1, 96:FOV1

set = [set_FOV1, set_FOV2, set_FOV3];

% Reynolds numbers for each set ID
%          [ A,  B] x 1000
Re(1,1:2) = [100, 100]; % gap 50
Re(2,1:2) = [ 40, 100];
Re(3,1:2) = [ 40,  40];
Re(4,1:2) = [ 80, 100];
Re(5,1:2) = [ 60, 100];

Re(6,1:2) = [100, 100]; % gap 20
Re(7,1:2) = [ 40, 100];
Re(8,1:2) = [ 40,  40];
Re(9,1:2) = [ 80, 100];
Re(10,1:2) = [ 60, 100];

Re(11,1:2) = [100, 100]; % gap 10
Re(12,1:2) = [ 40, 100];
Re(13,1:2) = [ 40,  40];
Re(14,1:2) = [ 80, 100];
Re(15,1:2) = [ 60, 100];

% gap thickness for each set ID
h_gap(11:15) = 10;
h_gap(6:10) = 20;
h_gap(1:5) = 50;

```

```

%% retrieve data

N_folder = length(Folder);
freq_dom = zeros(N_folder,1); % dominant frequency of each run

record_movie = 'no';

for i=1:N_folder
    fprintf('\ni = %d \n',i)

    % if folder name is empty, skip
    if ~isempty(Folder(i).Ave)
        % read run ID
        tmp_str = regexp(Folder(i).Ave, 'rrun_\d*', 'match');
        runID = str2double(tmp_str{1}(6:end));

        % read set ID
        [setID, FOV] = find(set == runID);
        % if setID does not exist in the set list, then skip
        if ~isempty(setID)

            % Y origin
            Yorigin = 5.374 * 625.423 - 3286.5; % constant
            switch FOV
                case 1
                    YCoord = 0;
                case 2
                    YCoord = 456;
                case 3
                    YCoord = 920.2;
            end

            % X origin
            if setID <=5
                XCoord = 30; % xoffset (mm)
            else
                XCoord = 14; % xoffset (mm)
            end

            YShift = Yorigin + YCoord;
            XShift = XCoord;
        end
    end
end

```

```
        % read raw data, save processed SVD data, and return
        dominant frequency
        freq_dom(i) = vc7_read_v8(Folder(i).Ave, YShift, XShift,
            record_movie, force_overwrite);
    end
end
end

%% save dominant frequency data
save([prefix 'freq_5b.mat'], 'freq_dom');

%% copy data (rearrange processed data based on its runID)
batch_copy_file
batch_copy_file2
```

C.1.2 vc7_read_v8.m

```
function freq_dom = vc7_read_v8(file_path, YShift, XShift, rec_movie,
    force_overwrite)
%VC7_READ_V8
% Read vc7 binary files, compute singular vector decompositions
% output:
%   freq_dom: dominant frequency of the given set and FOV
%
% input:
%   file_path: string variable that indicates where vc7 files are
    located
%   YShift, XShift: origin of the FOV
%   rec_movie: (not used any more)
%   force_overwrite: overwrite existing files if true, load existing
    files if false
%
% Note: No vorticity computation in this file. See 'record_movie.m' for
    vorticity computation & video conversion.
% Note: velocity is stored in m/s unit, while all other variables are in
    mm.
% Written by Seongjin Yoon, University of Michigan, 2017

%% raw data read parameters
file_name_raw = 'B*.vc7'; % VC7 file name convention
f_sampling = 12; % sampling frequency of the raw data (Hz)
dt = 1/f_sampling; % time step of the raw data

%% processed data store parameters
% subdirectory to store processed data
dir_proc = 'Processed_SJ\';
% SVD parameters
N_svd = 8; % # of singular values to be evaluated
% figures / movie setting
print_figure = true;

%% channel geometry parameters
d_hyd = 127; % hydraulic diameter (mm)
w_gap = 228.6; % gap width (mm)

%% raw data loading
disp(['Move to ' file_path])
cd(file_path);
if ~exist(dir_proc, 'dir')
```

```

        mkdir(dir_proc);
end

vc7_list = dir(file_name_raw);
N_t = length(vc7_list); % total number of frames

tmp = readimx(vc7_list(N_t).name); % read the last PIV file to get the
    axis information
tmp_v = create2DVec_SJ(tmp.Frames{1});
grd_T = (0:N_t-1)*dt; % time grid
grd_F = (0:N_t/2)/N_t*f_sampling;% frequency grid
% Note: camera is 90 degrees rotated, so the vertical axis is x, and
    transverse axis is y in the PIV (.vc7) file.
grd_Y = tmp_v.X+YShift; % spatial y grid (X in the PIV file)
grd_X = tmp_v.Y+XShift; % spatial x grid (Y in the PIV file)
[grd_YY, grd_XX] = ndgrid(grd_Y, grd_X); % Note: data is stored in
    ndgrid format
[N_y, N_x] = size(tmp_v.U);
N_xy = N_y * N_x;

im_name = 'raw_data_v3.mat';
if exist([dir_proc, im_name], 'file')
    fprintf('load Matlab-formatted raw data \n \n');
    load([dir_proc, 'raw_data_v3.mat']);
else
    fprintf('perform raw data loading \n'); tic;
    % initialize arrays
    t_stamp = zeros(N_t,1);
    U_dat{1} = zeros(N_y, N_x, N_t); % vertical velocity (V)
    U_dat{2} = zeros(N_y, N_x, N_t); % transverse velocity (U)

    % find AcqTimeSeries (believed to be actual acquisition time, but
        unreasonably fluctuating)
    % AcqTimeSeries has not been used for analysis as it is unreliable.
    for i=1:length(tmp.Frames{1}.Attributes)
        if strcmp(tmp.Frames{1}.Attributes{i}.Name, 'AcqTimeSeries')
            ATS_idx = i;
            break;
        elseif i == length(tmp.Frames{1}.Attributes)
            error('AcqTimeSeries not found.')
        end
    end
end
end

```



```

% read raw velocity data & save into 3-D matrix (y,x,t) format
for i=1:N_t
    tmp = readimx(vc7_list(i).name);
    tmp_v = create2DVec_SJ(tmp.Frames{1});
    t_stamp(i) = getTimeStamp(tmp.Frames{1},ATS_idx);
    U_dat{1}(:, :, i) = tmp_v.U; % vertical velocity (V), (90 degrees
        rotated)
    U_dat{2}(:, :, i) = tmp_v.V; % transverse velocity (U), (90
        degrees rotated)
end
save([dir_proc, im_name], 't_stamp', 'U_dat')
fprintf('data loading finished, elapsed time = %0.3f s \n \n', toc);
end

% % time stamp (time stamp in the raw data is unreliable, even step size
    is used instead.)
% grd_T = (t_stamp - t_stamp(1)) / 10^6; % convert microsecond to second
    , and set the start time as zero.
% % plot time steps
% t_dt = circshift(t_stamp, [-1 0]) - t_stamp;
% t_dt(end) = mean(t_dt(1:end-1));
%
% figure(fig_num); clf; fig_num = fig_num + 1;
% plot(t_dt)
% xlabel('Frame')
% ylabel('\Deltat [\mus]')

%% move to the processed data directory
cd(dir_proc)
if force_overwrite == true
    delete('*.png');
    delete('*.mp4');
else
    delete('*.png');
end

%% frequency analysis
fprintf('perform peak frequency analysis \n'); tic;
U_freq = cell(2);
U_max_coef = cell(2);
U_max_f = cell(2);
for i=1:2
    U_freq{i} = fft(U_dat{i}, N_t, 3);

```

```

[U_max_coef{i}, U_max_f{i}] = max(abs(U_freq{i}(:, :, 2:N_t/2+1))
    , [], 3); % find peak index excluding the mean
U_max_f{i} = grd_F(U_max_f{i}+1); % find peak frequency excluding
    the mean
end
freq_dom = mode(col([U_max_f{1}; U_max_f{2}])); % dominant peak
    frequency
fprintf('peak frequency analysis finished, elapsed time = %0.3f s \n \n'
    , toc);

%% plot peak frequencies
figure(1)
imagesc([min(grd_Y), max(grd_Y)]/w_gap, [max(grd_X), min(grd_X)]/w_gap,
    U_max_f{1}', [0 3]);
text(0.1, -0.4, sprintf('dominant peak frequency = %.4f', freq_dom), '
    HorizontalAlignment', 'left', 'VerticalAlignment', 'top')
axis xy
% title('Peak frequency map, V (Hz)')
ylabel('x/w_g')
xlabel('y/w_g')
colorbar
drawnow;

figure(2)
imagesc([min(grd_Y), max(grd_Y)]/w_gap, [max(grd_X), min(grd_X)]/w_gap,
    U_max_f{2}', [0 3]);
text(0.1, -0.4, sprintf('dominant peak frequency = %.4f', freq_dom), '
    HorizontalAlignment', 'left', 'VerticalAlignment', 'top')
axis xy
% title('Peak frequency map, U (Hz)')
ylabel('x/w_g')
xlabel('y/w_g')
colorbar
drawnow;

%% power spectral density of V
shift_up = 5; % shift up the spectrum for visualization purpose
[~, c_idx] = min(abs(grd_X));
step_idx = floor(min(c_idx-1, length(grd_X)-c_idx)/2);

figure(3)
tmp_psd = abs(col(U_freq{1}(round((end+1)/2), c_idx + step_idx*2, 1:N_t
    /2+1))).^2/(f_sampling*N_t);

```

```

tmp_psd(2:end-1) = 2*tmp_psd(2:end-1); % double the value except zero
    and Nyquist frequency
semilogy(grd_F, imfilter(tmp_psd,fspecial('gaussian',[7 1],0.75),'
    replicate'))
hold on;

tmp_psd = abs(col(U_freq{1}(round((end+1)/2),c_idx + step_idx,1:N_t/2+1)
    )).^2/(f_sampling*N_t);
tmp_psd(2:end-1) = 2*tmp_psd(2:end-1); % double the value except zero
    and Nyquist frequency
semilogy(grd_F, imfilter(tmp_psd*10^(shift_up*1),fspecial('gaussian',[7
    1],0.75),'replicate'))

tmp_psd = abs(col(U_freq{1}(round((end+1)/2),c_idx,1:N_t/2+1)).^2/(
    f_sampling*N_t);
tmp_psd(2:end-1) = 2*tmp_psd(2:end-1); % double the value except zero
    and Nyquist frequency
semilogy(grd_F, imfilter(tmp_psd*10^(shift_up*2),fspecial('gaussian',[7
    1],0.75),'replicate'))

tmp_psd = abs(col(U_freq{1}(round((end+1)/2),c_idx - step_idx,1:N_t/2+1)
    )).^2/(f_sampling*N_t);
tmp_psd(2:end-1) = 2*tmp_psd(2:end-1); % double the value except zero
    and Nyquist frequency
semilogy(grd_F, imfilter(tmp_psd*10^(shift_up*3),fspecial('gaussian',[7
    1],0.75),'replicate'))

tmp_psd = abs(col(U_freq{1}(round((end+1)/2),c_idx - step_idx*2,1:N_t
    /2+1)).^2/(f_sampling*N_t);
tmp_psd(2:end-1) = 2*tmp_psd(2:end-1); % double the value except zero
    and Nyquist frequency
semilogy(grd_F, imfilter(tmp_psd*10^(shift_up*4),fspecial('gaussian',[7
    1],0.75),'replicate'))
hold off;
xlim([min(grd_F)-0.1 max(grd_F)+0.1])
ylim([10^-5 10^25])

% title('Power spectral density of V')
xlabel('frequency (Hz)')
ylabel('\Phi_V (m^2/s)')

text(0.15, 10^(shift_up*4-1), '1','HorizontalAlignment','left','
    VerticalAlignment','top')

```

```

text(0.15, 10^(shift_up*3-1), '2', 'HorizontalAlignment', 'left', '
    VerticalAlignment', 'top')
text(0.15, 10^(shift_up*2-1), '3', 'HorizontalAlignment', 'left', '
    VerticalAlignment', 'top')
text(0.15, 10^(shift_up*1-1), '4', 'HorizontalAlignment', 'left', '
    VerticalAlignment', 'top')
text(0.15, 10^(shift_up*0-1), '5', 'HorizontalAlignment', 'left', '
    VerticalAlignment', 'top')

%% power spectral density of U
figure(4)
tmp_psd = abs(col(U_freq{2}(round((end+1)/2), c_idx + step_idx*2, 1:N_t
    /2+1))).^2/(f_sampling*N_t);
tmp_psd(2:end-1) = 2*tmp_psd(2:end-1);
semilogy(grd_F, imfilter(tmp_psd, fspecial('gaussian', [7 1], 0.75), '
    replicate'))
hold on;

tmp_psd = abs(col(U_freq{2}(round((end+1)/2), c_idx + step_idx, 1:N_t/2+1)
    )).^2/(f_sampling*N_t);
tmp_psd(2:end-1) = 2*tmp_psd(2:end-1);
semilogy(grd_F, imfilter(tmp_psd*10^(shift_up*1), fspecial('gaussian', [7
    1], 0.75), 'replicate'))

tmp_psd = abs(col(U_freq{2}(round((end+1)/2), c_idx, 1:N_t/2+1))).^2/(
    f_sampling*N_t);
tmp_psd(2:end-1) = 2*tmp_psd(2:end-1);
semilogy(grd_F, imfilter(tmp_psd*10^(shift_up*2), fspecial('gaussian', [7
    1], 0.75), 'replicate'))

tmp_psd = abs(col(U_freq{2}(round((end+1)/2), c_idx - step_idx, 1:N_t/2+1)
    )).^2/(f_sampling*N_t);
tmp_psd(2:end-1) = 2*tmp_psd(2:end-1);
semilogy(grd_F, imfilter(tmp_psd*10^(shift_up*3), fspecial('gaussian', [7
    1], 0.75), 'replicate'))

tmp_psd = abs(col(U_freq{2}(round((end+1)/2), c_idx - step_idx*2, 1:N_t
    /2+1))).^2/(f_sampling*N_t);
tmp_psd(2:end-1) = 2*tmp_psd(2:end-1);
semilogy(grd_F, imfilter(tmp_psd*10^(shift_up*4), fspecial('gaussian', [7
    1], 0.75), 'replicate'))
hold off;

```

```

xlim([min(grd_F)-0.1 max(grd_F)+0.1])
ylim([10^-5 10^25])

% title('Power spectral density of U')
xlabel('frequency (Hz)')
ylabel('\Phi_U (m^2/s)')

text(0.15, 10^(shift_up*4-1), '1', 'HorizontalAlignment', 'left', '
    VerticalAlignment', 'top')
text(0.15, 10^(shift_up*3-1), '2', 'HorizontalAlignment', 'left', '
    VerticalAlignment', 'top')
text(0.15, 10^(shift_up*2-1), '3', 'HorizontalAlignment', 'left', '
    VerticalAlignment', 'top')
text(0.15, 10^(shift_up*1-1), '4', 'HorizontalAlignment', 'left', '
    VerticalAlignment', 'top')
text(0.15, 10^(shift_up*0-1), '5', 'HorizontalAlignment', 'left', '
    VerticalAlignment', 'top')

if print_figure == true
    print_sj_png('freq_analysis', 4/3);
end
close all;

%%
% mean velocity field
U_dat_mean = cell(2,1);
for i=1:2
    U_dat_mean{i} = mean(U_dat{i},3);
end

% plot mean velocity field
close all;
figure(1); clf;

sline = streamline(grd_YY'/w_gap, grd_XX'/w_gap,...
    U_dat_mean{1}',...
    U_dat_mean{2}',...
    downsample2(grd_YY'/w_gap, [2 2], 'warn', false),...
    downsample2(grd_XX'/w_gap, [2 2], 'warn', false), [0.1 80]);
set(sline, 'Color', [0.2 0.6 1]);
hold on;
quiver( downsample2(grd_YY/w_gap, [3 3], 'warn', false),...
    downsample2(grd_XX/w_gap, [3 3], 'warn', false),...

```

```

        downsample2(U_dat_mean{1}, [3 3], 'warn', false), ...
        downsample2(U_dat_mean{2}, [3 3], 'warn', false), ...
        'r', 'LineWidth', 0.75);

% Below indicate where the data for the power spectral densities are
% sampled on the mean velocity field figure
% plot(grd_Y(ceil((end+1)/2))/w_gap, grd_X(c_idx + step_idx*2)/w_gap, 'k
% *');
% plot(grd_Y(ceil((end+1)/2))/w_gap, grd_X(c_idx + step_idx*1)/w_gap, 'k
% *');
% plot(grd_Y(ceil((end+1)/2))/w_gap, grd_X(c_idx + step_idx*0)/w_gap, 'k
% *');
% plot(grd_Y(ceil((end+1)/2))/w_gap, grd_X(c_idx + step_idx*-1)/w_gap, 'k
% *');
% plot(grd_Y(ceil((end+1)/2))/w_gap, grd_X(c_idx + step_idx*-2)/w_gap, 'k
% *');
% text((grd_Y(ceil((end+1)/2))+5)/w_gap, (grd_X(c_idx + step_idx*2)+10)/
% w_gap, '5', 'Color', 'k', 'FontSize', 14);
% text((grd_Y(ceil((end+1)/2))+5)/w_gap, (grd_X(c_idx + step_idx*1)+10)/
% w_gap, '4', 'Color', 'k', 'FontSize', 14);
% text((grd_Y(ceil((end+1)/2))+5)/w_gap, (grd_X(c_idx + step_idx*0)+10)/
% w_gap, '3', 'Color', 'k', 'FontSize', 14);
% text((grd_Y(ceil((end+1)/2))+5)/w_gap, (grd_X(c_idx + step_idx*-1)+10)
% /w_gap, '2', 'Color', 'k', 'FontSize', 14);
% text((grd_Y(ceil((end+1)/2))+5)/w_gap, (grd_X(c_idx + step_idx*-2)+10)
% /w_gap, '1', 'Color', 'k', 'FontSize', 14);
hold off;

% title('Time-averaged velocity field')
ylabel('x/w_g')
xlabel('y/w_g')
xlim([min(grd_Y)-1 max(grd_Y)+1]/w_gap)
ylim([min(grd_X)-1 max(grd_X)+1]/w_gap)

if print_figure == true
    print_sj_png('VEL_time_avg', 4/3);
end
close all;

%% SVD without phase averaging
if exist(sprintf('SVD_Ns=%.0f.mat', N_svd), 'file') && (force_overwrite
== false)
    fprintf('load SVD data \n \n');

```

```

    load(sprintf('SVD_Ns=%.0f.mat', N_svd))
else
    fprintf('perform SVD, without phase averaging \n'); tic;

    % mean subtraction
    U_dat_sub{1} = bsxfun(@minus, U_dat{1}, U_dat_mean{1});
    U_dat_sub{2} = bsxfun(@minus, U_dat{2}, U_dat_mean{2});

    % perform velocity SVD
    [U_L_svd, U_S_svd, U_R_svd] = svds([reshape(U_dat_sub{1}, [N_xy,N_t
        ]);...
        reshape(U_dat_sub{2}, [N_xy,N_t])], N_svd);

    % FFT
    U_R_svd_freq = fft(U_R_svd, size(U_R_svd,1), 1);

    % total energy
    energy_sum_vel = sum(col(U_dat_sub{1}).^2) + sum(col(U_dat_sub{2})
        .^2);

    fprintf('SVD finished, elapsed time = %0.3f s \n\n', toc);
end

% compute energy ratio
energy_par_sum = 0;
energy_ratio_vel = zeros(N_svd,1); % cumulative energy of modes divided
    by the total energy
for i=1:N_svd
    energy_par_sum = energy_par_sum + U_S_svd(i,i).^2;
    energy_ratio_vel(i) = energy_par_sum / energy_sum_vel;
    fprintf('Modes up to %d contain %2.2f%% of total energy \n', i,
        energy_ratio_vel(i)*100)
end

% prefix for the SVD plot
im_name = sprintf('SVD_vel');

% plot singular values
close all;
% singular values
figure(1); clf;
subplot('Position',[0.13 0.15 0.78 0.75]);
bar(diag(U_S_svd)/sqrt(N_xy*N_t))

```

```

ylim([0 0.35])
xlabel('mode')
ylabel('$\sigma_i / (N_x N_y N_t)^{1/2}$ \hspace{5pt} (m/s)', '
    interpreter','latex')

% energy ratio
figure(2); clf;
bar(diag(U_S_svd).^2 / energy_sum_vel)
ylim([0 0.7])
xlabel('mode')
ylabel('$\sigma_i^2 / \sum_{\{i,j\}} \sigma_j^2$', 'interpreter','latex')

if print_figure == true
    print_sj_png([im_name '_sval']);
end
close all;

% plot singular vectors u & v, in stream lines
for s=1:6
    figure(s); clf;
    subplot('Position',[0.15 0.37 0.75 0.58]);

    sline = streamline(grd_YY'/w_gap, grd_XX'/w_gap,...
        reshape(U_L_svd(1:N_xy,s), [N_y,N_x]),...
        reshape(U_L_svd(N_xy+1:2*N_xy,s), [N_y,N_x]),...
        downsample2(grd_YY'/w_gap,[2 2],'warn',false),...
        downsample2(grd_XX'/w_gap,[2 2],'warn',false),[0.1 80]);
    set(sline,'Color',[0.2 0.6 1]);
    hold on;
    quiver( downsample2(grd_YY/w_gap,[3 3],'warn',false),...
        downsample2(grd_XX/w_gap,[3 3],'warn',false),...
        downsample2(reshape(U_L_svd(1:N_xy,s), [N_y,N_x]),[3 3], '
            warn',false),...
        downsample2(reshape(U_L_svd(N_xy+1:2*N_xy,s), [N_y,N_x]),[3
            3],'warn',false),...
            'r','LineWidth',0.75);
    hold off;
    xlim([min(grd_Y)-1 max(grd_Y)+1]/w_gap)
    ylim([min(grd_X)-1 max(grd_X)+1]/w_gap)
    ylabel('x/w_g')
    xlabel('y/w_g')
    title([str_ord(s) ' left (spatial) singular vector, stream line'])
    % str_ord: return ordinal number in string

```



```

    subplot('Position',[0.15 0.1 0.75 0.1]);
    plot(grd_T, U_R_svd(:,s));
    title([str_ord(s) ' right (temporal) singular vector'])
    xlim([0 1/freq_dom*10]);
    xlabel('time (s)')
end

if print_figure == true
    print_sj_png([im_name '_svec_stream'],4/3);
end
close all;

% plot singular vectors u in contour plot
for s=1:6
    figure(s); clf;
    subplot('Position',[0.15 0.37 0.75 0.58]);
    contour(grd_YY/w_gap, grd_XX/w_gap,...
        reshape(U_L_svd(1:N_xy,s),[N_y,N_x]),40);
    colormap(jet); colorbar;
    xlim([min(grd_Y)-1 max(grd_Y)+1]/w_gap)
    ylim([min(grd_X)-1 max(grd_X)+1]/w_gap)
    ylabel('x/w_g')
    xlabel('y/w_g')
    title([str_ord(s) ' left (spatial) singular vector, contour of V'])

    subplot('Position',[0.15 0.1 0.75 0.1]);
    plot(grd_T, U_R_svd(:,s));
    title([str_ord(s) ' right (temporal) singular vector'])
    xlim([0 1/freq_dom*10]);
    xlabel('time (s)')
end

if print_figure == true
    print_sj_png([im_name '_svec_contour_V'],4/3);
end
close all;

% plot singular vectors v in contour plot
for s=1:6
    figure(s); clf;
    subplot('Position',[0.15 0.37 0.75 0.58]);
    contour(grd_YY/w_gap, grd_XX/w_gap, reshape(U_L_svd(N_xy+1:2*N_xy,s)

```

```

        , [N_y,N_x]),40);
colormap(jet); colorbar;
xlim([min(grd_Y)-1 max(grd_Y)+1]/w_gap)
ylim([min(grd_X)-1 max(grd_X)+1]/w_gap)
ylabel('x/w_g')
xlabel('y/w_g')
title([str_ord(s) ' left (spatial) singular vector, contour of U'])

subplot('Position',[0.15 0.1 0.75 0.1]);
plot(grd_T, U_R_svd(:,s));
title([str_ord(s) ' right (temporal) singular vector'])
xlim([0 1/freq_dom*10]);
xlabel('time (s)')
end

if print_figure == true
    print_sj_png([im_name '_svec_contour_U'],4/3);
end
close all;

%% power spectral density of right singular vectors (without phase-
    averaging)
figure(1); clf;
shift_up = 1; % shift up each spectrum by shift_up*(mode-1) for
    visualization purpose
hold on;
for s=1:6
    tmp_psd = abs(col(U_R_svd_freq(1:(N_t/2+1), s))).^2/N_t;
    tmp_psd(2:end-1) = 2*tmp_psd(2:end-1);
    plot(col(grd_F)/freq_dom, col(tmp_psd)+shift_up*(s-1));
    text(1/16, shift_up*(s-1) + 0.15 ,str_ord(s));
end
hold off;
xlim([0 4])
ax = gca;
set(ax,'XTick',[0 1 2 3 4 5 6]);
title('Power spectral density of right singular vectors');
xlabel('$f/f_d$', 'interpreter','latex')

% zoomed-in plot for 1st right singular vector
figure(2)
subplot(211)
tmp_psd = abs(col(U_R_svd_freq(1:N_t/2+1, 1))).^2/N_t;

```

```

tmp_psd(2:end-1) = 2*tmp_psd(2:end-1);
plot(col(grd_F)/freq_dom, col(tmp_psd));
xlim([0.95 1.05])
xlabel('$f/f_d$', 'interpreter', 'latex')

% zoomed-in plot for 3rd right singular vector
subplot(212)
tmp_psd = abs(col(U_R_svd_freq(1:N_t/2+1, 3))).^2/N_t;
tmp_psd(2:end-1) = 2*tmp_psd(2:end-1);
plot(col(grd_F)/freq_dom, col(tmp_psd));
xlim([1.95 2.05])
xlabel('$f/f_d$', 'interpreter', 'latex')

if print_figure == true
    print_sj_png([im_name '_svec_FFT'], 4/3);
end
close all;

%% save data
if exist(sprintf('SVD_Ns=%.0f.mat', N_svd), 'file') && (force_overwrite
    == false)
    % The file already exists, and do not overwrite
else
    save(sprintf('SVD_Ns=%.0f.mat', N_svd), ...
        'freq_dom', 'grd_X', 'grd_Y', 'grd_T', 'grd_F', ...
        'U_dat_mean', ...
        'U_L_svd', 'U_S_svd', 'U_R_svd', 'U_R_svd_freq', 'energy_sum_vel'
    );
end

```

C.2 Matlab codes for mixing coefficient estimation

C.2.1 batch_compute_mixing_v5.m

```
% BATCH_COMPUTE_MIXING_V5
% Define set ID, then call 'compute_mixingxx.m' for each set to compute
    mixing coefficients
% based on the SVD data obtained by 'batch_read_PA_SVD.m'.
%
% Written by Seongjin Yoon, University of Michigan, 2017

clear variables; cls;
src_folder = 'C:/task 5b_processed/';

%% set definition
% set ID      1  2  3  4  5      6  7  8  9 10      11 12 13
    14 15
set_FOV1 = [ 1,  6,  5,  2,  3,      89, 92, 93, 90, 91,      63, 66, 67,
    64, 65]'; % FOV 1 (lower window)
set_FOV2 = [12, 15, 16, 13, 14,      84, 87, 88, 85, 86,      68, 71, 72,
    69, 70]'; % FOV 2 (middle window)
set_FOV3 = [ 7, 10, 11,  8,  9,      78, 81, 83, 79, 80,      73, 76, 77,
    74, 75]'; % FOV 3 (upper window)

% Reynolds numbers for each set ID
%      [ A,  B] x 1000
Re(1,1:2) = [100, 100]; % gap 50
Re(2,1:2) = [ 40, 100];
Re(3,1:2) = [ 40,  40];
Re(4,1:2) = [ 80, 100];
Re(5,1:2) = [ 60, 100];

Re(6,1:2) = [100, 100]; % gap 20
Re(7,1:2) = [ 40, 100];
Re(8,1:2) = [ 40,  40];
Re(9,1:2) = [ 80, 100];
Re(10,1:2) = [ 60, 100];

Re(11,1:2) = [100, 100]; % gap 10
Re(12,1:2) = [ 40, 100];
Re(13,1:2) = [ 40,  40];
Re(14,1:2) = [ 80, 100];
```

```

Re(15,1:2)= [ 60, 100];

% nominal flow speed based on the Renolds number
d_hyd = 127; % hydraulic diameter (mm)
mu_water = 1; % kinematic viscosity (mm^2/s)
V_nominal = Re*1000/d_hyd*mu_water; % nominal flow speed based on Re (mm
/s)

% gap thickness for each set ID
h_gap(1:5) = 50;
h_gap(6:10) = 20;
h_gap(11:15)= 10;

% balanced flow set ID
set_100_100 = [ 1, 6, 11];
set_40_40 = [ 3, 8, 13];
% unbalanced flow set ID
set_40_100 = [ 2, 7, 12];
set_60_100 = [ 5, 10, 15];
set_80_100 = [ 4, 9, 14];

% compute mixing coefficients
N_set = length(set_FOV1);

steady_mix_coeff = zeros(2,N_set);
coherent_mix_coeff = zeros(2,N_set);
coherent_FOV = init_cell([N_set,1],zeros(2,3));

for setID = 1:15
    file_path{1} = [src_folder 'rrun_' num2str(set_FOV1(setID),'%2.0f')
        '/'];
    file_path{2} = [src_folder 'rrun_' num2str(set_FOV2(setID),'%2.0f')
        '/'];
    file_path{3} = [src_folder 'rrun_' num2str(set_FOV3(setID),'%2.0f')
        '/'];
    [steady_mix_coeff(:,setID), coherent_mix_coeff(:,setID),
        coherent_FOV{setID}] = ...
        compute_mixing5(file_path, h_gap(setID), V_nominal(setID)
            ,:));
end

total_mix_coeff = steady_mix_coeff+coherent_mix_coeff;

```

```
save('mix_coeff_PIV')
```

C.2.2 compute_mixing5.m

```
function [steady_mix_coeff, coherent_mix_coeff, coherent_FOV] =
    compute_mixing5(file_path, h_gap, v_nominal)
% COMPUTE_MIXING5
% approximate mixing coefficients based on the given SVD data
% output:
%   steady_mix_coeff: returns steady mixing coefficients x and y
%       computed base on mean flow velocity data of FOV{1}, FOV{2}, and
%       FOV{3}
%   coherent_mix_coeff: returns coherent mixing coefficients x and y
%       computed base on singular modes of FOV{1}, FOV{2}, and FOV{3}
%   coherent_FOV: returns coherent mixing coefficient x and y for each
%       FOV
%
% input:
%   file_path: cell array (3x1) of file paths for SVD data of FOV{1},
%       FOV{2}, and FOV{3}
%   h_gap: gap height
%   v_nominal: (1x2) nominal velocities of channel A and B based on the
%       Reynolds numbers.
%
% Written by Seongjin Yoon, University of Michigan, 2017

%#ok<*NASGU>    % suppress 'assigned variable never used' warning
%#ok<*ASGLU>    % suppress 'returned variable never used' warning

N_svd = 8; % # of singular modes

d_hyd = 127; % hydraulic diameter (mm)
w_gap = 228.6; % gap width (mm)

% initialize
temp_x = zeros(1,4);
temp_y = zeros(1,4);
steady_mix_coeff = zeros(2,1);
coherent_mix_coeff = zeros(2,1);
coherent_FOV = zeros(2,3);

steady_flow = 0;
coherent_flow_AtoB = 0;
coherent_flow_BtoA = 0;
% load data
for fovID = 1:3
```

```

load([file_path{fovID}, sprintf('SVD_Ns=%.0f.mat', N_svd)]);

N_x = length(grd_X);
N_y = length(grd_Y);
N_T = length(grd_T);
N_xy = N_x * N_y;

dx = grd_X(2)-grd_X(1);
dy = grd_Y(2)-grd_Y(1);
dT = grd_T(2)-grd_T(1);

[grd_YY, grd_XX] = ndgrid(grd_Y, grd_X);
cnt_YY = grd_Y';
cnt_XX = zeros(size(grd_Y))';

% FOV correction factor beta and gamma
switch(fovID)
    case 1
        beta = 1.0;
        gamma = 1.275;
    case 2
        beta = 2.114;
        gamma = 1.537;
    case 3
        beta = 1.0;
        gamma = 1.328;
end

% steady mixing
U_A = sum(U_dat_mean{2}(:,3)) * dy*h_gap*1000;
U_B = sum(U_dat_mean{2}(:,N_x-1)) * dy*h_gap*1000;
steady_flow = steady_flow + (U_A + U_B)/2*beta;

% coherent mixing
for svdID=1:2
    T = U_R_svd(:,svdID);
    T_plus = sum(T(T>0))/N_T;
    T_minus = -sum(T(T<0))/N_T;
    % line integral of the transverse velocity along the edges of A
    and B
    % (not exactly a transverse velocity because the temporal
    singular vector is not multiplied)
    U = reshape(U_L_svd(N_xy+1:2*N_xy,svdID), [N_y,N_x]) * U_S_svd(

```



```

        svdID,svdID);
U_Ain = -sum(min(U(:,3),0))*dy*h_gap*1000; % convert from m/s to
        mm/s
U_Aout= sum(max(U(:,3),0))*dy*h_gap*1000;
U_Bin = sum(max(U(:,N_x-1),0))*dy*h_gap*1000;
U_Bout= -sum(min(U(:,N_x-1),0))*dy*h_gap*1000;

U_in = U_Ain + U_Bin;
U_out = U_Aout + U_Bout;
U_diff = U_in - U_out;

% FOV correction factor alpha
if U_diff > 0 % in > out
    U_Aout = U_Aout + U_diff * U_Ain/U_in;
    U_Bout = U_Bout + U_diff * U_Bin/U_in;
    alpha = 1-abs(U_diff)/(U_in);
else % in < out
    U_Ain = U_Ain - U_diff * U_Aout/U_out;
    U_Bin = U_Bin - U_diff * U_Bout/U_out;
    alpha = 1-abs(U_diff)/(U_out);
end
% Note: after correction, U_Ain + U_Bin = U_Aout + U_Bout

F_AtoB = (U_Ain) / (U_Ain + U_Bin) * U_Bout;
F_BtoA = (U_Bin) / (U_Ain + U_Bin) * U_Aout;

coherent_flow_AtoB = coherent_flow_AtoB + (F_AtoB*T_plus +
        F_BtoA*T_minus)*alpha*gamma;
coherent_flow_BtoA = coherent_flow_BtoA + (F_BtoA*T_plus +
        F_AtoB*T_minus)*alpha*gamma;

coherent_FOV(1,fovID) = coherent_FOV(1,fovID) + (F_AtoB*T_plus +
        F_BtoA*T_minus)*alpha;
coherent_FOV(2,fovID) = coherent_FOV(2,fovID) + (F_BtoA*T_plus +
        F_AtoB*T_minus)*alpha;
end
end

% steady mixing coefficients
if steady_flow > 0
    steady_mix_coeff(2) = steady_flow / (d_hyd^2 * v_nominal(2));
else
    steady_mix_coeff(1) = -steady_flow / (d_hyd^2 * v_nominal(1));
end

```

```
end
% coherent mixing coefficients
coherent_mix_coeff(1) = coherent_flow_AtoB / (d_hyd^2 * v_nominal(1));
coherent_mix_coeff(2) = coherent_flow_BtoA / (d_hyd^2 * v_nominal(2));
% coherent mixing at each FOVs
coherent_FOV(1,:) = coherent_FOV(1,:) / (d_hyd^2 * v_nominal(1));
coherent_FOV(2,:) = coherent_FOV(2,:) / (d_hyd^2 * v_nominal(2));
```